Polynuclear titanium complexes for the ring-opening polymerisation of lactide

Jean-Marie Eugène Pascal Cols

Submitted for the Degree of Doctor of Philosophy

Institute of Chemical Sciences

Heriot-Watt University

September 2017

Abstract

The research presented herein explores the synthesis and characterisation of polynuclear titanium complexes developed as initiators or catalysts for the production of the renewable and green polymer, polylactide. A series of polynuclear titanium isopropoxide initiators, existing as dynamic aggregates held by bridging carboxylate groups tethered to the ligand, were effective initiators in the ring-opening polymerisation of *rac*-lactide. The nuclearity of these aggregates in solution was related to the steric bulk on the ligand periphery and correlated with increasing activity. Controlled hydrolysis of these aggregated initiators led to the formation of air- and water-stable, tetrametallic, titanium-oxo pre-catalysts that were activated *in situ* under melt polymerisation conditions. In this case, activity was qualitatively linked to the solubility of the catalysts in molten lactide. These pre-catalysts could be further hydrolysed in the presence of 4-dimethylaminopyridine to form cyclic and linear tetrametallic titanium-oxo species, with Ti_4O_4 and Ti_4O_3 cores respectively, which were also active towards the ring-opening polymerisation of lactide. An alternative synthetic route to these species, a one-pot solvothermal synthesis, favoured the formation of cyclic titanium-oxo compounds, where the titanium-oxo nuclearity of the isolated species was found to decrease with increasing steric bulk around the ligand periphery. Overall, the homogeneity of the titanium compounds was key to studying their behaviour in detail, ultimately allowing for meaningful conclusions to be drawn between catalyst design and performance.

“If something is important enough, you should try.
Even if the probable outcome is failure.”

– Elon Musk

Acknowledgements

I thank Dr Ruaraidh D. McIntosh for his support and guidance with this research. Dr Scott. J. Dalgarno was my mentor throughout my undergraduate studies and he willingly stood as a supportive member of staff during my PhD studies. Dr Dave Ellis made time for demonstrations of NMR spectroscopy and subsequent scientific discussions to develop and validate NMR spectroscopy experiments. I am grateful to Heriot-Watt University for financial support.

I acknowledge the analytical services from: the EPSRC National Mass Spectrometry Facility (NMSF) and the University of Edinburgh for mass spectrometry and single crystal X-ray diffraction data; the Advanced Light Source Facility at the Lawrence Berkeley National Laboratory for single crystal X-ray diffraction data. The Advanced Light Source is supported by the Director, Office of Science, Office of Basic Energy Sciences, of the U.S. Department of Energy under contract No. DE-AC02-05CH11231

I enjoyed the supervision of undergraduate projects in the laboratory and the following undergraduate students contributed to the pieces of work outlined below:

Victoria G. Hill: for her work with amine bis(2,4-di-*tert*-butylphenolate) ligand precursors and titanium complexes.

Stella K. Williams: for her work on amine bis(phenolate) ligand precursors with *L*-alanine and *L*-phenylalanine cores.

Table of Contents

Chapter 2: Polynuclear titanium isopropoxide initiators

Chapter 3: Titanium-oxo tetragonal disphenoids

Chapter 4: Tetrametallic titanium-oxo compounds

Chapter 5: Tetrametallic titanium-oxo compounds for the ROP of *rac*-lactide

Chapter 6: Towards solution stable titanium-oxo compounds

Chapter 7: Conclusions

Chapter 8: Appendix

Abbreviations

CIF – crystallographic information file

COSY – homonuclear correlation spectroscopy

CP-MAS – cross polarisation magic angle spinning

CSD – Cambridge Structural Database

DOSY – diffusion ordered spectroscopy, referring to NMR experiment

EAS – electrophilic aromatic substitution

EI – electron impact

ESI – electrospray ionisation, referring to MS experiment

EXSY – exchange spectroscopy, referring to NMR experiment

GPC – gel permeation chromatography, referring to the SEC technique

HMQC – heteronuclear multiple-quantum correlation

MALDI – matrix-assisted laser desorption ionisation

MS – mass spectrometry

MW – molecular weight

NMR – nuclear magnetic resonance

NOESY – nuclear Overhauser effect spectroscopy

PDI – polydispersity index

PDLA – poly-*D*-lactide

PLA – polylactide

PLLA – poly-*L*-lactide

ROESY - rotating frame nuclear Overhauser effect spectroscopy

ROP – ring-opening polymerisation

RT – room temperature (ambient temperature)

SCXRD – single crystal X-ray diffraction

TOF – time-of-flight

Units

h – hour(s)

Hz – Hertz

mins - minutes

Compounds

Bn – benzyl

BnOH – benzyl alcohol

DCM – dichloromethane

DMAP – 4-dimethylaminopyridine

DMSO – dimethylsulfoxide

*i*Pr – isopropyl

Me – methyl

MeCN – acetonitrile

*n*Pr – propyl

Ph – phenyl

Py – pyridyl

rac – racemic

*t*Bu – *tert*-butyl

tert – tertiary

THF – tetrahydrofuran (C_4H_8O)

Chapter 1: Introduction

1.1 The interface of homogeneous and heterogeneous catalysis

Only in recent years has it been recognised that an interface exists between homogeneous and heterogeneous catalytic systems, with comprehensive reviews by Finke,[1] Gates,[2] Crabtree[3,4] and Ananikov.[5] A prominent example of complexity between homogeneous and heterogeneous catalysts in the palladium(II)-catalysed arylation of olefins was reported over forty years ago during the advent of homogeneous palladium catalysts.[6,7] In this work, the catalytic activities of homogeneous palladium(II) dichloride and heterogeneous palladium black were found to be equal. The authors' investigations concluded that under the catalytic conditions, solubilised metallic palladium(0) was the active species. This was formed by leaching from the heterogeneous palladium black surface and formed by aggregation via destabilisation of palladium(II) dichloride.

Recent studies using electron microscopy have directly observed particles leaching into solution from a surface or nucleating in solution to form soluble aggregates. An example of this phenomenon was found in the study of a heterogeneous copper-oxide surface was reported, whereby the presence of small, solubilised nanoparticles in solution was captured using a powerful scanning electron microscopy (SEM) technique on vitrifed samples.[8] Metal-oxide surfaces are regarded as stable under catalytic conditions yet this study found a copper-oxide material can leach homogeneous, catalytically-active nanoparticles into solution. In this case, the catalytic system cannot be defined as homogeneous or heterogeneous, leading to greater difficulty in studying the chemical processes that are active on an atomic scale that could aid in defining and understanding the catalytic system.

This phenomenon of a "blurred definition" between homogeneous and heterogeneous systems is equally true when studying homogeneous catalysts that usually take the form of a single metal centre bound by one or more ligands. Another example of a palladium(II)-catalysed system forming nanoparticles under catalytic conditions has been recently reported.[9] This type of Suzuki-Miyaura system is widely-regarded as proceeding through active homogeneous species yet a mercury poisoning test indicated the presence of nanoparticles. These were formed *in situ* and characterised by transition electron microscopy (TEM) and X-ray photoelectron spectroscopy (XPS), indentifying

the particles to be palladium(II)-coated–palladium(0) composite species. Further studies revealed these were stable and reusable under catalytic conditions, confirming these nanoparticles are the catalytically-active species in the system.

These examples demonstrate that both surfaces and discrete metal complexes, traditionally-defined as heterogeneous and homogeneous species respectively, require thorough investigation to elucidate the identity of the active species. In turn, this greatly reinforces our understanding of catalytic systems and has prompted the scientific community to investigate and redefine the definition of heterogeneous and homogeneous systems. To summarise, the reviews by Finke,[1], Gates,[2] Crabtree[3,4] and Ananikov[5] describe catalytic systems that exhibit leaching/aggregation *in situ* by the mechanisms illustrated in Figure 1, through which the boundary between heterogeneous/homogeneous systems is blurred.

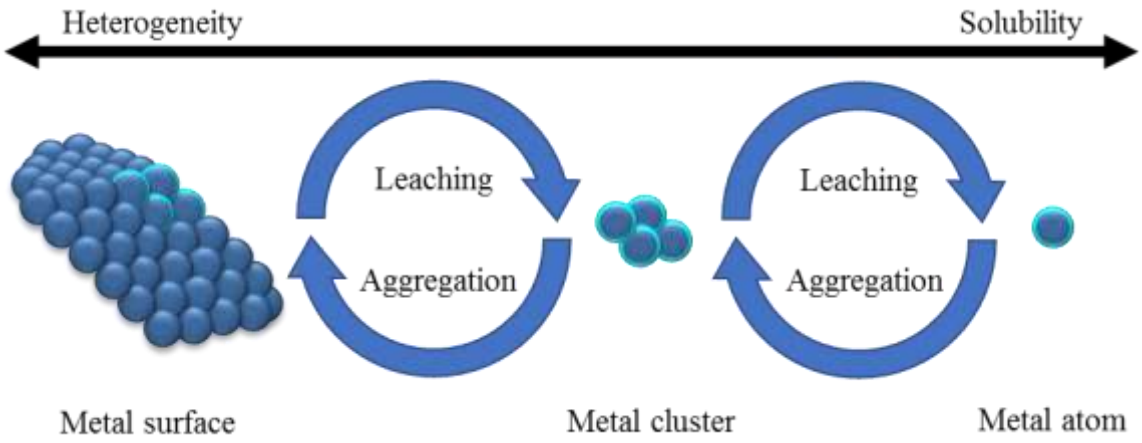

Figure 1. Schematic representation of leaching and aggregation processes experienced by a heterogeneous surface. Blue spheres indicate a metal centre with those highlighted in light blue partaking in leaching/aggregation processes.

1.2 Modelling heterogeneous systems

The lack of stability with regards to leaching/aggregation phenomena of catalysts has clouded our scientific understanding of catalytic systems. In light of this, the synthesis of stable and well-defined polymetallic complexes, such as metal clusters, is of great interest to better control the nature of the species formed during the catalytic cycle and accurately characterise the active species to improve future catalytic design.

A strategy to probe the catalytic performance of heterogeneous species is to use a model, with many reviews to cover this research area.[2,10-12] These models can make use of immobilised metal centres on a solid support or solubilised metal clusters, which mimic the performance of a metal/metal-oxo surface or nanoparticle. Recent work by Gates *et al.* found the activity of an immobilised iridium catalyst was highly sensitive to the support used, with a ten-fold increase in rate of catalytic ethene hydrogenation observed when an aluminosilicate zeolite was used in comparison to a magnesium-oxide surface.[13] This difference was attributed to differences in electron donating and withdrawing effects from the two supports, which act as ligands to the iridium metal centre, illustrating the important role the support can have on the performance of the catalytic centre. In turn, this example demonstrates the strong influence bulk metal atoms can have on surface atoms. Another case of a heterogeneously-supported catalyst was presented by Kitigawa *et al.*,[14] featuring a porous coordination polymer with nanochannels that provide a template for unsaturated terbium sites that could be thought to be akin to those found on a heterogeneous surface. In this way, it could be envisaged that a heterogeneous support with a well-defined, regular arrangement of unsaturated metal sites could act as a model to understand the properties that influence the performance of surface or nanoparticle catalysts. In this particular case, the copolymerisation of methyl methacrylate and styrene was studied, with infrared spectroscopy showing the importance of simultaneous coordination of methyl methacrylate to the unsaturated metal sites to increase its proportion in the resulting copolymer. Increased methyl methacrylate incorporation was granted by the regular dispersion of terbium centres in the structure, forcing these metal centres to retain a low coordination number and driving the simultaneous binding of methyl methacrylate. These examples by Gates and Kitigawa exemplify two key properties of heterogeneous systems that affect catalytic performance: first, the influence of the support that is related to the bulk metal or a surface

or nanoparticle; second, the regular arrangement of metal centres is representative of the coordination environment of the surface atoms of a surface or nanoparticle.

An example of a homogeneous model for metal surfaces was proposed by Floriani *et al.*, on the basis that the macrocycle calix[4]arene could act as a suitable support (Figure 2).[15] The lower-rim hydroxyl groups of the calix[4]arene are orientated in the same direction while the rigid nature of the macrocycle contributes to the regular arrangement of the oxygen atoms, resulting in a well-defined tetraoxo-anionic template that binds metals. In this particular example a molybdenum-oxo centre is held by the calix[4]arene lower-rim while the cavity of a second unit of calix[4]arene is supramolecularly-templated to encapsulate a nitrobenzene unit. The motif created by the regular arrangement of the four hydroxide centres bound to the molybdenum centre share similarity with a molybdenum-oxo surface while the calix[4]arene units could be modified, allowing a degree of flexibility to improve the model. Despite this, it was noted that the presence of a single molydenum centre may not be representative of a surface while the weaker, intermolecular interactions holding the second calix[4]arene unit could be easily disrupted by catalytic conditions such as donor solvents, heat and/or pressure.

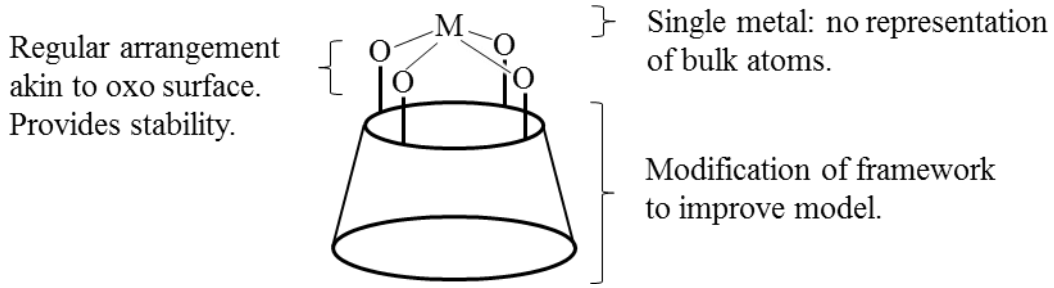

Figure 2. Schematic representation of a calix[4]arene-bound metal centre, highlighting advantages and disadvantages as a model for metal-oxo surfaces.

Improvement in terms of the number and arrangement of metal centres by the use of metal clusters as solubilised models was proposed by Muetterties. In his review of metal clusters in catalysis, the similarity in bonding between metal clusters and surfaces was illustrated by quoting the low-valent transition metal (LVTM) carbonyls as examples.[16] He argued that the neighbouring metal centres and the unique metal-ligand bonding found in metal clusters would enable them to mimic metal surface reactions to an extent, proposing metal clusters to be models for heterogeneous surfaces (Figure 3).

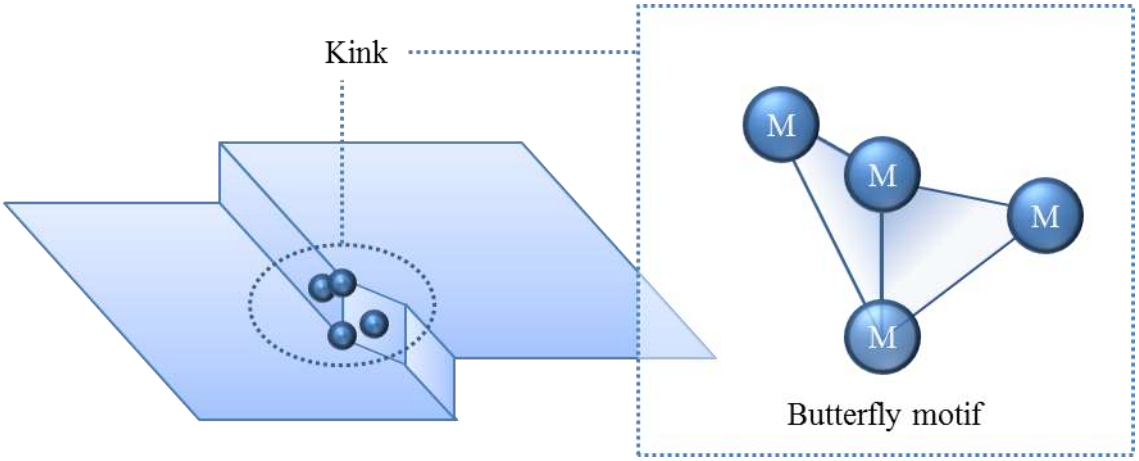

Figure 3. Example of a metal cluster as a model for a surface catalyst. A kink in a metal surface is analogous in terms of shape to a metal cluster with a butterfly motif.

This link between heterogeneous surfaces and polynuclear clusters is a flagship example of the blurred boundary between homogeneous and heterogeneous catalysis whereby a homogenous metal cluster can be attributed properties of a heterogeneous metal surface. In the study of the copper-oxide[8] and palladium(II) Suzuki-Miyaura[9] systems, it is noted that the nanoparticles formed by leaching or aggregation were referred to as "solublised" in the reaction medium and thus homogenous. This is due to their small size, exhibiting diameters less than 5 nm, in comparison to heterogeneous nanoparticles that are usually greater than 10 nm in diameter. These small nanoparticles have been referred to as metal clusters, which are at the heart of the boundary between homogeneous and heterogeneous catalysis, being soluble analogues of a heterogeneous system.

Single-site metal catalysts exhibit good solubility in a variety of solvents. This solubility can be imparted by the ligand framework that stabilises the metal centre. The ligand can also offer a degree of control over various aspects of the catalytic reaction, such as reactivity and selectivity. These homogeneous, ligand-supported catalysts have been extensively investigated and researchers are able to build a step-by-step picture of how a catalytic process takes place on a single metal site through mechanistic and theoretical studies using solution-state characterisation techniques. However, single-site catalysts have not found prominence within industrial applications due to impracticalities such as air-sensitivity and catalyst recovery from the reaction mixture. The result is that most industrial catalysts are heterogeneous or supported due to their improved stability and recovery characteristics, which lend themselves to a commercially-viable process. Metal clusters bound by similar ligands to single-site catalysts hold the potential to

harness the advantages of both homogeneous (in-depth study) and heterogeneous catalysts (activity and stability), as shown in Figure 4.

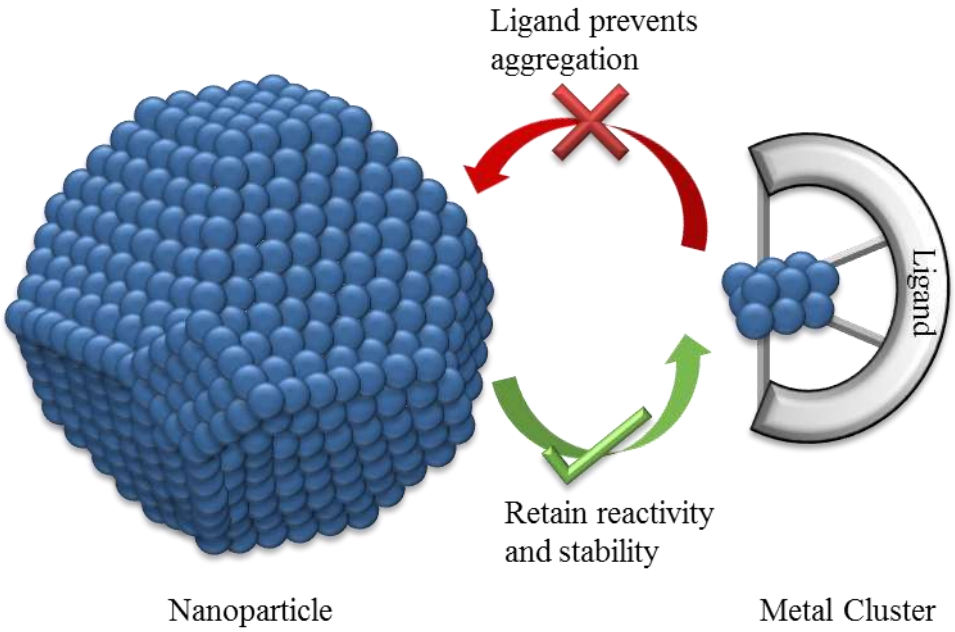

Figure 4. Summary of design principles to reconcile the homogeneity of single-site metal catalysts and reactivity and stability of nanoparticles. Blue spheres indicate a metal centre.

1.3 Metal clusters in catalysis

A metal cluster has been traditionally defined as two or more metals and their accompanying ligands exhibiting one or more metal-metal bonds. This definition has been somewhat relaxed to include polymetallic complexes held by a metal-oxygen-metal framework with no formal metal-metal bond, although arguably these should be referred to as metal-oxo clusters. When ligands act as bridges between metal centres, the term polynuclear metal complex is preferred and describes a compound that joins multiple metal centres through aggregation as opposed to metal–metal or metal–oxo bonds. Both of these types of polynuclear metal frameworks feature two or more metal centres (Figure 5) which are key the synthetic targets during the ensuing projects.

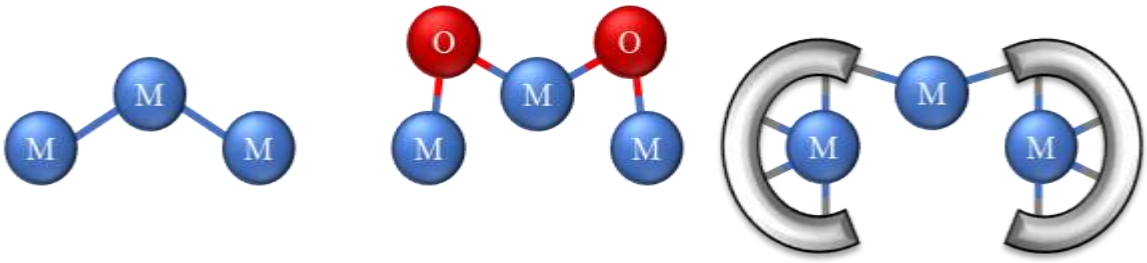

Figure 5. Schematic representations of (left to right): metal cluster, metal-oxo cluster and polynuclear complex. Dark blue M: metal atom; red O: oxygen atom; grey arc: ligand.

1.3.1 Synthetic strategies

The field of cluster chemistry expanded rapidly in the 1960s with the study and characterisation of boron,[17] Zintl[18] and low valent transition metal (LVTM) clusters.[19] Significant contributions were made by Wade[20] as well as Mingos and Hoffman[21,22] with the development and application of isolobal theory[21] to understand the assembly of fragments in cluster chemistry and electron counting rules (polyhedral skeletal electron pair and polyhedral electron counting theory) to rationalise cluster shape and stability, leading to greater control over synthetic routes. These advances deepened the understanding of bonding properties in cluster compounds, with the particular example of boron and Zintl clusters exhibiting a delocalised, electron-deficient bonding networks. This type of delocalised bonding could be thought as similar to that of a bulk metal surface where electrons can flow through the material from atom to atom, with the previously discussed review by Muetterties that drew parallels between LVTM clusters and surfaces.[16]

These LVTMs are examples of metal clusters that can be constructed by combination of two metal fragments in a "bottom-up" approach (Figure 6). The size of metal cluster that can be achieved by this method can approach nanoparticulate sizes.[23] The strategy used in this synthetic approach consists of an unsaturated metal cluster generated by removal of a ligand induced by physical conditions (photolysis or pyrolysis) or chemical reaction (ligand exchange or reducing agent). In this way, two smaller metal clusters can be condensed to give a larger cluster, such as the early example of using three equivalents of a tetranuclear $Rh_4(CO)_{12}$ precursor to access two equivalents of a larger hexanuclear $Rh_6(CO)_{16}$ at ambient conditions by the use of alkaline conditions (water-alcohol, lithium acetate) or wet, organic solvents. This early example demonstrates the ease of access to larger structures and these systems are tolerant to different synthetic conditions. A more detailed account of these synthetic methods can be found in an introductory text by Shriver, Kaesz and Adams describing examples of systematic approaches to synthesise metal clusters and predicting their stability.[24]

A "top-down" synthetic approach has been used in heterogeneous catalysis (Figure 6), where reducing the particle size is generally accompanied by a favourable increase in reaction rate. Upon reaching the size of small nanoparticles or clusters, these unsupported particles display instability,[3] resulting in an ambiguity in defining the catalytically-active species despite efforts to stabilise these smaller species. Examples of this type of leaching to metal clusters or monometallic species are delivered in recent reviews.[1-5]

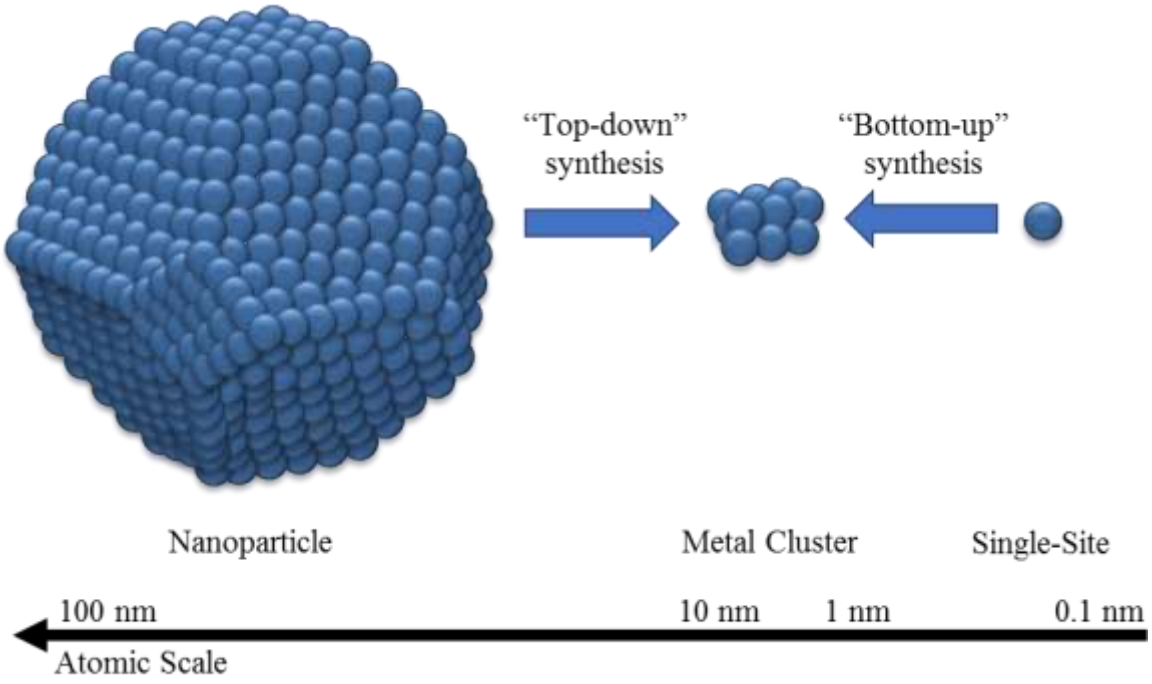

Figure 6. Illustration of "top-down" and "bottom-up" syntheses to access small, polynuclear metal particles such as a metal cluster. Blue spheres indicate a metal centre.

1.3.2 Characterisation techniques

The direct observation of metal cluster formation during catalysis is hindered by the insolublitity of heterogeneous systems, preventing in-depth characterisation using solution-state techniques. Large metal clusters and nanoparticles are typically insoluble, so conventional solution state characterisation techniques cannot be used to probe these larger structures. In these cases, surface characterisation techniques, such as adsorption studies or X-ray photoelectron spectroscopy, scanning electron microscopy or dynamic light scattering, are the characterisation techniques of choice to probe the structure of the surface or nanoparticles, revealing properties such as composition, electronic states and size. These techniques only probe the bulk properties, resulting in a lack of knowledge surrounding the processes occurring on the atomic scale due to difficulties in studying the system *in situ*. In turn, this reduces the overall understanding of the reactions taking place during the catalytic cycle and limits our ability to draw meaningful conclusions between design and performance, with progress relying largely on trial and error to improve the performance of heterogeneous systems.

Homogeneous metal clusters can be characterised in more detail since they lend themselves to analysis using solution-state techniques to complement solid-state techniques. Detailed structural characterisation can be obtained from single crystal X-ray

diffraction (SCXRD) studies, giving a three-dimensional model of the compound under study. Although SCXRD is a solid-state characterisation technique, the methods for growing single crystals require the compound to be soluble in a solvent, such as with slow evaporation, solvent diffusion and vapour diffusion, so heterogeneous compounds are less applicable to this technique. Furthermore, nuclear magnetic resonance (NMR) spectroscopy and mass spectrometry are indispensable tools for the determination of structural properties in solution as these may differ from the solid-state structure obtained from a SCXRD study when solubilised. However, it can be argued that even mass spectrometry is not representative of a sample in solution as the ionisation techniques can cause different species to form, such as electrospray ionisation (ESI) which involves high temperature and high voltage. To summarise, the study of particles in solution requires careful thought about how representative the experimental conditions are of the conditions in the catalytic system.

1.4 Synthesis of polynuclear metal complexes and clusters

Metal clusters have found use in a variety of research areas, with examples as precursors for assembling larger metal clusters or nanoparticles[25,26] and in the production of materials such as surfaces or films.[19] Of particular interest is their use in catalysis, with several examples of catalytically-active metal clusters in the literature featuring a wide range of transition metals (Mn, Fe, Co, Ni, Mo, W) and precious transition metals (Ru, Rh, Pd, Ag, Re, Os, Ir, Pt, Au).[11,27] There are a variety of catalytic reactions mediated by metal clusters, with examples of the catalyst existing as a homometallic or heterometallic cluster[28] that is homogeneous,[12] heterogeneous[29] or supported (i.e metal oxide surfaces and aluminosilicates)[2] in the reaction medium. However, many of these do not feature a multidentate ligand to support the metal centres.

A ligand has the potential to direct the assembly of the polynuclear metal complex, tailor its properties and therefore influence the activity of the catalyst as seen for traditional single-site metal catalysts. Crucially, the ligand will provide stability to the polynuclear metal complex to prevent aggregation to larger, insoluble species. Two “bottom-up” synthetic methods, conserving these key advantages, are present in the literature and will be discussed in this section with pertinent examples of titanium-oxo cluster formation.

1.4.1 Solvothermal synthesis

Solvothermal reactions have been shown to be useful in creating polynuclear complexes, providing thermal energy to drive the formation of thermodynamically-stable products with the particular example of metal-oxo cluster synthesis.[30-35] Such a class of metal-oxo clusters is the family of polyoxotitanates, typically synthesised by heating a titanium (IV) alkoxide in a mixture of alcohol and water to incite formation of titanium-oxo bridges,[36-38] with examples of large polyoxotitanates with Ti_{17} (Figure 7), Ti_{34} and Ti_{52} cores that enter nanoparticulate classification on the atomic scale.[39,40] These compounds have drawn interest with potential applications such as precursors for the synthesis of titanium oxide nanoparticles or as models for nanoparticles and surfaces.[41-43] Polyoxotitanates are supported by oxo ligands with bridging alkoxides or small bidentate ligands such as phenoxides and carboxylates and are another account of bridging donor atoms or groups stabilising a polynuclear metal cluster.[44,45] Smaller di-, tri- and pentanuclear polynuclear titanium complexes stabilised by bisphenoxide ligands and alkoxides were synthesised by altering the synthetic conditions (room temperature versus heating),[46] highlighting how solvothermal conditions can be used to access different polynuclear complexes using the same ligand system. Despite the forceful synthetic conditions that can be granted by solvothermal reactions, these examples demonstrate the ability of phenoxide and carboxylate ligands to stabilise polynuclear titanium complexes and clusters. However, the solvothermal synthesis of polynuclear clusters can lack systematic control, with the use of similar alkoxide and carboxylate donors leading to vastly different titanium-oxo cluster motifs. Nevertheless, the many examples of titanium/titanium-oxo clusters accessed using solvothermal conditions demonstrates it is a useful tool for the assembly of metal clusters.

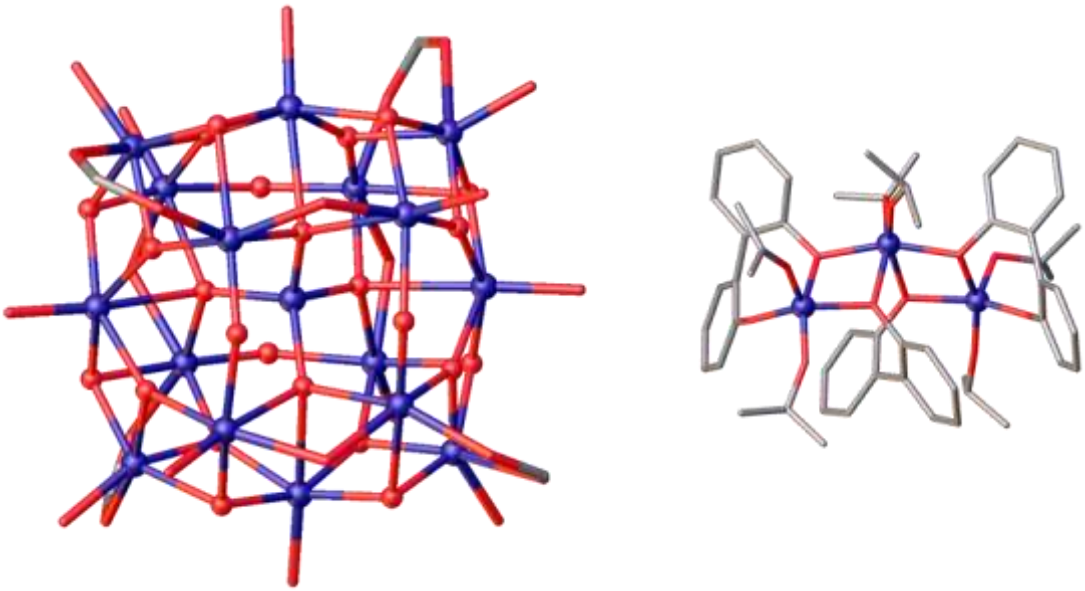

Figure 7. Polynuclear titanium complexes formed by solvothermal synthesis. Left:[39] polyoxotitanate with formula $Ti_{17}O_{24}L_4(OiPr)_{16}$ (L = 4-pyridinecarboxylic acid). Note pyridyl and *i*Pr groups are omitted for clarity; Right:[46] trinuclear titanium complex bound by 2,2′-biphenol (BIPOL) and O*i*Pr ligands with formula $Ti_3(BIPOL)_3(OiPr)_6$. Titanium centres and oxo ligands displayed as spheres; all other atoms displayed as tubes. Hydrogen atoms omitted for clarity. Ti = purple; C = grey; O = red.

1.4.2 Ligand directed assembly

A ligand with bridging capabilities can be used to build a polynuclear complex or metal cluster, making use of the ability of the ligand to impart stability to the metal centres. This synthetic approach was demonstrated in the work by Shaffer and Williams using phosphinate ligands to assemble and stabilise zinc-oxo clusters, which were identified as precursors in the synthesis of zinc oxide nanoparticles.[47] Ligand-supported zinc-oxo clusters composed of four, six and eleven zinc atoms were identified, with the Zn_{11} species found to sequester the phosphinate ligand prior to binding to the surface of the nanoparticle. The ligand acts as a surfactant, stabilising the nanoparticle and dictating its size, thus this type of study gives an atomic scale depiction of the nucleation and subsequent assembly processes involved in nanoparticle synthesis. This in-depth study was enabled by two key properties of the system: the use of a ligand to stabilise the clusters in solution and the retention of homogeneity of the particles so that they can be studied with solution-state techniques, in this case ^{31}P NMR spectroscopy.

There are many examples of ligand-supported metal clusters, particularly in molecular magnet research where control over cluster formation is desirable to explore

the effects on magnetic properties.[48,49] A select few of these metal clusters will be presented in this section with a focus on how the ligand has participated in the assembly of the metal cluster.

The work by Winpenny and coworkers showed pyridone ligands could stabilise gadolinium-copper clusters, with the pyridone group of the ligand acting as a bridge between the metal centres.[49] In this case, a single atom participated in a bridging interaction between two metal centres. Overall, there are a variety of demonstrations showing bridging groups or atoms have the ability to hold metal centres in close proximity to form a metal cluster.[48,49] As noted in the case of pyridone, the bridging group does not need to be a polydentate donor but can be a single donor atom in the correct spatial position to form two or more metal-donor bonds. The macrocycle calix[4]arene was found to support a Mn_4 cluster[50] and mixed-metal lanthanide-transition metal Ln_4Mn_4 clusters (Ln = Gd, Tb, Dy).[51,52] This example demonstrates how a ligand can promote the assembly of metal clusters by holding the phenoxide donors in a fixed spatial arrangement to form metal-donor bridges. A Co_{15} cluster stabilised by a bis(phenoxide) ligand featuring pendant aliphatic hydroxyl groups[53] also showed that more flexible phenoxide ligands could be used in the assembly of metal clusters. Gatteschi and coworkers[49] also provided examples of phenoxide bridged metal clusters using salen ligands, combining a nitrogen donor to stabilise the metal centres while the phenoxides act as bridging donors (Figure 8). It should be noted that these ligand-supported molecular magnets are typically studied in the solid-state, with characterisation relying heavily on SCXRD. Although this type of characterisation is suitable for applications such as structural and magnetic studies, the application of these clusters in solution-state system (i.e homogeneous catalysis) would more than likely lead to the formation of different species in solution due to the weaker binding of the ligands, such as the bridging anions and donor atoms used to bridge and stabilise the metals in the clusters together.

The first reported transition metal cluster to act as single-molecule magnet consisted of a $Mn_{12}(\mu_3\text{-}O)_{12}$ cluster with bridging acetate ligands on the periphery of the metal-oxo cluster, supporting adjacent manganese centres, demonstrating the potential of bridging ligands to support metal-oxo clusters.[54] In a similar fashion, the combination of alkoxide and carboxylate ligands were found to promote and stabilise the assembly of a titanium-oxo cluster with a $Ti_6(\mu_3\text{-}O)_6$ core (Figure 8),[55-57] where changing the alkoxide and carboxylate backbone consistently led to the formation of the same titanium-oxo cluster motif. This is contrasting to the use of solvothermal synthetic conditions led to different

titanium-oxo motifs despite the use of similar alkoxide and carboxylate ligands. From this comparison, we proposed solvothermal syntheses promote the formation of titanium-oxo bridges but reduce the extent of ligand-directed assembly.

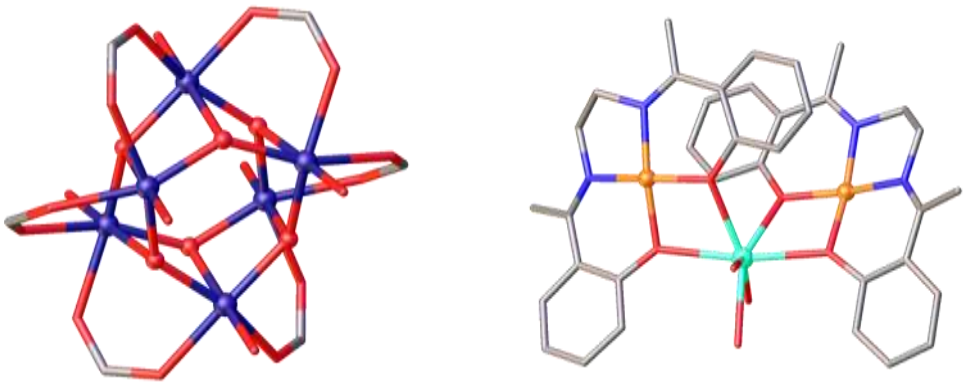

Figure 8. Left: an example of the framework of a $Ti_6(\mu_3\text{-}O)_6(\mu\text{-}COO^-)_6$ core. Right: salen ligand stabilised Cu_2Gd cluster displaying phenoxide bridging, with counter-ions and co-crystallised molecules omitted for clarity. Hydrogen atoms, solvent of crystallisation and counter-ions omitted for clarity. Gd: turquoise; Cu: orange; Ti: purple; C: grey; N: blue; O: red.

Simple hydrolysis by addition of water has been shown to convert multidentate ligand-supported titanium-isopropoxide species to titanium-oxo bridged analogues, with two recent examples, by Chen *et al.* and Chakraborty *et al.*, featuring amine-bis(benzotriazolephenolate) and salicylaldiminato supported polynuclear complexes applied to the ring-opening polymerisation of lactide.[58,59] By using a monometallic precursor with residual isopropoxide groups on the titanium centre, a hydrolysis can occur by substitution of the alkoxide and subsequent formation of a titanium-oxo bridge between two units of the monometallic precursor. This synthetic strategy makes use of a multi-dentate ligand to support the titanium centres during titanium-oxo bond formation, avoiding uncontrolled oxidation to larger titanium oxide species, and could lead to the synthesis of species with a greater number of titanium-oxo bridges. Design of the ligand, in particular its denticity and bite angle, avoids formation of a bis-homoleptic complex that will sequester the source of titanium and prevent further reaction to yield titanium-oxo motifs.

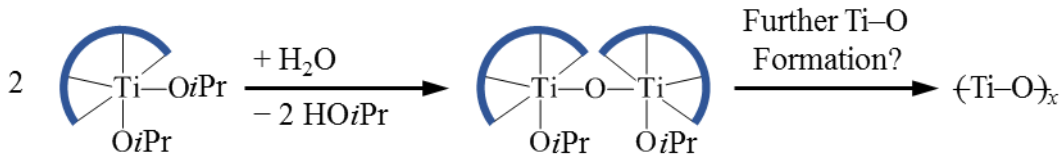

Figure 9. Schematic of the synthesis of dinuclear titanium-oxo bridged species from a monometallic precursor. The multidentate ligand is denoted by a dark blue arc.

As a final note, the polynuclear complex used by Chen *et al.* was found to be inactive towards the ring-opening polymerisation (ROP) of lactide under solution polymerisation conditions while the polynuclear complex in the work of Chakraborty *et al.* was highly active under melt conditions, reaching near-complete conversion (98 %) after 74 mins and producing high molecular weight polymers with low polydispersity index (PDI) values. These contrasting results from similar ligand-supported titanium-oxo frameworks reveal these compounds can be effective initiators in the ROP of lactide but the design and conditions need to be explored to determine their activity.

1.5 Polylactide production and catalysis

A range of biocompatible and biodegradable polymers have gained prominence due to their production from renewable feedstocks and environmentally-friendly properties.[60] Although polymers synthesised from petrochemical feedstocks deliver high performance in many applications, their reliance on fossil fuels requires a change to renewable resources to prevent a rise in production costs and preserve the availability of plastics for future generations as oil reserves deplete. Aliphatic polyesters, such as poly(*ε*-caprolactone) or polylactide (PLA), can be prepared from crops using a ring-opening polymerisation (ROP) strategy that is propagated by the relief of ring-strain in the cyclic monomer.[61,62]

Of these, poly(*L*-lactide) (PLLA) has become a significant polymer in worldwide plastics production, with 150 000 metric tons produced annually,[63-65] and can be derived from the annually-renewable feedstock of crops.[66] Bacterial fermentation of these crops, such as corn or sugar beet, leads to enantiopure *L*-lactic acid in contrast to the racemic mixture obtained from petrochemical feedstocks.[67] Improvements in fermentation and separation of *L*-lactic acid from crops made the extraction of this starting material economically-viable.[68] Cargill Dow LLC (now NatureWorks LLC) filed a patent[69] for depolymerisation of low molecular weight PLA to yield lactide, which was further purified by distillation and subsequently used in a catalysed ring-opening polymerisation to yield the high molecular weight PLA product. Tin(II) bis-2-ethylhexanoic acid (tin octanoate or stannous octanoate) is the preferred bulk lactide polymerisation catalyst due to its high catalytic activity, solubility in the melt and the imparted control over the polymer product obtained, with low racemisation yet high molecular weight.[66]

A key property of PLA is that it hydrolyses to non-toxic lactic acid, which in turn can be decomposed by microorganisms to carbon dioxide and water under aerobic conditions in the enviroment.[70] This forms a loop back to the corn or sugar beet crop that is used to start the process since the two products arising from biodegradation of PLA are the starting materials required for photosynthesis. This is referred to as the lactide cycle (Figure 10). Recycling the PLA plastic product by taking advantage of its easy degradation via hydrolysis in water under heat to lactic acid provides an eco-friendly and direct route back to the starting material.[68] Other environmental benefits of PLA production include significantly lower carbon dioxide emissions and total energy consumption in comparison to other common, petrochemically-derived polymers.[71,72]

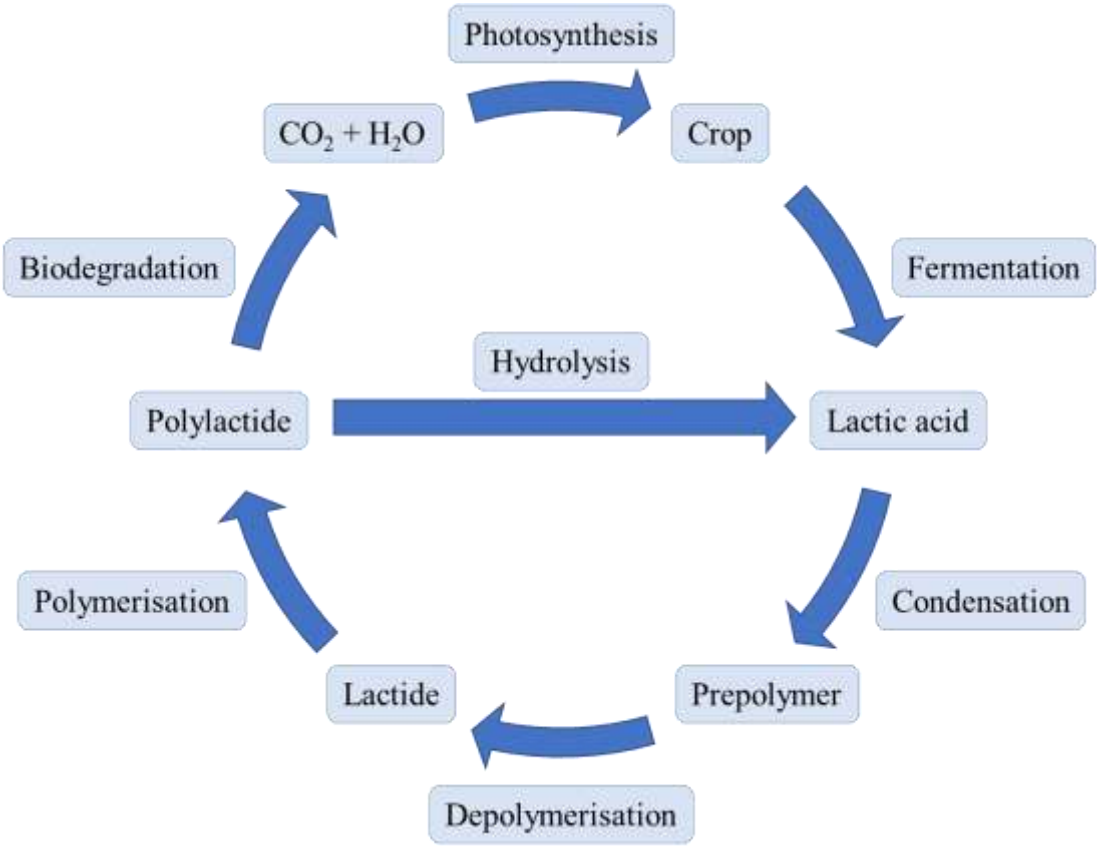

Figure 10. Stages and process of the lactide cycle.

In addition to meeting environmental and economic requirements, PLA has suitable properties for use as a commodity plastic, with similar physical and mechanical properties to polystyrene and poly(ethylene terephthalate).[73] Additional control of physical properties was achieved by blending linear and branched polymers[68] as well as the use of isotactically-enriched polymers.[74,75] Beside altering the chemical composition, the physical and mechanical properties can be further adjusted during polymer processing such as by introducing cross-linking to the polymer network.[76] This tunability of physical and mechanical properties of a polymer material is crucial for its implementation to a wide variety of applications. Examples of the uses of PLA materials are in packaging films, diapers and pharmaceuticals, with particular examples in food packaging and medical devices.[66-68,77-81]

1.5.1 Catalysts and mechanisms for the ROP of lactide

It has been generally found that a cationic mechanism (activated monomer mechanism) can result in lower polymer molecular weight and a lack of control exemplified by higher polydispersity indices, which will result in reduced thermal and mechanical performance of the product.[82,83] Similar problems occur for anionic

mechanisms where polymer molecular weight and polydispersity are difficult to control due to side reactions that terminate the growing chains.[84,85] Control over polydispersity and stereo-regularity is desirable since these correlate with improved physical properties of the polymeric product, which are important for polymer processing and applications. Polymerisations that proceed via coordination-insertion mechanisms under living or immortal conditions are preferred due to their control over polymer molecular weight and polydispersity.[86] Common initiators proceeding by this mechanism are tin octanoate[66] and aluminium isopropoxide.[87]

1.5.2 Tin octanoate – bulk polymerisation catalyst

Tin octanoate is the industry bulk polymerisation catalyst of choice for the ROP of lactide[66] and was found to proceed via a coordination-insertion mechanism.[88-90] Tin(II) activates the ester carbonyl group by a Lewis acid-base interaction while coordinating to the alcohol initiator (Figure 11, A), which is brought in proximity to the carbonyl carbon that it attacks in an S_N2 type mechanism. This initiation step resembles a chelating Lewis-acidic metal catalysed carbonyl nucleophilic attack. The cyclic ester is then opened with the ester C–O bond breaking, which is promoted by proton transfer from the alcohol initiator (Figure 11, B). The resulting aliphatic ester is chelated by the tin catalyst (Figure 11, C) leading to the propagating straight chain intermediate (Figure 11, D). This regenerates the tin-coordinated alkoxide initiator needed to give the coordination-insertion intermediate (Figure 11, A). An important note is that the tin octanoate catalyst is bound to the terminal alcohol of the polymer product, thus tin metal is leached into the polylactide product with further incorporation stemming from mechanical trapping between polylactide particles. This toxic impurity must be reduced to levels within safety standards from the end product in order for it to be used in the applications mentioned previously and for the polymer to be biodegradable to environmentally benign compounds. Furthermore, tin octanoate provides no control over stereochemistry, although low epimerisation occurs, leading to isotactically-pure PLLA. Finally, the lack of tunability provided by the 2-ethylhexanoate ligands prevents modification of the catalyst leading to no further control over the properties of the polylactide product. These drawbacks in using tin octanoate have been the drive in finding an alternative catalyst that is environmentally benign and provides control over the polylactide produced from the ROP process.

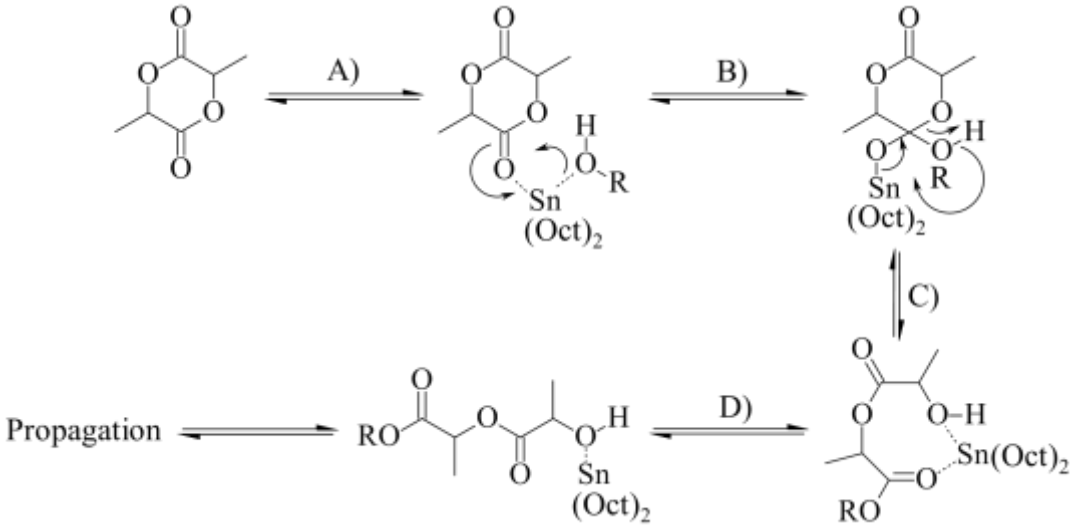

Figure 11. Coordination-insertion mechanism in the ROP of lactide by tin octanoate catalyst. Steps for the forward processes: A) Coordination; B) Insertion; C) Chelation; D) Decyclisation.

1.5.3 Aluminium isopropoxide

A well-studied catalyst for the ring-opening polymerisation of lactide is aluminium isopropoxide (Figure 12), which also proceeds via a coordination insertion mechanism.[87,91] It was found that trinuclear and tetranuclear aluminium aggregates bridged by the isopropoxide ligand were formed *in situ*, with the trimer being the more reactive and more abundant of the two species. The inter- and intramolecular termination reactions between growing chains were said to be caused by the tetranuclear aggregate, becoming more significant at higher molecular weights (*ca*. 90000 Da).[87] It was speculated that the mononuclear species, Al(O*i*Pr)$_3$, would impart better control over the polymerisation product whilst the trinuclear and tetranuclear clusters were undesired products.

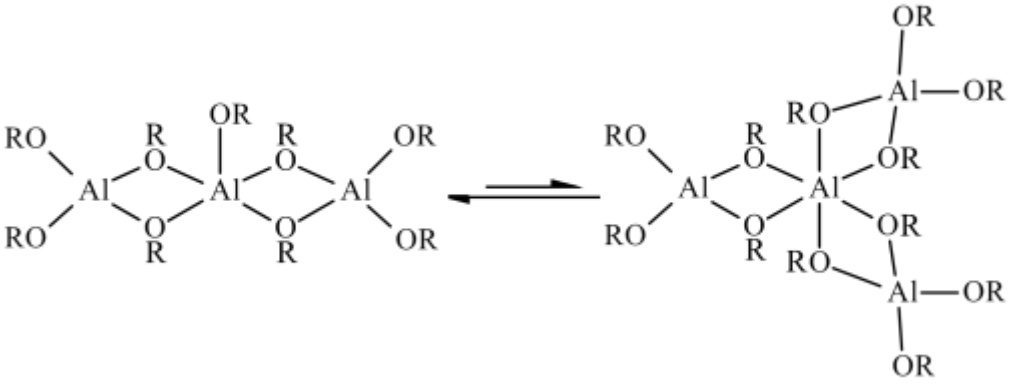

Figure 12. Trinuclear (left) and tetranuclear (right) aggregates of aluminium isopropoxide, where R = *i*Pr.

1.5.4 Single-site metal catalysts

Due to the lack of control stemming from termination reactions and lower activity exhibited by the aluminium isopropoxide clusters, focus turned to using a ligand framework to form stable single-site catalysts and increase control over the polymerisation. A range of metal centres have been reported to be active sites for the ROP of lactide include examples of alkali metals,[92,93] magnesium,[94-96] iron,[97,98] zinc,[95,96] aluminium,[87,99-101] tin[66,102,103] as well as the group IV metals[103,104], with yttrium[101,105] and lanthanide-based[105-107] initiators showing the highest activity. A variety of ligands are bound to the metals in these complexes of which β-diketiminate,[102] salen,[108] half-salen[109] and phenoxide[101,110] ligand frameworks are commonly used. In particular, the use of multidentate ligands has been successful in reducing ligand exchange processes and aggregation to yield stable complexes, in particular with yttrium and lanthanide complexes,[111] while providing a framework for tunability to enact control over the polymerisation, such as activity and stereochemistry.[112] The diversity of metals and ligands demonstrates the range of systems that can be applied to the ROP of lactide and the opportunities that could be taken by tuning the system.

1.5.5 Stereoselective control strategies

Lactide is a chiral molecule that can exist as the meso-, *R,R*- or *S,S*-diastereoisomers, with the *R,R*- or *S,S*-diastereoisomers commonly referred to as *D*- and *L*-lactide. Controlling the microstructure of the PLA product has been of great interest, with isotactic chiral, isotactic stereodiblock, isotactic multistereoblock and heterotactic microstructures being sought after (Figure 13).[113] Atactic and heterotactic PLAs show low crystallinity, which limits their potential applications due to reduced thermal and

mechanical properties. Isotactically-enriched PLAs exhibit higher crystallinity that can access melting temperatures in the range of 170 °C to 230 °C, resulting in polylactide products that are viable for commercial applications.[112] The upper limit melting temperature of 230 °C is achieved by formation of a stereocomplex by blending PLLA and PDLA. Many stereoselective initiators for the ROP of lactide exist with many reviews to cover this topic.[114-116] Stereocontrol was found to be induced by two possible mechanisms: a site control mechanism (SCM)[117] where the chiral information of the catalyst controls the insertion of the monomer or a chain end control mechanism (CEM)[96] where the last inserted repeat unit to the PLA chain controls the next inserted monomer. Each mechanism was found to produce a microstructure that can be predicted by the SCM or CEM statistical models and the stereoregularity of the polylactide chain expressed by the probability of racemic enchainment, P_r, which is related to the probability of meso enchainment, P_m, by $P_r + P_m = 1$ (see Analytical techniques section, Homonuclear decoupled proton NMR spectroscopy subsection for further details).

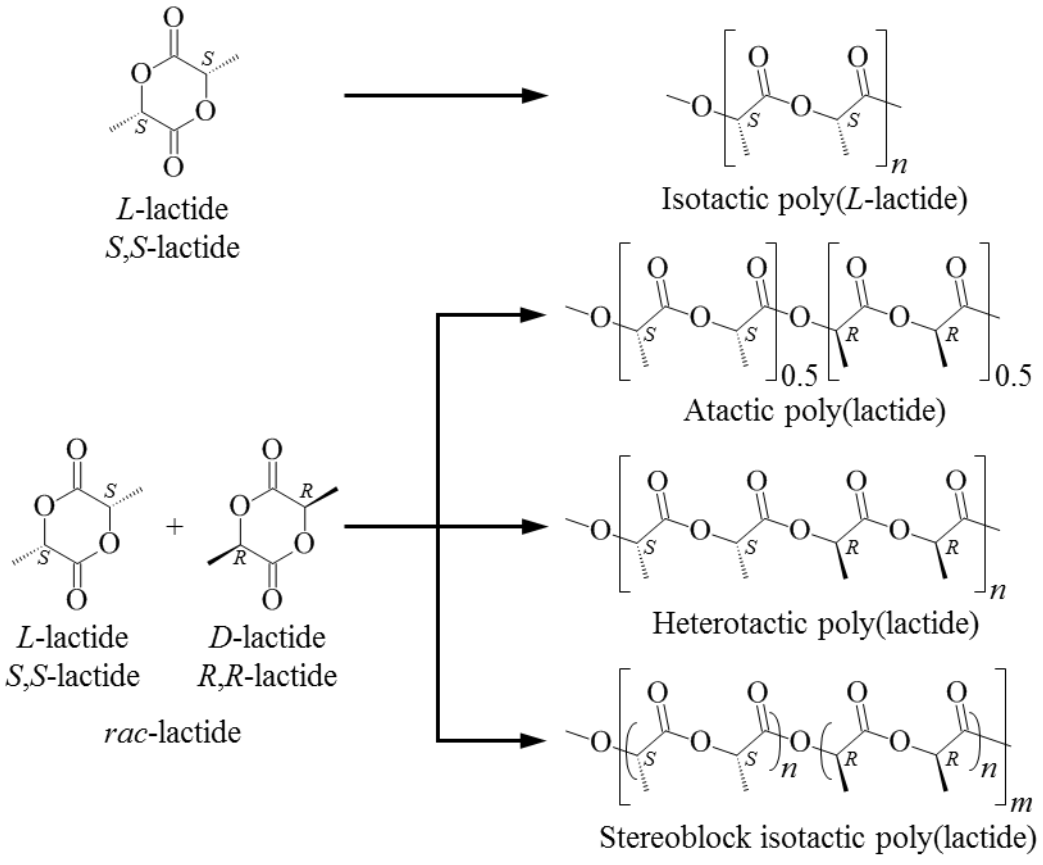

Figure 13. Stereochemistry of *L*- and *rac*-lactide and isotacticity of PLA microstructures.

The systems discussed above attempt to polymerise enantiopure *L*-lactide or *rac*-lactide, an equimolar mixture of *D*- and *L*-lactide, to give isotactic polymer chains. However, the recent availability of enantiopure *D*-lactide has prompted another method for stereoselective ROP of lactide, exemplified by the work of Kol *et al.*,[118] where a magnesium initiator was added to *L*-lactide then *D*-lactide in separate steps to produce stereoblock PLLA-PDLA. The pursuit for stereocontrol in the ROP of lactide is ongoing with new strategies and systems pushing our understanding of the processes that influence stereoselectivity.

1.5.6 Polynuclear complexes in the ROP of lactide

Pentanuclear alkoxide-bridged metal clusters with the general formula M_5-(μ_5-O)$(OR)_{13}$ (Figure 14) where (M = Fe, Y, La, Sm, Yb) have been studied as catalysts for the ROP of lactide.[119] The ferric alkoxide species was obtained by recrystallization of commercially available ferric ethoxide whilst the rare-earth metal alkoxide species were synthesised by reaction of the pure metal with the appropriate alcohol in the presence of a mercury catalyst under heat.[120]

Examples of interest include the work by Feijen and coworkers on the metal cluster of yttrium[121], Y_5-(μ_5-O)(O*i*Pr)$_{13}$, and Tolman and coworkers on iron[98], Fe_5-(μ_5-O)$(OEt)_{13}$, with both studies showing these clusters as effective catalysts for the ROP of lactide. These two metal clusters share the same geometry primarily held by alkoxides acting as bridging ligands, complemented by a μ_5-oxo ligand (Figure 14). In the case of the work done by Feijen and coworkers, adding bulk in the *ortho*-position of a phenoxide ligand resulted in the synthesis of a mononuclear yttrium alkoxide as opposed to the metal-oxygen-metal framework of the Y_5-(μ_5-O)(O*i*Pr)$_{13}$ cluster,[121] demonstrating how steric bulk can influence cluster design.

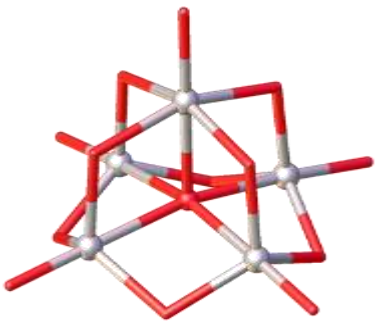

Figure 14. Metal-oxygen-metal framework of the general M_5-(μ_5-O)$(OR)_{13}$ core. Metal: silver; O: red.

In their report of the ROP of lactide using Fe_5-(μ_5-O)$(OEt)_{13}$, Tolman and coworkers[98] found that the pentanuclear iron cluster was highly active towards the ROP of lactide. Using a loading of four-hundred-and-fifty lactide units per iron atom, they achieved 97 % conversion in 21 min at 70 °C with a polydispersity of 1.17, with lower loadings of catalyst correlating with an increase in polydispersity. The group also reported that low racemisation occurred in the production of PLLA when starting from enantiopure *L*-lactide. Interestingly, Tolman and coworkers synthesised a dinuclear iron cluster bridged by 2-phenyl-2-propoxide ligands, $Fe_2(\mu$- $OCMe_2Ph)_2(OCMe_2Ph)_4$, and compared this to Fe_5-(μ_5-O)$(OEt)_{13}$ in the same study.[98] They found that the dinuclear cluster had similar activity for the ROP of lactide (four-hundred-and-fifty lactide units per iron atom, 98 % conversion in 35 min) but showed less control over the polymerisation, resulting in a polydispersity of 1.60 which is significantly higher than that of the pentanuclear cluster. This contrasts the lack of control over polymer chain weight and polydispersity induced by the trimeric and tetrameric aluminium propoxide clusters previously discussed. These successful examples of metal-oxo clusters applied to the ROP of lactide feature simple ligands with a limited framework for tunability. Using tuneable, multidentate ligands to bind a polynuclear metal/metal-oxo cluster could allow researchers to systematically alter the properties of these compounds and further push exploration into the opportunities this type of initiator/catalyst could bring to the ROP of lactide.

1.5.7 Titanium(IV) initiators for the ROP of lactide

Titanium(IV) and zirconium(IV) alkoxides were shown to be active initiators for ROP of lactide.[103,122] A variety of ligands have been investigated in a bid to improve reactivity and control of titanium(IV) alkoxide complexes. Examples of the types of ligands used to bind titanium catalysts for the ROP of lactide include salen,[123,124] tris(phenolate),[110,125,126] aminodiol,[127] N-heterocyclic carbene bis(phenolate)[128] and amine bis(phenolate)[129] supported systems.

Verkade and coworkers[110] used amine tris(phenolate) to form titanium(IV) complexes. It was shown that increasing bulk in the *ortho*-position of the aryloxide (methyl to *tert*-butyl group) resulted in a decrease in reactivity, polymer chain length and polymer yield. Overall, the report demonstrated that less steric shielding of the titanium centre resulted in higher reactivity towards the ROP of lactide by comparison with a range of titanium amine tris(ethoxide) derivatives. This concurs with the work undertaken by Kol and coworkers[129] in their study of several amine phenolate ligand complexes of

titanium and zirconium, where they concluded that a more open metal site in the catalyst results in higher catalytic activity.

Amine bis(phenolate) will be the ligand of choice due to the combination of tuneable phenoxide groups and pendant donor, *R*, both of which can affect catalytic performance (Figure 15).[130] The phenoxides provide stability to the titanium centre[131-135] and hold the potential to act as a bridge between metal centres, as seen in metal clusters supported by phenoxide ligands.[48,49,136,137] Kol and coworkers[138] explored the coordination of amine bis(phenolate) ligands with titanium by changing the groups on the pendant arm, *R*. No donor atom (e.g. propyl chain) gave bis-homoleptic titanium complexes while a donor atom on the pendant arm was found to prevent this. Evidently, omitting a donor atom on the pendant arm could sequester titanium to form a mononuclear complex, preventing the assembly of a polynuclear titanium complex. In addition, the additional donor from the pendant arm stabilises the metal centre, with a variety of groups installed (*R* = pyridyl, THF, furanyl, CH_2NMe_2, CH_2OH, CH_2OMe).[106,131-133,135] Kozak and coworkers studied bis-homoleptic magnesium-oxo dimers with pyridyl and CH_2NMe_2 groups in the *R* position and found the pyridyl donor granted increased activity in the ROP of *rac*-lactide, highlighting the influence the pendant donor *R* can have over the polymerisation.[135] Finally, the peripheral groups around the phenolate rings can be altered, providing additional tunability to the ligand framework.[131,132,134,135,138,139] In the previously mentioned work by Kol and coworkers,[138] increasing the bulk of the group on the *R″* position can favour the formation of the homoleptic titanium diisopropoxide complex over that of the bis-homoleptic complex, even with a non-donor *R* group. With a pyridyl group in the *R* position, Wong, Jones and coworkers[139] were able to improve activity towards the ROP of lactide of amine bis(phenolate) titanium diisopropoxide complexes by increasing steric bulk at the *R′*/*R″* positions of the phenolates. Contrastingly, a study of zinc complexes bound by similar amine bis(phenolate) ligands found increasing the bulk in the *R′*/*R″* positions led to a decrease in activity but an increase in stereoselective control.[140] This example gains further depth with the case of magnesium complexes bound by the same amine bis(phenolate) ligand that showed isotactically-enriched PLA from methyl or isopropyl groups in the *R′*/*R″* positions whereas chloride groups lead to atactic PLA.[141] Employing the tunability of amine bis(phenolate) ligands has been the key strategy to synthesising, stabilising and characterising a variety of complexes and tailoring their performance in the ROP of lactide.

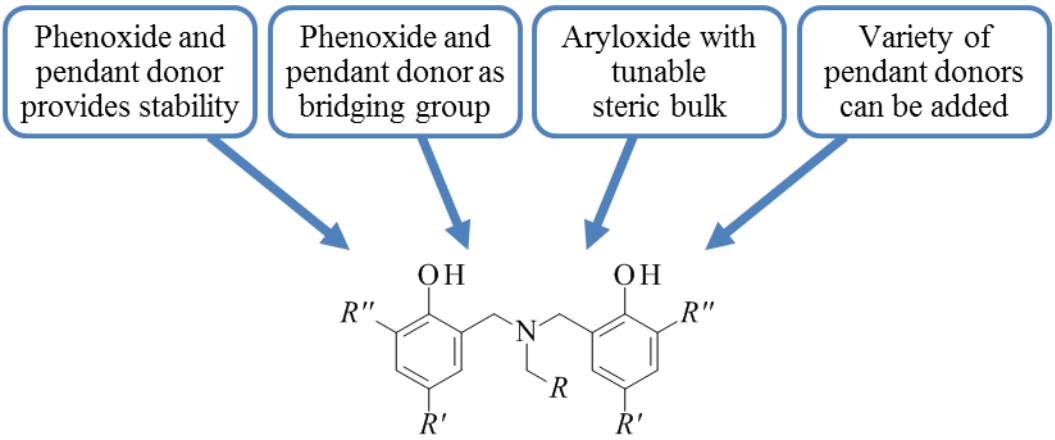

Figure 15. Summary of the principles taken into account in the ligand design.

1.6 Analytical techniques

1.6.1 Diffusion-ordered NMR spectroscopy – *MW* determination

Difficulties can arise in the study of aggregates in solution due to the complexity of these systems, which limits the techniques that can provide information on the nature of the species in the solution. In their study of cationic magnesium-chloride aggregates of magnesium-aluminate complexes, Robertson and coworkers[142] used a combination of solution-state ^{1}H NMR spectroscopy and positive mode electrospray ionisation (ESI^{+}) mass spectrometry to reveal the identity of the aggregates. While NMR spectroscopy will give an accurate representation of the aggregates in solution, it could be argued that ESI^{+} mass spectrometry provides unreliable insight into the system due to the ionisation conditions, which feature high temperature and high voltage. Nevertheless, this mass spectrometry data is supported by SCXRD and NMR studies and this work highlights the inherent difficulties in studying aggregates in solution. The key feature of the successful characterisation of these aggregates was the use of experimental data from many sources to correlate with solution-state data.

More closely related to the topic of initiators for the ROP of lactide, Mehrkhodavandi *et al.* studied the tendency of imino(phenolate) and diamino(phenolate) indium chloride complexes to exist as monomeric or dimeric forms in solution using diffusion-ordered NMR spectroscopy (DOSY).[143,144] Despite solid-state characterisation by SCXRD indicating the prevalence of dimeric compounds, the vastly different conditions (solvent, temperature) provoked by solute-solvent interactions was found to dissociate

the dimeric form to a monomeric form. In this case, DOSY NMR spectroscopy was used to directly observe the aggregates in solution.

DOSY NMR experiments have been widely used to estimate the sizes of particles in solution.[145,146] The diffusion coefficient, which is derived from a plot of signal intensity versus gradient field strength, is related to the hydrodynamic radius, r_H, of the particle by the Stokes-Einstein equation shown in equation 1.

$$D_t = \frac{kT}{6\pi\eta r_H}$$

where D_t is the diffusion coefficient, k is the Boltzman constant, T is absolute temperature, η is the fluid viscosity and r_H is the hydrodynamic radius.

Equation 1.

The diffusion coefficient is influenced by the shape of the particle and the sample conditions so modifications to the Stokes-Einstein equation have been used to improve the accuracy of the estimated hydrodynamic radius. Further work by Wirtz *et al.*[147], and subsequently improved by Chen *et al.*,[148] derived an expression for the size correction factor c as a function of r_{solv}/r_H to increase the accuracy when estimating r_H. Furthermore, the f_S coefficient takes into account deviations from a spherical particle (prolate or oblate ellipsoids).[149] Finally, the diffusion coefficient of an internal standard added to the sample is also measured and used to calibrate the diffusion coefficient of the analyte, mitigating the influence of sample conditions to allow for accurate comparison of estimated r_H between samples (Equation 2).[145,150] However, using this method to estimate the hydrodynamic radius r_H carries two disadvantages when studying complex, multi-component mixtures with unknown entities. First, if the particle is of unknown shape then no values can be provided for the semiaxes a and b to apply the f_S correction factor. Second, the hydrodynamic radius can only be extracted from a plot of cr_H versus r_H, requiring a manual derivation of r_H from each cr_H value obtained from each diffusion coefficient. The applicability of this method is therefore unreliable and unfeasible, in terms of time taken to extract all values of r_H and their accuracy, for large datasets with many diffusion coefficients for unknown species in solution.

$$c^{sa} r_H^{sa} = \frac{D_t^{st} c^{st} f_s^{st} r_H^{st}}{D_t^{sa} f_s^{sa}}$$

where the superscript "sa" indicates the analyte and "st" indicates the internal standard; D_t is the diffusion coefficient, c is the size correction factor, f_s is the shape correction factor and r_H is the hydrodynamic radius.

Equation 2.

An alternative method is to use the diffusion coefficients derived from the DOSY experiment to estimate the *MW* via external calibration curves (ECCs), published by Stalke and coworkers.[151,152] These ECCs take into account variables when measuring the diffusion coefficient such as the solvent, analyte shape and concentration, temperature and the spectrometer used. Each ECC was plotted for a given solvent and molecular shape; these two variables are accounted for by selecting the appropriate ECC for the system under experimental study. An external spectrometer can be used if an internal reference exists in the sample. With both values of the diffusion coefficient for the internal reference measured on the external spectrometer and the original spectrometer, the diffusion coefficients for the analytes are normalised. Using the published parameters for the ECCs and internal references, the only experimental values required to use the ECCs are the diffusion coefficients of the internal reference and analytes. Estimated *MW*s are obtained from Equation 3 in which the only variable is the diffusion coefficient of the analyte, D_x: K and α are provided for each ECC; $D_{ref,fix}$ is fixed for the internal reference used and D_{ref} is a constant for the sample under analysis. This method can be applied to large datasets since the *MW* is directly calculated using an equation with a single variable, D_x, which is the measured diffusion coefficient from the DOSY NMR experiment.

$$MW = 10^{\frac{\log D_{ref,fix} - \log D_{ref} + \log D_x - \log K}{\alpha}}$$

where *MW* is molecular weight, $D_{ref,fix}$ is the fixed value of the diffusion coefficient of the internal reference, D_{ref} is the measured value of the diffusion coefficient of the internal reference, D_x is the measured value of the diffusion coefficient of the analyte, K is a molecule dependent constant and α is a density/shape factor.

Equation 3.

Although these ECCs are useful tools for estimating *MW*s from diffusion coefficients, their limitations must not be overlooked. The authors noted that the ECCs provided accurate *MW* determinated (± 10 % error) for molecules with a molar density between 4.3×10^{29} g·mol^{-1}·m^{-3} and 5.9×10^{29} g·mol^{-1}·m^{-3}. Molecules with heavy atoms, in relation to organic atoms, exceed the molar density range stated for the ECCs and results in an underestimation of the *MW*. For the analytes studied herein, the heavier atom titanium leads us to expect an underestimation of *MW* although this will be consistent throughout the measurements.

The study of dynamic, multi-component systems carries uncertainty when extracting the diffusion coefficient from the experimental data. It should be noted that when deriving a diffusion coefficient from a given peak associated with species under exchange, an average diffusion coefficient between the species associated with that peak will be observed. In addition, if the peak is composed of overlapping signals for several species then this can have the same effect on the derived diffusion coefficient. These effects will give rise to errors in the diffusion coefficients and in turn the estimation of *MW*. Thus, we expect larger deviations in the values obtained from these samples of dynamic species than would be expected for samples of discrete, non-interacting molecules. For this reason, using a large amount of data points was important to obtain a distribution from which we could obtain a reliable estimate of the *MW*.

1.6.2 Homonuclear decoupled proton NMR spectroscopy

Decoupling is routinely used in ^{13}C NMR spectroscopy to suppress coupling between the ^{1}H and ^{13}C nuclei, leading to a simplified spectrum with each carbon signal appearing as a singlet regardless of the number of attached protons. Thus, typical carbon NMR spectra should formally be described as ^{13}C{^{1}H} NMR experiments with broadband decoupling of the ^{1}H and ^{13}C nuclei across the whole spectrum. By simplifying the ^{13}C NMR spectrum through decoupling of ^{1}H nuclei, two advantages are offered: the number of signals correlates with the number of carbons in the structure and overlap from signals in similar magnetic environments, such as aromatic carbons, are kept to a minimum. This gives researchers a clearer spectrum from which to extract structural data. The same principle can be applied to ^{1}H NMR spectra to simplify the spectrum although homonuclear ^{1}H decoupling requires high power radiofrequency (RF) pulses that exceed the tolerances of the instrumentation. Two decoupling techniques that adhere to instrument compatibility and limit sample heating exist: a broadband “sweep” decoupling pulse sequence (WALTZ-16) or a selective homonuclear decoupling pulse.

To understand how a decoupling NMR experiment works, it is useful to reiterate how nuclei couple during an NMR experiment with the example of proton H_A and H_B on two adjacent carbon atoms in an organic molecule. Statistically, the spin of the H_B nuclei will be aligned with the external magnetic field ("up") in half of the molecules in the sample while in the other half the H_B nuclei will be aligned opposite to the external magnetic field ("down"). The "up" and "down" alignments of the H_B nuclei will perturb the field about the adjacent H_A proton, resulting in an upfield and downfield shift of the resonant frequency leading to a doublet being observed. The distance between the two peaks is defined as the coupling constant, *J*. Since the effect is mutual between H_A and H_B, whereby both nuclei experience the same perturbations in magnetic field, they share the same magnitude of the *J*-coupling constant in Hertz (Hz). Thus, decoupling of either H_A or H_B can be achieved by irradiating either H_B or H_A, respectively, with a continuous low-power RF pulse to "flip" the alignment of all instances of the nuclei opposite ("down") with respect to the external magnetic field (Figure 16). This will negate the coupling between H_A and H_B as they will no longer experience field perturbation from "up" and "down" nuclei.

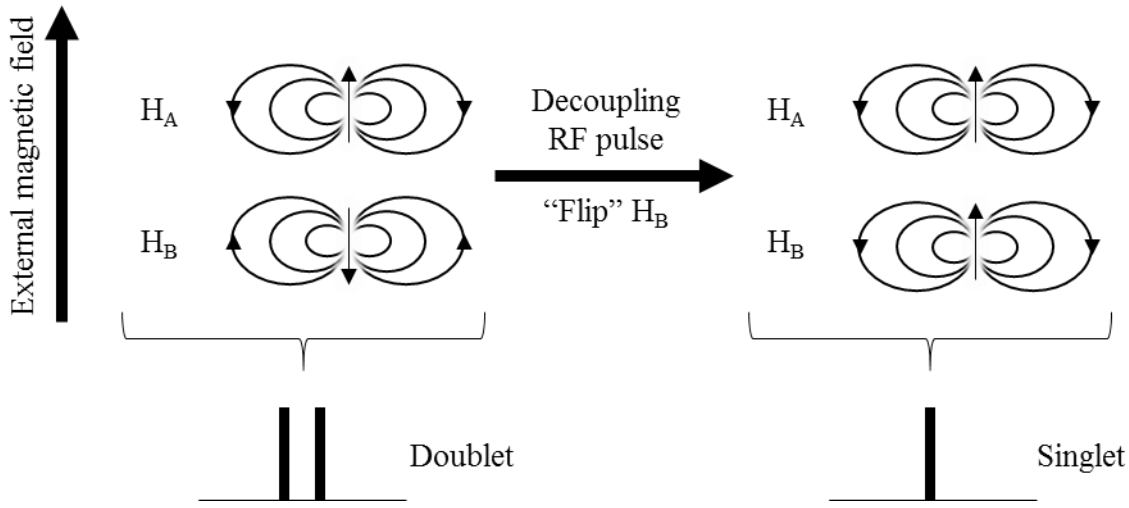

Figure 16. Diagram illustrating the effect of a decoupling RF pulse on the alignment of nuclei and its effect on the observed signals.

A selective homonuclear decoupling pulse was the method of choice for polylactide samples as only specific proton resonances over a narrow frequency range required decoupling. This is applicable to the particular case of microstructure analysis of polylactide samples that will exhibit two prominent resonances: a methyl resonance at approximately 1.6 ppm and a methine resonance at approximately 5.1 ppm. Studying the microstructure is key to develop our understanding of how an initiator/catalyst can

influence the tacticity of the polymer on the atomic scale, resulting in valuable information on research leads to further improve and develop future generations of initiators/catalysts.

Initial work by Munson *et al.* made use of ^{13}C and ^{1}H NMR spectroscopy to explore the microstructure through characterisation of isotactic and syndiotactic linkages in the polymer chain.[153] The use of heteronuclear correlation (HETCOR) experiments offered improvements in the characterisation of signals associated with isotactic/syndiotactic enchainment,[154] prompted by a communication by Chisholm and coworkers raising issues with their correct assignment.[155] A final, in-depth study by Munson and coworkers further confirmed the assignment of tetrads to isotactic/syndiotactic tetramers in the polylactide chains. This was imperative to ensure work by researchers in the field of stereoselective ROP of lactide was accurate.

Inspection of the methine region by homonuclear decoupled ^{1}H NMR spectroscopy, also expressed as a $^{1}H\{^{1}H\}$ experiment, revealed the presence of five tetrad signals relating to the linkages between lactide units. These tetrad linkages were identified to correspond to racemic ("*r*") and meso ("*m*") (Figure 17) or isotactic ("*i*") and syndiotactic ("*s*") linkages respectively and their relative intensities predicted by statistical models by Coates and coworkers[96,117] allowing for analysis of the isotacticity and heterotacticity of the polylactide chains. This can be expressed in two ways. The first utilises Bernoullian, or CEM, statistics to relate the relative intensity of the *rmr* tetrad to the probability of racemic enchainment, P_r. It should be noted that $P_m = 1 - P_r$ so is known if P_r is calculated. The second involves the prediction of the relative intensities of each tetrad using either SCM or CEM statistics,[96,117] leading to estimation of P_r and P_m values for the sample. The latter of these methods is more rigorous as the tetrad intensities must be inspected individually with the values predicted from the statistical models, where any deviation could reveal characteristics pertaining to the stereocontrol of the system and is an important tool to understand the effects of catalyst design on stereocontrol in the ROP of lactide.

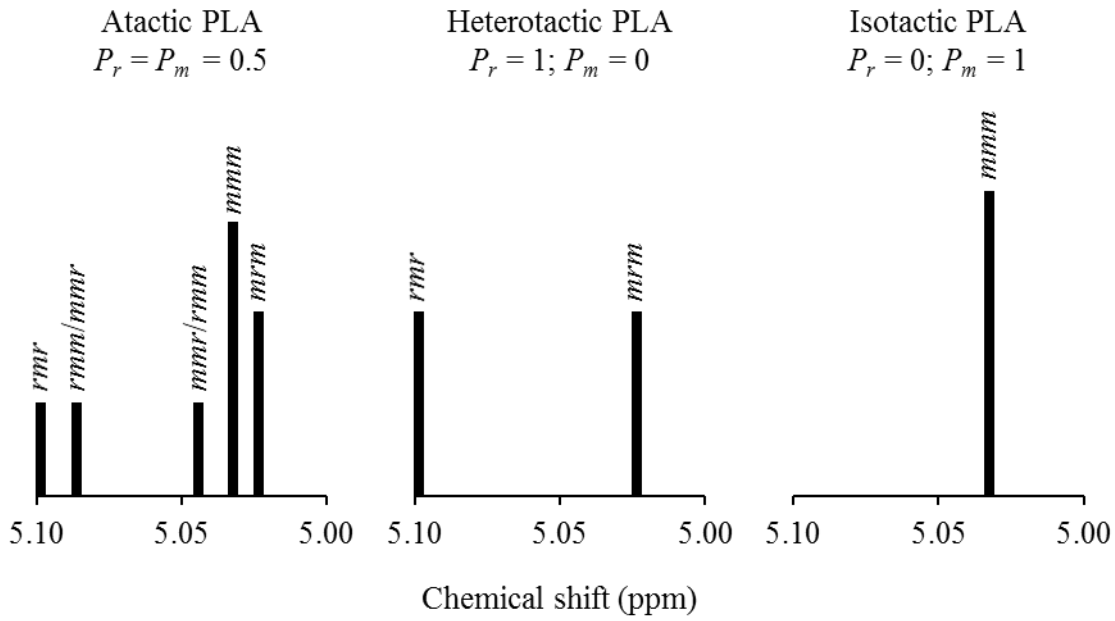

Figure 17. Schematic representations of idealised methine tetrad distributions for atactic, heterotactic and isotactic PLA with corresponding values of P_r and P_m.

1.7 Outlook

A bottom-up synthetic approach will be used to construct polynuclear titanium complexes from mononuclear units. These mononuclear units will act as synthetic building blocks and be subject to further reaction to form polynuclear complexes. Furthermore, ligand-directed assembly will also be a strategy for expansion from the mononuclear units to polynuclear complexes, where the effect of a carboxylate pendant arm on the ligand will be explored. The use of the multi-dentate amine bis(phenolate) ligand will provide stability to the polynuclear complexes while the tunability of the ligand framework will allow for further improvement upon the initial ligand design (see Section 1.5.7 for details on ligand design). As a further synthetic strategy, hydrolysis reactions will be employed to incite the formation of titanium-oxo bonds, leading to titanium-oxo-titanium motifs within the complexes formed. The reaction conditions will also be modified to explore polynuclear complex formation, with an emphasis on solvothermal reaction conditions to favour the formation of thermodynamically-stable products featuring titanium-oxo-titanium bridges. The synthesised polynuclear titanium complexes will be applied to the ring-opening polymerisation of lactide to study their applicability to a catalytic process.

1.8 References

1. J. A. Widegren and R. G. Finke, *J. Mol. Catal. A: Chem.*, 2003, **198**, 317-341.
2. P. Serna and B. C. Gates, *Acc. Chem. Res.*, 2014, **47**, 2612-2620.
3. R. H. Crabtree, *Chem. Rev.*, 2012, **112**, 1536-1554.
4. R. H. Crabtree, *Chem. Rev.*, 2015, **115**, 127-150.
5. D. B. Eremin and V. P. Ananikov, *Coord. Chem. Rev.*, 2017, **346**, 2-19.
6. K. Mori, T. Mizoroki and A. Ozaki, *Bull. Chem. Soc. Jpn.*, 1973, **46**, 1505-1508.
7. T. Mizoroki, K. Mori and A. Ozaki, *Bull. Chem. Soc. Jpn.*, 1971, **44**, 581-581.
8. Y. S. Panova, A. S. Kashin, M. G. Vorobev, E. S. Degtyareva and V. P. Ananikov, *ACS Catal.*, 2016, **6**, 3637-3643.
9. M. Gorna, M. S. Szulmanowicz, A. Gniewek, W. Tylus and A. M. Trzeciak, *J. Organomet. Chem.*, 2015, **785**, 92-99.
10. C. R. Kim, T. Uemura and S. Kitagawa, *Chem. Soc. Rev.*, 2016, **45**, 3828-3845.
11. E. L. Muetterties and M. J. Krause, *Angew. Chem. Int. Ed. Eng.*, 1983, **22**, 135-148.
12. L. N. Lewis, *Chem. Rev.*, 1993, **93**, 2693-2730.
13. J. Lu, P. Serna and B. C. Gates, *ACS Catal.*, 2011, **1**, 1549-1561.
14. T. Uemura, S. Mochizuki and S. Kitagawa, *ACS Macro Lett.*, 2015, **4**, 788-791.
15. F. Corazza, C. Floriani, A. Chiesivilla and C. Guastini, *J. Chem. Soc., Chem. Comm.*, 1990, 640-641.
16. E. L. Muetterties, *Bull. Soc. Chim. Belg.*, 1975, **84**, 959-986.
17. E. L. Muetterties, *J. Organomet. Chem.*, 1980, **200**, 177-190.
18. T. Fässler and G. S. Armatas, *Zintl ions : principles and recent developments*, Springer, Heidelberg ; New York, 2011.
19. B. H. S. Thimmappa, *Coord. Chem. Rev.*, 1995, **143**, 1-34.
20. K. Wade, *J. Chem. Soc. Chem. Comm.*, 1971, 792-793.
21. M. Elian, M. M. L. Chen, D. M. P. Mingos and R. Hoffmann, *Inorg. Chem.*, 1976, **15**, 1148-1155.
22. R. Hoffmann, *Angew. Chem. Int. Ed. Eng.*, 1982, **21**, 711-724.
23. S. Zacchini, *Eur. J. Inorg. Chem.*, 2011, 4125-4145.
24. D. F. Shriver, H. D. Kaesz and R. D. Adams, *The Chemistry of metal cluster complexes*, VCH, New York, 1990.
25. Y. Z. Lu and W. Chen, *Chem. Soc. Rev.*, 2012, **41**, 3594-3623.
26. L. Guczi, A. Beck, A. Horvath and D. Horvath, *Top. Catal.*, 2002, **19**, 157-163.
27. R. D. Adams and F. A. Cotton, *Catalysis by di- and polynuclear metal cluster complexes*, Wiley-VCH, New York, 1998.
28. P. Buchwalter, J. Rose and P. Braunstein, *Chem. Rev.*, 2015, **115**, 28-126.
29. M. Boudart, *J. Mol. Catal.*, 1985, **30**, 27-38.
30. Y. L. Fu, Y. L. Liu, Z. Shi, B. Z. Li and W. Q. Pang, *J. Solid State Chem.*, 2002, **163**, 427-435.
31. S. Ali, C. A. Muryn, F. Tuna and R. E. P. Winpenny, *Dalton Trans.*, 2010, **39**, 124-131.
32. S. Ali, C. A. Muryn, F. Tuna and R. E. P. Winpenny, *Dalton Trans.*, 2010, **39**, 9588-9597.
33. I. S. Tidmarsh, L. J. Batchelor, E. Scales, R. H. Laye, L. Sorace, A. Caneschi, J. Schnack and E. J. L. McInnes, *Dalton Trans.*, 2009, 9402-9409.
34. K. Hong, W. Bak and H. Chun, *Inorg. Chem.*, 2014, **53**, 7288-7293.
35. Y. Y. Wu, W. Luo, Y. H. Wang, Y. Y. Pu, X. Zhang, L. S. You, Q. Y. Zhu and J. Dai, *Inorg. Chem.*, 2012, **51**, 8982-8988.

36. V. W. Day, T. A. Eberspacher, W. G. Klemperer and C. W. Park, *J. Am. Chem. Soc.*, 1993, **115**, 8469-8470.
37. C. F. Campana, Y. Chen, V. W. Day, W. G. Klemperer and R. A. Sparks, *J. Chem. Soc., Dalton Trans.*, 1996, 691-702.
38. N. Steunou, G. Kickelbick, K. Boubekeur and C. Sanchez, *J. Chem. Soc. Dalton Trans.*, 1999, 3653-3655.
39. J. D. Sokolow, E. Trzop, Y. Chen, J. J. Tang, L. J. Allen, R. H. Crabtree, J. B. Benedict and P. Coppens, *J. Am. Chem. Soc.*, 2012, **134**, 11695-11700.
40. W. H. Fang, L. Zhang and J. Zhang, *J. Am. Chem. Soc.*, 2016, **138**, 7480-7483.
41. J. B. Benedict, R. Freindorf, E. Trzop, J. Cogswell and P. Coppens, *J. Am. Chem. Soc.*, 2010, **132**, 13669-13671.
42. P. Coppens, Y. Chen and E. Trzop, *Chemical Reviews*, 2014, **114**, 9645-9661.
43. S. Omwoma, C. T. Gore, Y. Ji, C. Hu and Y.-F. Song, *Coord. Chem. Rev.*, 2014, Ahead of Print.
44. J. B. Benedict and P. Coppens, *J. Am. Chem. Soc.*, 2010, **132**, 2938-2944.
45. K. Hong, W. Bak and H. Chun, *Inorg. Chem.*, 2014, **53**, 7288-7293.
46. J. P. Corden, W. Errington, P. Moore, M. G. Partridge and M. G. H. Wallbridge, *Dalton Trans.*, 2004, 1846-1851.
47. S. D. Pike, E. R. White, M. S. P. Shaffer and C. K. Williams, *Nat. Commun.*, 2016, **7**.
48. Y. Z. Zheng, G. J. Zhou, Z. P. Zheng and R. E. P. Winpenny, *Chem. Soc. Rev.*, 2014, **43**, 1462-1475.
49. R. E. P. Winpenny, *Chem. Soc. Rev.*, 1998, **27**, 447-452.
50. G. Karotsis, S. J. Teat, W. Wernsdorfer, S. Piligkos, S. J. Dalgarno and E. K. Brechin, *Angew. Chem., Int. Ed.*, 2009, **48**, 8285-8288.
51. G. Karotsis, M. Evangelisti, S. J. Dalgarno and E. K. Brechin, *Angew. Chem. Int. Ed.*, 2009, **48**, 9928-9931.
52. G. Karotsis, S. Kennedy, S. J. Teat, C. M. Beavers, D. A. Fowler, J. J. Morales, M. Evangelisti, S. J. Dalgarno and E. K. Brechin, *J. Am. Chem. Soc.*, 2010, **132**, 12983-12990.
53. R. McLellan, J. Reze, S. M. Taylor, R. D. McIntosh, E. K. Brechin and S. J. Dalgarno, *Chem. Commun.*, 2014, **50**, 2202-2204.
54. T. Lis, *Acta Crystallogr., Sect. B: Struct. Sci*, 1980, **36**, 2042-2046.
55. P. Piszczek, A. Radtke, T. Muziol, M. Richert and J. Chojnacki, *Dalton Trans.*, 2012, **41**, 8261-8269.
56. M. Czakler, C. Artner and U. Schubert, *Eur. J. Inorg. Chem.*, 2012, 3485-3489.
57. R. Papiernik, L. G. Hubert-Pfalzgraf, J. Vaissermann and M. C. H. B. Goncalves, *J. Chem. Soc. Dalton.*, 1998, 2285-2287.
58. C. K. Su, H. J. Chuang, C. Y. Li, C. Y. Yu, B. T. Ko, J. D. Chen and M. J. Chen, *Organometallics*, 2014, **33**, 7091-7100.
59. D. Chakraborty, D. Mandal, V. Ramkumar, V. Subramanian and J. V. Sundar, *Polymer*, 2015, **56**, 157-170.
60. S. Ebnesajjad, *Pdl Handb Ser*, 2013, 1-462.
61. W. Saiyasombat, R. Molloy, T. M. Nicholson, A. F. Johnson, I. M. Ward and S. Poshyachinda, *Polymer*, 1998, **39**, 5581-5585.
62. S. Strandman, J. E. Gautrot and X. X. Zhu, *Polym. Chem.*, 2011, **2**, 791-799.
63. L. Shen, E. Worrell and M. Patel, *Biofuel Bioprod. Biorefin.*, 2010, **4**, 25-40.
64. S. M. Guillaume and J. F. Carpentier, *Catal. Sci. Technol.*, 2012, **2**, 898-906.
65. Y. Q. Zhu, C. Romain and C. K. Williams, *Nature*, 2016, **540**, 354-362.
66. R. E. Drumright, P. R. Gruber and D. E. Henton, *Adv. Mat.*, 2000, **12**, 1841-1846.
67. J. Lunt, *Polym. Degrad. Stab.*, 1998, **59**, 145-152.

68. J. R. Dorgan, H. J. Lehermeier, L. I. Palade and J. Cicero, *Macromol. Symp.*, 2001, **175**, 55-66.
69. P.R. Gruber, E. S. Hall, J. J. Kolstad, M. L. Iwen, R. D. Benson and R. L. Borchardt, *US Pat.*, US5142023A, 1992.
70. E. Chiellini and R. Solaro, *Adv. Mat.*, 1996, **8**, 305-313.
71. D. E. Henton, P. Gruber, J. Lunt and J. Randall, *Polylactic acid technology*, CRC Press LLC, 2005.
72. E. T. H. Vink, K. R. Rabago, D. A. Glassner and P. R. Gruber, *Polym. Degrad. Stab.*, 2003, **80**, 403-419.
73. R. A. Auras, B. Harte, S. Selke and R. Hernandez, *J. Plast. Film*, 2003, **19**, 123-135.
74. H. Tsuji, *Macromol. Biosci.*, 2005, **5**, 569-597.
75. H. Tsuji and Y. Ikada, *Polymer*, 1999, **40**, 6699-6708.
76. A. O. Helminen, H. Korhonen and J. V. Seppala, *Macromol. Chem. Phys.*, 2002, **203**, 2630-2639.
77. M. Vert, *Macromol. Symp.*, 2000, **153**, 333-342.
78. A. C. Albertsson and I. K. Varma, *Biomacromolecules*, 2003, **4**, 1466-1486.
79. B. Gupta, N. Revagade and J. Hilborn, *Prog. Polym. Sci.*, 2007, **32**, 455-482.
80. C. K. Williams, *Chem. Soc. Rev.*, 2007, **36**, 1573-1580.
81. S. Slomkowski, S. Penczek and A. Duda, *Polym. Adv. Technol.*, 2014, **25**, 436-447.
82. M. Basko and P. Kubisa, *J. Polym. Sci. Pol. Chem.*, 2006, **44**, 7071-7081.
83. D. Bourissou, B. Martin-Vaca, A. Dumitrescu, M. Graullier and F. Lacombe, *Macromolecules*, 2005, **38**, 9993-9998.
84. D. S. McGuinness, E. L. Marshall, V. C. Gibson and J. W. Steed, *J. Polym. Sci. Pol. Chem.*, 2003, **41**, 3798-3803.
85. A. Bhaw-Luximon, D. Jhurry, N. Spassky, S. Pensec and J. Belleney, *Polymer*, 2001, **42**, 9651-9656.
86. S. Inoue, *J. Polym. Sci. Pol. Chem.*, 2000, **38**, 2861-2871.
87. P. Dubois, C. Jacobs, R. Jerome and P. Teyssie, *Macromolecules*, 1991, **24**, 2266-2270.
88. Y. J. Du, P. J. Lemstra, A. J. Nijenhuis, H. A. M. Vanaert and C. Bastiaansen, *Macromolecules*, 1995, **28**, 2124-2132.
89. F. E. Kohn, J. G. Van Ommen and J. Feijen, *Eur. Polym. J.*, 1983, **19**, 1081-1088.
90. M. Ryner, K. Stridsberg, A. C. Albertsson, H. von Schenck and M. Svensson, *Macromolecules*, 2001, **34**, 3877-3881.
91. A. Kowalski, A. Duda and S. Penczek, *Macromolecules*, 1998, **31**, 2114-2122.
92. L. N. Saunders, L. N. Dawe and C. M. Kozak, *J. Organomet. Chem.*, 2014, **749**, 34-40.
93. F. M. Garcia-Valle, R. Estivill, C. Gallegos, T. Cuenca, M. E. G. Mosquera, V. Tabernero and J. Cano, *Organometallics*, 2015, **34**, 477-487.
94. M. H. Chisholm and N. W. Eilerts, *Chem. Commun.*, 1996, 853-854.
95. M. H. Chisholm, N. W. Eilerts, J. C. Huffman, S. S. Iyer, M. Pacold and K. Phomphrai, *J. Am. Chem. Soc.*, 2000, **122**, 11845-11854.
96. B. M. Chamberlain, M. Cheng, D. R. Moore, T. M. Ovitt, E. B. Lobkovsky and G. W. Coates, *J. Am. Chem. Soc.*, 2001, **123**, 3229-3238.
97. B. J. O'Keefe, L. E. Breyfogle, M. A. Hillmyer and W. B. Tolman, *J. Am. Chem. Soc.*, 2002, **124**, 4384-4393.
98. B. J. O'Keefe, S. M. Monnier, M. A. Hillmyer and W. B. Tolman, *J. Am. Chem. Soc.*, 2001, **123**, 339-340.
99. T. Aida and S. Inoue, *Acc. Chem. Res.*, 1996, **29**, 39-48.
100. L. Trofimoff, T. Aida and S. Inoue, *Chem. Lett.*, 1987, 991-994.

101. Y. C. Liu, B. T. Ko and C. C. Lin, *Macromolecules*, 2001, **34**, 6196-6201.
102. A. P. Dove, V. C. Gibson, E. L. Marshall, H. S. Rzepa, A. J. P. White and D. J. Williams, *J. Am. Chem. Soc.*, 2006, **128**, 9834-9843.
103. H. R. Kricheldorf, M. Berl and N. Scharnagl, *Macromolecules*, 1988, **21**, 286-293.
104. M. Hu, M. Wang, H. Zhu, L. Zhang, H. Zhang and L. Sun, *Dalton Trans.*, 2010, **39**, 4440-4446.
105. A. Amgoune, C. M. Thomas, T. Roisnel and J. F. Carpentier, *Chem. Eur. J.*, 2006, **12**, 169-179.
106. S. Yang, K. Nie, Y. Zhang, M. Xue, Y. Yao and Q. Shen, *Inorg. Chem.*, 2014, **53**, 105-115.
107. K. Nie, L. Fang, Y. Yao, Y. Zhang, Q. Shen and Y. Wang, *Inorg. Chem.*, 2012, **51**, 11133-11143.
108. D. Pappalardo, M. Bruno, M. Lamberti, M. Mazzeo and C. Pellecchia, *J. Mol. Catal. A: Chem.*, 2013, **379**, 303-308.
109. S. L. Hancock, M. F. Mahon and M. D. Jones, *New J. Chem.*, 2013, **37**, 1996-2001.
110. Y. Kim, G. K. Jnaneshwara and J. G. Verkade, *Inorg. Chem.*, 2003, **42**, 1437-1447.
111. B. J. O'Keefe, M. A. Hillmyer and W. B. Tolman, *J. Chem. Soc. Dalton.*, 2001, 2215-2224.
112. S. M. Guillaume, E. Kirillov, Y. Sarazin and J. F. Carpentier, *Chem. Eur. J.*, 2015, **21**, 7988-8003.
113. P. J. Dijkstra, H. Z. Du and J. Feijen, *Polym. Chem.*, 2011, **2**, 520-527.
114. O. Dechy-Cabaret, B. Martin-Vaca and D. Bourissou, *Chem. Rev.*, 2004, **104**, 6147-6176.
115. J. F. Carpentier, *Macromol. Rapid Commun.*, 2010, **31**, 1696-1705.
116. C. M. Thomas, *Chem. Soc. Rev.*, 2010, **39**, 165-173.
117. T. M. Ovitt and G. W. Coates, *J. Am. Chem. Soc.*, 2002, **124**, 1316-1326.
118. T. Rosen, I. Goldberg, W. Navarra, V. Venditto and M. Kol, *Chem. Sci.*, 2017.
119. V. Simic, N. Spassky and L. G. HubertPfalzgraf, *Macromolecules*, 1997, **30**, 7338-7340.
120. O. Poncelet, W. J. Sartain, L. G. Hubertpfalzgraf, K. Folting and K. G. Caulton, *Inorg. Chem.*, 1989, **28**, 263-267.
121. W. M. Stevels, M. J. K. Ankone, P. J. Dijkstra and J. Feijen, *Macromolecules*, 1996, **29**, 6132-6138.
122. Y. J. Kim and J. G. Verkade, *Macromol. Rapid Commun.*, 2002, **23**, 917-921.
123. C. K. A. Gregson, I. J. Blackmore, V. C. Gibson, N. J. Long, E. L. Marshall and A. J. P. White, *Dalton Trans.*, 2006, 3134-3140.
124. A. L. Zelikoff, J. Kopilov, I. Goldberg, G. W. Coates and M. Kol, *Chem. Commun.*, 2009, 6804-6806.
125. S. K. Russell, C. L. Gamble, K. J. Gibbins, K. C. S. Juhl, W. S. Mitchell, A. J. Tumas and G. E. Hofmeister, *Macromolecules*, 2005, **38**, 10336-10340.
126. P. S. Umare, G. L. Tembe, K. V. Rao, U. S. Satpathy and B. Trivedi, *J. Mol. Catal. A: Chem.*, 2007, **268**, 235-243.
127. D. Deivasagayam and F. Peruch, *Polymer*, 2011, **52**, 4686-4693.
128. C. Romain, L. Brelot, S. Bellemin-Laponnaz and S. Dagorne, *Organometallics*, 2010, **29**, 1191-1198.
129. S. Gendler, S. Segal, I. Goldberg, Z. Goldschmidt and M. Kol, *Inorg. Chem.*, 2006, **45**, 4783-4790.
130. O. Wichmann, R. Sillanpaa and A. Lehtonen, *Coord. Chem. Rev.*, 2012, **256**, 371-392.

131. Y. Kim and J. G. Verkade, *Organometallics*, 2002, **21**, 2395-2399.
132. C. A. Huang and C. T. Chen, *Dalton Trans.*, 2007, 5561-5566.
133. D. T. Dugah, B. W. Skelton and E. E. Delbridge, *Dalton Trans.*, 2009, 1436-1445.
134. R. K. Dean, A. M. Reckling, H. Chen, L. N. Dawe, C. M. Schneider and C. M. Kozak, *Dalton Trans.*, 2013, **42**, 3504-3520.
135. K. Devaine-Pressing, J. H. Lehr, M. E. Pratt, L. N. Dawe, A. A. Sarjeant and C. M. Kozak, *Dalton Trans.*, 2015, **44**, 12365-12375.
136. E. Kober, Z. Janas, T. Nerkowski and L. B. Jerzykiewicz, *Dalton Trans.*, 2013, **42**, 10847-10854.
137. E. Kober, R. Petrus, P. Kociecka, Z. Janas and P. Sobota, *Polyhedron*, 2015, **85**, 814-823.
138. E. Y. Tshuva, I. Goldberg, M. Kol and Z. Goldschmidt, *Inorg. Chem.*, 2001, **40**, 4263-4270.
139. A. J. Chmura, M. G. Davidson, M. D. Jones, M. D. Lunn, M. F. Mahon, A. F. Johnson, P. Khunkamchoo, S. L. Roberts and S. S. F. Wong, *Macromolecules*, 2006, **39**, 7250-7257.
140. S. Song, X. Zhang, H. Ma and Y. Yang, *Dalton Trans.*, 2012, **41**, 3266-3277.
141. Z. H. Tang and V. C. Gibson, *Eur. Polym. J.*, 2007, **43**, 150-155.
142. E. V. Brouillet, A. R. Kennedy, K. Koszinowski, R. McLellan, R. E. Mulvey and S. D. Robertson, *Dalton Trans.*, 2016, **45**, 5590-5597.
143. K. M. Osten, D. C. Aluthge and P. Mehrkhodavandi, *Dalton Trans.*, 2015, **44**, 6126-6139.
144. D. C. Aluthge, J. M. Ahn and P. Mehrkhodavandi, *Chem. Sci.*, 2015, **6**, 5284-5292.
145. C. S. Johnson, *Prog. Nucl. Magn. Reson. Spectrosc.*, 1999, **34**, 203-256.
146. G. A. Morris, 2002.
147. A. Gierer and K. Wirtz, *Z Naturforsch A*, 1953, **8**, 532-538.
148. H. C. Chen and S. H. Chen, *J. Phys. Chem.*, 1984, **88**, 5118-5121.
149. F. Perrin, *J. Phys. Radium*, 1936, **7**, 1-11.
150. A. Macchioni, G. Ciancaleoni, C. Zuccaccia and D. Zuccaccia, *Chem. Soc. Rev.*, 2008, **37**, 479-489.
151. R. Neufeld and D. Stalke, *Chem. Sci.*, 2015, **6**, 3354-3364.
152. S. Bachmann, R. Neufeld, M. Dzemski and D. Stalke, *Chem. Eur. J.*, 2016, **22**, 8462-8465.
153. K. A. M. Thakur, R. T. Kean, E. S. Hall, J. J. Kolstad, T. A. Lindgren, M. A. Doscotch, J. I. Siepmann and E. J. Munson, *Macromolecules*, 1997, **30**, 2422-2428.
154. K. A. M. Thakur, R. T. Kean, M. T. Zell, B. E. Padden and E. J. Munson, *Chem. Commun.*, 1998, 1913-1914.
155. M. H. Chisholm, S. S. Iyer, M. E. Matison, D. G. McCollum and M. Pagel, *Chem. Commun.*, 1997, 1999-2000.

Chapter 2: Polynuclear titanium isopropoxide initiators

Abstract

The majority of homogeneous titanium catalysts applied in the ROP of lactide feature an alkoxide initiating group. The initiating group provides control over the initiation step during the polymerisation by activating the monomer and subsequently leaving a vacant, Lewis acidic site on the titanium centre that is capable of propagating growth of the polymer chain. The use of polynuclear initiators for the ROP of lactide has been demonstrated to be both active and tolerant to air/moisture. However, the active species in these reactions is often poorly defined and relationships between nuclearity and catalytic performance have not been established. We sought to synthesise polynuclear initiators to investigate the effect of nuclearity on performance in the ROP of lactide, noting that facile exchange between aggregates of varying size is a significant challenge in such reactions. While a wide variety of amine bis(phenolate) ligands had been used to support titanium alkoxide initiators in the ROP of lactide, none used a carboxylate pendant donor. Carboxylates are ambidentate donors and hold the potential to act as bridges in a polynuclear complex than the more commonly observed alkoxides. The multidentate, amine bis(phenolate) ligand would stabilise the metal centres all the while providing an anchor for the carboxylate bridges to form. These traits were envisaged to direct the assembly of a polynuclear titanium complex that would be active towards the ROP of *rac*-lactide.

2.1 Introduction

The majority of initiators applied to the ring-opening polymerisation (ROP) of lactide feature a single-site, Lewis acidic metal centre to enact greater control over the polymerisation process.[1] While these initiators show good activity and control towards the ROP of lactide, they can lack stability outside of the glovebox. This reduced lifetime limits the ability to handle the compounds to perform in-depth studies of the catalytic system and to be applied to industrial scale reactions. Polynuclear initiators have been observed to be more tolerant to air/moisture and therefore potentially more attractive initiators.[2] Several polynuclear initiators for the ROP of lactide have been reported but these are all restricted by the challenges faced when attempting to identify the active species and defining a relationship between nuclearity and performance.[3-10]

A well-studied example of a metal alkoxide aggregate applied to the ROP of *rac*-lactide, is aluminium isopropoxide.[11,12] It was reported that trinuclear and tetranuclear aluminium clusters, bridged by the isopropoxide ligand, were formed under the polymerisation conditions. The trinuclear species was found to be the more reactive and more abundant of the two species. Additionally, varying the conditions of the reaction to promote formation of the trinuclear species resulted in a decrease in the PDI of the polymer. This increase in control was attributed to reducing the degree of exchange between the trinuclear and tetranuclear species and therefore reducing the disruption which affects propagation.

Further examples of metal alkoxide aggregates include a group of compounds with general formula $M_5(\mu_5\text{-}O)(OR)_{13}$ (M = Fe, Y, La, Sm, Yb; R = alkyl). In the case of M = Y,[13] similar levels of activity in the ROP of lactide was reported for the pentanuclear and mononuclear activators. This indicates that larger aggregates can retain the activity of the monometallic complexes. In the work of Tolman *et al.* (M = Fe),[14] the activity of the pentanuclear activator was observed to be similar to the dinuclear activator but in contrast, another iron(III) system found the dinuclear species to be more active than the mononuclear species,[15] suggesting that there is no obvious relationship between complex size and catalytic activity.

All of these examples are polynuclear complexes[13-15] bridged by alkoxide ligands. These ligands are labile by definition, as they also act as initiating groups in the ROP of lactide, therefore have limited ability to stabilising cluster formation.

To stabilise the cluster formation, and develop a clearer view of the effect aggregate size has on activity, we utilise a multidentate amine bis(phenolate) ligand which can also enacting control and tunability over the polymerisation process. The pendant carboxylate is envisaged to promote stability of the aggregates through a stronger bridging interaction (*cf.* alkoxide). The polynuclear complexes presented herein represent out first efforts in the synthesis of polynuclear titanium initiators for the ROP of *rac*-lactide that could be assembled and stabilised through ligand design.

2.2 Synthesis and Characterisation.

Compounds **1**-**4**$(H)_3$ were obtained using adapted procedures from the literature.[16-19] Starting from a glycine core, two synthetic routes were used to access these ligand precursors: two successive reductive aminations were required to obtain compound **1**$(H)_3$ while one-pot Mannich condensations produced compounds **2**-**4**$(H)_3$ (Figure 18). A substituent in the *para*-position of the phenol is necessary to block any polyphenolic condensation side reactions during the Mannich condensation. Compounds **2**-**4**$(H)_3$ can therefore be accessed by simple substitution of the phenolic starting material to incorporate the corresponding *R*′ group. The corresponding salicylaldehyde derivatives are significantly more expensive starting materials from commercial sources and, in some cases, unavailable from chemical vendors. As a result, the Mannich condensation was found to be the most versatile synthetic route to amine bis(phenolate) ligands. The substituents around the phenol rings were altered to allow for analysis of structural trends in assembling a polynuclear titanium complex and tunability of the system under polymerisation conditions.

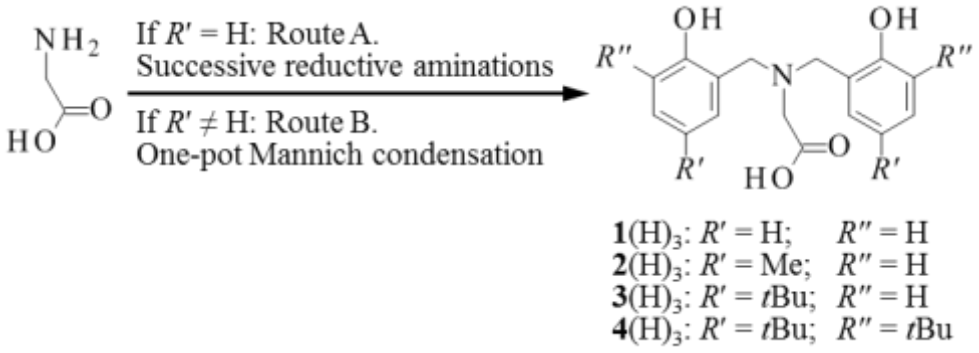

Figure 18. Synthetic routes to amine bis(phenolate) ligand precursors **1**-**4**$(H)_3$. Route A: salicylaldehyde and sodium hydroxide in methanol and stir for 2h then add sodium borohydride under N_2, repeat. Route B: *R*′/*R*″-substituted phenol, paraformaldehyde and sodium hydroxide reflux in methanol under N_2 for 24 h or 48 h.

A ligand substitution reaction was used to synthesise the titanium complexes. With titanium isopropoxide as the source of titanium, the isopropoxides deprotonate the ligand precursor, acting as an *in situ* base, while leaving free coordination sites for the ligand to bind the titanium centre. At room temperature, compounds **1**-**3**$(H)_3$ were suspended in dry THF under a dry N_2 atmosphere whereas **4**$(H)_3$ appeared as a colourless solution. Following the addition of titanium isopropoxide, an instant colour change from white

precipitate to yellow or orange solution occurred. A yellow solution was briefly observed when compound **1**$(H)_3$ was used, after which the reaction returned a yellow precipitate.

Following the example of amine bis(phenolate) complexes from the literature, the complexes **5-8** in Figure 19 was proposed. Taking into consideration the source of titanium is in a 4+ oxidation state and the ligand can bind as an LX_3 type donor with 3− oxidation state, only one isopropoxide is anticipated to remain bound to the metal centre, conserving an overall neutral complex. This would leave a vacant coordination site on the titanium centre providing it would aim to reach a six-coordinate geometry.

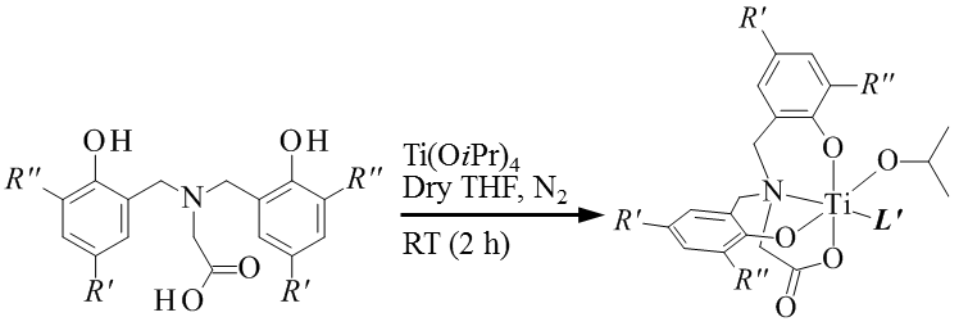

1$(H)_3$: R' = H; R'' = H
2$(H)_3$: R' = Me; R'' = H
3$(H)_3$: R' = *t*Bu; R'' = H
4$(H)_3$: R' = *t*Bu; R'' = *t*Bu

5: R' = H; R'' = H
6: R' = Me; R'' = H
7: R' = *t*Bu; R'' = H
8: R' = *t*Bu; R'' = *t*Bu

Figure 19. Proposed structure of the complex resulting from the reaction of ligand precursors **1-4**$(H)_3$ with titanium isopropoxide. Note: ***L'*** denotes a vacant site on the titanium centre of **5-8**, occupied by a ligand or solvent molecule.

The aforementioned yellow precipitate from the reaction of compound **1**$(H)_3$ and titanium isopropoxide, compound **5**, was found to be insoluble in common organic solvents. Solution-based NMR experiments were therefore not practical but CP-MAS NMR spectroscopy allowed for a ^{13}C NMR of the solid-state sample. Spinning the sample at 5 kHz led to side bands coinciding with genuine signals from the sample. Increasing the spinning rate to 10 kHz reduced the intensity of these signals to give a cleaner spectrum. Further analysis was conducted by a CP phase-sensitive experiment to identify quaternary carbons, methyne, methylene and methyl carbons. All ^{13}C signals were distinguished and conform to the expected frequencies for this type of compound.[20-22] Further to this, ^{1}H signals were obtained by a HMQC experiment. Nevertheless, the spectrum appears to be more complex than expected for **5** even with the increased line broadening associated with CP-MAS NMR experiments.

The solution-state ^{1}H NMR experiments of the collected products **6-8** in $CDCl_3$ also showed more complex spectra, featuring overlapping multiplets over segments of significant spectral width that are symptomatic of a dynamic mixture. By integrating these broad regions of signals in these spectra, the expected integrals for the aromatic, methylene and *R′*/*R″* groups are approximately found. An EXSY experiment revealed an exchange process was present in $CDCl_3$, which we attributed to coordination of a variety of donors to the labile site, ***L′***, on the titanium centre. When bound by amine bis(phenolate) ligands, titanium 4+ centres show a strong preference for a six-coordinate geometry.[20-22] For this reason, we propose the vacant site in Figure 19 would be filled by a suitable donor, ***L′***, which includes the possibility of mononuclear units aggregating as shown in Figure 20.

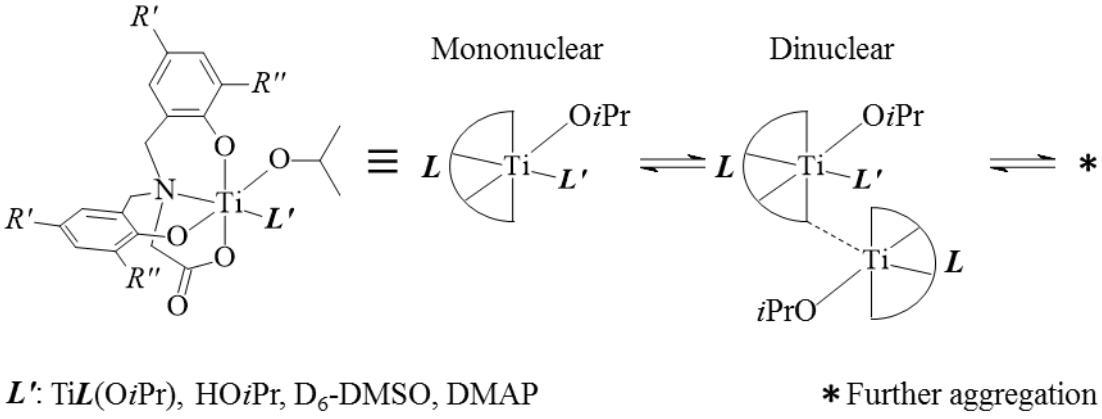

Figure 20. Figure illustrating the proposed binding site, ***L′***, and the mechanism by which aggregation occurs. The bridging interaction is indicated by a dashed bond. A legend summarises suitable donors identified while studying these compounds.

2.2.1 Single crystal X-ray diffraction

Single crystals suitable for X-ray diffraction were grown by placing a saturated solution of **12** in dry THF at –20 °C. The resulting large, orange, irregular crystals readily dissolved once the solution returned to room temperature. An initital dataset was obtained at 100 K with limited diffraction (*ca.* d_{min} = 1.02 Å). The experiment was repeated with further samples to give diffraction to the CCD detector limit (d_{min} = 0.78 Å). Unfortunately, these larger crystals cracked when placed under the cryostream temperatures of 100 K, 120 K and 150 K. For this reason, data was collected at 173 K.

Refinement of the dataset revealed an aggregate of the proposed structure of **8** with formula [Ti**4**(O*i*Pr)]$_2$[Ti**4**(O*i*Pr)(HO*i*Pr)]. The three units of **8**, held together by bridging carboxylates from the ligands, can be described as a trinuclear aggregate of the proposed structure of **8**, with one titanium centre terminated by a coordinated isopropanol ligand (Figure 21). This terminal isopropanol can be distinguished from the isopropoxides with its longer O–Ti bond length (2.091(2) Å versus 1.771(2) Å) as well as the freely-refined proton that was located in the difference Fourier map attached to O16. Furthermore, no counter-ions are present in the crystal structure so the overall compound needs to be neutral. Ligand **4** contributes a charge of −3, isopropoxide a charge of −1 and titanium a charge of +4. With three of each of these, an overall charge balance of 0 is achieved. Thus, it is necessary to assign the remaining isopropoxy group as an isopropanol to preserve an overall neutral charge. Bond distance analysis of the average native and bridging carboxylate O–Ti (2.058(2) and 2.063(2) Å) and C–O (1.261(3) and 1.255(3) Å) bond distances are in agreement with related structures.[19,23,24] The similarity in bond distances between native and bridging interactions supports the view that the carboxylates are delocalised in their bridging interaction with the titanium centres in the structure. If we consider the three ligands **4** in the structure as propellers, they are bound in ΛΔΔ and ΛΛΔ modes. The terminal unit adopts the opposite chirality to reduce steric interactions and allow for the intramolecular hydrogen bond between O16–H16···O2 to form. The O16···O2 and H16···O2 distances of 2.556(3) Å and 1.80(4) Å respectively are within expected hydrogen bonding values.[27]

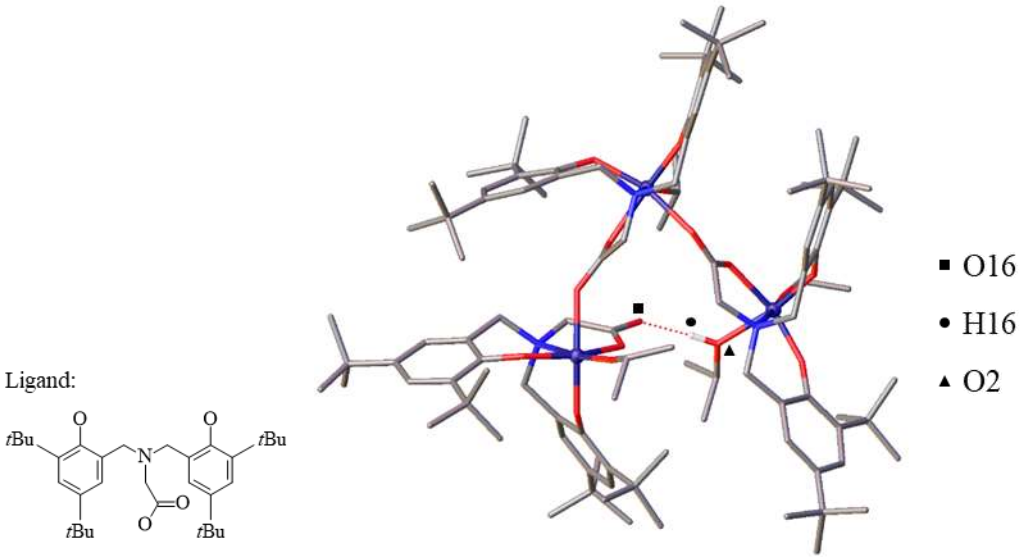

Figure 21. Asymmetric unit obtained by SCXRD of a sample of **8** with formula [Ti**4**(O*i*Pr)]$_2$[Ti**4**(O*i*Pr)(HO*i*Pr)] or **8**$_3$(HO*i*Pr). Titanium centres displayed as spheres and ligands displayed as tubes. Hydrogen atoms omitted for clarity with exception of the proton that displays an intramolecular hydrogen bond (dashed red lines) between the isopropanol ligand and the carboxylate native to Ti1. Ti = purple; C = grey; N = blue; O = red, H = white.

Crystals of **8** were dissolved in $CDCl_3$ and the ^{1}H NMR spectrum of this sample revealed that some of the peaks overlapped with those of the mother liquor, of which a ^{1}H NMR was previously taken. After leaving the sample to stand for 1 day at RT under a dry N_2 atmosphere, further ^{1}H NMR spectra were taken to reveal the trinuclear aggregate had reverted to a similar dynamic mixture previously observed. This was strong evidence that the mixtures observed by ^{1}H NMR spectroscopy of **6**-**8** are of a pure product undergoing dynamic exchange in solution, where each spectrum displays an equilibrium of these species in solution. Further sample analysis was achieved with ^{1}H COSY and ROESY NMR experiments that both concur with the proposed dynamic nature of **8**, whereby these experiments show through-bond and through-space coupling between the species in solution.

In both the ^{1}H NMR spectra of the crystals of **8** and their mother liquor, a sharp doublet is noticeable at 10.41 ppm. This was unexpected as no carboxylic protons are typically observed in the ^{1}H NMR spectrum of the free ligand and we would assume that all of these acidic protons have been deprotonated after reaction with the *in situ* isopropoxide base. A key feature in the crystal structure is the intramolecular hydrogen bond between the isopropanol bound to Ti1 and a carboxylate native to Ti3. A ^{1}H COSY experiment showed this proton is coupling with a proton at 4.36 ppm, which

correspond to the isopropanol C*H* methine and explain why this appears as a doublet with a *J* coupling constant of 7.60 Hz. A ROESY experiment also shows through space contacts to methylene and methyl protons that are found on the ligands and isopropanol respectively, The ROESY experiment also showed an exchange signal between the doublet at 10.41 ppm associated with the intramolecular hydrogen bond and the isopropanol O*H* at 1.60 ppm. An unfortunate effect of this exchange is this intramolecular hydrogen-bonded proton is unreliable for trying to estimate the proportion of trinuclear aggregate in the mixture by integration of the proton signals in the spectrum. Nevertheless, its presence in the spectra confirms that the solid-state trinuclear structure also persists in solution.

Having used the solid-state and solution-state studies of **8** as a model for the class of compound TiL(O*i*Pr) where L = **1**-**4**, data was gathered to translate the properties determined for **8** with **5**-**7**. As previously stated, **5** was found to be largely insoluble which hampered its characterisation using solution-based techniques. Attempts to grow crystals of **6** and **7** using slow evaporation, solvent diffusion and vapour diffusion under dry conditions were unsuccessful. This may be unsurprising as the probability of nucleation prior to crystal growth would be reduced due to the dynamic nature of these species in solution. Nevertheless, solution-based techniques were used to gather data on **6** and **7**. The ^{1}H NMR spectra of these two compounds show the same broad aromatic, methylene and isopropoxide regions that were observed for **8** but the chemical shifts are different, as would be expected for three compounds bound by different ligands. The signals associated with the different *R′*/*R″* groups are clearly visible in the spectra of **6** and **7**. Additionally, integration of the broad regions in these spectra found the correct number of protons associated with the aromatic, methylene, *R′*/*R″* and isopropoxide groups, indicating that the compounds were formed. Again, an EXSY NMR experiment showed the mixtures were under exchange while ^{1}H COSY and ROESY NMR experiments showed through-bond and through-space coupling between the species in the dynamic mixture.

Close inspection of the ^{1}H NMR spectra of **6**-**8** using the data from the COSY, EXSY and ROESY experiments allowed for an estimation of the nuclearities of the aggregates in solution by focussing on signals associated with key structural features such as the *R′*/*R″* groups or methylene signals. Using complex **6** (*R′* = Me, *R″* = H) as an example (Figure 22), the presence of two methyl signals would be expected for a mononuclear form, four for a dinuclear form, six for a trinuclear form, and so on. Likewise, we would

anticipate three pairs of methylene signals for the mononuclear form, six for the dinuclear form and nine for the trinuclear form. Furthermore, a mixture of two aggregates would lead to a fixed a number of signals: for example, a mixture of dinuclear and trinuclear aggregates would display a total of fifteen methylene proton signals. Thus, by combining 1D and 2D NMR spectra, the number of signals for specific groups on the complexes can reveal the nuclearity of the aggregates in solution.

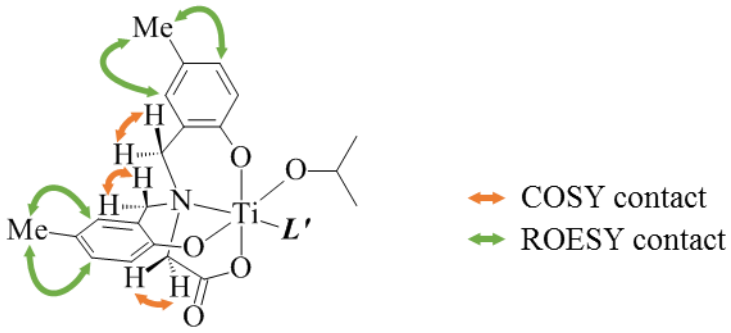

Nuclearity	Expected methyl signals	Expected methylene signals
1	2 singlets	3 pairs of doublets
2	4 singlets	6 pairs of doublets
3	6 singlets	9 pairs of doublets
2 and 3 (mixture)	10 singlets	15 pairs of doublets

Figure 22. Mononuclear unit of complex **6** with selected COSY and ROESY contacts highlighted, which were used to estimate the nuclearity of the aggregate in solution.

For **6**, the spectrum was particularly complex in comparison to **7** and **8**. Five distinct methyl signals could be discerned which would correspond to a trinuclear aggregate although the complexity of the aromatic region is suggestive of higher nuclearity. In the case of **7**, the spectrum displayed a set of clearly pronounced diastereotopic protons of similar intensity in the methylene region. These were paired by using cross-coupling signals from the COSY and ROESY experiments to give a total of nine pairs of methylene protons, equating to a trinuclear aggregate. The lower intensity methylene peaks in the spectrum are under exchange with those from the trinuclear form and were attributed to a tetranuclear aggregate due to their larger number, although it is clear that the trinuclear aggregate is the major species in solution with its higher intensity signals. Finally, the methylene protons in complex **8** could be counted in the ^{1}H COSY 2D spectrum to yield fifteen pairs of signals, indicating a mixture of dinuclear and trinuclear aggregates in solution. This is in agreement with the signals found for the crystal structure of **8**$_3$(HO*i*Pr) in dry $CDCl_3$.

Aggregation through the *L′* site was proposed to be the source of the complexity of the NMR spectra of 6-8. Blocking the *L′* site with a strong donor would reduce the tendency of 6-8 to aggregate and lead to less complexity in the NMR spectra that would give well-defined signals attributed to the structures. Complex 8 was studied by ^{1}H NMR spectroscopy in dry D_6-DMSO as a strong donor solvent that could bind to the *L′* site. In comparison to the spectrum obtained in $CDCl_3$, fewer signals were observed in the spectrum in D_6-DMSO. Notably, a set of signals corresponding to a mononuclear form, were identified. An EXSY experiment showed this set of signals was under exchange with other signals in a 1:0.4 ratio. Close inspection of the aromatic region in the ^{1}H NMR spectrum identified four pairs of aromatic signals as opposed to a myriad of signals as seen in $CDCl_3$ (Figure 23). This was confirmed by a ^{1}H COSY experiment. This reduction in the number of signals is expected when aggregation through the *L′* site is blocked by a strongly coordinated ligand such as D_6-DMSO.

Dissolving **8** in D_6-DMSO reduced the complexity of the ^{1}H NMR spectrum. In an attempt to block aggregation and further simplify the ^{1}H NMR spectrum of **8**, a sample was dissolved in $CDCl_3$ along with 4-dimethylaminopyridine (DMAP). This additive is a strong Lewis base and we envisaged it would bind to the ***L′*** site, blocking aggregation. This method was effective in reducing the number of aromatic signals to a pair of doublets and as expected, are the only signals observed (Figure 23). This highlights that the dynamic nature of these complexes can be suppressed by use of donor solvent or a Lewis base additive allowing for a simpler ^{1}H NMR spectroscopy to be recorded and act as a reference to the more complex aggregates. Importantly, this was strong evidence the ^{1}H NMR spectra obtained for **6-8** in $CDCl_3$ are of the pure compounds forming several aggregated species in solution. Since adding DMAP to a sample of **8** in $CDCl_3$ was successful in reducing aggregation to give a more interpretable spectrum, this method for NMR sample preparation was repeated for complexes **6** and **7**.

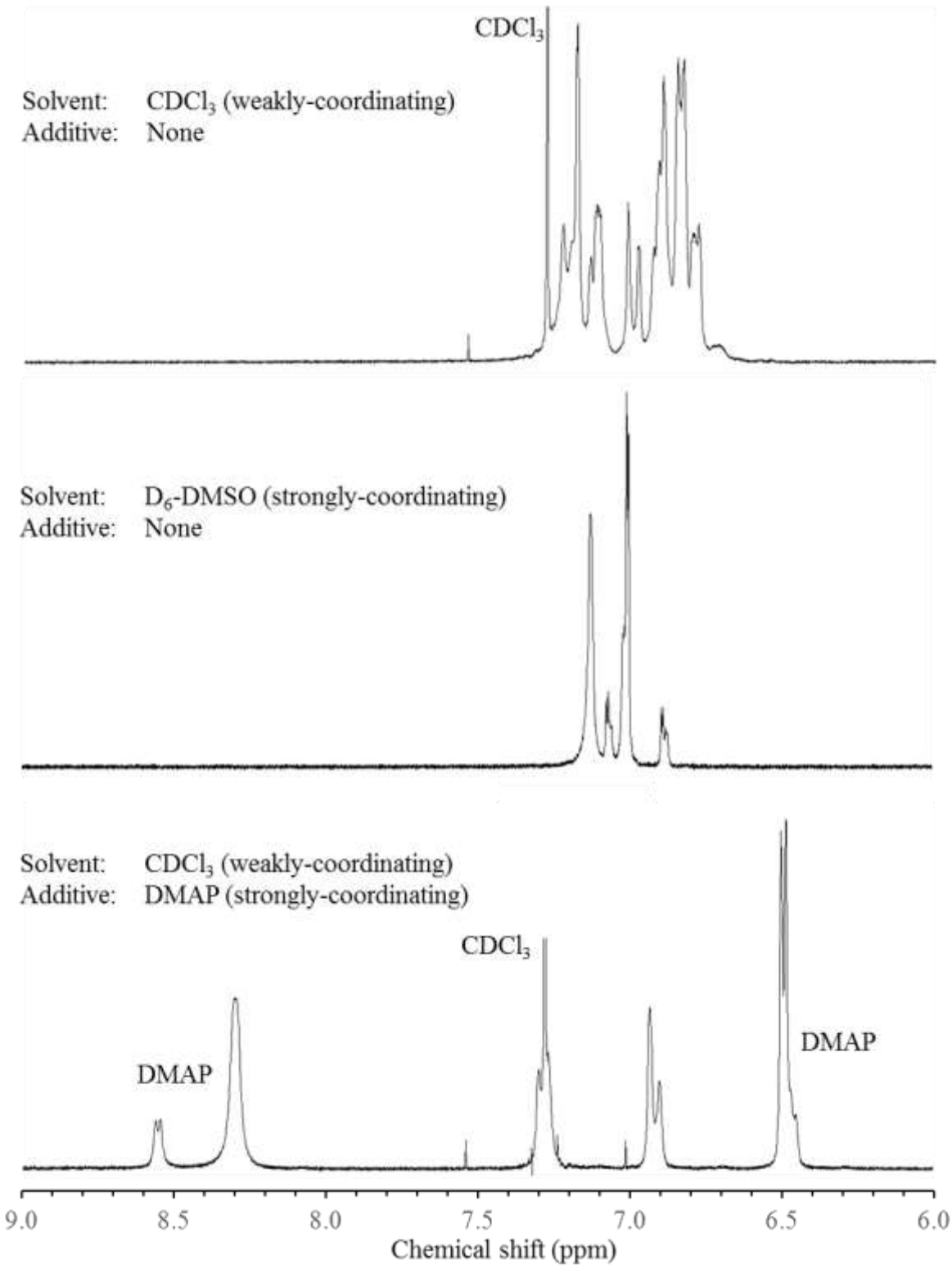

Figure 23. Example ^{1}H NMR spectra of the aromatic region of complex **8**. From left to right: complex chemical environments in $CDCl_3$; reduced number of chemical environments (four pairs of doublets) in D_6-DMSO; two doublets observed in $CDCl_3$ with DMAP as an additive.

The ^{1}H NMR spectra of the samples showed the presence of a single species, in solution with DMAP, under exchange. These detailed experiments confirm the proposed structures of **6**-**8** (Figure 19) exist in solution but that the nature of the species is solvent dependent. A feature in all of the ^{1}H NMR spectra of **6**-**8** with DMAP in $CDCl_3$ is the difficulty in identifying the methylene bridge protons, as these show significant line broadening. We interpreted this as an indication that the ligand framework in the complexes is flexible. Through-space contacts between the carboxylate and phenolate donors in the ligand framework and DMAP were clearly defined in the well-resolved spectra of **8**. This evidence indicates that DMAP is bound at the ***L′*** position (Figure 19). The strong *trans*-influence of DMAP will weaken the phenolate O–Ti bond, inciting flexibility about this position and elucidating the loss and broadening of this methylene arm signal in the NMR spectra.

Further characterisation of **5** was sought using mass spectrometry (MS) as a more sensitive technique. Initially, the sample was dissolved in DCM/methanol for ESI-MS and mass ion analysis, in positive mode, allowed for the insoluble, yellow precipitate **5** to be identified. The mass ion peak in the spectrum is proposed to be the methyl ester of **5** with the addition of a sodium methoxide to the ***L′*** site of the titanium centre. The same sample in negative mode yielded an ion peak for **5** bound by a hydroxide on the vacant site. Additional ion peaks corresponding to the methyl ester bound by acetates, incorporated during the MS sample preparation, were also found. The mass ion peak of **5** was not present as the compound was seen to be undergoing a reaction under the MS conditions (190 °C, 0.4 bar nebuliser, capillary voltage 4500 V) for both positive and negative modes. The experiment was repeated using THF/MeCN to avoid reaction with methanol. In this case, a number of large aggregates, exceeding the maximum upper range of 2000 m/z were detected, indicating the presence of a hexanuclear aggregate. Finally, analysis of **5** using EI-MS led to the identification of the mass ion peak at 391.0 m/z and its subsequent fragmentation with losses of methyl (from isopropyl), isopropyl, carboxylate and phenol groups identified in the spectrum. Through these MS experiments, we were able to further structurally characterise compound **5**.

The reaction of **5** with methanol prompted us to conduct ESI-MS of **6** and **7** in THF/MeCN but no mass ions were detected between 40 and 2000 m/z in positive mode. Negative mode yielded a single mass ion peak in the mass spectra for **6** and **7** corresponding to the addition of three protons to the complexes. This could be explained

by the addition of protons to the double bonds in the structures, resulting in a negative charge around the ligand framework.

A variety of mass spectrometry techniques were required to detect mass ions of complexes **5-8**. The reactivity of the carboxylate arm and labile site ***L'*** have caused their characterisation to be more difficult in comparison to other amine bis(phenolate) titanium compounds.[20-22] The MS analysis showed large aggregates, of an estimated nuclearity of six, were visible in a sample of **5**. Larger aggregates could cause the insolubility of **5**, much like a polymer decreases in solubility with increasing chain length. If **5** were insoluble due to the presence of large aggregates, they could be dissociated by the application of energy or coordinating additives. Samples of **5** were stirred in dry THF with DMAP, leading to no improvement in solubility even when heating was applied. Either the **5** is insoluble in all common solvents or its high nuclearity aggregates are stable under these conditions.

Compound **5** is poorly-defined in comparison to **8** due to its heterogeneity, its characterisation therefore lacks the detail that was achieved for **8**. This is an example of the difficultly faced when attempting to fully characterise a heterogeneous species in comparison to a homogeneous species. In turn this limits the level of understanding we can achieve of the catalytic system.

2.3 Application in the polymerisation of *rac*-lactide

Metal alkoxide compounds are well-suited to initiate/catalyse the polymerisation of cyclic esters. There are several accounts, in particular relating to the use of titanium alkoxide compounds in the ROP of *rac*-lactide, with reviews covering a range of species which exhibit high levels of control over the polymerisation.[25,26] For this reason, we believed that the titanium isopropoxide aggregates **5**-**8** would be well-suited to this application. Crucially, the ROP of *rac*-lactide can be performed under solution polymerisation conditions, which allows study of the system using solution-based techniques, and melt polymerisation conditions that test the limits of the activity of the system. The data collected from these experiments are summarised in Table 1. The monomer:titanium loadings were calculated assuming the solid samples were of the mononuclear unit of **6**-**8** (Figure 19) with the ***L′*** position vacant.

Compound **5** showed near-zero conversions under various polymerisation conditions and no data could be gathered. We proposed this low activity to be exacerbated by the heterogeneous nature of the compound. Using the more soluble analogues of **5** with alkyl *R′*/*R″* groups was key to achieving an active compound for the ROP of *rac*-lactide.

Initial experiments were conducted in solution with a 100:1 monomer:titanium ratio where the monomer concentration was 1 $mol \cdot L^{-1}$ in dry toluene under a dry N_2 atmosphere. Both compounds **6** and **7** showed low activity under these conditions, demonstrated by the low conversion of monomer to polymer they were able to achieve after 24 h (< 5 %). In light of this, oligomerisation reactions with a loading of 20:1 under the same conditions were used to explore if these compounds were at all active. Compound **6** showed low conversion but compound **7** was able to convert the monomer to the polymer close to completion. This contrasting observation between the conversions achieved by **6** and **7** was surprising since the only structural difference is the *R′* group change from methyl to *tert*-butyl. Further to this, compound **8** incorporates an extra *tert*-butyl group at the *R″* position. Again, this resulted in an increase in activity in the ROP of *rac*-lactide where a 100:1 monomer:titanium loading was used. Lower titanium loading of 50:1 was sufficient to achieve high conversion (90 %) in comparison to the 20:1 loading required with compound **7**. It is worth noting that if we increase the loading of compounds **6**-**8**, there is an increase in conversion in comparison to lower loading. This is suggestive that under the solution polymerisation conditions, the loading has a greater effect on performance than aggregation. This aligns with the design concept that the

ligand is preventing further aggregation to larger species even in the instance where the loading, and concentration, was increased.

Solution polymerisation conditions ($[M]_0$ = 1 mol·L^{-1}, toluene, 130 °C)							
Entry	Activator	$[M]_0/[Ti]_0$	Time	Conv.[a]	M_n[b]	$M_{n(NMR)}$[c]	PDI[d]
1	**6**	20	24 h	4	-	-	-
2	**6**	100	24 h	0	-	-	-
3	**7**	20	24 h	92	4120	7260	1.24
4	**7**	50	24 h	19	4070	4790	1.09
5	**7**	100	24 h	13	-		-
6	**8**	50	24 h	90	7360	11300	1.24
7	**8**	100	24 h	62	9420	13500	1.18
Melt polymerisation conditions (130 °C)							
Entry	Activator	$[M]_0/[Ti]_0$	Time	Conv.[a]	M_n[b]	$M_{n(NMR)}$[c]	PDI[d]
8	**6**	300	2 h	5	-	-	-
9	**6**	300	6 h	21	5040	4640	1.32
10	**6**	300	24 h	83	10000	9810	1.47
11	**7**	300	2 h	18	-	-	-
12	**7**	300	6 h	74	13500	13000	1.64
13	**7**	300	24 h	96	15000	10700	1.54
14	**7**	600	24 h	93	14800	11800	2.03
15	**8**	300	2 h	14	-	-	-
16	**8**	300	6 h	47	6780	8320	1.26
17	**8**	300	24 h	89	14100	12000	1.40
18	**8**	600	24 h	80	12200	11500	1.39

Table 1. Polymerisation data using titanium isopropoxide complexes **6**-**8**. Data is displayed for both solution and melt polymerisation conditions. [a] Conversion (%) from ^{1}H NMR spectra evaluated by integration of the methine regions of polylactide versus lactide. [b] Polymer number average molar mass determined from GPC traces. [c] Calculated polymer molecular weight by ^{1}H NMR end-group analysis. [d] Polydispersity indices (M_w / M_n) obtained from GPC traces.

Initial melt polymerisation reactions were undertaken with 300:1 monomer:titanium loading under dry N_2 atmosphere, in a sealed flask, for 24 h. Under these conditions, it was revealed that all three of compounds **6**-**8** could achieve high conversion after 24 h. To begin to reveal differences in activity between these compounds we must reduce the polymerisation time. All compounds displayed similar but drastically reduced conversion when the polymerisation time was 2 h. Efforts to recover the polymer formed were unsuccessful, indicating that very short chains are being formed. Lengthening the polymerisation time to 6 h was successful in revealing the different properties between compounds **6**-**8**. We note that the PDI values are consistently lower for **8** in comparison to **6** and **7**. This can be explained by additional *tert*-butyl *R″* group present in **8** that

imparts greater control over the polymer formed, which is in accord with what is found for a variety of other ROP of lactide systems.[20,26,27]

It is initially clear that like in solution, changing the *R′*/*R″* groups to increase the extent of alkyl groups on the compounds results in an increase in conversion. In contrast to what was observed under solution conditions, compound **7** is more active than compound **8** under melt conditions. This difference in activity is attributed to the additional *tert*-butyl group in the *R″* position of **8**, which primarily contributes additional steric congestion around the metal centre, hindering the interaction of the monomer/polylactide chains with the titanium centre, resulting in reduced activity in comparison to compound **7**.

The microstructure of the polylactide produced by **6**-**8** was inspected using NMR spectroscopy. The P_m values indicate a slightly heterotactic polymer was obtained (Table 3). Calculating the M_n from the ^{1}H NMR of the polylactide chain ($M_{n(NMR)}$) are in good agreement with the M_n values obtained from GPC, suggesting linear polylactide is produced. End group analysis of the ^{1}H NMR spectra show the insertion of the isopropoxide group into the PLA chain.[28-31]

Further testing of the catalytic system under melt conditions was undertaken by increasing the monomer:titanium ratio to 600:1 for compound **8**. A slight decrease in the conversion was observed in comparison to a monomer:titanium ratio of 300:1. In addition, the M_n values are similar. This is unexpected as a lower loading of active sites typically leads to lower conversion and, in turn, decreased polymer chain lengths. In this case, the values obtained for conversion, M_n and $M_{n(NMR)}$ all agree with a small change in activity despite the number of active sites was halved. Comparing compounds **8** to typical titanium alkoxide catalysts, it is clear the defining feature is a vacant site. We tentatively propose that the lack of change in activity and M_n when decreasing catalytic loading is caused by polymeryl exchange. This is facilitated by the high reaction temperature (130 °C) and the presence of two active sites (isopropoxide and ***L′***) on the titanium centre.

2.4 Ligand modification: introducing chirality.

Work to control the stereoselectivity of the ROP of *rac*-lactide is sought to control the various isotacticities of the resulting polylactide product. The isotacticity has been shown to influence the properties of the polymer product and altering these is essential for the successful application of polylactide in the plastics industry and widen its potential uses.[32,33]

Ligands **1**-**4** incorporate an amino acid glycine core bound by two phenolate units. Amino acids are available as enantiomerically pure compounds with commercial samples derived from natural sources. This presented an opportunity to introduce chirality to the amine bis(phenolate) ligands by replacing the original glycine-based core with a chiral amino acid. We anticipated that this chiral group would increase the isotacticity of the polylactide produced in comparison to the titanium isopropoxide compounds bound by achiral ligands **1**-**4**.

2.4.1 Synthesis and characterisation of chiral analogues.

The chiral amino acids selected for the synthesis of chiral amine bis(phenolate) ligands are presented in Figure 24. The Mannich condensation reaction was selected as this was previously found to be the most versatile synthetic route in the synthesis of ligands **1**-**4**. Using *L*-alanine and *L*-phenylalanine as starting materials, would create a chiral centre at the C-atom adjacent to the *X* position (Figure 24). The *R′*/*R″* groups were selected to be *tert*-butyl groups due to the previous successes of compounds **7** and **8** as homogeneous activators in the ROP of *rac*-lactide. By retaining an identical ligand framework, we minimise the variables in the system so that changes can be attributed to the group introduced at the *X* position.

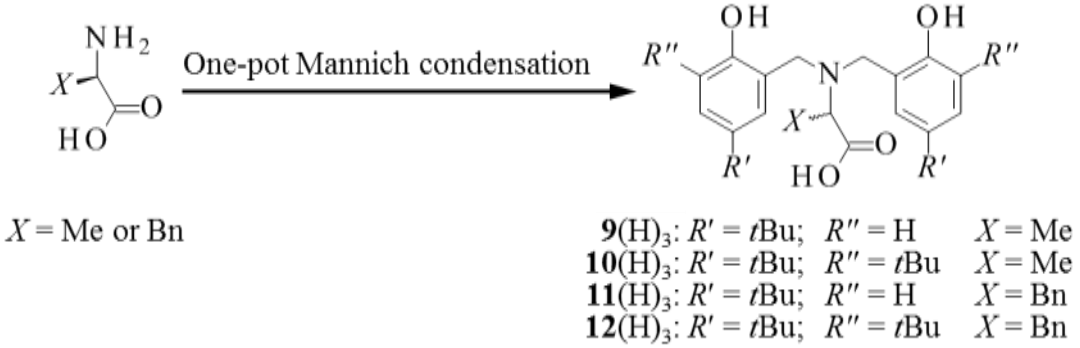

Figure 24. Synthesis of chiral ligand precursor targets **9**-**12**$(H)_3$.

A procedure existed in the literature[34] for the synthesis of *L*-**10**$(H)_2Na$, a Mannich-condensation in ethanol/water with sodium hydroxide followed by precipitation of the sodium salt by addition of excess aqueous sodium hydrogen carbonate. Unfortunately, in our hands, several attempts to obtain the pure compound were unsuccessful. An aliquot of the crude mixture was purified by column chromatography but this was found to have racemised. Upon further investigation, we found that this was a common problem under various reaction conditions (warming at 35 °C or reflux in solvents methanol or ethanol/water) and noted that the reported preparation did not include any characterisation confirm the enantiopurity of the compound. Nonetheless, the synthesis of compounds **9**-**12**$(H)_3$ as a racemic ligand would lead to the synthesis of a racemic catalyst that may display enhanced rates in the ROP of each diastereoisomer of *rac*-lactide. Accepting that racemisation would occur but that yields could be improved, we utilised the same reaction conditions as were used for compounds **1**-**4**$(H)_3$. The introduction of the new group at the *X* position induced a change in the work-up to purify compounds **9**-**12**$(H)_3$. To remove the majority of unreacted phenol the reaction mixture was acidified in methanol and the off-white solids were purified by column chromatography to give the pure ligands in reasonable yields. It was noted that the isolated yields for compounds **11**$(H)_3$ and **12**$(H)_3$ were significantly lower than ligand **9**$(H)_3$ and **10**$(H)_3$. The cause was interpreted as the bulkier benzyl group in the *X* position of ligands **11**$(H)_3$ and **12**$(H)_3$, which would sterically hinder the attack of the phenol on the imine/iminium ion during the electrophilic aromatic substitution step in the mechanism of the Mannich condensation. This step is more sterically hindered during the installation of the second phenol group. This was observed when the monophenolate of **12**$(H)_3$ was isolated from the reaction. For this reason, reflux at successively higher temperatures in propan-2-ol and toluene were attempted to increase the yield but were unsuccessful in producing workable quantities of **11**$(H)_3$ or **12**$(H)_3$.

Characterisation by ^{1}H NMR spectroscopy of **9**$(H)_3$ and **10**$(H)_3$ showed more signals than achiral ligands **1**-**4**$(H)_3$ due to the asymmetry introduced by the chirally-inducing *X* position. Furthermore, **9**$(H)_3$ suffered from spectral broadening that was caused by an exchange process as indicated by an EXSY NMR experiment. This could occur from bond rotations about the methylene bridges stemming from the amino core, which would result in magnetically inequivalent environments for the same proton signals. This effect is observed in **9**$(H)_3$ due to the lack of steric bulk in the *R″* positions in comparison to **10**$(H)_3$, which does not show ^{1}H NMR spectral broadening. This lack of bond rotation in **10**$(H)_3$ allows the methylene protons to appear as diastereotopic protons with separate doublets for each proton environment, as would be expected with induced chirality by the presence of the *X* group.

Large colourless block crystals of **10**$(H)_3$ were grown from a saturated solution in methanol. This sample was analysed by SCXRD using Cu-K_α radiation to determine the absolute configuration of the molecule by anomalous dispersion. The excellent quality of the single crystal samples enabled the acquisition of a dataset that determined the molecule was in the *S*-configuration with high certainty shown by the reported flack parameter of 0.00(2). This result demonstrated the retention of stereochemistry when moving from *S*-alanine to *S*-**10**$(H)_3$.

However, a single crystal sample is not representative of the bulk sample. This crystalline sample could be composed of a mixture of **10**$(H)_3$ in the characterised *S*-configuration, *R*-configuration and even co-crystallised *R*-/*S*-configurations. The chirality of the bulk powder was still to be determined. Polarimetry was used to gain insight on the stereochemistry of **10**$(H)_3$. If the single crystal sample of **10**$(H)_3$ was chirally pure *S*-**10**$(H)_3$, this would act as a chirally pure reference for **10**$(H)_3$ that would allow us to calculate the enantiomeric excess. The polarimetry values obtained for the crystalline sample and bulk sample of **10**$(H)_3$ were -0.01 and 0.00 respectively. This showed that the *L*-pure amino acids had racemised during the Mannich condensation reaction. This may be unsurprising as the strong base sodium hydroxide is used in an equimolar quantity as the amino acid. Furthermore, the reaction mixture is heated to reflux for several days. These harsh conditions would allow for racemisation of the amino acid through deprotonation/reprotonation[35-37]of the proton adjacent to the *X* position. This analysis characterised the ligand produced from the Mannich reaction as *rac*-**10**$(H)_3$ despite the chirally pure structure obtained from the SCXRD dataset.

Using the same synthetic conditions to produce compounds **5-8**, compounds *rac*-**9**$(H)_3$ and *rac*-**10**$(H)_3$ were stirred with titanium isopropoxide to give the proposed structures **13** and **14** (Figure 25). Due to the use of a racemic ligand precursor, we can assume that the resulting titanium complexes are also racemic.

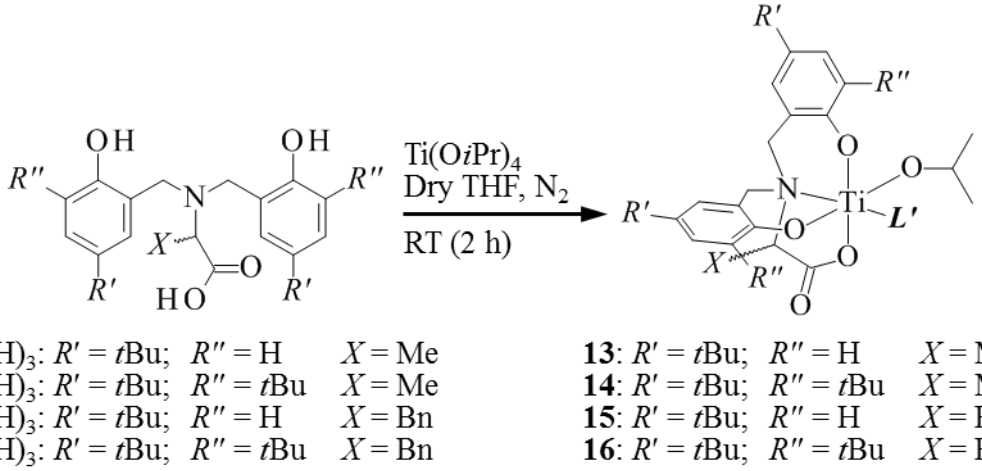

9$(H)_3$: *R′* = *t*Bu; *R″* = H *X* = Me
10$(H)_3$: *R′* = *t*Bu; *R″* = *t*Bu *X* = Me
11$(H)_3$: *R′* = *t*Bu; *R″* = H *X* = Bn
12$(H)_3$: *R′* = *t*Bu; *R″* = *t*Bu *X* = Bn

13: *R′* = *t*Bu; *R″* = H *X* = Me
14: *R′* = *t*Bu; *R″* = *t*Bu *X* = Me
15: *R′* = *t*Bu; *R″* = H *X* = Bn
16: *R′* = *t*Bu; *R″* = *t*Bu *X* = Bn

Figure 25. Expected structures **13-16** from the reactions of compounds **9-12**$(H)_3$ with titanium isopropoxide under dry conditions. Note: ***L′*** denotes a vacant site on the titanium centre occupied by a ligand.

Comparison of the ^{1}H NMR spectra of the ligand precursors *rac*-**9**$(H)_3$/*rac*-**10**$(H)_3$ and compounds *rac*-**13**/*rac*-**14** show loss of the ligand precursor signals with gain of typical signals associated with the bound ligand confirming the deprotonation of *rac*-**9**$(H)_3$/*rac*-**10**$(H)_3$ and its subsequent binding to the titanium centre. Interestingly, the spectra of *rac*-**13** and *rac*-**14** display one set of pronounced signals corresponding to a mononuclear form. However, an EXSY NMR experiment shows exchange in all regions (aromatic, methylene/isopropoxide, *tert*-butyl/isopropoxide) between the more intense mononuclear signals and lower intensity signals associated with another species, which was best observed in the *tert*-butyl groups due to the greater intensity granted by the larger number of protons in these groups. The presence of more than the expected two *tert*-butyl group signals for *rac*-**13** and four *tert*-butyl group signals for *rac*-**14** leads us to believe the exchange is between mononuclear and dinuclear forms.

Samples of *rac*-**13** and *rac*-**14** were prepared in $CDCl_3$ with DMAP as additive to further reduce the extent of aggregation. In a similar fashion to the spectra of **6**-**8** obtained under the same conditions, the ^{1}H NMR spectra of *rac*-**13** and *rac*-**14** showed the presence of a single species in solution with DMAP under exchange. Akin to the achiral compounds **5**-**8**, the methylene bridge protons in the ^{1}H NMR spectra of *rac*-**13** and *rac*-**14** displayed line broadening. A ROESY NMR experiment revealed through-space contacts between the carboxylate and phenolate donors in the ligand framework and DMAP, explaining the loss and broadening of the methylene arm signal through its increased lability.

2.5 Stereoselective control in the ROP of *rac*-lactide

Stereoselective ROP of rac-lactide is sought to control the tacticity of the resulting polylactide product. Increasing the isotacticity of polylactide has been shown to influence the properties of the polymer product and altering these is essential for the successful application of polylactide in the plastics industry and widen its potential uses.[32,33] Our aim was to determine the effect of the chirally-inducing *X* group on the activity and stereocontrol delivered by *rac*-**13** and *rac*-**14** in the ROP of *rac*-lactide despite the high temperature (130 °C) and dynamic nature of the complexes. Compounds **7** and **8** were the most successful initiators for the ROP of *rac*-lactide under both solution and melt polymerisation conditions. For this reason, the analogous compounds *rac*-**13** and *rac*-**14** would make for the best control experiment to test the effect of the chirally-inducing *X* group on the ROP of *rac*-lactide. The data is presented in Table 2.

Solution polymerisation conditions ([M]$_0$ = 1 mol·L^{-1}, toluene, 130 °C)							
Entry	Activator	[M]$_0$/[Ti]$_0$	Time	Conv.[a]	M_n[b]	$M_{n(NMR)}$[c]	PDI[d]
3	**7**	20	24 h	92	4120	7260	1.24
4	**7**	50	24 h	19	4070	4790	1.09
5	**7**	100	24 h	13	-		-
6	**8**	50	24 h	90	7360	11300	1.24
19	*rac*-**13**	20	24 h	86	6080	4780	1.54
20	*rac*-**13**	50	24 h	26	4400	4330	1.24
21	*rac*-**13**	100	24 h	13	-	-	-
22	*rac*-**14**	20	24 h	93	4050	5640	1.27
23	*rac*-**14**	50	24 h	59	5260	5880	1.22
Melt polymerisation conditions (130 °C)							
Entry	Activator	[M]$_0$/[Ti]$_0$	Time	Conv.[a]	M_n[b]	$M_{n(NMR)}$[c]	PDI[d]
11	**7**	300	2 h	18	-	-	-
12	**7**	300	6 h	74	13500	13000	1.64
13	**7**	300	24 h	96	15000	10700	1.54
14	**7**	600	24 h	93	14800	11800	2.03
15	**8**	300	2 h	14	-	-	-
16	**8**	300	6 h	47	6780	8320	1.26
17	**8**	300	24 h	89	14100	12000	1.40
24	*rac*-**13**	300	2 h	45	6300	5470	1.46
25	*rac*-**13**	300	6 h	82	9700	7550	1.58
26	*rac*-**13**	300	24 h	92	10500	8910	1.65
27	*rac*-**13**	600	24 h	87	13700	10900	1.55
28	*rac*-**14**	300	2 h	8	-	-	-
29	*rac*-**14**	300	6 h	60	7830	5200	1.22
30	*rac*-**14**	300	24 h	90	11000	12000	1.42

Table 2. Comparison of polymerisation data for achiral (**7** and **8**) and chiral (*rac*-**13** and *rac*-**14**) initiators in the ROP of *rac*-lactide. [a] Conversion (%) from ^{1}H NMR spectra evaluated by integration of the methine regions of polylactide versus lactide. [b] Polymer number average molar mass determined from GPC traces. [c] Calculated polymer molecular weight by ^{1}H NMR end-group analysis. [d] Polydispersity indices (M_w / M_n) obtained from GPC traces.

Under solution polymerisation conditions, there is a disparity in the activity of **8** and *rac*-**14**. Surprisingly, *rac*-**14** shows a much lower conversion from monomer to polymer that is less than half what is achieved by the analogous **8**. The *X* group was observed to reduce aggregation in *rac*-**14** and this reinforces our previous observation that aggregation effects are not the dominant factor affecting activity in this system. In this case, we could envisage two effects, directed by the *X* group, are reducing the activity of *rac*-**14** in comparison to **8**. First, the *X* group causes greater steric hindrance for both monomer and polymer chain approach to the titanium centre, reducing the activity of the titanium centre. Second, the chirality induced by the *X* group causes *S*-**14** and *R*-**14** to be

more selective in choosing which diastereoisomer of lactide can interact with the chiral titanium centre, whether this is free monomer of ring-opened monomer on the polymer chain. This will reduce the observed, overall activity of *rac*-**14**. In contrast, **8** and *rac*-**14** show very similar performance in the ROP of *rac*-lactide under melt polymerisation conditions with good agreement between the conversion, M_n and PDI values.

By inspection of the intensities of each tetrad in the homonuclear decoupled ^{1}H NMR spectra of **6**-**8**/*rac*-**13** and *rac*-**14**, a difference in microstructure between the polylactide samples produced becomes apparent (Figure 26). The *mmm* tetrad, representative of isotactic enchainment, is inflated in the PLA samples produced by *rac*-**14** in comparison to the samples produced by **6**-**8** and *rac*-**13**. Further understanding of this isotactic enrichment was sought by comparing the effectiveness of site control mechanism (SCM)[38] or chain end control mechanism (CEM)[39] statistics for tetrad intensity prediction followed by comparison of the P_m value between the achiral and chiral initiators (Table 3).

Initiator (achiral/chiral)	Entries (achiral/chiral)	Achiral $P_{m(CEM)}$	Chiral $P_{m(CEM)}$	Chiral $P_{m(SCM)}$
7 / *rac*-**13**	3 / 19	0.47	0.43	N/A
7 / *rac*-**13**	4 / 20	-	0.34	N/A
7 / *rac*-**13**	5 / 21	0.44	-	-
7 / *rac*-**13**	16 / 24	-	0.45	N/A
7 / *rac*-**13**	17 / 25	0.47	0.40	N/A
7 / *rac*-**13**	18 / 26	0.42	0.42	N/A
7 / *rac*-**13**	19 / 27	0.40	0.43	N/A
8 / *rac*-**14**	- / 22	-	0.53	0.61
8 / *rac*-**14**	6 / 23	0.46	0.52	0.58
8 / *rac*-**14**	20 / 28	-	-	-
8 / *rac*-**14**	21 / 29	0.41	0.59	0.68
8 / *rac*-**14**	22 / 30	0.36	0.51	0.59

Table 3. Comparison of P_m data obtained for achiral versus chiral initiators **7**/*rac*-**13** and **8**/*rac*-**14** in the ROP of *rac*-lactide.

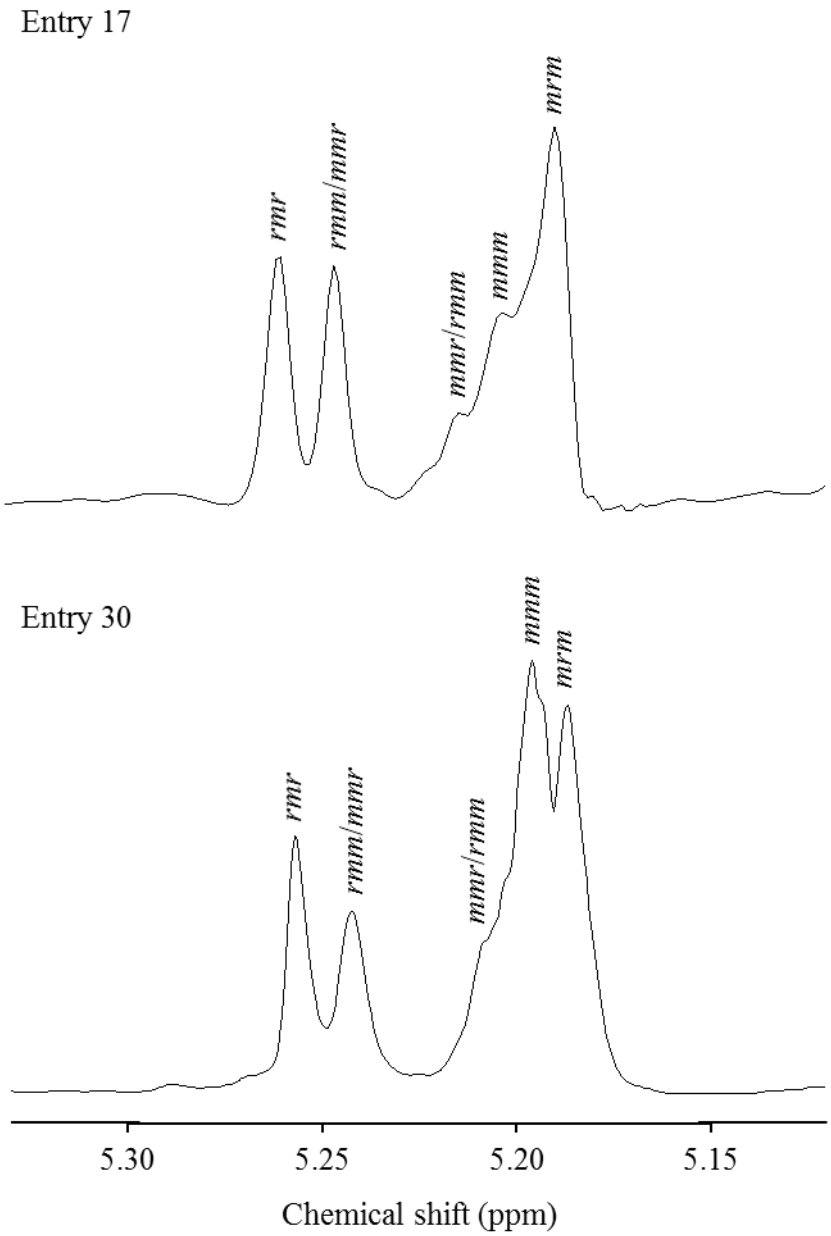

Figure 26. Comparison of PLA microstructure produced by **12** (top, entry 17) and *rac*-**14** (bottom, entry 30).

Applying a SCM of CEM statistical model to predict the observed tetrad intensities of PLA samples is a common method to elucidate the mechanism by which stereocontrol is imparted to the PLA chains.[40] Here, our atypical systems with competing achiral and chiral sites will complicate the use of SCM or CEM statistics to predict the tetrad intensities, resulting in deviations from these models. A direct comparison of the polylactide microstructures produced by our analogous achiral (**7** and **8**) and chiral initiators (*rac*-**13** and *rac*-**14**) will also be used to investigate stereoselective control and the direct effect of the chirally-inducing *X* group.

The SCM statistical model failed to predict the tetrad intensities for PLA samples produced by *rac*-**13**, in which case CEM statistics were more appropriate. This initiator essentially acts like its achiral analogue **11**, imparting little stereocontrol through a SCM by action of the chirally-inducing *X* group. For polylactide samples produced by *rac*-**14**, SCM statistics were more successful in the prediction of tetrad intensities than CEM statistics. Thus, for *rac*-**14** we see an increase in intensity of the *mmm* tetrad associated with an increase in influence of a SCM over enchainment during the polymerisation.

The lack of stereoselectivity imparted by *rac*-**13** in comparison to *rac*-**14** can be explained by referring to Figure 27. The achiral site ***A*** is not sterically disfavoured in *rac*-**13** due to the lack of *tert*-butyl groups in the *R″* positions. With no differentiation between the achiral and chiral sites, the influence on stereoselectivity imparted by *rac*-**13** was minimal. In the case of *rac*-**14**, *tert*-butyl groups in the *R″* position enforce steric crowding about achiral site ***A***. This steric crowding will favour polymer insertion via the chiral active site ***A****, explaining how *rac*-**14** was able to successfully increase the probability of isotactic enchainment despite the presence of a competing achiral active site and the high temperature (130 °C). The achiral site needs to be disfavoured for a polynuclear initiator to successfully impart stereoselectivity over the ROP of *rac*-lactide.

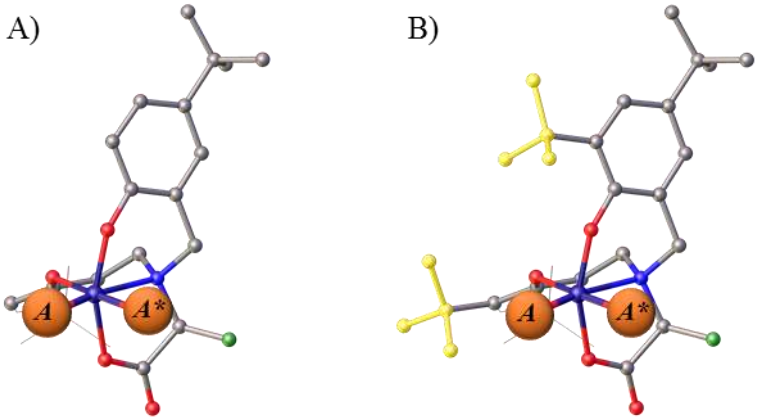

Figure 27. Models showing the achiral (***A***) and chiral (***A****) sites for: A) *S*-**13** B) *S*-**14**; constructed using a mononuclear unit from the asymmetric unit of $\mathbf{8}_3$(HO*i*Pr). A portion of the model is displayed as wireframe for clarity. Yellow: *tert*-butyl groups in the R″ positions. Green: methyl group in the *X* position. Orange: labelled achiral (***A***, occupied by isopropoxide) and chiral (***A****, accommodating ***L′*** donors). Purple: titanium. Grey: carbon. Blue: nitrogen. Red: oxygen.

To further elucidate the mechanism of stereocontrol, a kinetic study using *rac*-lactide or *L*-lactide polymerised by *rac*-**14** was undertaken. A semi-logarithmic plot of lactide consumption against time gives a linear fit for both *rac*- and *L*-lactide, from which the observed rate constant k_{app} was calculated to be 2.89×10^{-2} min^{-1} and 2.44×10^{-2} min^{-1} respectively (Figure 28). The almost equal rates indicate there is no preference for *rac*- or *L*-lactide consumption by *rac*-**14**. This is symptomatic of a CEM being prevalent during the polymerisation.[40-42] This is contrary to the tetrad analysis for polylactide samples produced by *rac*-**14** that correlate with a SCM.

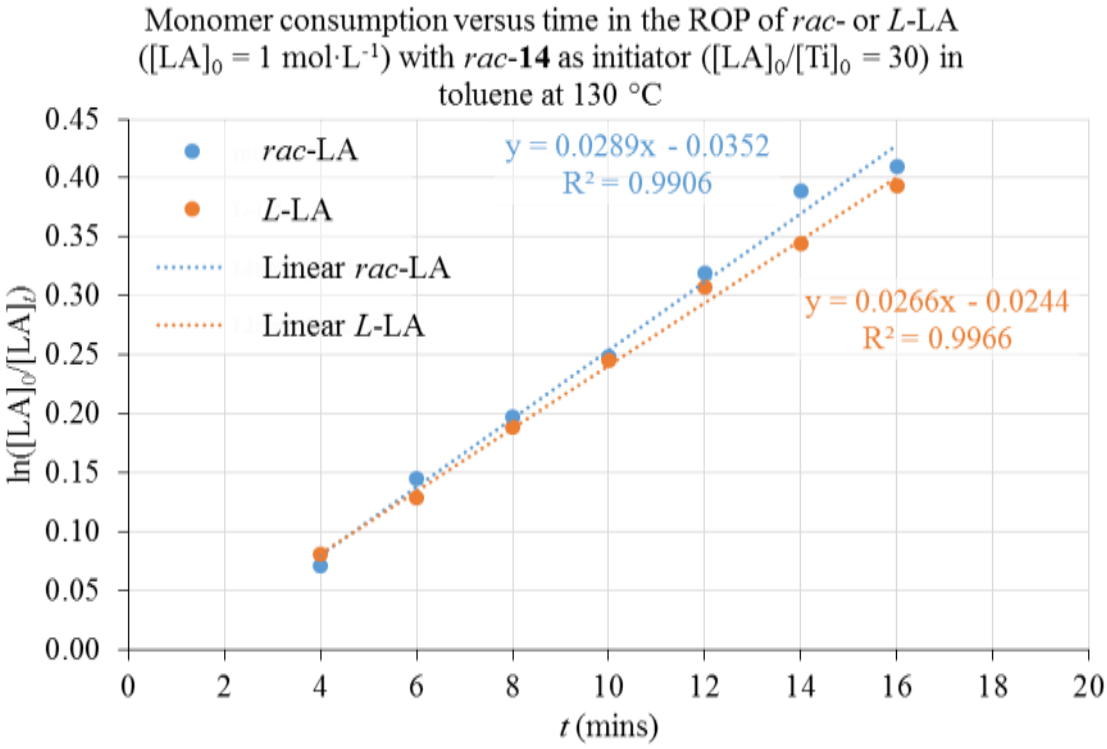

Figure 28. Semi-logarithmic plot of monomer consumption versus time in the ROP of lactide using *rac*-**14**.

However, a SCM can appear as a CEM if polymeryl exchange is present and this is observed to be the case with these systems.[43] Additionally, the model of *rac*-**14** shows the chirally-inducing *X* group can induce site control over which lactide diastereoisomer is more easily inserted and leading to greater isotactic enchainment in comparison to the achiral analogue **12**. Finally, *rac*-**13** showed no increase in P_m, this can be attributed to the lack of steric hindrance around the achiral site, highlighting the importance of the site control enacted by the *X* group. This evidence supports a SCM is in effect but the polymeryl exchange is reducing its effect on isotactic enchainment. However, the assignment that SCM is in effect remains tentative as the challenges in distinguishing between a SCM and CEM are well documented.[40-43]

2.6 Relating activity to aggregate nuclearity

By comparing the conversion achieved by **6**-**8** under different $[M]_0/[Ti]_0$ loadings and using the solution polymerisation conditions, an increase in activity described by **6** < **7** < **8** (0 % to 13 % to 62 % conversion at $[M]_0/[Ti]_0$ = 100) was apparent. The significant difference in performance was unexpected for a simple change from methyl to *tert*-butyl to di-*tert*-butyl *R′*/*R″* groups, prompting us to further investigate the underlying cause.

Having observed aggregation to be a feature of these complexes, the tendency of **6**-**8**/*rac*-**13**/*rac*-**14** to aggregate in solution was investigated. A ^{1}H DOSY NMR experiment would allow the determination of the diffusion coefficients of the species in solution that can be used to estimate the *MW*s of the aggregates using external calibration curves (ECCs). These ECCs, published by Stalke and coworkers,[44,45] take into account variables when measuring the diffusion coefficient such as the solvent, analyte shape and concentration, temperature and the spectrometer used. The estimated *MW*s were converted to estimated nuclearities by dividing the *MW*s by the *MW* of a mononuclear unit (Equation 4). The data is summarised in .

$$\text{Estimated Nuclearity} = \frac{\text{Estimated } MW}{MW_{n=1}}$$

where $MW_{n=1}$ is the molecular weight of a mononuclear unit [TiLO*i*Pr].

Equation 4

The external calibration curves will give accurate *MW* estimation for molecules with a molar density between 4.3×10^{29} g·mol^{-1}·m^{-3} and 5.9×10^{29} g·mol^{-1}·m^{-3}. For molecules with molar density that exceeds this range, such as complexes **10**-**14** with the presence of the titanium atom, underestimation of *MW* is expected. This error will be carried for all samples and will not influence the comparative study of the size of these aggregates in solution.

The ^{1}H DOSY NMR data revealed the complexes formed larger aggregates in the order **6** > **7** > **8** (Figure 29), which correlated with the increase of steric bulk from **6** to **7** to **8**. The crystal structure of **8**$_3$(HO*i*Pr) also gives insight into the effect of the *R′* and *R″* groups on aggregation of the mononuclear units (Figure 30). Close steric interactions between C24D/C47C show how bulk in the *R″* position prevents aggregation. Importantly, close proximity between C12/C29B and C22/C45C demonstrates how bulk

in the *R′* also hinders aggregation, explaining the aggregational trends observed for compounds **6-8**. As a final note, if we consider the three ligands **4** in the structure as propellers, they are bound in a ΛΔΔ and ΔΛΛ modes in this crystal structure. This showed a mixed symmetry possible within each aggregate that may further contribute to a more complex NMR spectrum in solution.

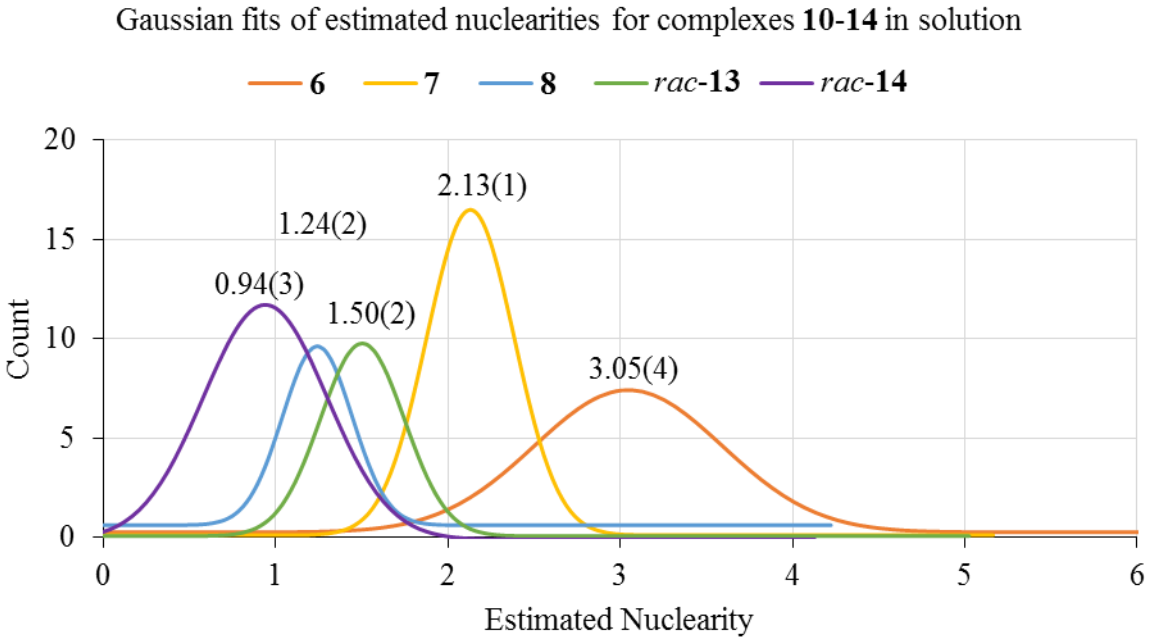

Figure 29. Plot of Gaussian fitting curves for datasets of estimated nuclearities of **10-14** in $CDCl_3$ versus the count of data points corresponding to said nuclearity. Inset are the means for the Gaussian distributions. The estimated nuclearities were obtained by ^{1}H DOSY NMR experiments via estimated *MW*s derived from diffusion coefficients.

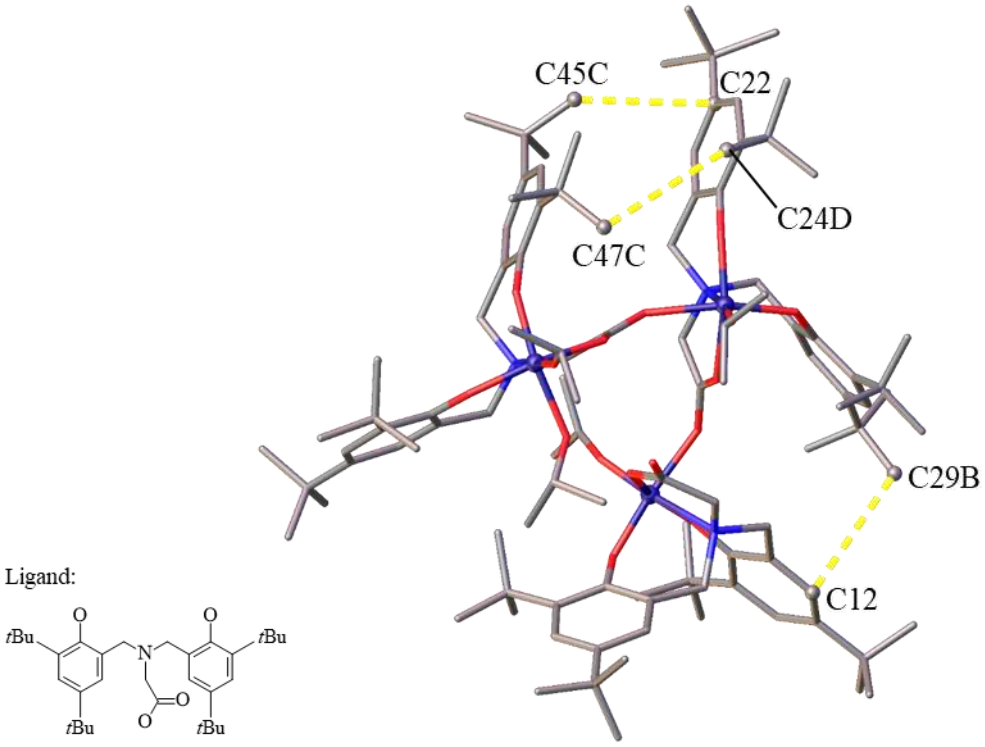

Figure 30. Dashed yellow bonds indicate the close proximity between C24D/C47C, C12/C29B and C22/C45C. These steric interactions show how steric bulk on the *R′* and *R″* groups can prevent aggregation. Ligand framework displayed as tubes. C24D, C47C, C12, C29B, C22 and C45C displayed as balls. Hydrogen atoms omitted for clarity. Ti = purple; C = grey; N = blue; O = red.

Since aggregational effects would compete with the monomer and polymer chains for time on the active site on the titanium centre, it would follow that a greater tendency for aggregation would lead to a decrease in activity. For this reason, we propose aggregational effects to correlate with the activity of these compounds, whereby **6** exhibits low activity in solution due to its propensity to aggregate while **8** has a lower tendency to aggregate and displayed better performance than **6** and **7**. In these systems comprised of dynamic polynuclear aggregates, we found reducing nuclearity resulted in increased activity towards the ROP of rac-lactide. Other systems[10-14] typically found nuclearity to have little or no effect on performance. In contrast, some systems with metal centres supported by multidentate ligands[15,46] showed the mononuclear form to be the most active form. Our observations agree with these systems whereby the additional unit(s) during aggregation cause an increase in steric bulk around the active site.

Focussing the discussion comparatively between the achiral/chiral initiators **7**/*rac*-**13** and **8**/*rac*-**14**, the distributions of estimated nuclearities show the equilibrium for aggregates in a solution of *rac*-**13** or *rac*-**14** favours the mononuclear form. This may be unsurprising because more intense peaks corresponding to the mononuclear form are present in the ^{1}H NMR spectra of *rac*-**13** and *rac*-**14**, which is further evidence that the mononuclear form is the main component in the mixture. This change in equilibrium can be explained by the addition of the methyl substituent in the alanine core of the ligand at the *X* position, causing greater steric hindrance that blocks aggregation. Another example of this can be found chapter 3 where the alanine core was observed to prevent dimerisation in comparison to analogues with a glycine core. However, a mixture of aggregates still exists from the ^{1}H DOSY NMR data and the COSY/ROESY NMR experiments that show discrete units under exchange, albeit weaker in intensity than those observed for **7** and **8** due to the favoured mononuclear form in *rac*-**13** and *rac*-**14**.

2.7 Conclusions

Our initial attempts in using a carboxylate arm on amine bis(phenolate) ligands were successful in forming polynuclear titanium compounds. These presented themselves as dynamic mixtures in solution whereby the carboxylate arm allowed different nuclearities of a mononuclear form to bridge together to dinuclear, trinuclear and tetranuclear species. An in-depth solution-state 1D/2D NMR study was key to developing our understanding of the aggregates in solution and relating this to their performance in the ROP of *rac*-lactide. Subsequently, ^{1}H DOSY NMR studies probed the size distributions of aggregates in solution, establishing a trend; increasing steric bulk around the ligand periphery reduced the nuclearity of the aggregates. These aggregates were applied to the ROP of *rac*-lactide under solution and melt polymerisation conditions. Increasing the steric bulk of the peripheral phenolate groups resulted in an increase in activity. The largest, with di-*tert*-butyl phenolate donors, was observed to significantly increase the activity of the polynuclear complex, which was attributed to the restricted aggregation of the titanium species. Unfortunately, this group also hindered polymerisation under melt conditions due to the restriction it causes about the titanium centre – a contrasting result to our previous findings whereby enhanced solubility had the greatest influence over activity under melt polymerisation conditions.[19] Finally, a chiral backbone was introduced to the ligand framework to form analogous titanium species with both achiral and chiral sites. When steric bulk hindered access to the achiral site, a SCM imparted a greater degree of isotactic enchainment in the polylactide chain. This key factor should be taken into account for future polynuclear initiator designs. These polynuclear titanium aggregates showcase how careful design on the molecular scale can have a great effect on the performance of initiators and macromolecular properties of the polymer they produce.

A drawback of the complexes presented in this chapter was their water-sensitivity. Although they displayed a certain tolerance to air in the solid-state, the complexes would readily undergo reaction if water was present in solution. We sought to improve the air/water-stability of our polynuclear complexes by incorporating titanium-oxo motifs by hydrolysis in pursuit of catalysts for the ROP of lactide.

2.8 References

1. P. J. Dijkstra, H. Z. Du and J. Feijen, *Polym. Chem.*, 2011, **2**, 520-527.
2. M. Shavit and E. Y. Tshuva, *Eur. J. Inorg. Chem.*, 2008, 1467-1474.
3. B. T. Ko and C. C. Lin, *J. Am. Chem. Soc.*, 2001, **123**, 7973-7977.
4. Z. H. Liang, M. Zhang, X. F. Ni, X. Li and Z. Q. Shen, *Inorg. Chem. Commun.*, 2013, **29**, 145-147.
5. D. C. Aluthge, E. X. Yan, J. M. Ahn and P. Mehrkhodavandi, *Inorg. Chem.*, 2014, **53**, 6828-6836.
6. K. M. Osten, D. C. Aluthge and P. Mehrkhodavandi, *Dalton Trans.*, 2015, **44**, 6126-6139.
7. F. M. Garcia-Valle, R. Estivill, C. Gallegos, T. Cuenca, M. E. G. Mosquera, V. Tabernero and J. Cano, *Organometallics*, 2015, **34**, 477-487.
8. D. C. Aluthge, J. M. Ahn and P. Mehrkhodavandi, *Chem. Sci.*, 2015, **6**, 5284-5292.
9. A. Thevenon, C. Romain, M. S. Bennington, A. J. P. White, H. J. Davidson, S. Brooker and C. K. Williams, *Angew. Chem. Int. Ed.*, 2016, **55**, 8680-8685.
10. Y. J. Kim and J. G. Verkade, *Macromol. Rapid Commun.*, 2002, **23**, 917-921.
11. P. Dubois, C. Jacobs, R. Jerome and P. Teyssie, *Macromolecules*, 1991, **24**, 2266-2270.
12. A. Kowalski, A. Duda and S. Penczek, *Macromolecules*, 1998, **31**, 2114-2122.
13. W. M. Stevels, M. J. K. Ankone, P. J. Dijkstra and J. Feijen, *Macromolecules*, 1996, **29**, 6132-6138.
14. B. J. O'Keefe, S. M. Monnier, M. A. Hillmyer and W. B. Tolman, *J. Am. Chem. Soc.*, 2001, **123**, 339-340.
15. B. J. O'Keefe, L. E. Breyfogle, M. A. Hillmyer and W. B. Tolman, *J. Am. Chem. Soc.*, 2002, **124**, 4384-4393.
16. A. S. Ceccato, A. Neves, M. A. De Brito, S. M. Drechsel, A. S. Mangrich, R. Werner, W. Haase and A. J. Bortoluzzi, *J. Chem. Soc., Dalton Trans.*, 2000, 1573-1577.
17. Y.-L. Wong, Y. Yan, E. S. H. Chan, Q. Yang, T. C. W. Mak and D. K. P. Ng, *J. Chem. Soc., Dalton Trans.*, 1998, 3057-3064.
18. Z. Taheri, B. Ghanbari and H. Hajibabaei, *Chem. Pap.*, 2014, **68**, 989-994.
19. J. M. E. P. Cols, C. E. Taylor, K. J. Gagnon, S. J. Teat and R. D. McIntosh, *Dalton Trans.*, 2016, **45**, 17729-17738.
20. A. J. Chmura, M. G. Davidson, M. D. Jones, M. D. Lunn, M. F. Mahon, A. F. Johnson, P. Khunkamchoo, S. L. Roberts and S. S. F. Wong, *Macromolecules*, 2006, **39**, 7250-7257.
21. E. Y. Tshuva, M. Versano, I. Goldberg, M. Kol, H. Weitman and Z. Goldschmidt, *Inorg. Chem. Commun.*, 1999, **2**, 371-373.
22. E. Y. Tshuva, I. Goldberg, M. Kol and Z. Goldschmidt, *Inorg. Chem.*, 2001, **40**, 4263-4270.
23. D. T. Dugah, B. W. Skelton and E. E. Delbridge, *Dalton Trans.*, 2009, 1436-1445.
24. S. Barroso, A. M. Coelho, S. Gomez-Ruiz, M. J. Calhorda, Z. Zizak, G. N. Kaluderovic and A. M. Martins, *Dalton Trans.*, 2014, **43**, 17422-17433.
25. G. A. Jeffrey, *Crystallogr. Rev.*, 2003, **9**, 135-176.
26. B. J. O'Keefe, M. A. Hillmyer and W. B. Tolman, *J. Chem. Soc. Dalton.*, 2001, 2215-2224.
27. A. Sauer, A. Kapelski, C. Fliedel, S. Dagorne, M. Kol and J. Okuda, *Dalton Trans.*, 2013, **42**, 9007-9023.
28. D. Takeuchi, T. Nakamura and T. Aida, *Macromolecules*, 2000, **33**, 725-729.

29. J. X. He, Y. L. Duan, X. Kou, Y. Z. Zhang, W. Wang, Y. Yang and Y. Huang, *Inorg. Chem. Commun.*, 2015, **61**, 144-148.
30. M. Mandal and D. Chakraborty, *J. Polym. Sci. Pol. Chem.*, 2016, **54**, 809-824.
31. B. Gao, Q. Duan, Y. H. Li, D. N. Li, L. Q. Zhang, Y. Cui, N. H. Hu and X. Pang, *RSC Adv.*, 2015, **5**, 13437-13442.
32. B. Gao, X. Li, R. L. Duan and X. Pang, *New J. Chem.*, 2015, **39**, 2404-2408.
33. Y. Ikada, K. Jamshidi, H. Tsuji and S. H. Hyon, *Macromolecules*, 1987, **20**, 904-906.
34. M. J. Stanford and A. P. Dove, *Chem. Soc. Rev.*, 2010, **39**, 486-494.
35. S. Barroso, P. Adao, A. M. Coelho, J. C. Pessoa and A. M. Martins, *J. Mol. Catal. A: Chem.*, 2016, **412**, 107-116.
36. G. G. Smith and T. Sivakua, *J. Org. Chem.*, 1983, **48**, 627-634.
37. E. D. Stroud, D. J. Fife and G. G. Smith, *J. Org. Chem.*, 1983, **48**, 5368-5369.
38. R. Baum and G. G. Smith, *J. Am. Chem. Soc.*, 1986, **108**, 7325-7327.
39. T. M. Ovitt and G. W. Coates, *J. Am. Chem. Soc.*, 2002, **124**, 1316-1326.
40. B. M. Chamberlain, M. Cheng, D. R. Moore, T. M. Ovitt, E. B. Lobkovsky and G. W. Coates, *J. Am. Chem. Soc.*, 2001, **123**, 3229-3238.
41. Y. Q. Cui, C. J. Chen, Y. Y. Sun, J. C. Wu and X. B. Pan, *Inorg. Chem. Front.*, 2017, **4**, 261-269.
42. Z. H. Tang, X. S. Chen, Y. K. Yang, X. Pang, J. R. Sun, X. F. Zhang and X. B. Jing, *J. Polym. Sci. Pol. Chem.*, 2004, **42**, 5974-5982.
43. H. B. Wang, Y. Yang and H. Y. Ma, *Macromolecules*, 2014, **47**, 7750-7764.
44. A. Pilone, N. De Maio, K. Press, V. Venditto, D. Pappalardo, M. Mazzeo, C. Pellecchia, M. Kol and M. Lamberti, *Dalton Trans.*, 2015, **44**, 2157-2165.
45. R. Neufeld and D. Stalke, *Chem. Sci.*, 2015, **6**, 3354-3364.
46. S. Bachmann, R. Neufeld, M. Dzemski and D. Stalke, *Chem. Eur. J.*, 2016, **22**, 8462-8465.
47. T. Rosen, I. Goldberg, W. Navarra, V. Venditto and M. Kol, *Chem. Sci.*, 2017.

Chapter 3: Titanium-oxo tetragonal disphenoids

Abstract

Akin to many amine bis(phenolate)-supported titanium isopropoxide initiators, the aggregates presented in chapter 2 exhibited a lack of stability in the presence of water and air. This resulted in the need to handle these compounds under dry conditions, limiting their stability. Furthermore, the monomer used in the polymerisation, *rac*-lactide, is hygroscopic and will react in the presence of water to form lactic acid. Typical initiators for the ROP of *rac*-lactide are intolerant to impurities in the monomer meant that *rac*-lactide required purification and drying as well as storage under dry atmosphere; such conditions are less industrially-viable. To overcome these limitations, we proposed titanium-oxo complexes to be more stable alternatives that could form suitable catalysts for the ROP of *rac*-lactide. It was found that the titanium aggregates, presented in chapter 2, reacted with water to form polynuclear Ti_4 complexes with a distorted tetrahedron geometry. The synthesis and characterisation of these compounds are discussed and their subsequent application as pre-catalysts in the ROP of *rac*-lactide was investigated.

3.1 Introduction

In order to explore the boundary between homogeneous and heterogeneous catalytic systems, well-defined polynuclear catalysts are needed to draw meaningful conclusions. The titanium aggregates presented in chapter 2 are dynamic in solution, which made their characterisation more challenging in comparison to existing titanium alkoxide initiators. Furthermore, the complexes reacted in the presence of water limited their handling to dry conditions. Much like titanium dioxide nanoparticles in catalysis, it would follow that a titanium-oxo complex would be stable in the presence of water and be a reusable catalyst. Having noted the reaction of titanium isopropoxide aggregates in the presence of water, we wanted to characterise the products formed from these reactions. In this way, the hydrolysis of monometallic fragments could be used to create a reliable route to larger titanium-oxo clusters that can subsequently be studied, characterised and applied to the ROP of lactide.

Amine bis(phenolate) ligands have been exploited in the ROP of lactide for their ability to strongly bind metals and ease of modification.[1-5] For example, a variety of donors can be installed on the pendant arm and the phenol moieties can be appended with a range of substituents, both of which can be used to affect/influence catalytic activity.[1,2,4-7] We noted that no amine bis(phenolate) ligands featuring a carboxylate group on the pendant arm had been reported for application in the ROP of cyclic esters. This carboxylate could act as a bridge to other metal centres, leading to expansion of the metal complex into a polynuclear aggregate.[8-11]Moreover, the ambidentate carboxylate group would saturate the coordination sphere, facilitate changes in oxidation state and enhance catalyst stability under melt polymerisation conditions.

Titanium(IV) catalysts have been used extensively for the ring-opening polymerisation (ROP) of lactide in conjunction with many different ligands[12-22] with some examples featuring an oxo-bridged titanium (*cf.* Ti–O–Ti) core.[23-27] These complexes often feature alkoxide initiating groups that are ultimately incorporated into the polymer chains. As a result, these complexes are more accurately described in the literature as initiators rather than catalysts since regeneration of the alkoxide would be necessary for subsequent reuse. As with many titanium isopropoxide complexes, polynuclear aggregates **5-8** quickly hydrolyse in the presence of water. We predicted that we could utilise this to direct the formation of a polynuclear titanium-oxo aggregate and we sought to characterise the compounds formed from the hydrolysis of **5-8**, supported

by reported synthetic examples of ligand-supported titanium-oxo species.[28-35] Two contrasting examples highlighted the use of dinuclear titanium-oxo compounds for the ROP of lactide. One complex reaching near-complete conversion after 74 mins whilst the other displaying no activity at all (trace PLA production).[24,25] This stark difference in activity provoked our investigations into the use of titanium-oxo complexes to further elucidate their activity and applicability in the ROP of lactide. Herein, we present the synthesis and characterisation of air/water-stable, tetrametallic titanium-oxo catalysts for use in the ROP of *rac*-lactide.

3.2 Synthesis and characterisation of polynuclear complexes

Modifying the peripheral groups of the amine bis(phenolate) ligands in the *R′*/*R″* positions was previously observed to significantly affect the performance of initiators for the ROP of *rac*-lactide (chapter 2 and reported examples[1,2,4-7,36]). The synthesis of another analogue of compound **1**$(H)_3$ with fluoro groups in the *R′* positions, **17**$(H)_3$, was a valuable synthetic target to investigate the effect of a polar groups on the ligand periphery. A Mannich condensation was a reliable methods for the synthesis of **2-4**$(H)_3$, akthough lower yielding for **17**(H). The cause was interpreted as the electronically-deactivated phenolic ring in the 4-fluorophenol starting material, hindering the electrophilic aromatic substitution step in the Mannich condensation. Several reaction conditions were tested (reflux in methanol, isopropanol, toluene, solvothermal conditions, use of formaldehyde solution or paraformaldehyde) with little or no production of **17**$(H)_3$. The crude mixture could be purified by column chromatography to give **17**$(H)_3$ in 7 % yield. Different reaction conditions, a triethylamine-catalysed Mannich condensation in an ethanol/water mix, gave an improved yield of 14 %. The latter synthetic procedure was favoured due to a simpler work-up, only requiring a less time-consuming filtration and recrystallisation as opposed to column chromatography. Conversion was tracked over 14 days to determine optimal reaction conditions.

Stable and well-defined polymetallic catalysts are of great interest to study the boundary between homogeneous and heterogeneous catalysis. Although solvothermal reactions have been shown to be useful in the synthesis of polymetallic compounds they often lack control over the products formed in the reaction. We sought to establish a more reliable protocol whereby the ligand is used to direct the assembly of the polynuclear complex. The assembly of polynuclear titanium compounds **5-8** relied on a carboxylate bridging between titanium centres. This was taken as a beneficial feature for the design of polynuclear titanium complexes. Due to the general lack of stability of titanium isopropoxide complexes in the presence of water, it was predicted that titanium-oxo derivative would be a more robust compound and a potential mimic of titanium dioxide nanoparticles, which are used as heterogeneous catalysts. We investigated the hydrolysis of amine bis(phenolate) titanium complexes **5-8** as a synthetic route to these compounds, whereby an isopropoxide ligand is replaced by hydroxide and thereafter a titanium-oxo-titanium bridge is formed.

Having observed the instability of the polynuclear titanium isopropoxide aggregates **5**-**8** in the presence of water, we sought to investigate their hydrolysis through the deliberate addition of stochiometric amounts of water and characterise the products formed. The simplest method of hydrolysis involved stirring the titanium isopropoxide aggregates in air. After stirring a THF solution of **5** overnight in an open flaskunder ambient conditions, a yellow precipitate was recovered and recrystallised from THF. A vapour diffusion in THF/acetonitrile yielded small, yellow plate-like crystals that were analysed by SCXRD. This structurally characterised the hydrolysis product as titanium-oxo tetragonal disphenoid **18**, with formula Ti_4O_2**1**$_4$. The Ti_4 core is bound by two oxo ligands and four carboxylate ligands. The longer Ti-carboxylate bridges (*cf.* Ti–O–Ti) result in an ordered, natural elongation of a tetrahedron whereby the four titanium centres form the vertices of a tetragonal disphenoid. A more consistent hydrolysis could be performed by adding 4 equivalents of water to the reaction mixture and stirring overnight. This allowed full conversion when the reaction scale was increased. The same synthetic procedure was used to synthesise analogous compounds to **18** with alternative groups in the *R′*/*R″* positions of the ligand. **19**, **20**, **21** and **22** (Figure 31).

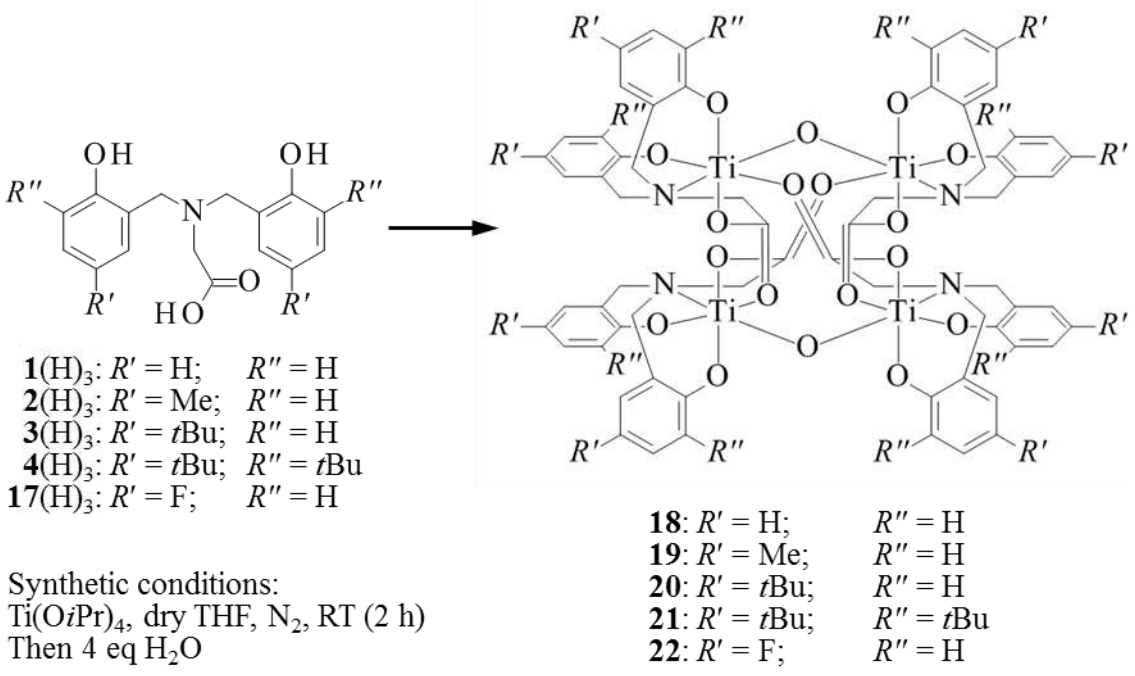

Figure 31. Synthesis of compounds **18**-**22** with general formula $Ti_4O_2L_4$.

3.2.1 Single crystal X-ray diffraction study

Single crystals suitable for SCXRD analysis characterised **19**-**22** as tetragonal disphenoids analogous to **18** with general formula $Ti_4O_2\mathbf{L}_4$. Crystals were grown by vapour diffusion in THF/acetonitrile for **19**. Slow evaporation of a toluene solution of **20** yielded large, orange, tetrahedron-shaped crystals. Compound **21** could be readily crystallised from many crystallisation conditions (slow evaporation of chloroform or toluene/chloroform solutions; vapour diffusion of toluene/diethyl ether, toluene/petroleum ether 40-60 °C, toluene/hexane). Contrastingly, several crystallisation conditions were unsuccessful for **22** with many combinations of solvents investigated. Despite this, diffraction quality single crystals were produced from a vapour diffusion of a toluene solution with acetonitrile. This gave a dataset with $Z' = 3$ featuring large voids containing highly disordered solvent as well as positional disorder within one moiety of the asymmetric unit. Single crystals obtained from a vapour diffusion of a DCM solution of **22** and petroleum ether 40-60 °C were weakly diffracting (d_{min} = 1.00 Å) but gave the dataset, with a Z' value of 1 and no disorder about **22**.

Compounds **18**-**22** are structurally similar (Figure 32) therefore the next part of the discussion will focus on **18**, which will serve as an example for the structural analysis of all five structures. Complex **18** features four supporting ligands (**1**), each supporting a single titanium centre. Two oxo bridging ligands complete the coordination sphere of the titanium centres, each of which is bound by all but one donor atom from ligand **1**. This remaining unbound oxygen donor atom, of the carboxylate group, bridges to an adjacent titanium centre. We term this a 'bridging' carboxylate oxygen herein, while the bound carboxylate oxygen atom is termed 'native'. The complex is overall neutral, established by the absence of counter-ions in the solid state structure, and confirmed by the balance of charges between the four amine bis(phenolate) ligands (**1**), two oxo ligands and four titanium centres. We use the bond distances from the crystal structure of **18** to characterise the native or bridging oxygen as L- or X-type donors. The mean carbon-oxygen bond distances for the native and bridging carboxylate are 1.263(3) Å and 1.253(2) Å respectively, indicating a delocalised carboxylate donor. Furthermore, the average bond distance between a titanium centre and the oxygen from the native carboxylate is 2.012(1) Å whereas the average bond distance between a titanium and the oxygen from an adjacent carboxylate is 2.094(2) Å. The lack of significant difference in bond lengths can be explained by delocalision of the electronic charge throughout the structure. This implies the two carboxylate oxygens can consecutively alternate between L- and X-type

donation with each titanium centre conserving an oxidation state of +4. We anticipate that these delocalised carboxylate groups will have the potential to stabilise a metal centre during redox processes associated with a catalytic cycle. Despite the observed delocalisation we classify each amine bis(phenolate) ligand as a formal LX_3 type donor with the native carboxylate oxygen acting as an X donor to satisfy an oxidation state of +4 to each titanium centre.

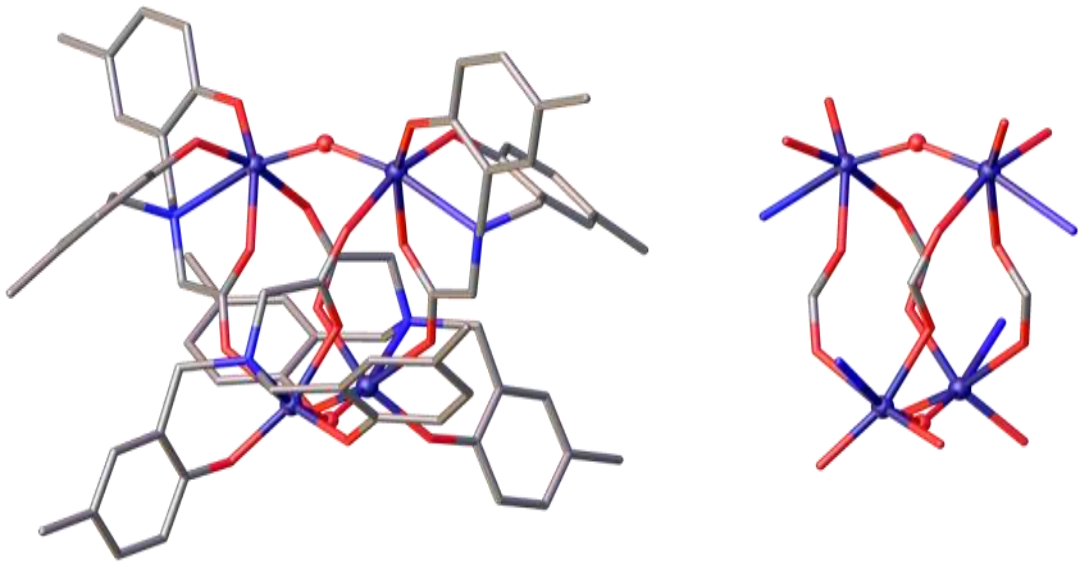

Figure 32. Left: Crystal structure of **19** grown from the asymmetric unit; Right: view of the coordination spheres of the titanium centres in **19**. Titanium-oxo core is shown as spheres and ligand framework displayed as tubes. Solvent of crystallisation and hydrogen atoms omitted for clarity. Ti = purple; C = grey; N = blue; O = red.

Selected geometrical parameters for the crystal structures of **18**-**22** are presented in Table 4. Comparison of these geometrical parameters with those from published crystal structures of similar titanium amine bis(phenolate) complexes[37-39] and related titanium compounds that contain titanium-oxo-titanium bridges[24,28,40] are in agreement. The titanium-oxo-titanium bridges in compounds **18**-**22** adopt a bent conformation with an internal angle of 145.7(1)° to accommodate the bridging carboxylate interactions. Both native and bridging Ti–OCO bonds are found to be shorter than the L-type donation found in a pendant CH_2CH_2OMe group[37,38] but longer than an X-type $CH_2CH_2O^-$ group.[1,39] A bridging $CH_2CH_2O^-$ group[39] with a L- and X-type donation shows comparable Ti–OCO distances to those found in compound **5**. A further example consisting of a salicylaldiminato titanium complex featuring bridging carboxylates also shares similar native and bridging Ti–OCO and TiO–CO bond distances to compound **5**.[41]

Comparison of the geometrical parameters between compounds **18**-**22** showed no significant deviations (< 0.5 %). From this, we can infer that **18**-**22** are isostructural and the combinations of *R′*/*R″* groups screened in this work have had little effect on the observed bond lengths and angles of structures **18**-**22**. Moreover, the nature of the *R′*/*R″* groups have not diminished the formation of the favourable $Ti_4O_2L_4$ motif.

Parameter	Mean	Deviation	Deviation %
Ti–O	1.821(2)	0.004	0.21
Ti–O–Ti	145.8(1)	0.307	0.21
Ti–OPh	1.851(2)	0.004	0.22
$Ti–O_{native}CO$	2.018(2)	0.005	0.23
$Ti–O_{bridging}CO$	2.101(2)	0.010	0.46
$TiO_{native}–CO$	1.267(4)	0.004	0.31
$TiO_{bridging}–CO$	1.256(4)	0.004	0.28

Table 4. Means and deviations of selected bond lengths (Å) and angles (°) for compounds **18**-**22**.

3.2.2 Solution state characterisation

Further characterisation was sought using solution-state NMR spectroscopy. Compound **18** was characterised by 1D and 2D NMR experiments (COSY, EXSY, NOESY, ROESY, HSQC) in $CDCl_3$, enabling its characterisation in solution. Further characterisation by nanoelectrospray mass spectrometry in DCM/methanol only found a $M+H^+$ peak at half of the mass expected for compounds **18**-**22**. This suggests the Ti_2OL_2 fragments are separating under the conditions of the experiment which is unsurprising as we previously found that the bridging carboxylate interactions in the polynuclear aggregates **5**-**8** and *rac*-**13**-**14** were labile in solution. A ^1H and ^{13}C NMR spectra were obtained for **18** in D_6-DMSO. This led to significant line broadening that was confirmed to be an exchange process by EXSY spectroscopy. Aggregation and relaxation effects were ruled out by repeating ^1H NMR experiments at lower concentrations of **18** and longer D1 delays (12 s). If the weaker, L-type bridging carboxylate interactions in **18** were broken then a Ti_2 species with half the molecular weight would be formed, featuring a ‘vacant site’ on each titanium centre. In the presence of a suitable donor, such as D_6-DMSO, the Ti_4 form can be stabilised to the Ti_2 form where the vacant sites can be filled by the suitable donor, ***S*** (Figure 33). Experiments with **19**-**22** also exhibited broadened ^1H NMR spectra in D_6-DMSO, further evidence that this observation is a feature of these $Ti_4O_2L_4$ species. In particular, a ^{19}F NMR of **22** shows line broadening in comparison the sharp spectrum obtained in $CDCl_3$, with the appearance of four lower

intensity signals at −125.97 ppm. −126.17 ppm, −127.13 ppm and −127.85 ppm alongside two more intense signals at −124.24 ppm and −125.11 ppm. We propose these lower intensity signals to be associated with the formation of the Ti_2 monomeric form in D_6-DMSO.

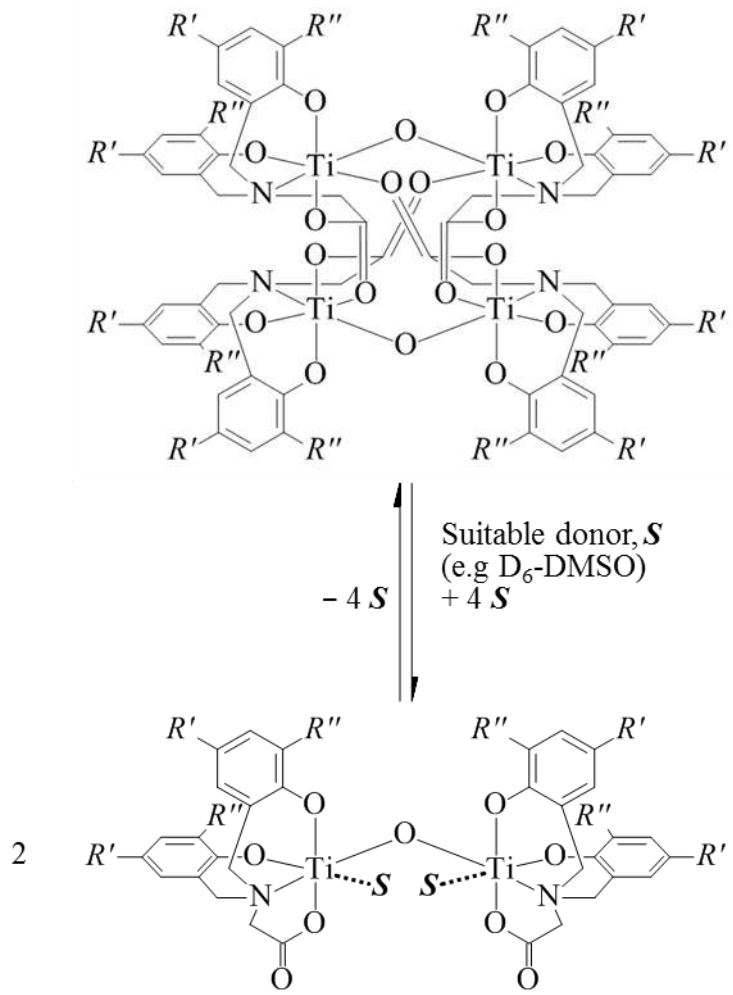

Figure 33. Proposed equilibrium of compounds **18**–**22** between the dimeric $Ti_4O_2L_4$ (top) and monomeric Ti_2OL_2 forms (bottom) in the presence of a strong donor solvent ***S***.

The solution-state structure of **18** in the weakly-coordinating solvent $CDCl_3$ was indeed the dimeric Ti_4 form. This analysis was also extended to **19**-**22** which found similar behaviour. A primary indication that the Ti_4 dimeric form was present in $CDCl_3$ was the absence of cross-coupling peaks in the NOESY NMR spectra of these species, which can be expected for molecules exceeding 1000 Da in mass.[42] Through-space contacts, that could only be observed in the Ti_4 dimeric structure, were identified using the crystal structure of **18**-**22** using the HSQC, COSY and ROESY NMR spectra from **18**-**22** in $CDCl_3$. Each diastereotopic methylene and aromatic signal in the ^1H NMR spectra of **18**-**22** was assigned to individual protons in the structures. As an example, these

assignments will be detailed for compound **19**, where the methyl groups in the *R′* positions were particularly useful as further evidence in the assignment of individual protons to each signal with certainty (Figure 34). The ROESY experiment of compound **19** revealed through-space contacts with methyl protons H_{Me1} and H_{Me2} that enabled the assignment of H_B and H_C as aromatic protons *ortho* to the methyl *R′* group. Since H_A and H_B showed through-bond coupling from the COSY experiment, H_B could be distinguished from H_C. The individual methylene proton signals could be paired per methylene group using C–H correlation and through-bond coupling. Individual proton assignments were made by using through-space contacts, specifically the relationships between $H_{D1}\cdots H_{E1}\cdots H_{F1}$ and $H_{D1}\cdots H_{F2}\cdots H_{D2}$ were key to achieving this. With these assignments, the methylene-aromatic region was inspected. Cross-coupling peaks were found for $H_{D1}\cdots H_{B1}$ and $H_{F2}\cdots H_{A1}$ and these were identified as distinct to the Ti_4 dimeric form using the crystal structure. Additionally, the through-space contacts for $H_{D1}\cdots H_{Me1}$ and $H_{D2}\cdots H_{Me1}$ were also observed and further support the presence of the dimeric form. These cross-coupling peaks are in agreement with the intramolecular hydrogen distances (< 5 Å)[42] obtained from the crystal structures (Figure 34). From this evidence, we can ascertain that the NMR spectra, in a weakly coordinating solvent, are of the dimeric forms of compounds **18**-**22**. Similar investigations by combined 1D/2D/SCXRD studies of **19** in D_3-acetonitrile and **22** in D_8-toluene revealed the same dimeric structure exists in these weakly-coordinating solvents.

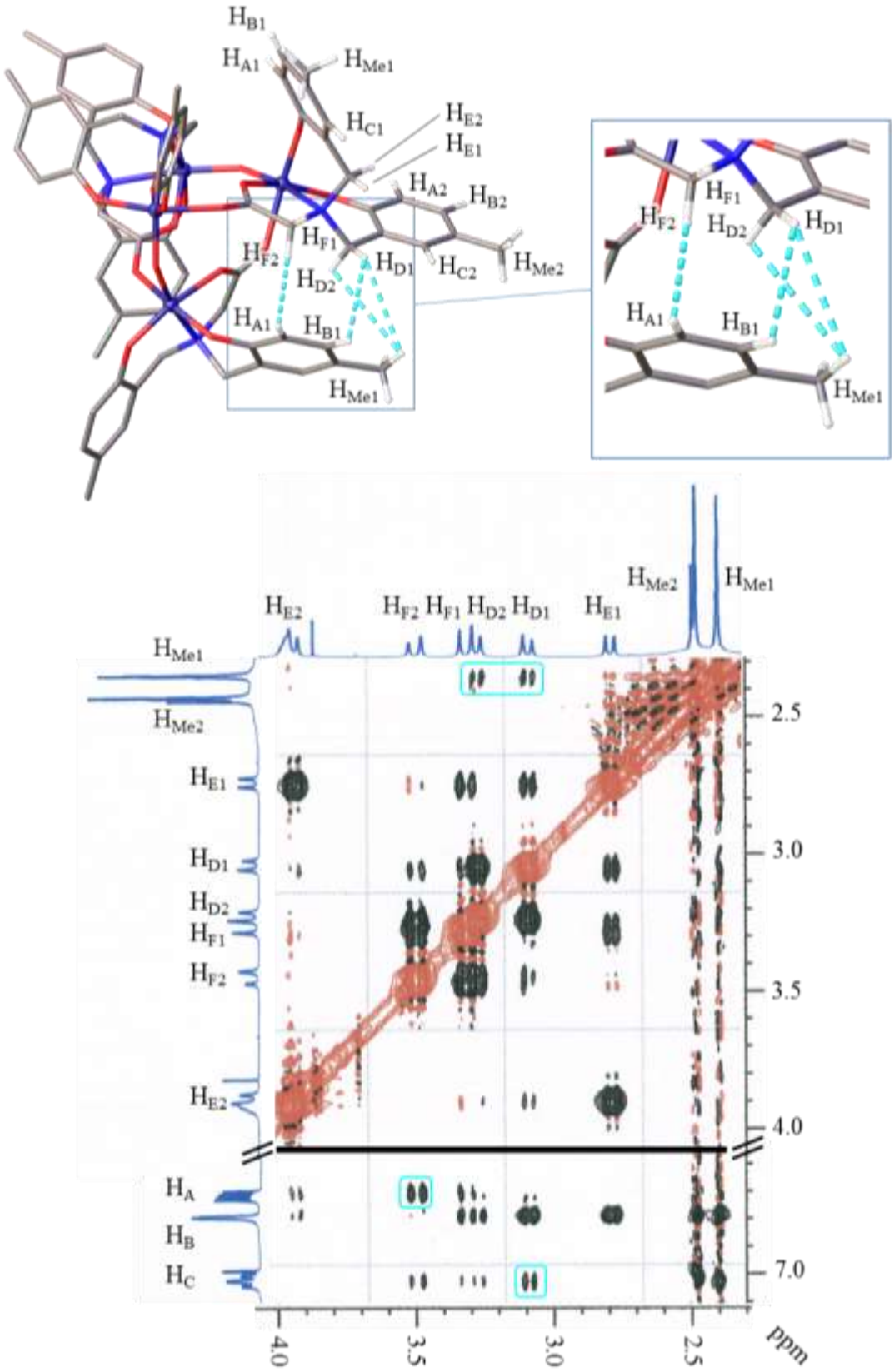

Figure 34. Selected proton assignments from NMR studies labelled in the crystal structure of **19**. Through-space contacts specific to the dimeric structure, shown by light blue fragmented bonds, are highlighted in the ROESY spectrum. Solvent of crystallisation and selected hydrogen atoms omitted for clarity. Ti = purple; C = grey; N = blue; O = red.

The Ti_4 dimeric and Ti_2 monomeric forms differ significantly in volume and *MW*, thus additional characterisation could be obtained from DOSY NMR experiments comparing the estimated *MW* of **19** in $CDCl_3$ and D_6-DMSO. Using external calibration curves (ECCs) published by Stalke and coworkers,[43,44] the *MW* of **19** in solution can be estimated from the experimentally-derived diffusion coefficients. The data obtained from this analytical method for **19** in $CDCl_3$ and D_6-DMSO is summarised in Table 5. If the monomeric Ti_2 form is stabilised in D_6-DMSO, the estimated *MW* of **19** in D_6-DMSO will be half that of the estimated *MW* in $CDCl_3$, as shown by the calculated *MW* shown in Table 5. The estimated *MW* of **19** in D_6-DMSO and $CDCl_3$ agrees with this expected trend, although the values obtained are lower than expected. This is unsurprising as the molar density of **19** exceeds the tolerance range of the ECCs, with a calculated molar density of 1.41×10^{30} $g \cdot mol^{-1} \cdot m^{-3}$, which exceeds the the molar density range of 4.3×10^{29} $g \cdot mol^{-1} \cdot m^{-3}$ and 5.9×10^{29} $g \cdot mol^{-1} \cdot m^{-3}$ for the ECCs therefore we would expect the ECC to be underestimated for our complexes. Inspecting the diffusion coefficients obtained for **19** reveals that a larger value was obtained in D_6-DMSO, inferring a larger species is present in D_6-DMSO, which would be contrary to the smaller size of the proposed monomeric Ti_2 form. This is an example of how ECCs can account for differences in solvent effects as D_6-DMSO is more polar and will cause greater drag of **19** in solution, resulting in an inflated value for diffusion coefficient in comparison to less polar solvent $CDCl_3$. Using this technique, we were able to compare the DOSY NMR data obtained in different solvents to further characterise the monomeric Ti_2 and dimeric Ti_4 forms of **19** in solution.

Solvent	Mean *D* ($m^2 \cdot s^{-1}$)	Mean Error *D*	Estimated *MW*	Calculated *MW*
$CDCl_3$	6.91×10^{-10}	7.24 %	1126 $g \cdot mol^{-1}$	1473 $g \cdot mol^{-1}$
D_6-DMSO	1.19×10^{-10}	4.43 %	427 $g \cdot mol^{-1}$	736 $g \cdot mol^{-1}$

Table 5. Estimated and expected *MW* of **19** in $CDCl_3$ and D_6-DMSO, with the corresponding mean diffusion coefficients, *D* and errors.

Although the Ti_4 dimeric form was shown to exist in weakly-coordinating solvents through a variety of NMR experiments, the thermal stability of the species was still to be confirmed. A variable temperature NMR study in D_8-toluene of **22** was performed to test the thermal stability of the Ti_4 dimeric structure in a weakly-coordinating solvent. Coalescence of the methylene bridge signals was of interest since this would be indicative of hemi-lability in the ligand upon heating. Changes in chemical shift were attributed to temperature, with methylene protons H_{E1} and H_{E2} experiencing the greatest deviation in

chemical shift over the temperature range –40 °C to 80 °C (Figure 35). This was thought to be due to greater thermal motion of the aromatic rings in the vicinity and/or greater interaction with the solvent whereby the anisotropic magnetic field of D_8-toluene and/or phenolate rings causes changes in the magnetic environment of the protons. Despite incremental changes in chemical shift, no evidence of coalescence was observed in the temperature range from –40 °C to 80 °C. In addition, identical ^{1}H NMR spectra were obtained at 20 °C before and after heating to 80 °C, demonstrating that the aggregates are thermally stable in weakly-coordinating D_8-toluene. If the dimeric Ti_4 structure were to dissociate to the monomeric Ti_2 structure, the apparition of different chemical environments or broadening of the signals would be anticipated but no such change in the NMR spectra was observed.

The aggregates are thermally stable in a weakly-coordinating solvent but we have already shown that they can be disrupted with a more strongly-coordinating solvent, with a direct observation of this phenomenon by a DOSY NMR study in the strong donor solvent D_6-DMSO. It is reasonable to expect that a diester, such as lactide, will have a similar, disruptive effect on the aggregate. It is therefore more accurate to describe these Ti_4 compounds as pre-catalysts that are capable of forming the active species *in situ* under the polymerisation conditions we describe further in this chapter.

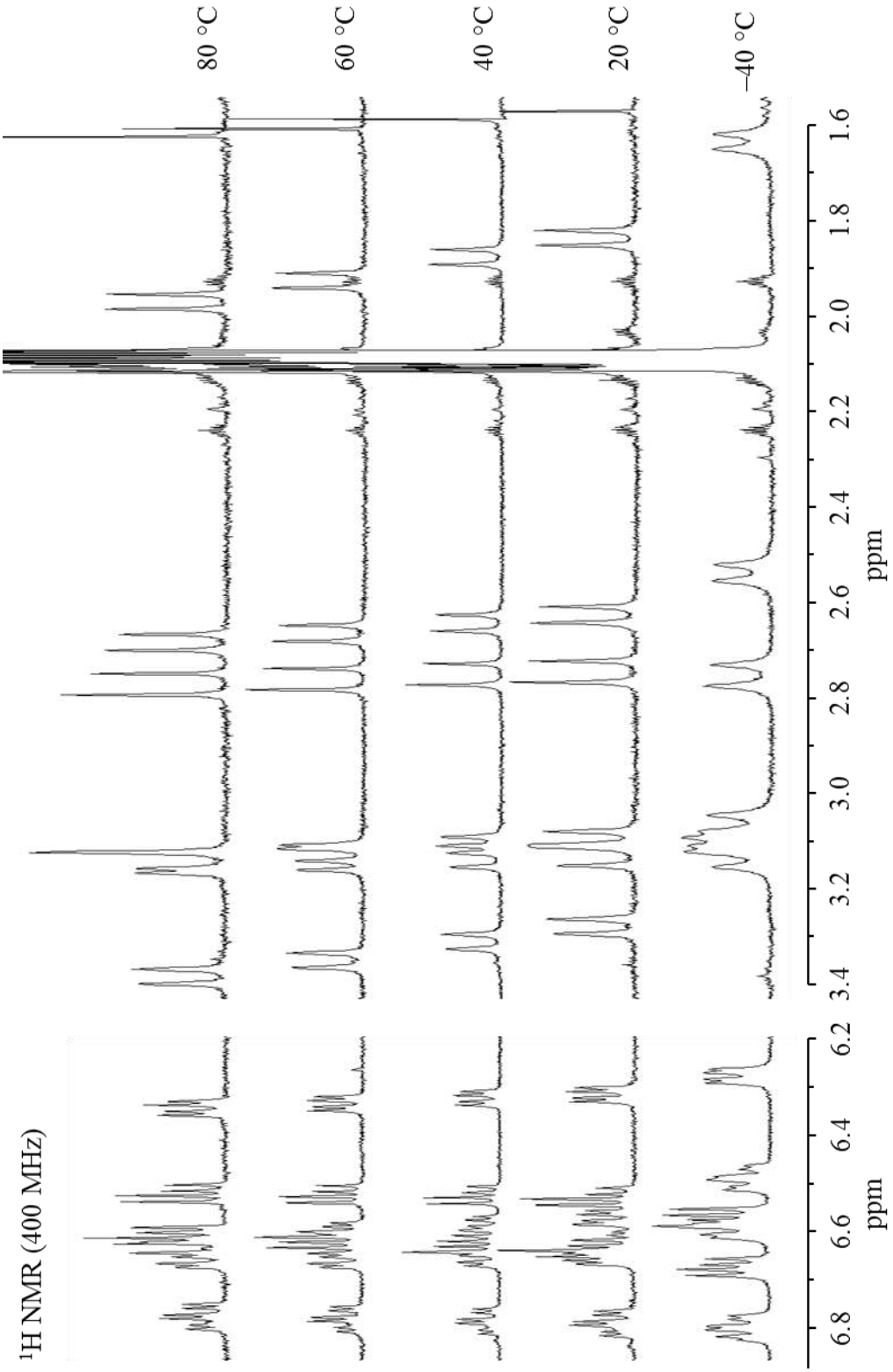

Figure 35. Variable temperature ^{1}H NMR (400 MHz) spectra of compound **22** in D_8-toluene over a temperature range of −40 °C and 80 °C. The methylene and aromatic regions are highlighted.

3.3 Application in the ROP of *rac*-lactide

Throughout this work, it was observed that the titanium-oxo complexes **18**-**22** could be stored and handled under ambient conditions, with no need for exclusion of moisture or air. This may be unsurprising as the synthesis of these compounds involves excess amounts of water in THF, with warming the mixture in the case of **21**, which served as a strong evidence as to the air- and water-stability of these titanium-oxo complexes. A comparative study of the performance of polynuclear complexes **18**-**22** under solution or melt polymerisation conditions was undertaken using the same conditions as for the polynuclear titanium isopropoxide intitiators in chapter 2. Due to the greater stability in the presence of water observed with **18**-**22**, we were able to use technical grade *rac*-lactide, which was a key difference in the ensuing investigations, making these catalyst more industrially-viable. The impurities contained within this starting material, such as water and lactic acid, will be a further test of the stability of these polynuclear complexes. This would make use of the improved stability in the presence of air and water of these titanium-oxo complexes and test their suitability under similar conditions to those used industrially.

3.3.1 Melt polymerisation conditions

Compounds **18**-**22** exhibited thermal stability leading us to propose that they would be well-suited to catalyse the ROP of lactide in the melt. Melt polymerisation conditions are more strenuous on catalysts and initiators due to the high temperature (130 °C) of the reaction and strong polarity of the melted lactide solvent. To verify the stability of the catalyst under these conditions, the ^{1}H NMR spectra for **19** and a quenched sample of **19** from a reaction with lactide-to-titanium ratio of 10:1 under melt conditions at 130 °C were inspected. All of the ^{1}H NMR signals for **19** were found to be present at similar chemical shift and integrations, asserting the catalyst was stable under the reaction conditions and can be recovered and reused.

Performance data for **18**-**22** under melt polymerisation conditions are presented in Table 6 and Table 7. Initial polymerisations were performed with **18** as catalyst in the melt polymerisation of *rac*-lactide at 130 °C with a monomer-to-titanium ratio of 300:1. Low conversion (17 %) of the monomer to the polymer was observed after 24 h. The lack of initiating group in the design of **18**-**22** prompted use to introduce benzyl alcohol at the same concentration as titanium to act as an *ex situ* initiator but this was not found to

increase the conversion after 24 h. In comparison it was found that the addition of alkyl groups in the *R′*/*R″* positions (**19**-**21**) significantly increased the conversion after 24 h. Again, using benzyl alcohol as an additive resulted in no increase in conversion after 24 h. An increase in the solubility from **19** to **20** to **21** correlated with an upward trend in catalytic activity (**19** < **20** < **21**) demonstrated by the increases in conversion. Finally, catalyst **22** was of interest for two reasons: to investigate the effect of an electron withdrawing substituent and to make the catalyst more polar to increase solubility in the melt. This catalyst gave the highest conversion after 24 h at 91 %. The increased catalytic activity of **22** could be rationalised by either electronic effects or solubility imparted by the fluoro group. However, inspection of the crystal structures revealed the compounds **18**-**22** are isostructural indicating that the change in *R′* group has little electronic influence over the bond lengths in the complex. Therefore, it is likely that the increase in catalytic activity for catalyst **22** is due to its increased solubility in molten lactide, with the polarity of the fluoro group increasing the solubility in the polar molten *rac*-lactide solvent. Furthermore, the crystal structures of **18**-**22** show the *R′*/*R″* groups are facing the exterior of the catalysts where they affect the primary solvation sphere. This is strongly supportive that the increase in solubility from **18** to **22** in molten *rac*-lactide is the cause for the correlating trend of increased activity.

As the most active catalysts, melt polymerisations with **21** and **22** were repeated with a monomer-to-titanium ratio of 600:1 to further test their activity in the ROP of *rac*-lactide. This led to a conversions of 42 % and 66 % after 24 h for **21** and **22** respectively. The polymerisation time was extended to 48 h and the conversion reached 72 and 96 % respectively. A similar trend showing an increase in conversion with polymerisation times was observed with the equivalent systems where benzyl alcohol was introduced (Table 6, entries 10-12 and 16-18). This demonstrates that catalysts **21** to **22** are not deactivated until the polymerisation is terminated at the desired time, which is suggestive of a living polymerisation.

Entry	Catalyst	$[M]_0$ / $[Ti]_0$	Additive	Time	Conv.[a]	P_r[b]
1	**18**	300	-	24 h	17	0.66
2	**18**	300	BnOH	24 h	11	0.53
3	**19**	300	-	24 h	46	0.66
4	**19**	300	BnOH	24 h	40	0.63
5	**20**	300	-	24 h	84	0.62
6	**20**	300	BnOH	24 h	86	0.56
7	**21**	300	-	24 h	88	0.55
8	**21**	600	-	24 h	42	0.55
9	**21**	600	-	48 h	72	0.54
10	**21**	300	BnOH	24 h	91	0.62
11	**21**	600	BnOH	24 h	76	0.54
12	**21**	600	BnOH	48 h	85	0.52
13	**22**	300	-	24 h	91	0.63
14	**22**	600	-	24 h	66	0.60
15	**22**	600	-	48 h	96	0.60
16	**22**	300	BnOH	24 h	84	0.59
17	**22**	600	BnOH	24 h	64	0.54
18	**22**	600	BnOH	48 h	78	0.56

Table 6. Melt polymerisation data using titanium isopropoxide complexes **18**-**22**. Data is displayed for both solution and melt polymerisation conditions. [a] Conversion (%) from ^{1}H NMR spectra evaluated by integration of the methine regions of polylactide versus lactide. [b] Calculated from analysis of the homonuclear decoupled ^{1}H NMR spectrum of the polymer sample.

Moreover, we observed a general increase in polymer molecular weight, M_n, and conversion, even when polymerisation time was extended from 24 h to 48 h (Table 7, Entries 7-12 and 13-18). This is further evidence that the polymerisation proceeds under living conditions. The relatively low polydispersity indices, M_w /M_n, are also symptomatic of a living polymerisation, which would be expected for catalysts **18**-**22** as they are stable under the melt polymerisation conditions. It was noted that longer polymer chain lengths were obtained for catalyst **22** at similar conversions to catalysts **20** and **21**. It could be thought that the increased solubility of **22** allows for better mass transfer of the catalyst during the melt polymerisation, leading to longer polymer chains. Furthermore, the higher conversion and longer polymer chain lengths obtained with **22** showed that maximising homogeneity was beneficial to increase performance in these systems.

Focussing on entries 10-12 and 16-18 in Table 7, it can be seen that addition of benzyl alcohol has hindered the polymerisation, evidenced by short chain lengths and greater PDI values. We observed lower conversion, shorter polymer chain lengths and higher polydispersity indices (PDIs) in comparison to entries 7-9 and 13-15. This decrease in performance could be explained by considering that benzyl alcohol can displace the growing polylactide chains from the metal centres, resulting in an increase in the rate of transesterification reactions. Noticeably, the gel permeation chromatography (GPC) traces for polylactide samples from systems with benzyl alcohol exhibited bimodal molecular weight distributions with shoulder peaks as well as evidence of high molecular weight chains with unimodal peaks at lower retention times, equivalent to approximately double the molecular weight of the bimodal peak. The high molecular weight chains are likely due to intermolecular transesterification whereas the bimodal traces occur from intramolecular transesterification, whereby the difference in hydrodynamic volume between linear polylactide and macrocyclic polylactide results in the appearance of a shoulder peak.[45,46] In general, the addition of benzyl alcohol brought no significant benefit to these systems and confirmed that an accompanying initiator is not a necessity for catalysts **18**-**22** to ring-open lactide. Without the addition of benzyl alcohol, catalysts **18**-**22** showed reasonable control over the ROP of *rac*-lactide with PDI values ranging between 1.12 and 1.59 where conversion exceeded 40 % peak.

Entry	Catalyst	$[M]_0$ / $[Ti]_0$	Additive	Time	M_n[a]	M_{calc}[b]	M_w/M_n[c]
1	**18**	300	-	24 h	4130	8250	1.35
2	**18**	300	BnOH	24 h	6700	1120	1.06
3	**19**	300	-	24 h	3150	8470	1.12
4	**19**	300	BnOH	24 h	4380	4560	1.10
5	**20**	300	-	24 h	11100	16000	1.41
6	**20**	300	BnOH	24 h	8530	5690	1.49
7	**21**	300	-	24 h	17100	15200	1.50
8	**21**	600	-	24 h	19300	18500	1.53
9	**21**	600	-	48 h	33800	30400	1.56
10	**21**	300	BnOH	24 h	17100*	5470	1.42*
11	**21**	600	BnOH	24 h	9260*	6750	1.35*
12	**21**	600	BnOH	48 h	38200*	15600	2.93*
13	**22**	300	-	24 h	22300	20000	1.59
14	**22**	600	-	24 h	15700	23500	1.36
15	**22**	600	-	48 h	42000	41200	1.50
16	**22**	300	BnOH	24 h	10500*	6050	1.73*
17	**22**	600	BnOH	24 h	11800*	7140	1.76*
18	**22**	600	BnOH	48 h	24700*	9100	1.59*

Table 7. Melt polymerisation data using titanium isopropoxide complexes **18**-**22**. Data is displayed for both solution and melt polymerisation conditions. [a] Polymer number average molar mass determined from GPC traces. [b] Calculated polymer molecular weight by ^{1}H NMR end-group analysis. [c] Polydispersity indices (M_w/M_n) obtained from GPC traces. * From unresolved peaks showing bimodal data – see discussion.

The microstructure of the polylactide samples was investigated by ^{1}H NMR spectroscopy. Determination of the polymer chain lengths by end-group analysis correlates well with the polymer chain lengths obtained from GPC traces. This supports the view that linear polylactide terminated by water was obtained from catalysts **18**-**22**. Further analysis by MALDI TOF mass spectrometry of representative polylactide samples (Entries 5, 6, 13 and 14) confirmed the incorporation of water as an initator, with the polylactide chains exhibiting protonated end groups. We assume the water incorporated into the polylactide chains was present in the unpurified *rac*-lactide used in the polymerisation. Further detailed analysis of the polylactide chains can be obtained through inspection of the methine region by homonuclear decoupled proton NMR experiments. These enabled the determination of the probability of racemic enchainment, P_r.[47,48] These values, presented in Table 6, indicate the polylactide chains produced using catalysts **18**-**22** display a slight tendency for heterotactic enchainment.

3.3.2 Characterisation of the active species

Solution polymerisation experiments are commonly used to determine the kinetics of initiators and catalyst in the ROP of lactide. In the case of **18**-**22**, the nature of the solvent was shown to be critical to the stabilisation of the dimeric Ti_4 pre-catalysts, with coordinating solvents leading to the formation of a proposed monomeric Ti_2 form. Therefore without careful consideration of the reaction conditions, the solution polymeriation kinetic data would not be relevant to the melt polymerisation reactions of **18**-**22**. Thus, the most accurate kinetic study of these systems would require direct measurements under melt polymerisation conditions which is impossible without specialised equipment.[49] In the absence of this kinetic data, it would be difficult to elucidate the active species in the ROP of *rac*-lactide for **18**-**22**. As an alternative approach, we used a variety of solution-state NMR experiments in combination with SCXRD data to probe the active species.

Compounds **18**-**22** exhibited lability in strong donor solvents, a comparable environment to the molten lactide 'solutions' in the catalytic system. We propose that the active species involves a transition from the saturated dimeric $Ti_4O_2L_4$ to the monomeric Ti_2OL_2 form stabilised by coordinated polylactide chains, allowing access to all four titanium centres. Rotation about the Ti–O–Ti bridge would relieve any steric strain resulting from the accommodation of two growing polylactide chains in close proximity (Figure 36).

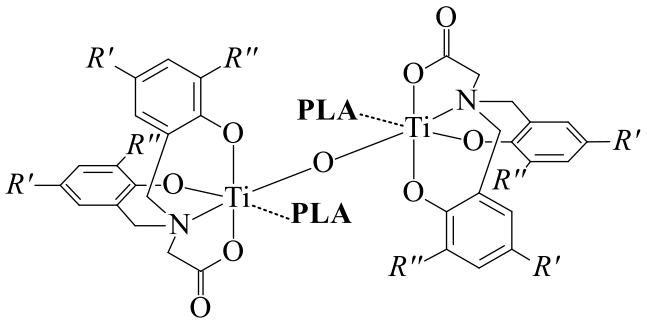

Figure 36. Proposed active species in the melt polymerisation of *rac*-lactide. The monomeric Ti_2OL_2 structure is stabilised by the growing polylactide chains bound to the titanium centres and denoted by **PLA**.

To gain further insight into the proposed Ti_2 active species during the melt polymerisation, a control ^1H NMR experiment involving a 10:1 mixture of *rac*-lactide and catalyst **19** in $CDCl_3$ was carried out to probe for interactions between the monomer and catalyst in the system. We observed an upfield shift of specific proton signals when compared to the ^1H NMR of the pure catalyst (Figure 37). The shift in these proton signals is not accompanied by the same magnitiude of shift for vicinal protons, indicative of a localised interaction between the **19** and *rac*-lactide. The protons in question are highlighted in green in the crystal structure of **19** in its dimeric form (Figure 37). It was noted that protons H_{D2} and H_{F2} are inaccessible to the solvation sphere and cannot interact directly with *rac*-lactide. The upfield shift of these proton signals is symptomatic of greater magnetic shielding, which can be explained by greater proximity to the face of an aromatic ring or carboxylate. It can be envisaged that *rac*-lactide interacts with the catalyst causing a bending of the phenolate rings, resulting in more pronounced magnetic shielding of individual protons. We proposed that *rac*-lactide was interacting with **19** in an approach to displace a carboxylate arm. This caused bending of the aromatic rings, resulting in an increase in proximity between Ar2 and H_{E2} as well as Ar1 and H_{D2} and H_{F2}. The bending of Ar1 would also move H_{A1} closer to the plane perpendicular to the carboxylate denoted by "*" (Figure 37), explaining the change in chemical shift for these specific protons.

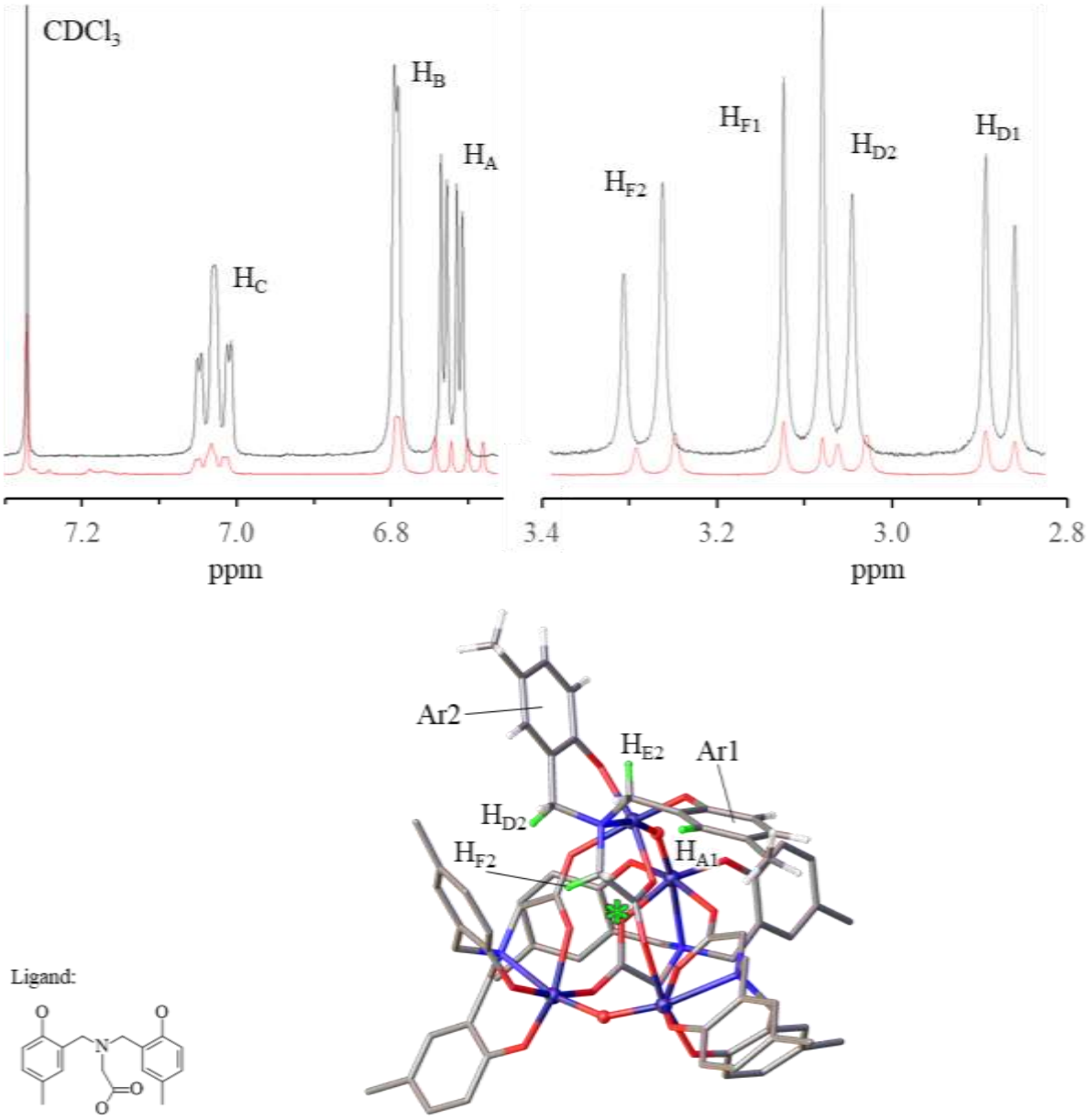

Figure 37. Top: ^{1}H NMR spectra of **19** (black) and a 10:1 mixture of *rac*-lactide and **19** (red) in $CDCl_3$ with selected proton assignments inset. Bottom: crystal structure of **19** with selected protons highlighted in green and aromatic rings Ar1 and Ar2. The carboxylate arm involved in bending is highlighted by a green "*". Solvent of crystallisation and selected hydrogen atoms omitted for clarity. Ti = purple; C = grey; N = blue; O = red; H = white.

To locate possible areas *rac*-lactide can interact with **19**, the solvent-accessible void space in the crystal structure of **19** was calculated using Mercury CSD software (Figure 38). This revealed four areas, highlighted in yellow, that correspond to the only sterically-viable approach pathway *rac*-lactide can take to displace the bridging carboxylate and access the titanium centres, ultimately leading to the monomeric Ti_2OL_2 form. In conjunction with the localised proton signal shifts, we find this is strong evidence of the proposed active species, as shown in Figure 36.

Comparing the performance of **18**-**22** in the melt polymerisation of *rac*-lactide to other Ti(IV) systems is difficult as the majority of those are initiated by pre-existing alkoxide groups bound to the titanium centre, a feature that is not present in our complexes (**18**-**22**). Further to this, our Ti_4 pre-catalyst requires activation *in situ* and therefore our systems, unsurprisingly, show lower activity when compared to other initiators featuring a Ti–O–Ti core.[25,27] Despite this, **18**-**22** retain the advantage of being air- and water-stable pre-catalysts that are capable of ring-opening unpurified *rac*-lactide and can be collected and reused without additives due to the absence of a pre-existing initiating group and do not require purified lactide.

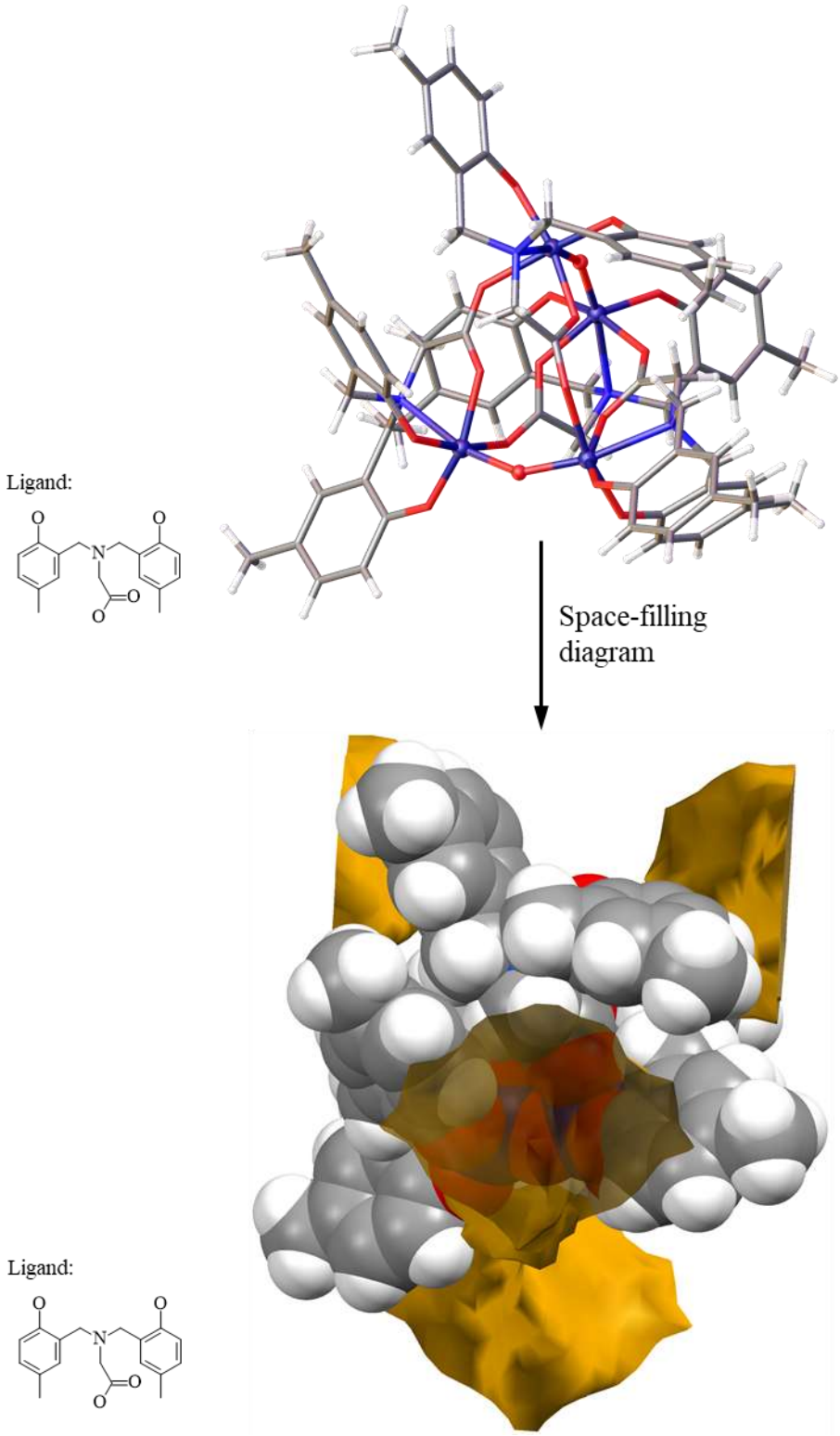

Figure 38. Crystal structure of **19** (top) and corresponding space-filling model (bottom). The yellow shaded areas show the solvent accessible voids, through which *rac*-lactide could access all four titanium centres via displacement of carboxylate arms. Solvent of crystallisation and selected hydrogen atoms omitted for clarity. Ti = purple; C = grey; N = blue; O = red; H = white; solvent-accessible voids = yellow.

3.3.3 Solution polymerisation conditions

The conversion of *rac*-lactide to PLA in was monitored over time in a solution of toluene at 130C for compounds **18**-**22** at a monomer to titanium ratio of 100:1 (Figure 39). After 48 h, low conversion was observed (< 20 %) which prompted us to investigate ways catalytic performance could be improved. The lack of initiating group in compounds **18**-**22**, which typically takes the form of an alkoxide in titanium initiators for the ring-opening polymerisation of lactide,[19] led us to introduce an alcohol as an additive, acting as an *ex situ* initiator. This led to a significant improvement in performance of **20** and **21** that feature bulkier groups in the *R′*/*R″* positions. This could be interpreted as the bulkier groups favouring the formation of the previously proposed Ti_2 active species, with the hydroxyl group from the benzyl alcohol acting as a strong donor to activate the catalysts. Moving forward with this assumption, 4-dimethylaminpyridine (DMAP) was used as an additive as it is a stronger base than benzyl alcohol and therefore will promote this activation further. This resulted in a significant increase in activity for **18**-**22** towards the ROP of *rac*-lactide in solution. However, stability tests of the catalysts in the presence of DMAP in refluxing toluene revealed a reaction occurred, leading to several titanium products in solution. These were identified as further titanium-oxo species whose formation and structures are discussed in chapter 4. As a final step to explore the activity of **18**-**22** under solution polymerisation conditions, the solvent was changed from toluene to THF and compound **19** and **21** as illustrative examples. The use of a more polar solvent was thought to aid in stabilising the active Ti_2 species by providing a suitable, polar donor to occupy the ***S*** positions, thus increasing the activity of the catalysts. However, this led to a decrease in performance with no conversion observed after 144 h. This could be explained by two factors: first, the decreased boiling point of THF led to a lower polymerisation temperature of 90 °C which is suggestive that the thermal contribution is more important; second, the polar THF solvent is able to coordinate to the active species and since it is solvent, it is in large excess in comparison to the lactide monomer, blocking the ***S*** sites on the active species.

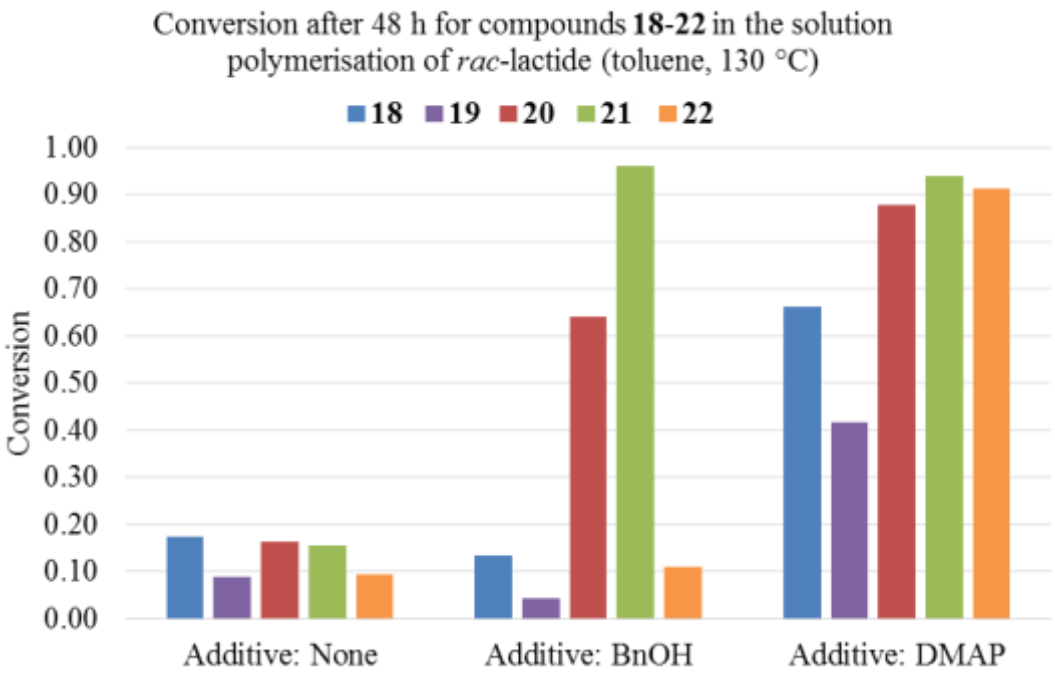

Figure 39. Comparison of the conversion of *rac*-lactide to polylactide catalysed by **18**-**22** with no additive, benzyl alcohol or DMAP.

Further information on the properties catalysts **18**-**22** in the solution polymerisation of *rac*-lactide was obtained by inspection of the trendlines for conversion versus time, presented in Figure 40. All systems were found to approximately agree with a linear increase in conversion with time, a further indication these systems are under living polymerisation conditions. An interesting observation was made when inspecting systems with DMAP as an additive: a sharp increase in conversion occurred after a polymerisation time of 4 h. After this initial increase, the conversion returns to the original approximate linear increase with time. Further details of the this phenomenon are discussed in chapter 4. Overall, the solution polymerisation data reinforces our understanding of catalysts **18**-**22** in the ROP of *rac*-lactide by presenting us with further evidence alluding to a Ti_2 active species and its living character under polymerisation conditions.

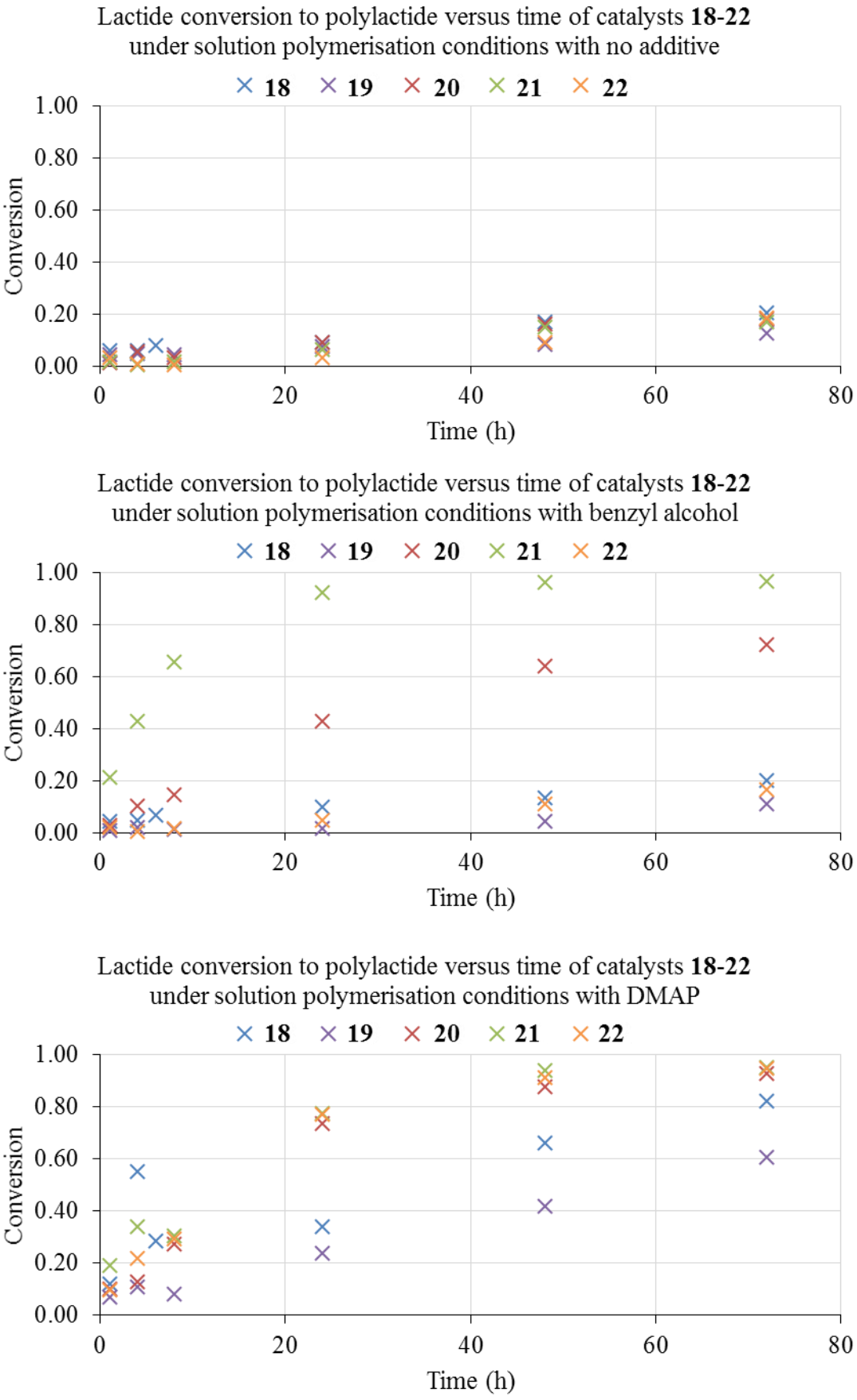

Figure 40. Conversion versus time of **18-22** under solution polymerisation conditions in the ROP of *rac*-lactide with no additive, benzyl alcohol and DMAP.

3.4 Conclusions

Five amine bis(phenolate) ligands with differing peripheral groups on the phenolates were used to support a series of well-defined tetrametallic, polynuclear titanium complexes with general formula $Ti_4O_2L_4$. The synthesis of these unique compounds was achieved by hydrolysis of monometallic titanium fragments, with the subsequent assembly of the Ti_4 species directed by the carboxylate arm of the ligand. Single crystal X-ray diffraction studies showed these discrete complexes were isostructural, demonstrating that varying the groups on the periphery of the ligands resulted in minimal influence over the overall architecture of the complex.

Exploiting the solubility of the polynuclear complexes enabled us to gain insight into their behaviour in solution and application in catalysis through analysis of the three-dimensional structure by combining solid- and solution-state techniques. Detailed NMR studies were critical to understanding the behaviour of these polynuclear complexes in solution and under polymerisation conditions. These studies allowed us to assign individual protons in the ^1H NMR spectra using a range of 2D NMR experiments. In particular, through-space contacts from ROESY experiments were identified as being specific to the dimeric Ti_4 form found in the solid-state crystal structures, confirming its presence in solution with non-coordinating solvents and establishing its stability in variable temperature NMR experiments. Broadening of the NMR spectra in a donor solvent highlighted exchange processes were occurring when a suitable donor was present in solution. We observed that these tetrametallic complexes are, in a strong donor solvent, in equilibrium with two dimetallic sub-units which are themselves stabilised by the donor solvent molecules. The relative stability of these two species is intrinsically linked to the carboxylate bridges, which exhibit a weaker, L-type bridging interaction. We propose that weakening these bridges will facilitate formation of the active dimetallic species and ultimately increase the rate with which our catalysts can ROP lactide. As a result we can conclude that these aggregates are only being activated *in situ* by the presence of the substrate.

We observed a significant difference in the rate with which these complexes polymerised *rac*-lactide under melt and solution conditions. Qualitatively, we observed those polynuclear complexes that were most soluble in molten lactide were also those which achieved the highest rates of polymerisation and longest polymer chain lengths. The more soluble complexes have the highest concentration in solution whilst also noting

that as the reaction proceeds, the concentration of PLA increases and the reaction medium becomes increasingly polar. The use of benzyl alcohol, a common additive, was employed as an *in situ* initiator and was found to slightly reduce conversion in most cases and promote unfavourable, transesterification side-reactions. In constrast, solution polymerisation conditions showed a drastic increase in conversion of *rac*-lactide to PLA when benzyl alcohol was introduced for catalysts with bulkier groups on the ligand periphery. We interpreted this observation as a combination of steric bulk and coordinating benzyl alchohol favouring the formation of the dimetallic active species. We anticipated a stronger donor would further improve the activity under solution polymerisation conditions, which was the case for all catalysts when DMAP was introduced as an additive. Interestingly, a control experiment involving a reflux of the catalysts and DMAP in toluene revealed the formation of new titanium-oxo species *in situ* and our efforts on the synthetic and structural investigations of these species are presented in the next chapter.

3.5 References

1. Y. Kim and J. G. Verkade, *Organometallics*, 2002, **21**, 2395-2399.
2. C. A. Huang and C. T. Chen, *Dalton Trans.*, 2007, 5561-5566.
3. D. T. Dugah, B. W. Skelton and E. E. Delbridge, *Dalton Trans.*, 2009, 1436-1445.
4. R. K. Dean, A. M. Reckling, H. Chen, L. N. Dawe, C. M. Schneider and C. M. Kozak, *Dalton Trans.*, 2013, **42**, 3504-3520.
5. K. Devaine-Pressing, J. H. Lehr, M. E. Pratt, L. N. Dawe, A. A. Sarjeant and C. M. Kozak, *Dalton Trans.*, 2015, **44**, 12365-12375.
6. E. Y. Tshuva, I. Goldberg, M. Kol and Z. Goldschmidt, *Inorg. Chem.*, 2001, **40**, 4263-4270.
7. A. J. Chmura, M. G. Davidson, M. D. Jones, M. D. Lunn, M. F. Mahon, A. F. Johnson, P. Khunkamchoo, S. L. Roberts and S. S. F. Wong, *Macromolecules*, 2006, **39**, 7250-7257.
8. S. Barroso, A. M. Coelho, S. Gomez-Ruiz, M. J. Calhorda, Z. Zizak, G. N. Kaluderovic and A. M. Martins, *Dalton Trans.*, 2014, **43**, 17422-17433.
9. P. Piszczek, A. Radtke, T. Muziol, M. Richert and J. Chojnacki, *Dalton Trans.*, 2012, **41**, 8261-8269.
10. M. Czakler, C. Artner and U. Schubert, *Eur. J. Inorg. Chem.*, 2012, 3485-3489.
11. R. Papiernik, L. G. Hubert-Pfalzgraf, J. Vaissermann and M. C. H. B. Goncalves, *J. Chem. Soc. Dalton.*, 1998, 2285-2287.
12. Y. J. Kim and J. G. Verkade, *Macromol. Rapid Commun.*, 2002, **23**, 917-921.
13. Y. Kim, G. K. Jnaneshwara and J. G. Verkade, *Inorg. Chem.*, 2003, **42**, 1437-1447.
14. S. H. Kim, J. Lee, D. J. Kim, J. H. Moon, S. Yoon, H. J. Oh, Y. Do, Y. S. Ko, J. H. Yim and Y. Kim, *J. Organomet. Chem.*, 2009, **694**, 3409-3417.
15. E. L. Whitelaw, M. D. Jones, M. F. Mahon and G. Kociok-Kohn, *Dalton Trans.*, 2009, 9020-9025.
16. M. D. Jones, M. G. Davidson and G. Kociok-Kohn, *Polyhedron*, 2010, **29**, 697-700.
17. E. L. Whitelaw, M. D. Jones and M. F. Mahon, *Inorg. Chem.*, 2010, **49**, 7176-7181.
18. E. L. Whitelaw, M. G. Davidson and M. D. Jones, *Chem. Commun.*, 2011, **47**, 10004-10006.
19. A. Sauer, A. Kapelski, C. Fliedel, S. Dagorne, M. Kol and J. Okuda, *Dalton Trans.*, 2013, **42**, 9007-9023.
20. B. Gao, Q. Duan, Y. H. Li, D. N. Li, L. Q. Zhang, Y. Cui, N. H. Hu and X. Pang, *RSC Adv.*, 2015, **5**, 13437-13442.
21. J. X. He, Y. L. Duan, X. Kou, Y. Z. Zhang, W. Wang, Y. Yang and Y. Huang, *Inorg. Chem. Commun.*, 2015, **61**, 144-148.
22. P. McKeown, M. G. Davidson, J. P. Lowe, M. F. Mahon, L. H. Thomas, T. J. Woodman and M. D. Jones, *Dalton Trans.*, 2016, **45**, 5374-5387.
23. R. R. Gowda, D. Chakraborty and V. Ramkumar, *Inorg. Chem. Commun.*, 2011, **14**, 1777-1782.
24. C. K. Su, H. J. Chuang, C. Y. Li, C. Y. Yu, B. T. Ko, J. D. Chen and M. J. Chen, *Organometallics*, 2014, **33**, 7091-7100.
25. D. Chakraborty, D. Mandal, V. Ramkumar, V. Subramanian and J. V. Sundar, *Polymer*, 2015, **56**, 157-170.
26. B. Rajashekhar, S. K. Roymuhury, D. Chakraborty and V. Ramkumar, *Dalton Trans.*, 2015, **44**, 16280-16293.

27. S. Pappuru, D. Chakraborty, J. Vijaya Sundar, S. K. Roymuhury, V. Ramkumar, V. Subramanian and D. K. Chand, *Polymer*, 2016, **102**, 231-247.
28. A. J. Nielson and J. M. Waters, *Polyhedron*, 2010, **29**, 1715-1726.
29. C. L. Boyd, T. Toupance, B. R. Tyrrell, B. D. Ward, C. R. Wilson, A. R. Cowley and P. Mountford, *Organometallics*, 2005, **24**, 309-330.
30. S. Meker, C. M. Manna, D. Peri and E. Y. Tshuva, *Dalton Trans.*, 2011, **40**, 9802-9809.
31. M. Miller and E. Y. Tshuva, *Eur. J. Inorg. Chem.*, 2014, **2014**, 1485-1491.
32. N. Sharma, V. Sharma, R. Bohra, V. S. Raju, I. P. Lorenz, C. Krinninger and P. Mayer, *Inorg. Chim. Acta*, 2007, **360**, 3002-3012.
33. T. Okamatsu, R. Irie and T. Katsuki, *J. Organomet. Chem.*, 2007, **692**, 645-653.
34. D. Peri, S. Meker, M. Shavit and E. Y. Tshuva, *Chem. Eur. J.*, 2009, **15**, 2403-2415.
35. D. Peri, S. Meker, C. M. Manna and E. Y. Tshuva, *Inorg. Chem.*, 2011, **50**, 1030-1038.
36. S. Song, X. Zhang, H. Ma and Y. Yang, *Dalton Trans.*, 2012, **41**, 3266-3277.
37. E. Y. Tshuva, I. Goldberg, M. Kol and Z. Goldschmidt, *Chem. Commun.*, 2001, 2120-2121.
38. S. Groysman, E. Y. Tshuva, I. Goldberg, M. Kol, Z. Goldschmidt and M. Shuster, *Organometallics*, 2004, **23**, 5291-5299.
39. P. M. Gurubasavaraj and K. Nomura, *Inorg. Chem.*, 2009, **48**, 9491-9500.
40. S. Barroso, F. Madeira, M. J. Calhorda, M. J. Ferreira, M. T. Duarte and A. M. Martins, *Inorg. Chem.*, 2013, **52**, 9427-9439.
41. J. Muller, G. Kehr, R. Frohlich and G. Erker, *Eur. J. Inorg. Chem.*, 2005, 2836-2841.
42. A. Pastor and E. Martinez-Viviente, *Coord. Chem. Rev.*, 2008, **252**, 2314-2345.
43. S. Bachmann, R. Neufeld, M. Dzemski and D. Stalke, *Chem. Eur. J.*, 2016, **22**, 8462-8465.
44. R. Neufeld and D. Stalke, *Chem. Sci.*, 2015, **6**, 3354-3364.
45. H. R. Kricheldorf, *J. Polym. Sci. Pol. Chem.*, 2010, **48**, 251-284.
46. J. Weil, R. T. Mathers and Y. D. Y. L. Getzler, *Macromolecules*, 2012, **45**, 1118-1121.
47. B. M. Chamberlain, M. Cheng, D. R. Moore, T. M. Ovitt, E. B. Lobkovsky and G. W. Coates, *J. Am. Chem. Soc.*, 2001, **123**, 3229-3238.
48. T. M. Ovitt and G. W. Coates, *J. Am. Chem. Soc.*, 2002, **124**, 1316-1326.
49. C. J. Chuck, M. G. Davidson, G. G. du Sart, P. K. Ivanova-Mitseva, G. I. Kociok-Kohn and L. B. Manton, *Inorg. Chem.*, 2013, **52**, 10804-10811.

Chapter 4 – Tetrametallic titanium-oxo compounds

Abstract

The titanium-oxo compounds, with formula $Ti_4O_2L_4$ (presented in chapter 3), exhibited thermal stability under melt lactide polymerisation conditions. However, exposing these compounds to DMAP led to the formation of new titanium-oxo products, identified as linear $[Ti_4O_3L_4(H_2O)_2][DMAP{\cdot}H]_2$ and cyclic $[Ti_4O_4L_4][DMAP{\cdot}H]_4$ compounds. Altering the synthetic conditions of the reaction granted a degree of synthetic control over the product formed, with solvothermal conditions favouring the formation of cyclic titanium-oxo compounds. The cyclic $[Ti_4O_4L_4][DMAP{\cdot}H]_4$ species were found to be dynamic in solution under ambient conditions and undergo a ligand rearrangement process, which was contrasting to the stability of the linear $[Ti_4O_3L_4(H_2O)_2][DMAP{\cdot}H]_2$ analogues. Solution NMR spectroscopy and SCXRD studies revealed that solubilising the cyclic $[Ti_4O_4L_4][DMAP{\cdot}H]_4$ favoured the breaking of a strong Ti–O–Ti bridge to form the linear $[Ti_4O_3L_4(H_2O)_2][DMAP{\cdot}H]_2$ analogue.

4.1 Introduction

The titanium-oxo tetragonal disphenoids of general formula $Ti_4O_2L_4$, where L denotes the ligand, were presented in chapter 3 where they were initially applied in the ROP of *rac*-lactide under solution polymerisation conditions. As presented in chapter 3, the activity in solution of these pre-catalysts was low. The additives benzyl alcohol and DMAP were trialled in a bid to improve the activity of the $Ti_4O_2L_4$ pre-catalysts towards the ROP of *rac*-lactide, with DMAP effecting the greater increase in activity. A control experiment to check the stability of the titanium-oxo compounds in the presence of DMAP under the solution polymerisation conditions revealed the formation of new titanium compounds. With fluoro groups in the *R′* positions, compound **22** was used to probe the formation of new products with the more NMR sensitive ^{19}F nucleus from a test reaction of compound **22** with DMAP (1:1 titanium:DMAP ratio) in toluene stirring at room temperature for 2 h. The ^{19}F NMR spectrum of the crude reaction revealed a change from two sextets for **22** to twenty-four distinguishable fluorine environments in the reaction mixture, of which more could exist. As expected, this experiment unequivocally showed that new products had formed when **22** was stirred in the presence of DMAP. This synthetic lead was a starting point for expansion of the titanium-oxo bridged compounds.

4.2 Stepwise synthesis and solid-state characterisation

Mixing compound **18** with DMAP (1:1 titanium:DMAP ratio) in toluene at 130 °C (Figure 41) led to a solubilised mixture, which indicated a reaction had occurred since **18** was found to be largely insoluble in toluene at 130 °C. As expected, a ^{1}H NMR spectrum showed a dynamic mixture of several complexes had formed in which the broadening of the signals was noted. An EXSY NMR experiment showed cross-coupling peaks between signals associated with the structure and between several DMAP signals, indicating the species in the mixture displays dynamic behaviour.

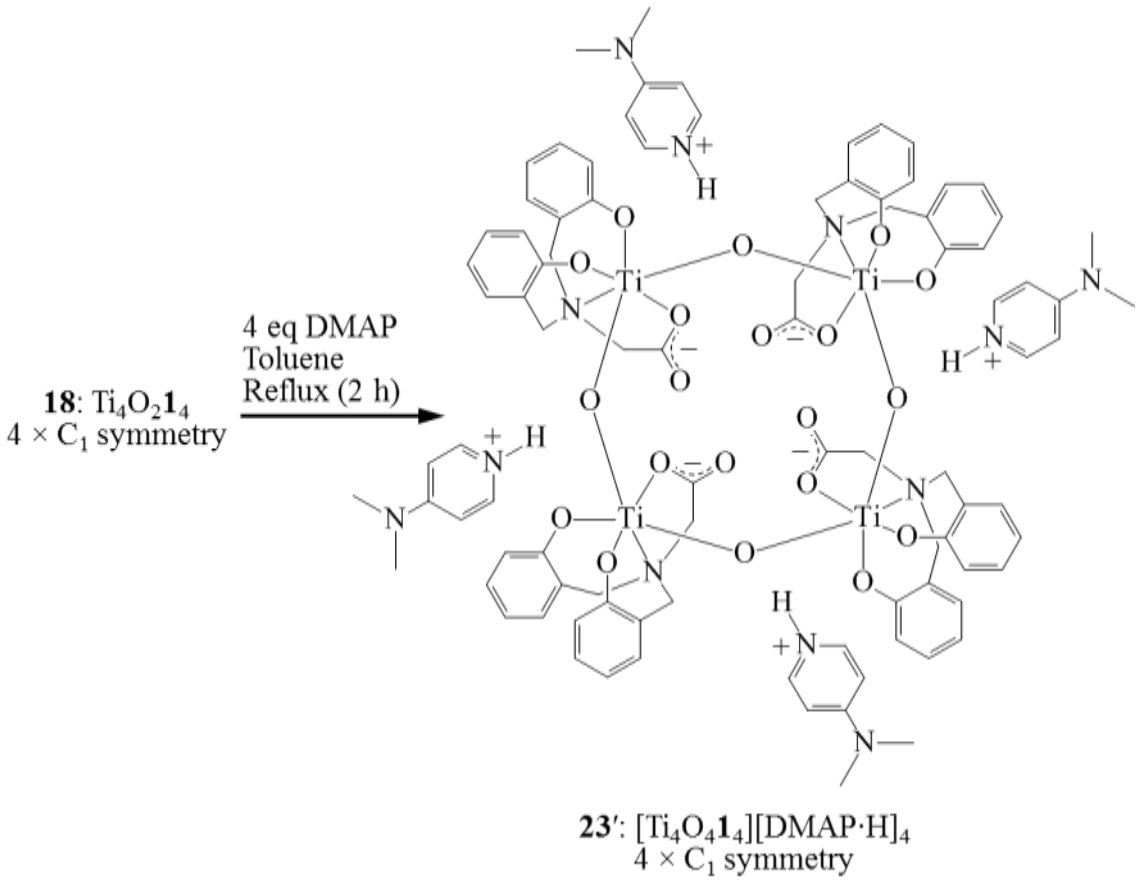

Figure 41. Scheme showing the reaction of **18** with DMAP in refluxing toluene gave an insoluble product, from which **23′** was identified.

Upon cooling, a yellow, amorphous solid accompanied by small, yellow crystals were formed. The crystals were collected and studied by SCXRD to reveal a cyclic tetrameric titanium-oxo compound **23′** had formed (Figure 42). Four DMAP·H^{+}, counter-ions are present in the crystal structure to give an overall formula of [Ti$_4$O$_4$**1**$_4$][DMAP·H]$_4$. The four titanium centres give a +16 charge while the four μ-oxo ligands and four **1** ligands contribute a −20 charge. The ligand-supported titanium-oxo

fragment has a residual −4 charge that is balanced by the four DMAP·H^+ counter-ions. These counter-ions intermolecularly hydrogen bond to the carboxylate arms through the N1AA–H1AA···O1 and N1AB–H1AC···O8 interactions, the former involving the carboxylate oxygen bound to the titanium centre and the latter featuring the unbound carboxylate oxygen. The DMAP·H^+ interaction to the non-bound oxygen experiences less steric interaction packing further away from $[Ti_4O_4\mathbf{1}_4]^{4-}$ fragment so the geometrical parameters for the intermolecular hydrogen bonding interaction are closer to idealised values, with a shorter H···A distance (2.692(7) Å versus 2.757(6) Å) and more linear D–H···A angle (177.9(6)° versus 161.1(3)°). In the case of the N1AA–H1AA···O1 interaction, the TiO–CO and TiOC–O bond distances of 1.296(3) Å and 1.219(4) Å agree with the standard C–O^- and C=O bond distances of 1.308(19) Å and 1.214(19) Å respectively,[3] indicating the C1–O1 bond has more single bond character. For the N1AB–H1AC···O8 interaction, the TiO–CO and TiOC–O bond distances of 1.283(4) Å and 1.245(4) Å show less agreement with the standard C–O and C=O bond distances, demonstrating the C–O bonds in this carboxylate moiety are delocalised. This coincides with the preference of the DMAP·H^+ intermolecular hydrogen bond towards the negative charges on bound oxygen O1 and unbound oxygen O8. Contrary to the indication of single bond character on bound oxygen O1, the mean Ti–OCO bond distance of 2.047(6) Å concurs with L-type donation from the carboxylate oxygen to the titanium centre, characterising ligand **1** as an L_2X_2-type donor in the structure of **23′** (see Appendix). It was noted the four **1** ligands remained in a C_1 symmetric binding mode as seen in the source of titanium in the reaction, compound **18**.

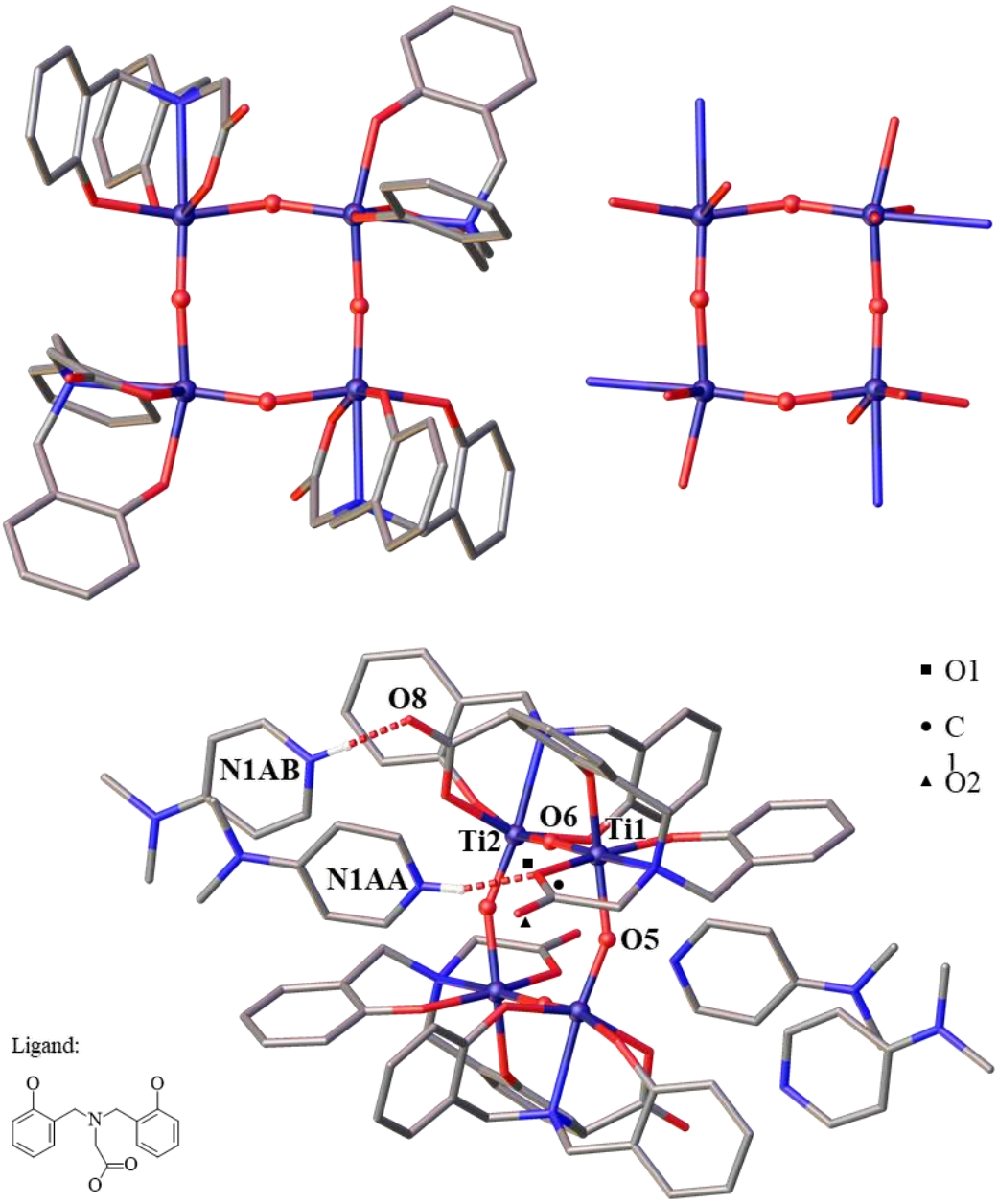

Figure 42. Top left: Crystal structure of **23′** grown from the asymmetric unit; Top right: view of the coordination spheres of the titanium centres in **23′**. A unit of **23′** in the asymmetric unit as well as four DMAP·H^+ counter-ions were omitted for clarity. Bottom: crystal structure of **23′** with selected atom labels. Titanium-oxo core is shown as spheres and ligand framework displayed as tubes. Solvent of crystallisation and hydrogen atoms omitted for clarity. Ti = purple; C = grey; N = blue; O = red.

Inspection of the bond distances in the $[Ti_2O_2\mathbf{1}_2]^{2-}$ in the asymmetric unit of **23′** revealed the bonding about Ti1 and Ti2 is asymmetric (Table 8). The parameters for the Ti_4O_4 core and the titanium-phenolate bonds show significant deviation. This was attributed to the difference in *trans*-influence of the donors *trans*- to the oxo ligands. For Ti1, a phenolate donor is *trans*- with regards to the oxo ligand O5 while for Ti2, the

tertiary nitrogen donor is *trans*- to the oxo ligand O5. The weaker *trans*-influence of the nitrogen donor, in comparison to the phenolate, allows the oxo ligand to draw electron density from the Ti2–N2 bond, resulting in a shortening of the Ti2–O5 bond in comparison to Ti1–O5.

Parameter	Mean1	Mean2	Deviation	Deviation %
Ti–O	1.750(5)	1.915(6)	0.082	4.5
Ti–OPh	1.893(5)	1.989(6)	0.048	2.5
Ti–OCO	2.039(6)	2.054(6)	0.007	0.4

Table 8. Selected bond lengths (Å) and angles (°) in the crystal structure of **23′**, highlighting differences between the bond distances when a phenolate is *cis*- (Mean1) or *trans*- (Mean2) to the Ti–O–Ti bridge.

A key difference between **18** and **23′** arose when assigning oxidation states to the individual donating atoms on the ligand. This analysis revealed that the ligand had changed its donation type from LX_3 in the source to L_2X_2 type donation, whereby the ambidentate carboxylate arm allows the ligand to change donor type. This change in ligand donation type allowed the titanium centre to conserve an overall charge of +4 while accommodating the extra negative charge of an additional bridging oxo ligand. Unfortunately, **23′** could only be isolated as a small quantity of crystalline mixed with amorphous solids from the crude mixture and the compound could not be further analysed.

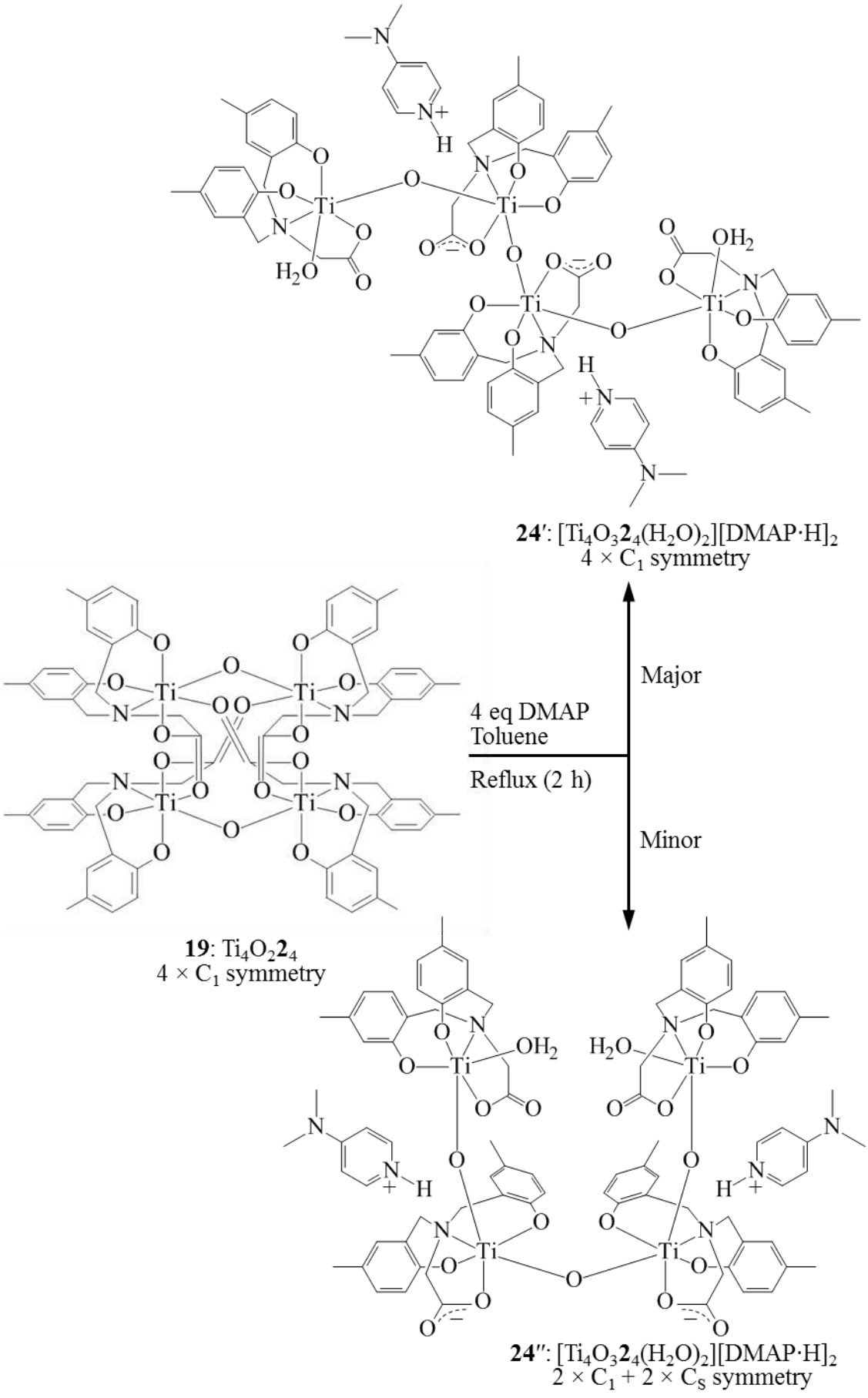

Figure 43. Major product **24′** and minor product **24″** from the reaction of **19** with DMAP in refluxing toluene.

Under the same reaction conditions (Figure 43), compound **19** also formed yellow crystals. A SCXRD study of this batch of crystals revealed two structures for a linear tetrametallic titanium-oxo species, compound **24** with structural formula $[Ti_4O_3\mathbf{2}_4(H_2O)_2][DMAP{\cdot}H^+]_2$ (Figure 44 and Figure 45). This type of linear titanium-oxo Ti_4O_3 core has not previously been reported in the literature. The structure is composed of four titanium centres, each supported by one **2** ligand. Two types of titanium centres exist: two terminal centres, bound by a single bridging oxo ligand and terminated by an aqua ligand, and two internal titanium centres bound by two bridging oxo ligands. The terminal aqua ligands were confirmed by agreement between the mean Ti–OH_2 bond distances of 2.045(4) Å and the mean reported Ti–OH_2 bond distance of 2.086(70) Å from the Cambridge Structural Database (CSD), which confirmed the Ti–OH_2 interactions in **24′** and **24″** would have to be 9 % shorter to be comparable to a Ti–OH bond (see Appendix).

Similarities can be drawn between structural isomers **24′** and **24″**. Firstly, they share the same structural formula. Secondly, the terminal titanium centres in the structures are terminated by aqua ligands. Thirdly, both structures incorporate two $DMAP{\cdot}H^+$ counter-ions hydrogen bonding to the carboxylate arms of the internal titanium centres, acting to balance the residual negative charge on these carboxylates. This structural feature is similar to what was observed in the structure of **23′** where the carboxylate donors have switched from X-type donation to L-type donation to stabilise the addition of additional oxo bridging ligands. Overall, both structures **24′** and **24″** are stabilised by four units of ligand **2**, of which the terminal ligands are involved in LX_3 type donation while the internal ligands employ L_2X_2 type donation to accommodate the newly formed oxo bridges. This was observed by the mean Ti–OCO bond lengths of 2.009(3) Å and 2.035(5) Å for **24′** and **24″** respectively, which agree with the mean distance of 2.063(99) Å for L-type Ti–O interactions as opposed to the shorter X-type Ti–O interactions with a mean distance of 1.850(84) (see Appendix).

Analysis of the bond parameters revealed interesting features about the charge distribution across the carboxylate moieties in **24′** and **24″**. The TiO–CO mean bond lengths of 1.308(5) Å and 1.296(10) Å are significantly different to the mean TiOC–O bond lengths of 1.214(5) Å and 1.228(9) Å, with the TiO–CO bond being comparable to the standard C–O bond length in carboxylic acids of 1.308(19) Å while the TiOC–O bond matches the C=O standard bond length of 1.214(19) Å.[3] This revealed the carboxylate moieties experience a localised negative charge on the oxygen bound to the titanium. In

particular, the DMAP·H$^+$ counter-ions participate in compound **24′** intermolecular hydrogen bonding to the bound carboxylate oxygens of the internal ligands, with H···Acceptor and Donor···Acceptor distances of 1.97(8) Å and 2.812(7) Å respectively in agreement with typical values for these parameters.[4] Closer inspection of the carboxylate bond lengths in **24″** show the TiO–CO and TiOC–O bond interactions for the internal ligands deviate towards a delocalised COO$^-$ system, exemplified by the DMAP·H$^+$ intermolecular hydrogen bonds to the unbound carboxylate oxygens with mean H···Acceptor and Donor···Acceptor distances of 2.182(6) Å and 3.049(10) Å respectively.[4]

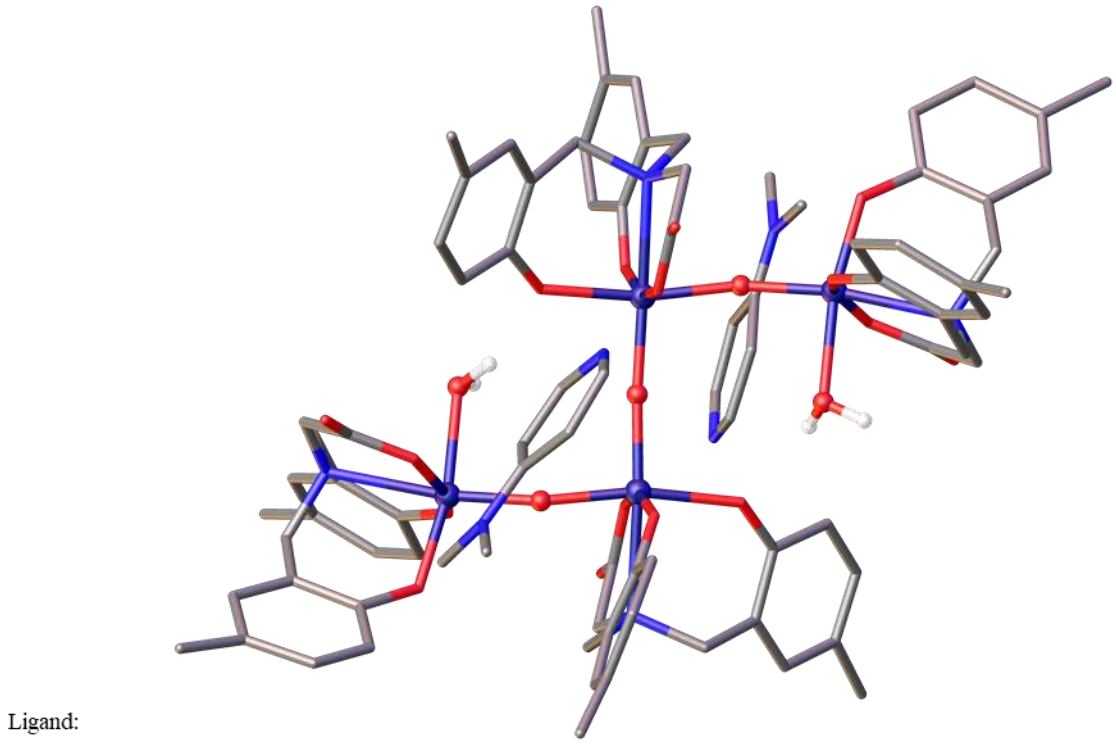

Figure 44. Crystal structure of **24′** grown from the asymmetric unit. Titanium-oxo core and aqua ligands are shown as spheres and ligand framework and DMAP·H$^+$ displayed as tubes. Solvent of crystallisation and hydrogen atoms omitted for clarity except in the case of aqua ligands. Ti = purple; C = grey; N = blue; O = red.

Furthermore, the Ti–O bonds about the Ti_4O_3 core between terminal and internal units in **24′** and **24″** are asymmetrical with mean distances of 1.784(4) and 1.859(4) for Ti1–O5 and Ti1–O6, which is contrasting with the more symmetrical Ti–O bonds found between internal units with a mean distance of 1.821(6) Å. The asymmetry of the

Ti–O–Ti bridge between terminal and internal units can be explained by the difference in *trans*-influence between the groups *trans*- to the Ti–O–Ti bridge, whereby the stronger *trans*-influence of the phenolate in the terminal unit leads to a longer Ti–O bond.

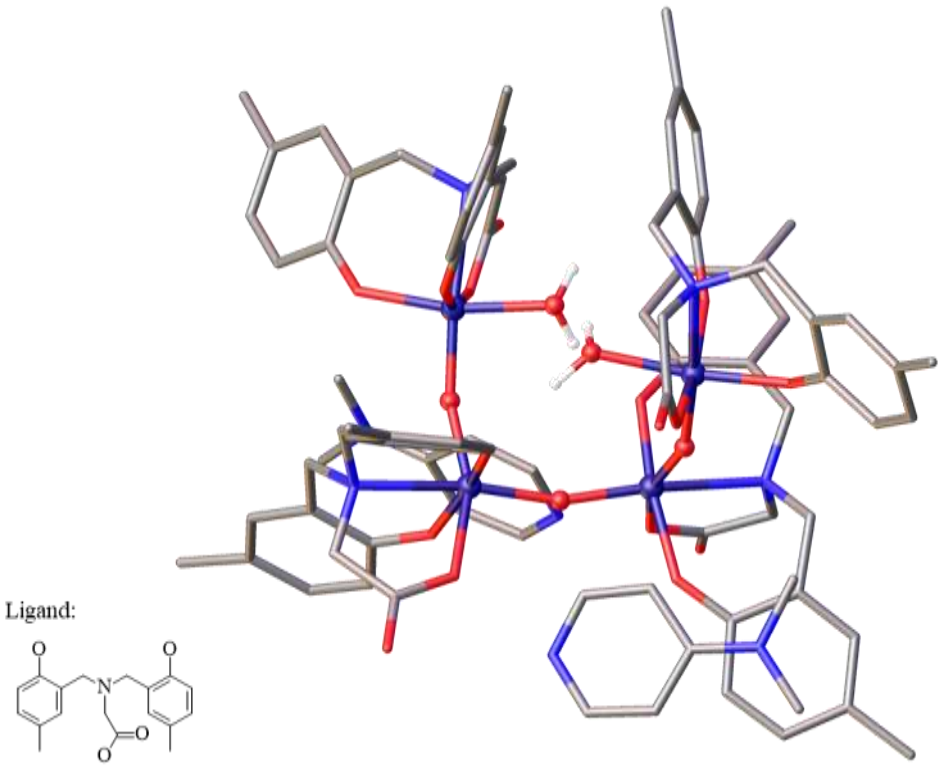

Figure 45. Asymmetric unit of **24″**. Titanium-oxo core and aqua ligands are shown as spheres and ligand framework and DMAP·H+ displayed as tubes. Solvent of crystallisation and hydrogen atoms omitted for clarity except in the case of aqua ligands. Ti = purple; C = grey; N = blue; O = red.

4.2.1 Ligand binding modes

Despite these structural similarities, compounds **24′** and **24″** share significant differences that prevent them to be classed as isostructural. Visually, an immediate dissimilarity arises from the two crystal structures, with **24′** showing an unfolded motif of the linear Ti_4O_3 core while **24″** exhibits a folded linear Ti_4O_3 core. The unfolded Ti_4O_3 core of **24′** is planar, displaying a small RMSD of 0.095 Å and eclipsing Ti1–Ti2–Ti3–Ti4 torsion angle of 180° (due to symmetry from inversion centre at special position of O10), while the folded Ti_4O_3 core of **24″** shows a larger RMSD of 0.562 Å and staggered Ti1–Ti2–Ti3–Ti4 torsion angle of 61.68(4)°. Upon further inspection, it became apparent that the ligand binding modes were different between the structures of **24′** and **24″** where the configuration differs according to the phenolate groups binding to

the titanium centre in a *cis*- or *trans*-configuration, resulting in C_1 or C_S symmetry at the metal centre (Figure 46).[5-7]

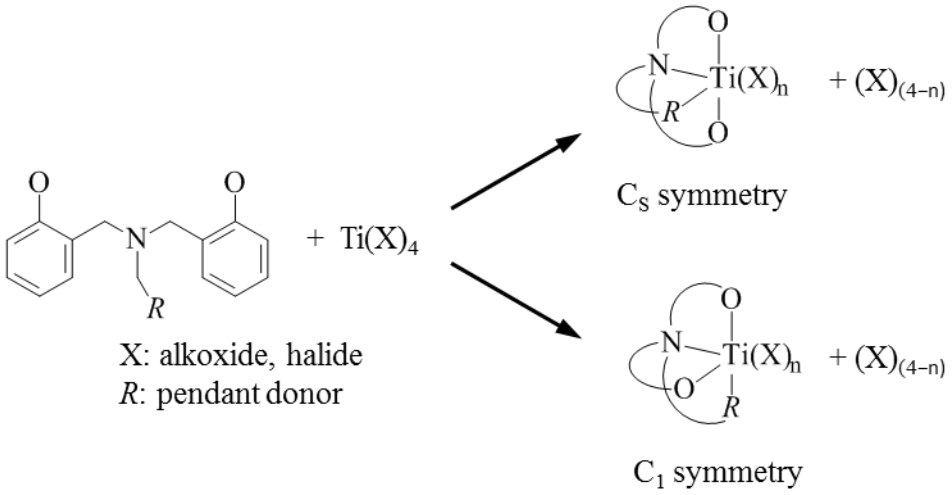

Figure 46. Schematic representation of the C_S or C_1 symmetric binding mode that can be adopted by an amine bis(phenolate) ligand when bound to a titanium centre.

In the case of the unfolded structure **24′**, the titanium centre symmetry observed is 4 × C_1 symmetry whereas the folded structure **24″** displays mixed 2 × C_1 and 2 × C_S symmetries at the terminal and internal titanium centres respectively. Since the source of titanium, the titanium-oxo tetragonal disphenoid **19**, displays all four ligands in the C_1 binding mode, a ligand rearrangement process is occurring under the reaction conditions. The ligand rearrangement observed in these systems was surprising as amine bis(phenolate) ligands are regarded as strongly-bound, chelating ligands that support the metal centre.[8-12] Therefore, under relatively benign conditions, we observed a ligand rearrangement process taking place. This has major implications for catalysis, in particular in chiral systems where this rearrangement would result in loss of chirality. In light of these results, these catalytic studies may need to be re-evaluated to ascertain the active species.[5-7]

4.2.2 Assembly of tetrametallic species

The fact that the two internal titanium centres display the ligand rearrangement process gives insight into the mechanism by which the **19** converts to **24′** and **24″**. We noted the original monomeric fragment of **19** with 2 × C_1 symmetry could not be superimposed on neither the terminal-internal nor internal-internal titanium fragments in **24″** (Figure 47). We propose two conceivable processes to accommodate the ligand rearrangement required for the formation of **24″** from **19**. First (Figure 47, Mechanism

A), the stepwise construction of **24″** could be directed by monometallic fragments that dissociate from the original Ti_2OL_2 fragments of **19** and subsequently undergo a ligand rearrangement (C_1 to C_S). Second (Figure 47, Mechanism B), the original Ti_2OL_2 fragment remains intact while ligand rearrangement occurs on the ligands without breaking of the Ti–O–Ti bridge. These two rearrangement processes would allow the formation of **24″** from **19** with the necessary change in symmetry. The ligand rearrangement illustrates the extent of the dynamic processes that are present in solution for the assembly of tetrametallic titanium-oxo species.

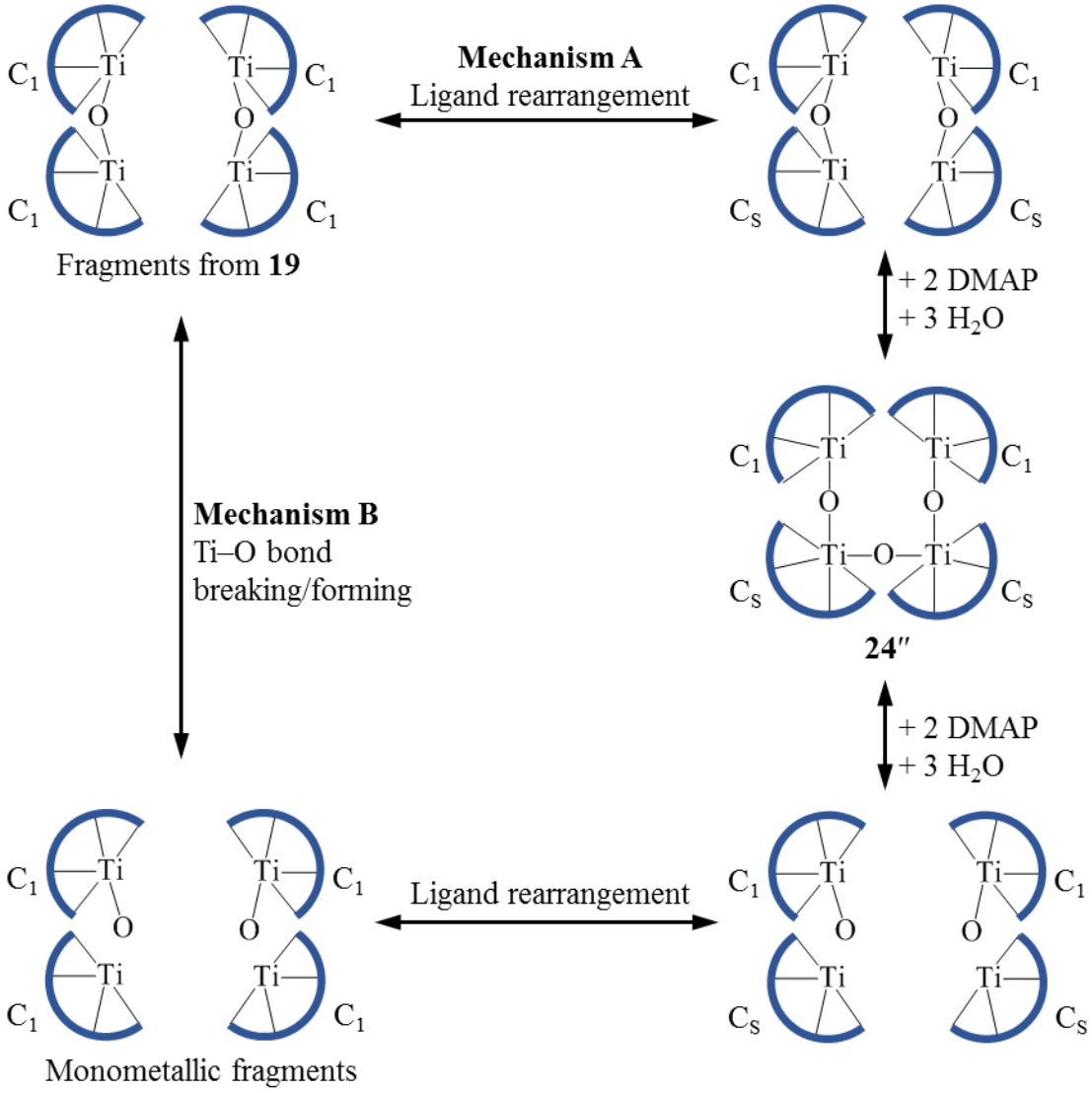

Figure 47. Schematic illustrating the symmetry mismatch between fragments of **19** and **24″**, demonstrating a ligand arrangement must occur during the reaction. The multidentate ligand, **2**, is denoted by a dark blue arc.

Altering the *R′* group on the source of titanium (i.e. utilising complexes **18** or **19**) in the above reactions resulted in different crystalline products: the cyclic, tetrameric

titanium-oxo compound **23′** and the linear, tetrametallic titanium-oxo compounds **24′** and **24″**. It could be anticipated that the loss of an aqua ligand followed by deprotonation of the remaining aqua ligand by two DMAPs to form an oxo ligand would lead to cyclisation of the compound (Figure 48). This would yield an analogous cyclic tetrameric titanium-oxo structure to **23′** but this is not observed in the case of **24′** and **24″**. The only variable between the two systems is the change in the *R′* group from proton to methyl, which results in an increase in steric bulk and a positive, inductive electronic effect to the phenolate donors. Therefore, we can attribute the change in product formed to a steric/electronic effect caused by the addition methyl groups in the *R′* positions.

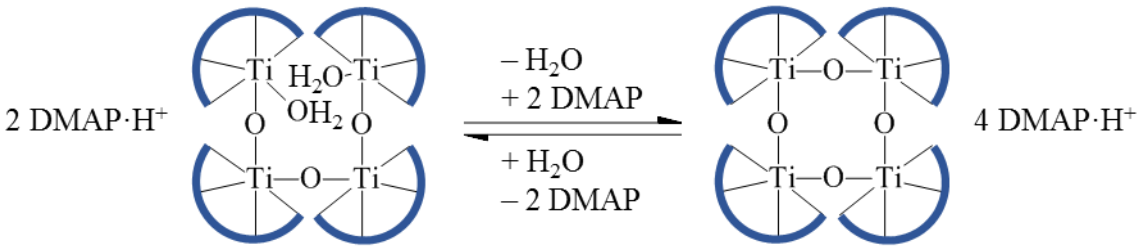

Figure 48. Schematic illustrating the cyclisation (forward arrow) and ring-opening (backward arrow) of linear and cyclic tetrametallic species. The multidentate ligand, **2**, is denoted by a dark blue arc.

At this stage in the discussion, it is worth noting that the reactions of **20** and **21** with DMAP in refluxing toluene were probed by ^{1}H NMR spectroscopy. The spectra of the crude mixtures showed a reaction had occurred in the case of **20** but no reaction had occurred when **21** was used. This indicated the bulky *tert*-butyl group in the *R″* position prevents reaction under these conditions. It is proposed that the steric and slight electron-donating effects of *tert*-butyl groups stabilise **21** in the presence of DMAP, pushing the activation energy needed for reaction of the Ti–O–Ti bridges above that of the reaction conditions. In a bid to overcome this barrier and disrupt the Ti–O–Ti bridges, a mixture of **21** and DMAP (1:1 titanium:DMAP ratio) was subjected to the solvothermal conditions shown in Figure 49. The ^{1}H NMR spectrum of the crude mixture showed a reaction had occurred. The more forcing solvothermal reaction conditions enabled a reaction to take place, justifying this synthetic method as an alternative to provide more energy to the systems studied here. However, isolation and identifying of pure compounds from the reaction mixture was unsuccessful.

4.3 Solvothermal synthesis and solid-state characterisation

By considering the linear, tetranuclear titanium-oxo compounds **24′** and **24″** as a precursor to a cyclic structure, we proposed that reflux in toluene did not provide enough energy (or sufficient time) for the system to cyclise. Also, the anticipated high energy barrier for ligand rearrangement associated with the source of titanium used could be slowing or preventing cyclisation. For these reasons, we thought solvothermal conditions starting from monometallic fragments of titanium would be particularly suited for the synthesis of cyclic tetrameric titanium-oxo structures analogous to **23′**. A 1:1 titanium:DMAP ratio was used to stabilise the L_2X_2 type donation seen in compounds **23′** and **24** as well as the construction process observed under the previous reaction conditions. The reaction conditions used are summarised in Figure 49. Searching the literature revealed that solvothermal conditions had been successfully used to synthesise cyclic tetrameric titanium-oxo cores.[13-17] In particular, one method conducted in the presence of water noted the temperature limit of 120 °C as this helped to prevent the formation of titanium dioxide from reaction of water with titanium propoxide.[13]

A one-pot solvothermal synthesis starting from the ligand precursor was sought to increase the yields of the titanium-oxo compounds. Three principles were incorporated into the design of the reaction conditions. First, solvothermal conditions should be used as they were previously found to lead to expansion of Ti–O–Ti bridges. Second, DMAP was seen as a key additive due to its basicity and ability to act as a counter-ion. Third, the change in ligand binding mode, from the source of titanium to the final product, was suggestive that monometallic units were involved in the assembly of the linear and cyclic tetrametallic titanium-oxo compounds. A one-pot synthesis starting from the ligand precursor, titanium propoxide and DMAP under solvothermal conditions (120 °C, 72 h) was proposed to be a suitable pathway to access cyclic analogues **24′** and **24″**. Titanium propoxide was used due to the higher boiling point of propanol in comparison to isopropanol, which would limit the pressure generated in the vessel. The reaction conditions are summarised in Figure 49.

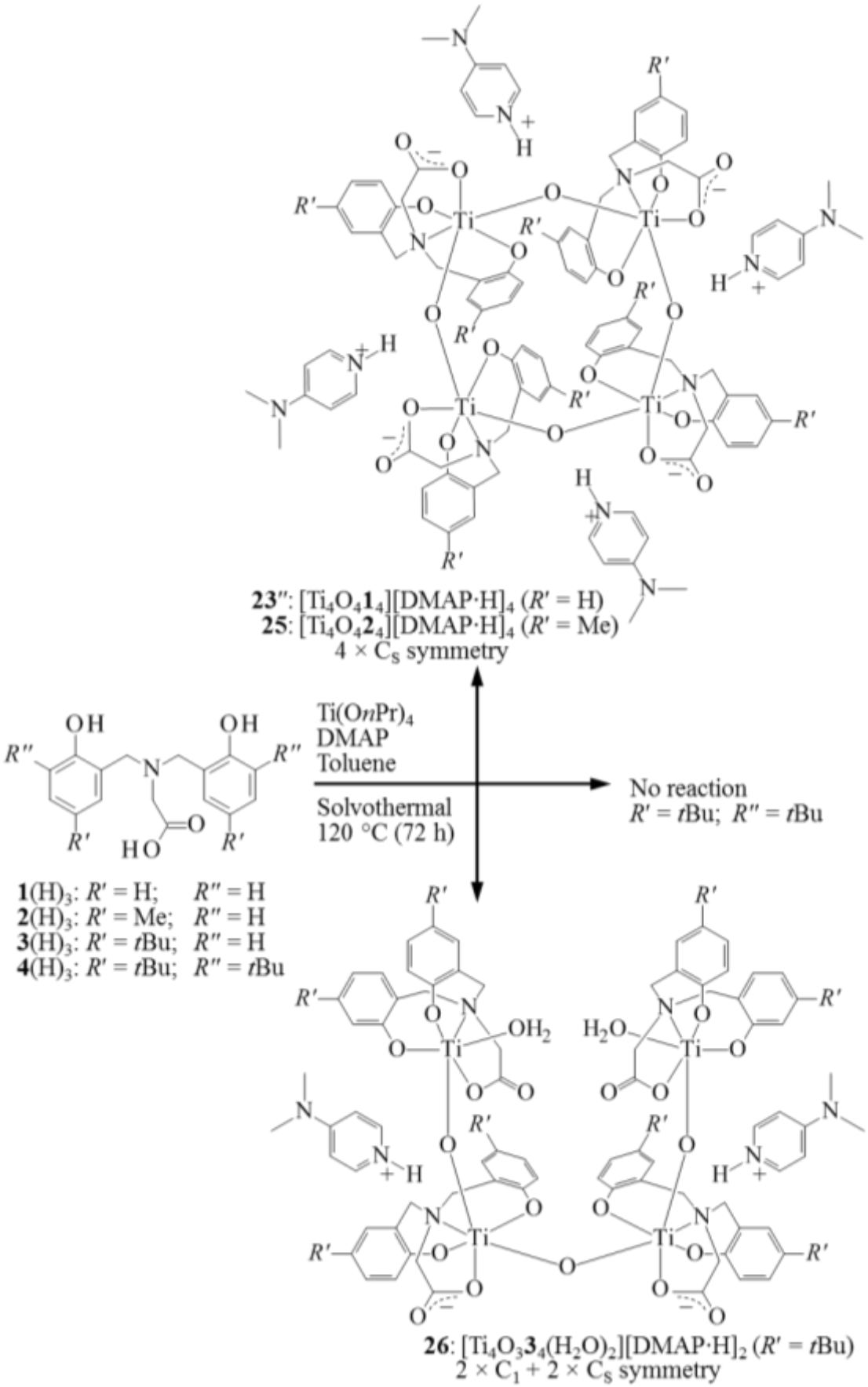

Figure 49. Reactivity of compounds **1**-**4**$(H)_3$ under solvothermal reaction conditions, leading to compounds **23″**, **25** and **26**.

In a similar fashion to the mixtures obtained under reflux, complex mixtures obtained from the solvothermal synthesis showed dynamic behaviour, demonstrated by the broadening of the DMAP signals in the ^{1}H NMR spectrum and the presence of exchange signals demonstrated by an EXSY NMR experiment. The dynamic nature of these mixtures makes their purification and characterisation more challenging in comparison to classical ligand-supported titanium species. As a result, it is not possible to unambiguously characterise these dynamic mixtures using ^{1}H NMR alone. Therefore, the purification of these species relied on fractional crystallisation techniques from which crystalline samples can be characterised by SCXRD.

Using these solvothermal conditions, two cyclic tetrameric titanium-oxo compounds **23**″ and **25** were identified by SCXRD (Figure 50 and Figure 51). From the reaction with **1**(H)$_3$, the Teflon vessel was opened to reveal pale yellow crystals of **23**″ directly from the reaction mixture. The SCXRD study of this crystal sample presented us with the structure of **23**″. In the case of **25**, the methyl groups in the *R*′ position increased the solubility of the compound and these were crystallised by slow evaporation of the reaction mixture.

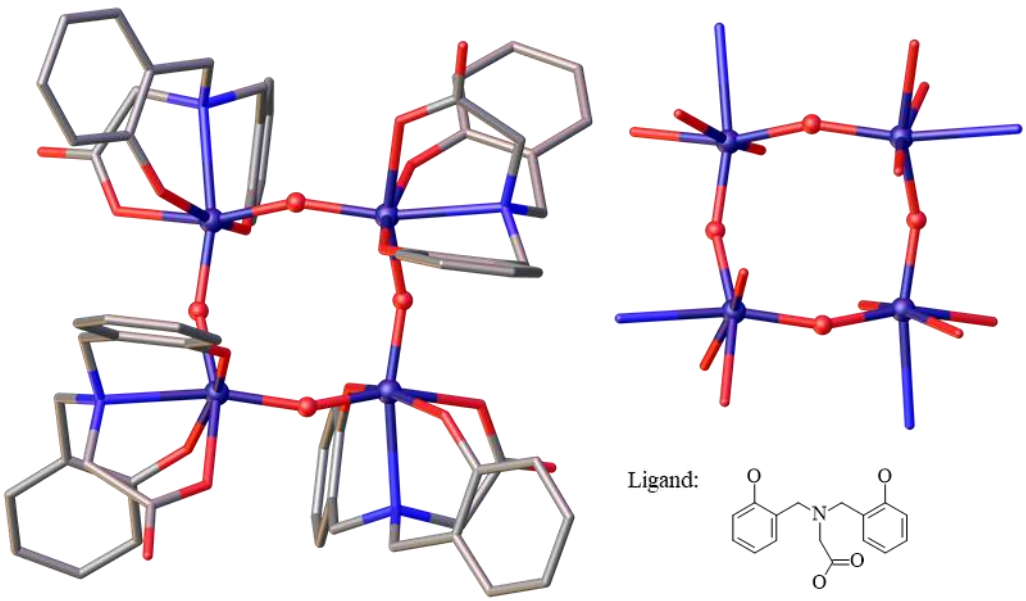

Figure 50. Left: Crystal structure of **23**″ grown from the asymmetric unit; Right: view of the coordination spheres of the titanium centres in **23**″. A unit of **23**″ in the asymmetric unit as well as four DMAP·H^{+} counter-ions were omitted for clarity. Titanium-oxo core is shown as spheres and ligand framework displayed as tubes. Solvent of crystallisation and hydrogen atoms omitted for clarity. Ti = purple; C = grey; N = blue; O = red.

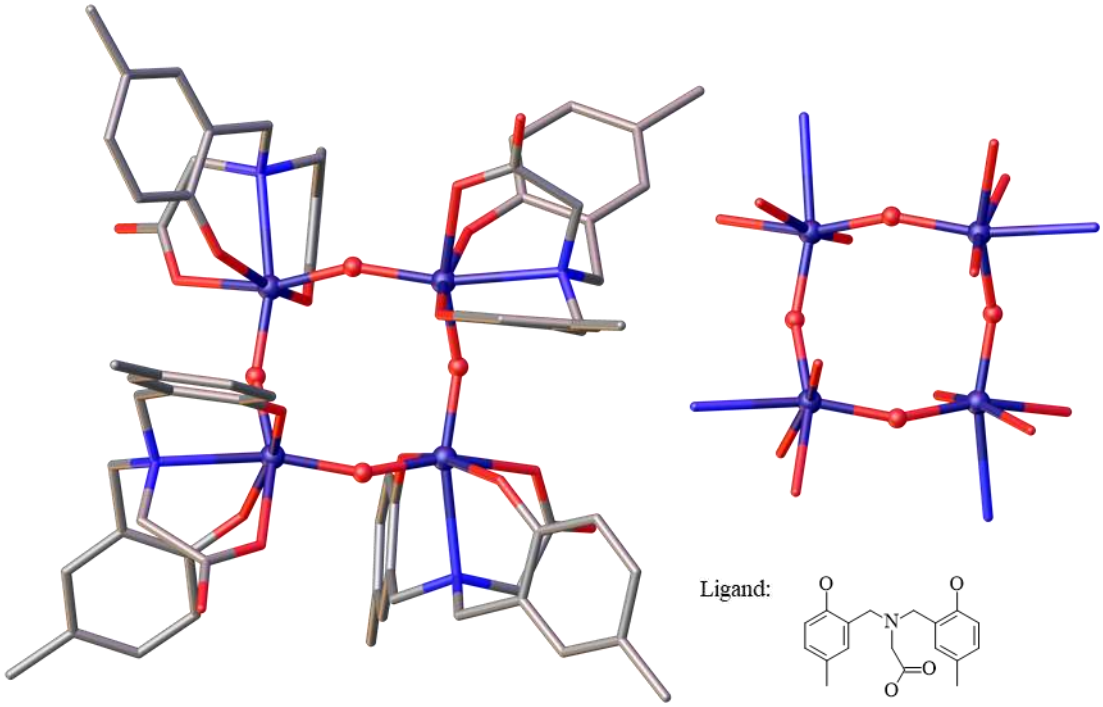

Figure 51. Left: Crystal structure of **25** grown from the asymmetric unit; Right: view of the coordination spheres of the titanium centres in **25**. Four DMAP·H^+ counter-ions were omitted for clarity. Titanium-oxo core is shown as spheres and ligand framework displayed as tubes. Solvent of crystallisation and hydrogen atoms omitted for clarity. Ti = purple; C = grey; N = blue; O = red.

Analysis of the SCXRD data for **23″** and **25** revealed the $[Ti_4O_4L_4]^{4-}$ units in these compounds are isostructural, with low deviation between selected geometrical parameters in both structures (Table 9). The geometrical parameters for the carboxylate geometrical parameters reveal structural features of **23″** and **25**: the mean TiO–CO and TiOC–O bond lengths of the carboxylate moieties of **23″** and **25** are 1.290(3) Å and 1.226(3) Å respectively are significantly different and demonstrate the carboxylate donors in these structures are not fully delocalised. The TiOC–O bond length of 1.226(3) Å shows better agreements with the standard carboxylate C=O bond distance of 1.214(19) Å whereas the TiO–CO bond length of 1.290(3) Å was found to be similar to the standard C–O bond distance of 1.308(19) Å.[3] This data reveals that the carboxylate C–O bond of the oxygen bound to the titanium centre has the most single bond character. Indeed, the DMAP·H^+ counter-ions show intermolecular hydrogen bonding to the carboxylate oxygens bound to the titanium centres, with mean H···A and D···A distances of 1.826(4) and Å 2.735(7) Å respectively.[4] These DMAP·H^+ counter-ions are positioned about the $[Ti_4O_4L_4]^{4-}$ unit to maximise intermolecular interactions with the phenolate rings through

π-π and CH-π interactions, with mean distances of 3.507(6) Å and 2.802(6) Å for **23**″ and 3.519(11) Å and 2.646(9) Å for **25**.

Parameter	Mean	Deviation	Deviation %
Ti–O	1.813(5)	0.010	0.53
Ti–O–Ti	151.6(10)	0.239	0.16
O–Ti–O	105.4(12)	0.039	0.04
Ti–OPh	1.930(5)	0.004	0.23
Ti–OCO	2.119(6)	0.011	0.53
TiO–CO	1.290(3)	0.005	0.41
TiOC–O	1.226(3)	0.006	0.53
Ti_4O_4 plane RMSD	0.422	0.006	1.36

Table 9. Means and deviations of selected geometrical parameters, bond lengths (Å) and angles (°) for compounds **23**″ and **25**.

We noted that the core conformation found in the structure of **23**″ was different to the core conformation found previously for **23**′. Figure 52 shows the cyclic 8-membered titanium-oxo cores of **23**′ and **23**″ are in the boat-chair and boat-boat conformations respectively. Additionally, the ligand binding modes are different between the two compounds, with **23**′ held by ligands with 4 × C_1 binding mode and **23**″ held by ligands with 4 × C_S symmetry. In the case of **23**′, the difference in *trans*-influence of the donors *trans*- to the oxo bridge resulted in an asymmetrical Ti_4O_4 core adopting a boat-chair conformation. The *trans*-influence of the donors *trans*- to the oxo bridges in **23**″ are more similar (C=O–Ti and N–Ti L-type interactions), resulting in a more symmetrical Ti_4O_4 core adopting a boat-boat conformation. The same observations are made with compound **25** (Table 10), analogous to **23**″, which also displays 4 × C_S symmetry and suggests that solvothermal conditions can drive the ligand to bind in C_S symmetry. However, the slightly stronger *trans*-influence of the C=O–Ti interaction in **25** results in a more pronounced *trans*-effect on one Ti–O bond and its subsequent lengthening is apparent by comparison of the bond distances (1.797(7) Å vs 1.845(7) Å, Table 10). The space group symmetry $P\bar{4}$ of structure **23**″ leads to an internal S_4 symmetry element to be applied around the asymmetric unit [TiO**1**][DMAP·H], growing to $[Ti_4O_4\mathbf{1}_4][DMAP{\cdot}H]_4$. This masks the slight deviations on the Ti_4O_4 core imparted by different *trans*-influence of the donor atoms about the titanium centres in **23**″. Structure **25** was solved in space group $P\bar{1}$ resulting in an asymmetric unit of $[Ti_4O_4\mathbf{2}_4][DMAP{\cdot}H]_4$ which revealed the deviations on the Ti_4O_4 core imparted by different *trans*-influence of the donor atoms about the titanium centres. These deviations in **25** are not translated to the Ti–O–Ti and O–Ti–O angles and we propose that the weaker *trans*-influence causes less geometrical strain on the Ti_4O_4,

explaining how **23″** can crystallise in an S_4 symmetric space group to mitigate these minor deviations.

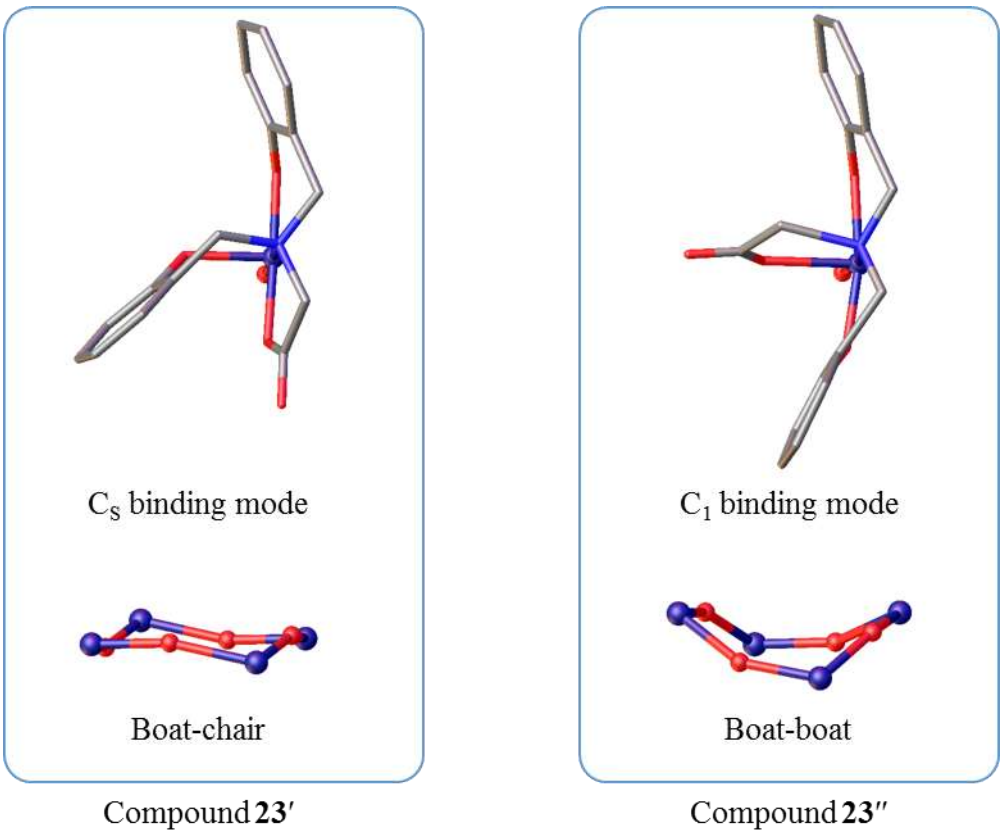

Figure 52. Ligand binding modes and core conformations in the SCXRD structures of **23′** (left) and **23″** (right). Ligand binding modes are illustrated by a monomeric unit [TiO**1**]$^{-}$ from the tetrameric structure $[Ti_4O_4]^{4-}$. Ti = purple; C = grey; N = blue; O = red.

Parameter	Mean1	Mean2	Deviation	Deviation %
Ti–O	1.797(7)	1.845(7)	0.026	1.4
Ti–O–Ti	150.5(13)	152.2(13)	0.8	0.5
O–Ti–O	105.6(20)	105.3(20)	0.2	0.2

Table 10. Means and deviations of selected bond lengths (Å) and angles (°) for compound **25**, illustrating slight deviations about the core geometry when a phenolate is *cis*- (Mean1) or *trans*- (Mean2) to the Ti–O–Ti bridge.

Linear or cyclic tetrametallic systems supported by ligand **2** could be accessed by either a stepwise reaction (toluene, heated to reflux for 2 h) or one-pot solvothermal reaction (toluene, 120 °C for 72 h). To rule out the possibility that the difference in source of titanium could be the cause for the isolation of linear or cyclic products, a test reaction

using compound **2**$(H)_3$, titanium propoxide and DMAP was dissolved in toluene and heated to reflux for 2 h. This resulted in the formation of the linear tetrametallic titanium-oxo compound **24′**, confirming that the linear Ti_4O_3 core was preferentially formed under these conditions while solvothermal conditions could force cyclisation to the Ti_4O_4 core. Also, this revealed the possibility that the stepwise method could be translated to a one-pot procedure with the formation of the Ti_4O_2**2**$_4$ precursor *in situ*. Nevertheless, the cleanest method for obtaining a crystalline product, with no amorphous deposit, remained the stepwise route initially employed.

4.3.1 Effect of steric bulk

In the case of the solvothermal reaction of **20** with DMAP, the linear tetrametallic titanium-oxo compound **26** was crystallised in low yield, only allowing for SCXRD analysis (Figure 53). This compound is isostructural with **24″** excluding the difference in *R′* group, demonstrated by the low deviation between geometrical parameters (Table 11), displaying the same folded linear Ti_4O_3 core with mixed 2 × C_1 and 2 × C_S symmetry. The cyclic, tetrameric analogues of **23″** and **25**, supported by ligand **3**, was not isolated despite the use of more forcing solvothermal conditions (120 °C, 24 h; then 180 °C, 12 h). Similarly, the structure of **21** was repeatedly isolated by fractional crystallisation from the reaction mixture when ligand **4** was used, further indication that the formation of tetrametallic titanium-oxo species was disfavoured when using ligand **4**. More forcing solvothermal conditions (120 °C, 24 h; then 180 °C, 12 h) also led to the isolation of **21**. As demonstrated in chapter 3, these titanium-oxo tetragonal disphenoids are thermally-stable species therefore this is not particularly surprising. As a final point, the crude ^{1}H NMR from the reaction revealed that **21** formed part of the mixture during the reaction. There was no reaction when **21** and DMAP were heated to reflux in toluene in a sealed flask for 2 h. This demonstrates that solvothermal conditions can force compounds to react by providing sufficient energy over prolonged periods of time to overcome greater activation energy barriers.

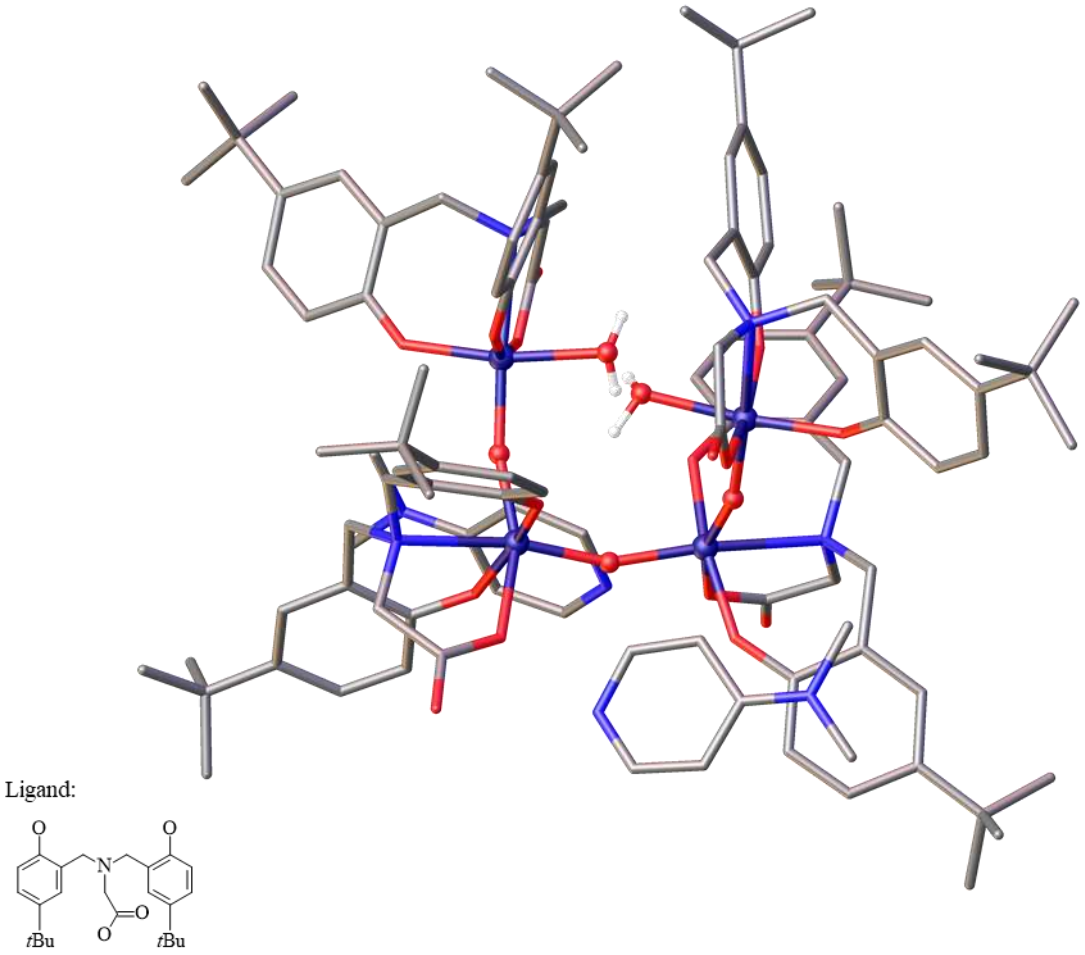

Figure 53. Crystal structure of **26** grown from the asymmetric unit. Titanium-oxo core and aqua ligands are shown as spheres and ligand framework and DMAP·H^+ displayed as tubes. Solvent of crystallisation and hydrogen atoms omitted for clarity except in the case of aqua ligands. Ti = purple; C = grey; N = blue; O = red.

Parameter	Mean	Deviation	Deviation %
Ti–O	1.821(4)	0.000	0.01
Ti–O–Ti	155.2(3)	0.600	0.39
Ti–OPh	1.905(4)	0.005	0.26
Ti–OCO	2.048(4)	0.013	0.64
TiO–CO	1.288(8)	0.008	0.58
TiOC–O	1.232(7)	0.004	0.37
Ti–OH_2	1.994(4)	0.006	0.28
Ti_4O_3 plane	0.555	0.008	1.35
Ti1–Ti2–Ti3–Ti4	60.26(4)	1.42	2.35

Table 11. Means and deviations of selected geometrical parameters, bond lengths (Å) and angles (°) for isostructural compounds **24″** and **26**.

Using the crystal structure of **25**, models of the analogous cyclic structures bound by ligand **3** or ligand **4** were constructed by addition of idealised, computed *tert*-butyl fragments to the *R′*/*R″* positions using Olex2 software.[18] As **23″** and **25** were found to be isostructural, it could be suggested that these could be used as base models to study the effect of steric bulk in the *R′*/*R″* positions. Using these calculated space-filling models allowed us to estimate the steric effects these ligands would have on the assembly of a $[Ti_4O_4L_4][DMAP{\cdot}H]_4$ (Figure 54 and Figure 55). Inspecting the model of $[Ti_4O_4\mathbf{4}_4][DMAP{\cdot}H]_4$ (Figure 55) shows the *tert*-butyl groups in the *R″* positions prevent cyclisation by a steric clash of ligands on adjacent titanium centres. This coincides with the lack of reactivity when using **21** under stepwise conditions and the inability to form tetrametallic titanium-oxo compounds under solvothermal conditions when using ligand **4**. A further steric clash between the *tert*-butyl groups in the *R′* and *R″* positions and $DMAP{\cdot}H^+$ counter-ions would disrupt the intermolecular hydrogen bonding stabilising the residual negative charge on the carboxylate moieties in the formation of a cyclic Ti_4O_4 core with ligand **3** or ligand **4**. This would explain why a cyclic Ti_4O_4 core with ligand **3** was not observed although it could be envisaged the $DMAP{\cdot}H^+$ counter-ion could move to a position with less steric interaction. What is certain is this interaction would prevent the $DMAP{\cdot}H^+$ counter-ions from packing in a position that is most favourable to form the intermolecular hydrogen bonding to the carboxylate moieties and by destabilisation of this interaction could preclude the formation of the cyclic $[Ti_4O_4\mathbf{3}_4][DMAP{\cdot}H]_4$ compound.

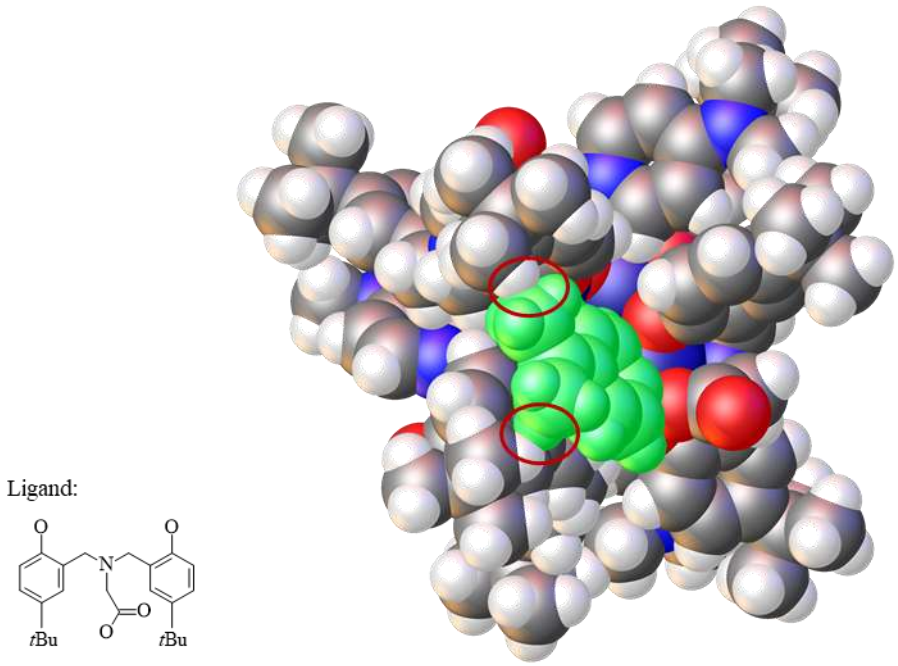

Figure 54. Sphere-packing model of $[Ti_4O_4\mathbf{3}_4][DMAP{\cdot}H]_4$ built from the crystal structure of compound **25**. A $DMAP{\cdot}H^+$ counter-ion, involved in a steric clash with the *tert*-butyl groups in the *R′* positions, is highlighted in green. Solvent of crystallisation omitted for clarity. Ti = purple; C = grey; N = blue; O = red; H = white.

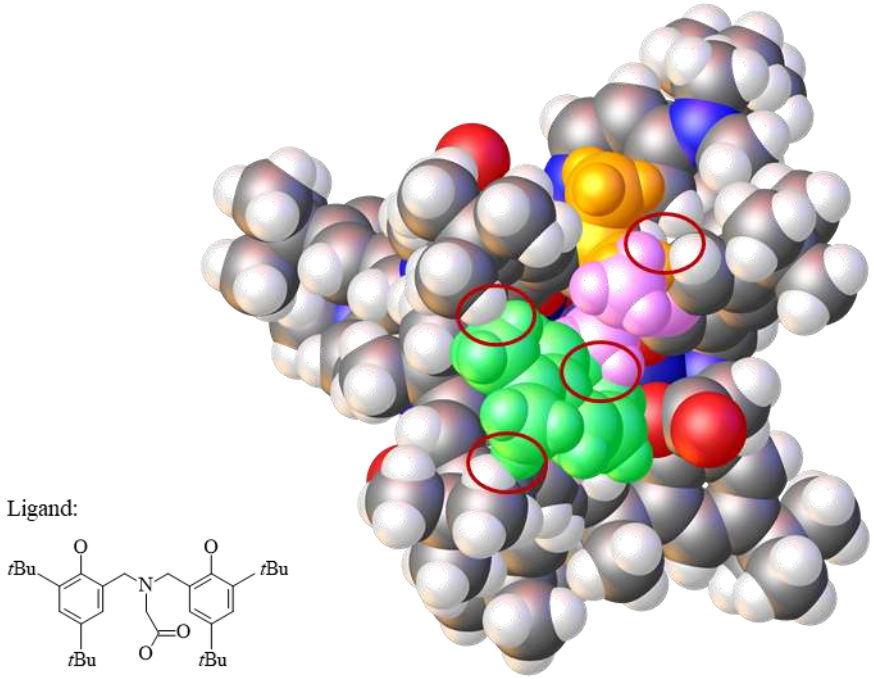

Figure 55. Model of $[Ti_4O_4\mathbf{4}_4][DMAP{\cdot}H]_4$ built from the crystal structure of compound **25**. A pair of *tert*-butyl groups in the *R″* positions of ligands bound to adjacent titanium centres exhibiting a steric clash are highlighted in pink and orange. A $DMAP{\cdot}H^+$ counter-ion involved in a steric clash with the *tert*-butyl groups in the *R′* and *R″* positions is highlighted in green. Solvent of crystallisation omitted for clarity. Ti = purple; C = grey; N = blue; O = red; H = white.

Altering the steric bulk of the *R′*/*R″* groups directed the formation of either cyclic or linear species (Table 12). For systems with ligand **1** (*R′* = *R″* = H), cyclic species were formed under stepwise conditions and solvothermal conditions. For systems with ligand **2** (*R′* = Me; *R″* = H), a linear species was accessed under stepwise conditions while a cyclic species was formed under solvothermal conditions. For systems with ligand **3** (*R′* = *t*Bu; *R″* = H), no isolable product was found under stepwise conditions while a linear species was characterised from the reaction mixture under solvothermal conditions. For systems with ligand **4** (*R′* = *R″* = *t*Bu), no reaction occurred under stepwise conditions and the titanium tetragonal disphenoid **21** was repeatedly isolated from the solvothermal reaction mixture.

Ligand	Stepwise reaction	Solvothermal reaction
1 (*R′* = *R″* = H)	$[Ti_4O_4\mathbf{1}_4][DMAP{\cdot}H]_4$	$[Ti_4O_4\mathbf{1}_4][DMAP{\cdot}H]_4$
2 (*R′* = Me; *R″* = H)	$[Ti_4O_3\mathbf{2}_4(H_2O)_2][DMAP{\cdot}H]_2$	$[Ti_4O_4\mathbf{2}_4][DMAP{\cdot}H]_4$
3 (*R′* = *t*Bu; *R″* = H)	No product isolated	$[Ti_4O_3\mathbf{3}_4(H_2O)_2][DMAP{\cdot}H]_2$
4 (*R′* = *R″* = *t*Bu)	No reaction	$Ti_4O_2\mathbf{4}_4$

Table 12. Summary of isolated SCXRD structures under solvothermal conditions ($Ti_4O_2L_4$, L = **1**-**4**, DMAP, toluene, 130 °C, 2h) and solvothermal conditions (compound **1**-**4**$(H)_3$, DMAP, Ti(O*n*Pr)$_4$, toluene, 120 °C, 72 h).

4.4 Solution state NMR characterisation

4.4.1 Cyclic $[Ti_4O_4L_4][DMAP{\cdot}H]_4$ compounds – dynamic species

Having obtained these new titanium compounds in crystalline form, allowing for solid-state characterisation by SCXRD, we studied the behaviour of these compounds in solution. Crystals of **23″** and **25** were dissolved in $CDCl_3$ and the samples analysed by NMR spectroscopy. As would be expected for isostructural compounds, the spectra share signals at similar chemical shifts, except for the extra aromatic protons in **23″** and the methyl groups in the *R′* positions of **25**. Broadening of the signals associated with DMAP and the presence of exchange in the spectrum (EXSY NMR) confirmed these species were dynamic in solution. Nevertheless, a number of prominent signals are observed in the spectra, which correspond to the expected signals for these the supporting ligands **1** and **2**. The spectra of **23″** and **25** feature a signal for the proton attached to the $DMAP{\cdot}H^+$ counter-ion at 14.05 ppm and 14.00 ppm respectively, confirming that these are protonated in the crystal structures. Interestingly, the spectra of **23** and **25″** displayed a methylene proton signal that was unusually downfield-shifted (6.23 ppm and 6.14 ppm respectively), a significant difference in chemical shift in comparison to the methylene proton signal (4.64 ppm and 4.57 ppm respectively) sharing the same carbon atom. Inspecting the crystals structures of **23″** and **25** showed a phenolate arm within close proximity of the methylene carbon C10 (Figure 56), with distances of 4.333(1) Å and 4.218(2) Å between H10B and the centroid for the aromatic ring carbons in structures **23″** or **25** respectively. Further to this, H10B was found to be coplanar with the phenolate ring showing low deviation (−0.158 Å and −0.180 Å) from the calculated plane formed by the aromatic ring, H10B and C10 with low RMSDs of 0.076 Å and 0.119 Å. This coplanar arrangement places the H10B proton on C10 in close proximity to the magnetically deshielding region of the phenolate ring, induced by the electron ring current.

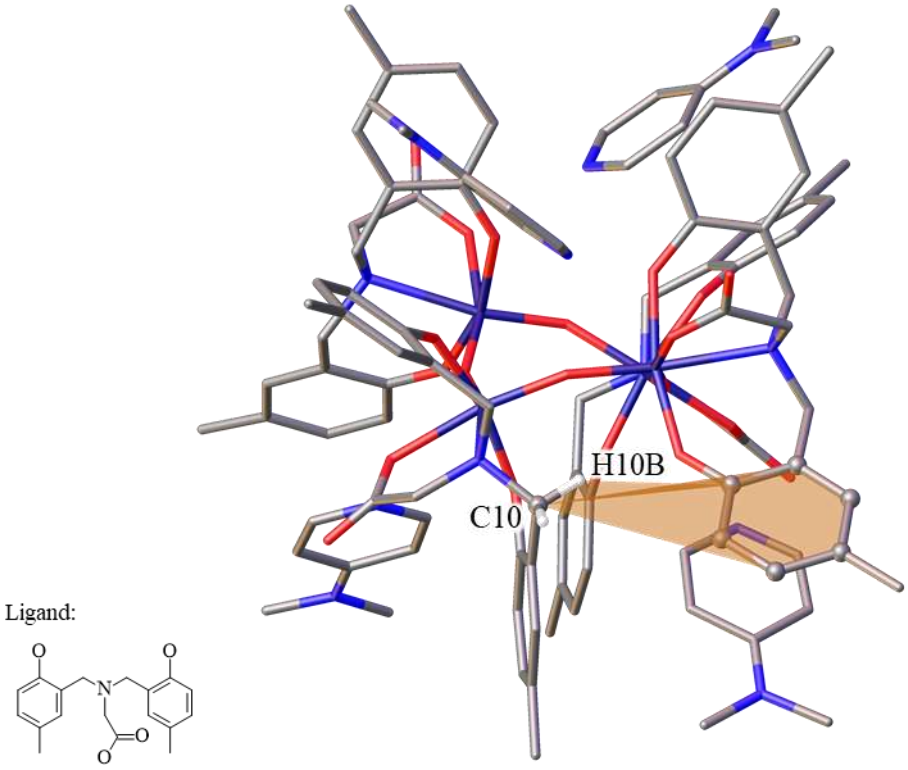

Figure 56. Coplanarity of C10, H10B and an adjacent phenolate ring which is the case of the significant downfield shift of a methylene proton signal. Asymmetric unit of **25** with solvent of crystallisation omitted for clarity. Orange: calculated plane C10–H10B–C59–C60–C61–C62–C63–C64; Ti = purple; C = grey; N = blue; O = red.

4.4.2 Linear $[Ti_4O_3L_4(H_2O)_2][DMAP{\cdot}H]_2$ compounds – stable species

When the crystals of the linear, tetrametallic titanium-oxo compound **24′** were dissolved in $CDCl_3$, the ^{1}H NMR spectrum showed low intensity signals to be present alongside a more intense set of signals. Since both **24′** and **24″** were identified by SCXRD in the crystalline sample, we propose the low intensity signals to correspond to the minor product **24″** while the more pronounced signals correlate with the expected signals for compound **24′**. For example, the C_2 axis of symmetry through O10 resulted in half the expected signals being observed, as shown by the four *R′* methyl signals integrating to twenty-four protons in the structure. Furthermore, a significantly downfield-shifted methylene proton signal at 6.10 ppm was found, much like proton H10B in the ^{1}H NMR spectra of **23″** and **25**. Similarly to H10B in **23″** and **25**, methylene protons H26B and H42B in **24′** are in a similar environment, exhibiting coplanarity with the phenolate rings (RMSD 0.081 Å and 0.041 Å) and close proximity with the centroid of the phenolate ring (4.942(2) Å and 4.697(2) Å).

An EXSY experiment revealed that no exchange was occurring, indicating **24′** was more stable than **25** in solution. For example, no exchange signals in the EXSY spectrum of **24″** was contrasting with the cyclised analogue **25** and suggestive that **24′** was more stable in solution. Furthermore, a ^{1}H ROESY NMR experiment showed clear through-space contacts between the aromatic and methyl proton signals of the $[Ti_4O_3L_4(H_2O)_2]^{4-}$ fragment and the methyl groups on the DMAP·H$^+$ counter-ions. This showed that when **24′** was in a $CDCl_3$ solution, the DMAP·H$^+$ were held closely to the structure. Finally, the DMAP·H$^+$ signals are sharp and appear as doublets; we might expect these signals to have been broadened if the DMAP·H$^+$ counter-ions were labile in solution such as was the case when **25** was solvated. A sample of **24′** was heated to reflux in toluene for 2 h to assess its thermal stability. Comparing the ^{1}H NMR spectra of **24′** before and after heating revealed the compound remained intact after heating. Performing the same experiment with **25** led to significant broadening of the signals in the ^{1}H NMR spectrum after heating.

4.4.3 Conversion of $[Ti_4O_4L_4][DMAP{\cdot}H]_4$ to $[Ti_4O_3L_4(H_2O)_2][DMAP{\cdot}H]_2$

We interpreted the lack of thermal stability exhibited by **25**, which was contrasting to **24′**, as strong evidence that **24′** to be the most stable form in solution of these tetrametallic compounds. If this is the case, the linear form is the thermodynamically stable product in solution and we proposed that the cyclic form is converting into the linear form to reach the energy minimum. Evidence of this was found when crystals were observed in a sample of **23″** in $CDCl_3$, with the SCXRD data revealing a linear tetrametallic compound analogous to **24′** had formed, **27** (Figure 57). The remaining solution was inspected by ^{1}H NMR spectroscopy to find no change had occurred from the mother liquor suggesting the equilibrium of species in this solution remained unchanged despite the precipitation of **27**.

The asymmetric unit of **27** exhibited diffuse electron density in solvent accessible voids occupied by $CDCl_3$ molecules. Samples of **27** were weakly-diffracting and limited the quality of data that could be acquired by SCXRD. This led to difficulty in modelling the second DMAP·H$^+$ counter-ion which showed disorder over two positions. A stable refinement was further disadvantaged by the high electron density of the chlorine atoms in the solvent accessible voids which, when modelled, let to an unstable refinement. In light of these difficulties, constraints were applied to the model while the solvent accessible voids were modelled using the SQUEEZE[19] routine. The disordered DMAP·H$^+$ fragment was too diffuse to model as two parts and further restraints were applied to idealise the position of the atoms according to a related fragment (see

compound **28**, Figure 61). These measures allowed for the best refinement of the $[Ti_4O_3\mathbf{1}_4(H_2O)_2][DMAP{\cdot}H]_2$ core for comparison with the analogous structures **24″** and **26**. Selected geometrical parameters for **27** show low deviation when compared to the mean geometrical parameters for **24″** and **26**, confirming these three compounds are isostructural (Table 13). Additionally, the well-refined DMAP·H···OCO intermolecular hydrogen bonding interaction was found to be in agreement with typical reported distances for a Donor···Acceptor interaction of 2.836(15) Å.[4]

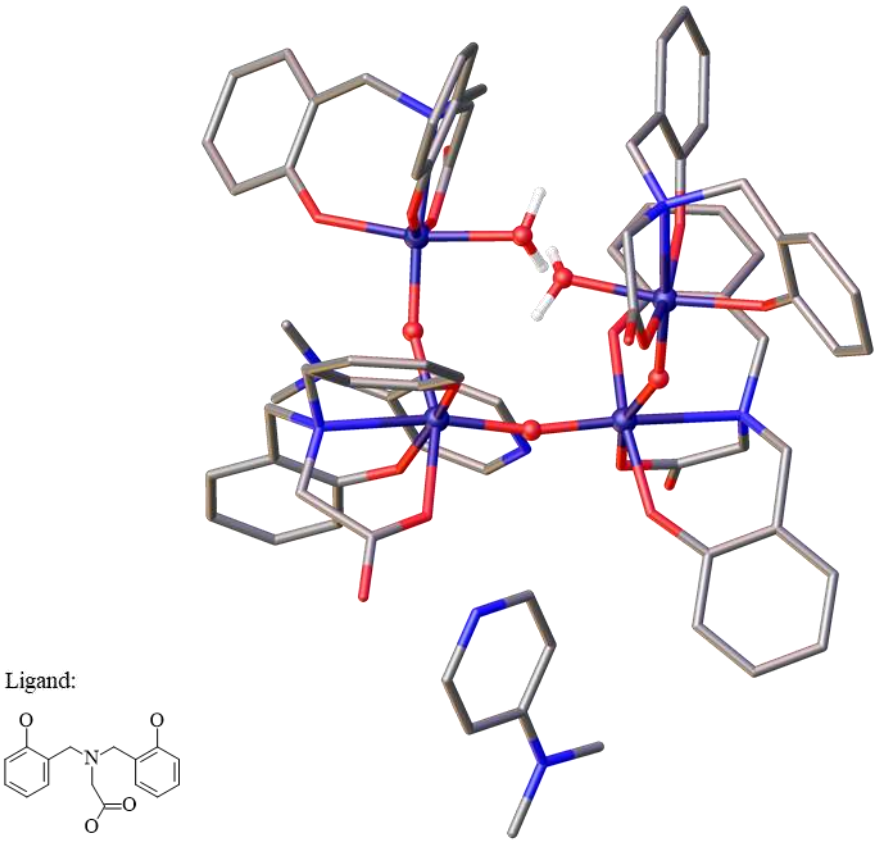

Figure 57. Asymmetric unit of **27**. Titanium-oxo core and aqua ligands are shown as spheres and ligand framework and $DMAP{\cdot}H^+$ displayed as tubes. Solvent of crystallisation and hydrogen atoms omitted for clarity except in the case of aqua ligands. Ti = purple; C = grey; N = blue; O = red.

Parameter	Mean1	Mean2	Deviation	Deviation %
Ti–O	1.821(4)	1.821(10)	0.000	0.01
Ti–O–Ti	155.2(3)	156.1(12)	0.457	0.29
Ti–OPh	1.905(4)	1.917(9)	0.006	0.33
Ti–OCO	2.048(4)	2.053(10)	0.003	0.13
TiO–CO	1.288(8)	1.249(7)	0.020	1.54
TiOC–O	1.232(7)	1.244(7)	0.006	0.49
$Ti–OH_2$	1.994(4)	1.987(11)	0.003	0.16
Ti_4O_3 plane RMSD	0.555	0.598	0.022	3.77
Ti1–Ti2–Ti3–Ti4	60.26(4)	60.67(5)	0.205	0.34

Table 13. Deviations for selected geometrical parameters, bond lengths (Å) and angles (°) for isostructural compounds **24″** and **26** (Mean1) and **27** (Mean2).

A sample of **25** in $CDCl_3$ was resubmitted for ^1H NMR analysis after standing for 4 days and then 7 days. Comparing these spectra with **25** and **24′** reveals the equilibrium in the sample tends towards **24′** over time (Figure 58). This observation further supports the drive for cyclic tetrametallic compounds to form linear analogues when solvated.

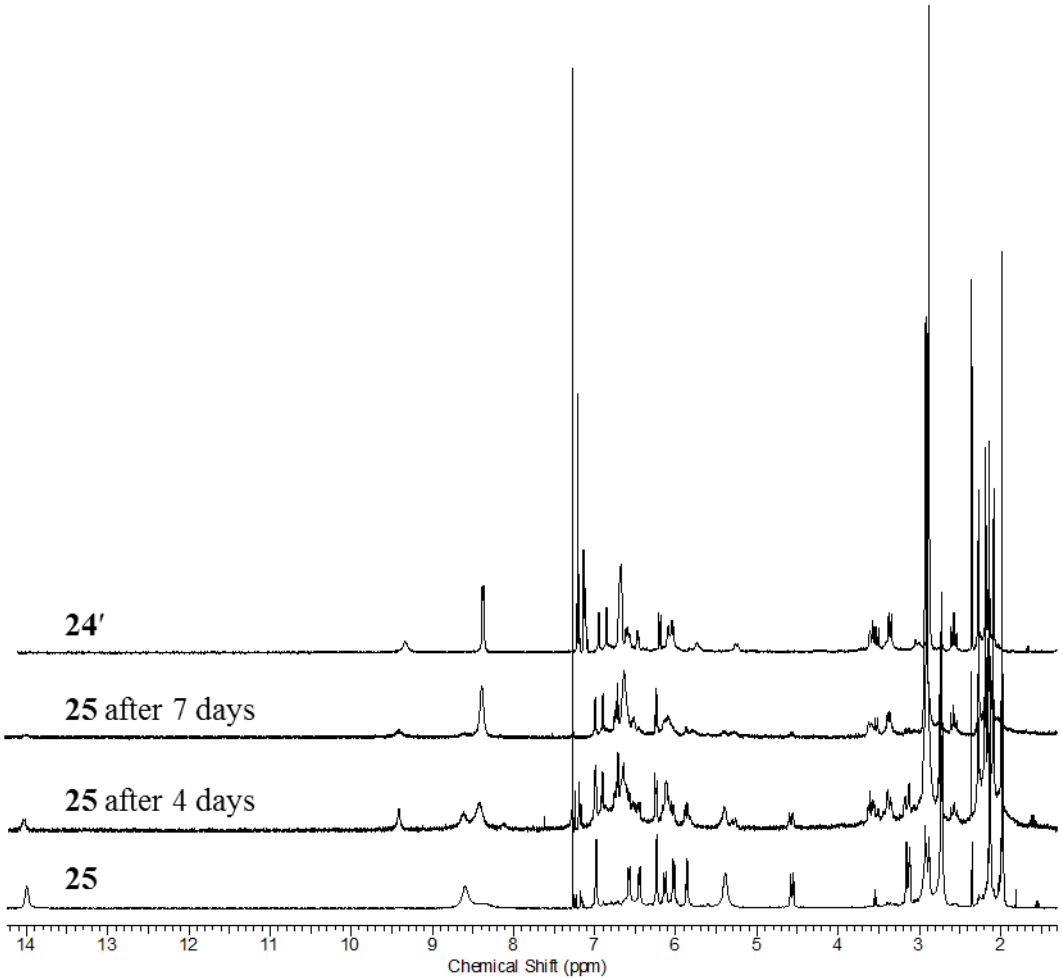

Figure 58. From bottom to top: ^{1}H NMR spectrum of **25**, **25** after 4 days, **25** after 7 days and **24′**.

Further investigation into the stability of linear versus cyclic tetrametallic compounds was sought by DOSY NMR experiments to probe the number of species in solutions for samples of **23″**, **25**, **24′**, **26** and **27**. The estimated *MW* distributions obtained by DOSY NMR experiments for **24′**, **26** and **27** show a single entity is present in solution (Figure 59), in accordance with the previously stability of both of these linear tetrametallic compounds. In contrast, the estimated *MW* distributions for the cyclic tetrametallic compounds **23″** and **25** show several species present in solution (Figure 60), concurring with previous observations indicating these compounds form a dynamic mixture in solution.

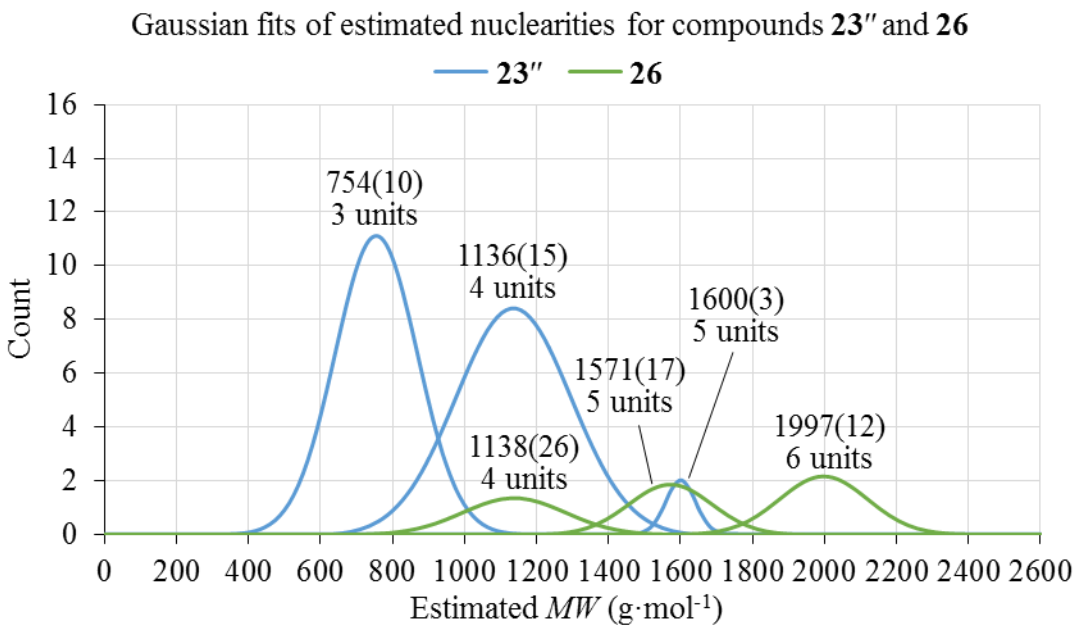

Figure 59. Plot of Gaussian fitting curves for datasets of estimated *MW*s of **23″** and **25** in $CDCl_3$ versus the count of data points corresponding to an estimated *MW* range (increments of 50 $g \cdot mol^{-1}$). Inset are the means for the Gaussian distributions with approximate number of units of [TiOL][DMAP·H] fragments. The estimated *MW*s were derived from diffusion coefficients obtained by ^1H DOSY NMR experiments.

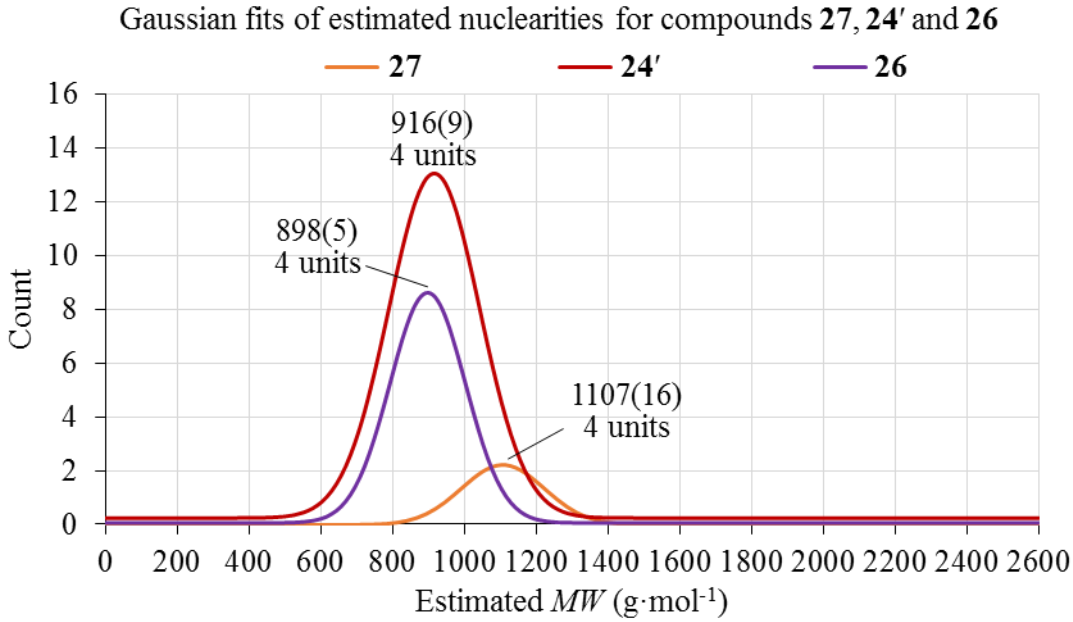

Figure 60. Plot of Gaussian fitting curves for datasets of estimated *MW*s of **27**, **24′** and **26** in $CDCl_3$ versus the count of data points corresponding to an estimated *MW* range (increments of 50 $g \cdot mol^{-1}$). Inset are the means for the Gaussian distributions. Inset are the means for the Gaussian distributions with approximate number of units of [TiOL][DMAP·H] fragments. The estimated *MW*s were derived from diffusion coefficients obtained by ^1H DOSY NMR experiments.

4.5 Conclusions

Through the use of two synthetic routes, a stepwise synthesis via $Ti_4O_2L_4$ or a one-pot solvothermal reaction, ligands **1**-**4** were once again found to be useful scaffolds to support titanium-oxo compounds. These new titanium-oxo compounds were classified into two types: cyclic tetrameric titanium-oxo compounds ($[Ti_4O_4L_4][DMAP{\cdot}H]_4$) and linear tetrametallic titanium-oxo compounds ($[Ti_4O_3L_4(H_2O)_2][DMAP{\cdot}H]_2$). Altering the steric bulk of the *R′* and *R″* groups on the ligand framework was found to give a degree of control over the product formed from the reactions, with the dynamic nature of the compounds hindering the techniques possible for purification. The reaction conditions were also found to influence the reactivity of the source of titanium, with solvothermal conditions required to promote a reaction to occur when the bulkier ligand **4** (*R′* = *R″* = *t*Bu) was used. Additionally, the core conformation of the cyclic compounds produced differed according to the synthetic method. Different Ti_4O_4 and Ti_4O_3 core geometries were concomitant with a change in ligand binding mode. Interestingly, the ligand binding mode was observed to change from reagent to product under the reaction conditions, indicating the presence of a ligand rearrangement reaction, even at room temperature. This was an unexpected observation as amine bis(phenolate) ligands are regarded as stable supports for catalysis. Due to the achiral and chiral nature of the two ligand binding modes, this could have implications for systems where amine bis(phenolate) ligands are used to support chiral catalysts. Using a variety of NMR spectroscopy experiments, it was shown that the linear compounds were more stable in solution than the cyclic compounds. Further evidence from ^{1}H NMR spectra and SCXRD structure supported our claim that the cyclic compounds were thermodynamically less stable, driven towards the linear analogues. A change in ligand donor type from LX_3 to L_2X_2, a feature granted by the ambidentate carboxylate arm, was proposed to be the cause of the dynamic nature of these compounds, a feature that could be changed in future systems for further investigation.

4.6 References

1. F. H. Allen, D. G. Watson, L. Brammer, A. G. Orpen and R. Taylor, in *International Tables for Crystallography Volume C: Mathematical, physical and chemical tables*, ed. E. Prince, Springer Netherlands, Dordrecht, 2004, p. 790-811.
2. G. A. Jeffrey, *Crystallogr. Rev.*, 2003, **9**, 135-176.
3. E. Y. Tshuva, I. Goldberg, M. Kol and Z. Goldschmidt, *Inorg. Chem.*, 2001, **40**, 4263-4270.
4. S. E. Reybuck, A. L. Lincoln, S. Ma and R. M. Waymouth, *Macromolecules*, 2005, **38**, 2552-2558.
5. T. Okamatsu, R. Irie and T. Katsuki, *J. Organomet. Chem.*, 2007, **692**, 645-653.
6. Y. Kim and J. G. Verkade, *Organometallics*, 2002, **21**, 2395-2399.
7. C. A. Huang and C. T. Chen, *Dalton Trans.*, 2007, 5561-5566.
8. D. T. Dugah, B. W. Skelton and E. E. Delbridge, *Dalton Trans.*, 2009, 1436-1445.
9. R. K. Dean, A. M. Reckling, H. Chen, L. N. Dawe, C. M. Schneider and C. M. Kozak, *Dalton Trans.*, 2013, **42**, 3504-3520.
10. K. Devaine-Pressing, J. H. Lehr, M. E. Pratt, L. N. Dawe, A. A. Sarjeant and C. M. Kozak, *Dalton Trans.*, 2015, **44**, 12365-12375.
11. Y. L. Fu, Y. L. Liu, Z. Shi, B. Z. Li and W. Q. Pang, *J. Solid State Chem.*, 2002, **163**, 427-435.
12. N. Steunou, G. Kickelbick, K. Boubekeur and C. Sanchez, *J. Chem. Soc., Dalton Trans.*, 1999, 3653-3655.
13. Y. Chen, J. D. Sokolow, E. Trzop and P. Coppens, *Dalton Trans.*, 2013, **42**, 15285-15287.
14. P. Coppens, Y. Chen and E. Trzop, *Chem. Rev.*, 2014, **114**, 9645-9661.
15. W. H. Fang, L. Zhang and J. Zhang, *J. Am. Chem. Soc.*, 2016, **138**, 7480-7483.
16. O. V. Dolomanov, L. J. Bourhis, R. J. Gildea, J. A. K. Howard and H. Puschmann, *J. Appl. Crystallogr.*, 2009, **42**, 339-341.
17. A. L. Spek, *Acta Crystallogr., Sect C: Cryst. Struct. Commun.*, 2015, **71**, 9-18.

Chapter 5 – Tetrametallic titanium-oxo compounds for the ROP of *rac*-lactide

Abstract

In chapter 3, the study of $Ti_4O_2L_4$ compounds in the ROP of *rac*-lactide showed that using DMAP as an additive resulted in increased activity under solution polymerisation conditions. However, we observed that mixing $Ti_4O_2L_4$ and DMAP led to the formation of new products, identified as linear tetrametallic compounds with formula $[Ti_4O_3L_4(H_2O)_2][DMAP{\cdot}H]_2$ and cyclic tetrameric compounds with formula $[Ti_4O_4L_4][DMAP{\cdot}H]_4$ in chapter 4. These titanium-oxo motifs have not been investigated in the ROP of *rac*-lactide and we sought to establish their performance. Due to the presence of $DMAP{\cdot}H^+$ counter-ions in these compounds, we studied the role of DMAP and $DMAP{\cdot}H^+$ in the ROP of *rac*-lactide, revealing the ability of DMAP to activate the monomer. The linear and cyclic titanium-oxo compounds were found to be active towards the ROP of *rac*-lactide, where the addition of a methyl group to the *para*-position of the phenolate groups led to decreased activity – a contrasting result to our previous observations. Comparing the microstructure of the polymer with other titanium initiators allowed us to confirm the titanium centres were active in the ROP of *rac*-lactide. A reusability study found that ROP after first-use was dominated by DMAP and not the titanium-oxo species.

5.1 Introduction

The linear and cyclic tetrametallic titanium-oxo compounds presented in this chapter feature Ti_4O_3 and Ti_4O_4 cores that have not been applied in the ROP of lactide, prompting us to establish their performance. Chakraborty and coworkers reported a salicylaldiminato-supported titanium-oxo species featuring a single Ti–O–Ti bridge to be highly active towards the melt polymerisation of lactide,[1] as previously discussed in chapter 1. Titanium-oxo cores with greater nuclearity have also been applied to the ROP of lactide, such as the trinuclear Ti_3O_3 and octanuclear $Ti_8(\mu\text{-}O)_4(\mu_3\text{-}O)_2(\mu\text{-}O\textit{i}Pr)_4$ cores reported by Chakraborty and coworkers.[2,3] These were found to convert *rac*- or *L*-lactide to polylactide under melt conditions to near completion after 5 mins and 30 mins respectively. Such examples show the potential polynuclear titanium-oxo complexes have as initiators/catalysts in the ROP of lactide.

Unlike the titanium-oxo species in the literature, the linear and cyclic tetrametallic titanium-oxo compounds herein feature DMAP·H^+ counter-ions. Before testing these compounds in the ROP of lactide, control experiments to gauge the role of the DMAP·H^+ counter-ions in the polymerisation needed to be completed. The application of DMAP, as well as a variety of sources of DMAP·H^+, have been reported in the literature as both organocatalysts and depolymerisation activators.[4-6] For this reason, we undertook control experiments with DMAP and DMAP·HCl, as a source of DMAP·H^+, under the exact conditions used in the ROP of *rac*-lactide with the titanium-oxo compounds. In this way, we could ascertain the contribution of the titanium-oxo species in the ROP of lactide despite the presence of DMAP·H^+ counter-ions.

5.2 The role of DMAP in the ROP of *rac*-lactide

In chapter 3, it was previously observed that under solution polymerisation conditions using the titanium-oxo pre-catalysts and DMAP led to a spurious increase in conversion from monomer to polymer. Further inspection of these ^{1}H NMR spectra reveals the apparition of a quartet signal at 4.35 ppm. Additionally, a control experiment under the same conditions with DMAP as activator shows the same effect, confirming that DMAP, rather than the titanium-oxo complex, is the cause of the observed increase in conversion. In an effort to elucidate the identity of this intermediate, reaction of DMAP with *rac*-lactide in equimolar quantities in refluxing toluene converted the *rac*-lactide to a single product. Comparing the ^{1}H NMR spectra from this reaction and the conversion experiments in chapter 3 revealed the unknown intermediate had been synthesised. Crystallisation by slow evaporation gave large colourless crystals that revealed the structure of this intermediate as compound **28**, shown in Figure 61. The crystal structure displays a ring-opened formed of *rac*-lactide with the insertion of water. The protonation of DMAP to DMAP·H^{+} implicates DMAP as an activator in the ring-opening of *rac*-lactide. Further to this, a reaction under the same conditions resulted in the formation of a mixture of compound **28** and another product. Crystals from the crude reaction mixture were studied by SCXRD, which revealed the structure of compound **29** presented in Figure 62. The asymmetric unit is composed of a unit of DMAP·H^{+} and a $C_3H_6O_3$ unit, the latter corresponding to the degraded form of *rac*-lactide, lactic acid.

Figure 61. Asymmetric unit of **28** with formula [DMAP·H][$C_6H_9O_5$] showing a unit of ring-opened *rac*-lactide with insertion of water. The *S*,*S*-form is presented in the figure. Note the space group is achiral, resulting in co-crystallisation of both *R*,*R*- and *S*,*S*-forms of the $C_6H_9O_5$ unit. Hydrogens displayed as spheres, all other atoms displayed as tubes. C = grey; N = blue;O = red; H = white.

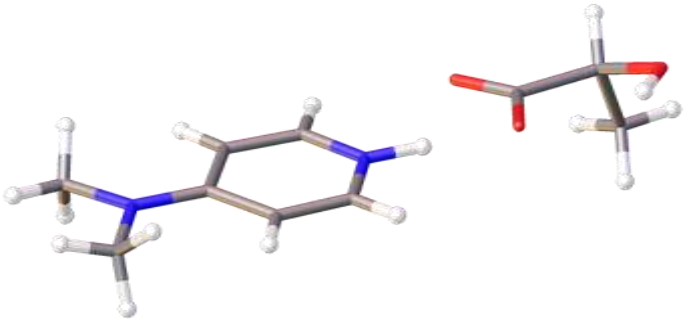

Figure 62. Asymmetric unit of **29** with formula [DMAP·H][$C_3H_5O_3$] showing a unit of ring-opened *rac*-lactide with insertion of water. The *S*-form is presented in the figure. Note the space group is achiral, resulting in co-crystallisation of both *R*- and *S*-forms of the $C_3H_5O_3$ unit. Hydrogens displayed as spheres, all other atoms displayed as tubes. C = grey; N = blue;O = red; H = white.

The degradation of lactide to lactic acid mediated by DMAP has implications for systems employing DMAP in the ROP of *rac*-lactide. Degradation of the *rac*-lactide monomer to lactic acid under polymerisation conditions will lead to half units of *rac*-lactide being incorporated in the polylactide product, an occurrence previously reported by Hedrik and coworkers.[1,2] Typically, it can be concluded that inter- and intra-molecular transesterification cause the insertion of monomer half-units. The presence of DMAP in the system would prevent this conclusion from being drawn with certainty.

This preliminary study into the role of DMAP in the ROP of *rac*-lactide will enable us to better understand its role during the polymerisation process in conjunction with the titanium-oxo compounds. Two comparative studies were undertaken. Firstly, monitoring conversion under solution conditions would compare the activity of the cyclic tetrameric titanium-oxo compounds and their DMAP·H^+ counter-ions in comparison to the titanium-oxo tetragonal disphenoid systems with DMAP as additive. Secondly, the melt polymerisation experiments tested the performance of the compounds to produce polylactide from *rac*-lactide and allowed for microstructures to be monitored.

5.3 Tetrametallic titanium-oxo species in the ROP of *rac*-lactide

Under the solution polymerisation conditions, **23″** was incorporated into solution within 10 mins. This was contradictory to previous observations in refluxing toluene **23″** would remain heterogeneous in refluxing toluene. The sole difference between these two reaction conditions is the addition of *rac*-lactide. From this, we can infer that **23″** is

undergoing a reaction in the presence of *rac*-lactide, as would be expected if **23″** were to act as an activator. With methyl groups in the *R′* positions to improve solubility, **25** readily dissolved in hot toluene. Comparing the conversion between the two titanium-oxo systems bound by ligand **1** shows compound **23″** is more active in the ROP of *rac*-lactide than compound **18** with DMAP as an additive. The opposite effect was observed in the case of **25** and the system of **19**/DMAP as an additive.

As previously discussed, the reaction of **18** or **19** with DMAP in refluxing toluene can lead to cyclic tetrameric or linear tetrametallic titanium-oxo compounds, where the cyclic tetrameric compounds are dynamic in solution. The solution polymerisation conditions are similar, undertaken in refluxing toluene, and it would not be unreasonable to anticipate the active species to form a similar equilibrium system (Figure 63). The time to form the active species from the two starting points, $Ti_4O_2L_4$ or $Ti_4O_4L_4$, is proposed to be related to their comparative conversion times. In the case of **23″**, this compound is able to form the most active species more quickly than a mixture of **18** and DMAP under the solution polymerisation conditions. On the other hand, **25** is slower to form these species in comparison to the system with **19** and DMAP, which could be due to the increased steric bulk in the *R′* position.

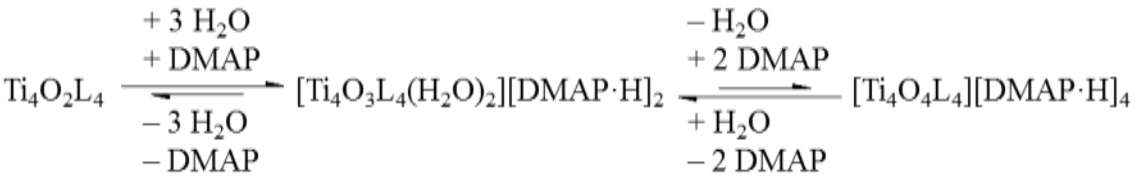

Figure 63. Proposed equilibria of $Ti_4O_2L_4$ with DMAP and $[Ti_4O_4L_4][DMAP{\cdot}H]_4$ in refluxing toluene, where L = **1** or **2**.

The plot of monomer conversion versus polymerisation time did not feature a spurious increase in conversion, with **23″** and **25** displaying linear trendlines at low conversion (Figure 64). The spurious increase in conversion noted during the control experiment with DMAP is not observed for the titanium-oxo systems. The ^{1}H NMR signals associated with compound **28** were not observed in the ^{1}H NMR spectra of the aliquots taken to monitor the reaction, implying that **28** is not present during the polymerisation. This evidence was strongly indicative that the titanium-oxo compounds **23″** and **25** are the source of active sites in these systems, displaying different curve profiles to **18**/DMAP and **19**/DMAP.

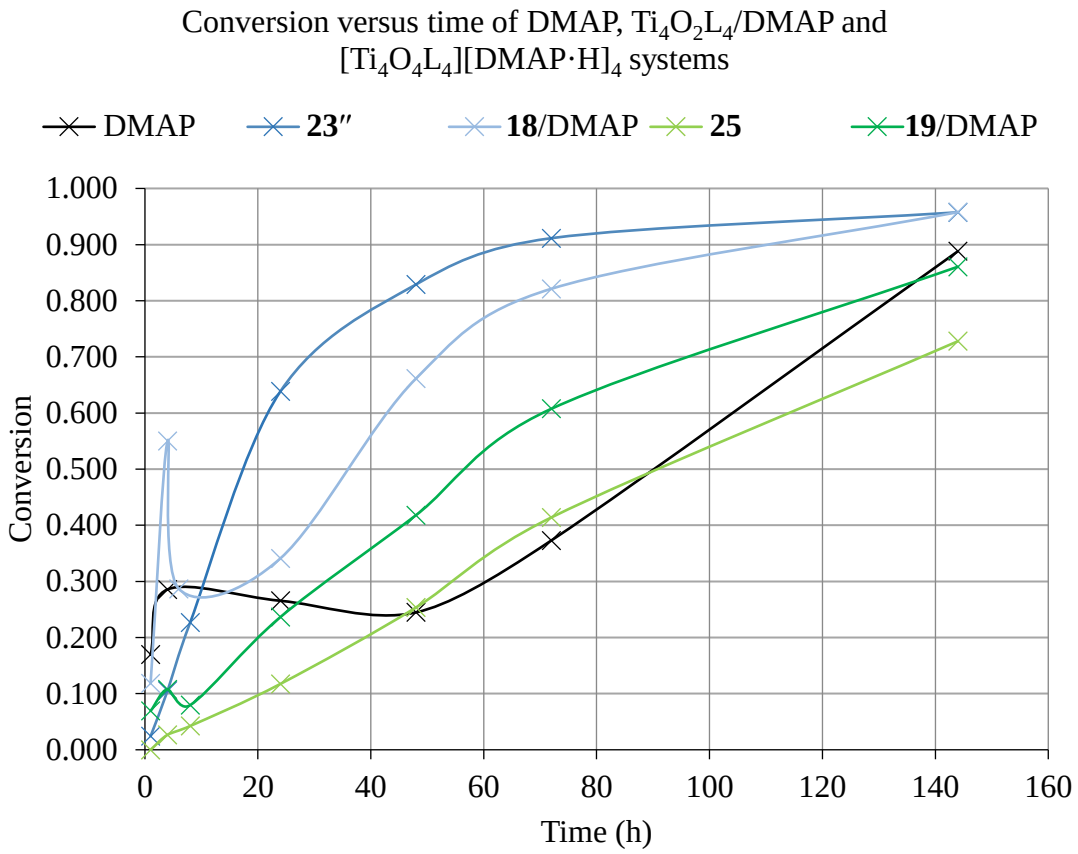

Figure 64. Plots of conversion against time for DMAP (control), **18**/DMAP and **19**/DMAP ($Ti_4O_2L_4$/DMAP systems) and **23″** and **25** ($[Ti_4O_4L_4][DMAP{\cdot}H]_4$ systems).

A typical titanium-based activator for the ROP of *rac*-lactide features a vacant site on a titanium centre, which can be activated *in situ* by dissociation of an initiating group.[4,5] In the case of **23″** and **25**, no vacant sites exist and the coordination spheres of the titanium centres are saturated by strong donor groups from the chelating glycine bis(phenolate) ligands and bridging oxo ligands. On the other hand, compounds **24′** and **24″** feature an active site through the terminal titanium-aqua bonds whereby the aqua ligand can dissociate and act as an initiator, leaving a vacant site on the titanium centre through which further monomer activation and chain propagation can occur. This can be likened to the more typical titanium-based initiators commonly used in the ROP of *rac*-lactide.[4] Considering the evidence that compound **24′** is accessible from both sides of the equilibrium and is stable in solution, we consider linear tetrametallic titanium-oxo structures with formula $[Ti_4O_3L_4(H_2O)_2][DMAP{\cdot}H]_2$ as the active species in these systems.

Compounds **23″**, **25** and **24′** were tested as activators in the ROP of *rac*-lactide under melt conditions. Crystalline samples of these compounds were used to control the loading

of DMAP·H^+. Experiments were carried out with a polymerisation time of 24 h and repeated with shorter polymerisation time of 6 h to compare the activity of the different compounds. The data is presented in Table 14.

Alongside these entries, the data for DMAP and DMAP·HCl control experiments are shown to better understand the role of the titanium-oxo units during the polymerisation. It was noted that DMAP was more active towards the ROP of *rac*-lactide than DMAP·HCl. Comparing the polymerisation data for isostructural compounds **23″** and **25** shows that the addition of a methyl group in the *R′* position has reduced the activity of **25** in comparison to **23″**. The same effect was observed for the titanium-oxo tetragonal disphenoid pre-catalysts used in the solution polymerisation of *rac*-lactide (chapter 3) but is contrasting with the increase in conversion observed under melt polymerisation conditions with the same compounds.[6]

Entry	Activator	Time	Conv.[a]	M_n[b]	$M_{n(NMR)}$[c]	PDI[d]	P_r[e]
1	DMAP	24 h	99	12500	13600	1.61	0.46
2	DMAP·HCl	24 h	53	6710	7800	1.44	0.47
3	**23″**	24 h	87	12900	16600	1.43	0.56
4	**24′**	24 h	94	10400	12000	1.57	0.48
5	DMAP	6 h	53	9180	14300	1.44	0.48
6	DMAP·HCl	6 h	30	8240	7890	1.58	0.49
7	**23″**	6 h	53	6570	11400	1.29	0.59
8	**25**	6 h	38	3620	4630	1.19	0.57

Table 14. Melt polymerisation data for DMAP, DMAP·HCl, **23″**, **25** and **24′**. [a] Conversion (%) from ^{1}H NMR spectra evaluated by integration of the methine regions of polylactide versus lactide. [b] Polymer number average molar mass determined from GPC traces. [c] Calculated polymer molecular weight by ^{1}H NMR end-group analysis. [d] Polydispersity indices (M_w / M_n) obtained from GPC traces. [e] Calculated from analysis of the homonuclear decoupled ^{1}H NMR spectrum of the polymer sample.

5.3.1 Active species

The proposed active species would be capable of initiation via coordination-insertion of the aqua ligand and subsequent propagation during the polymerisation. Evidence of this was found when the MALDI TOF mass spectrometry analysis revealed the polylactide samples from entries 3, 7 and 8 are terminated by hydroxyl end groups, confirming that the initiating group was water. The MALDI TOF mass spectra also showed the presence of half monomer mass series. Considering the lack of a side peak in the GPC traces that are symptomatic of side reactions, this is an indication that DMAP

has participated by activating the monomer to lactic acid. In this case, we have also demonstrated that DMAP·H^+ participates as an activator for both the cyclic tetrameric pre-catalyst (**23″** and **25**) and the *rac*-lactide monomer.

Comparison of the conversion between the DMAP control experiments (entries 1 and 5) and $[Ti_4O_4\mathbf{1}_4][DMAP{\cdot}H]_4$ systems (entries 3 and 7) under melt polymerisation conditions showed little difference in performance. The same can be seen between the M_n values obtained from GPC the traces of these polylactide samples. However, the PDI is lower for the polymers obtained from the cyclic tetrameric titanium-oxo compounds, suggesting the presence of the titanium complex to be beneficial for the control of the polymerisation process. Also, the P_r values are similar and were noted to be above the nominal value of 0.50, indicating slightly heterotactic polylactide is formed. The similarity and differences found in the polymerisation data between the cyclic tetrameric titanium-oxo compounds and DMAP control experiments shows that the titanium-oxo fragment and DMAP·H^+ counter-ions have a cooperative effect in the ROP of *rac*-lactide.

Perhaps the most significant evidence confirming the involvement of the titanium centres in $[Ti_4O_4L_4][DMAP{\cdot}HCl]$ (L = **1** or **2**) in the ROP of *rac*-lactide was the $^1H\{^1H\}$ NMR spectra for the polylactide samples produced. The spectra for these entries 3, 4, 7, 8 and 9 are similar to those for the slightly heterotactic polylactide produced for the titanium isopropoxide aggregates (chapter 2) and titanium-oxo tetragonal disphenoid (chapter 3). Importantly, these $^1H\{^1H\}$ NMR spectra are different from the $^1H\{^1H\}$ NMR spectra of the polylactide samples obtained from the control experiments with DMAP and DMAP·HCl, these organocatalysts producing a polylactide tending towards isotacticity. This preference for a slightly heterotactic microstructure between all types of polynuclear titanium compounds presented was strongly indicative that the titanium centres were the active species in these systems.

It was also noted that **24′** showed higher conversion than **23″** and **25**. Again, this is suggestive that the linear tetrametallic titanium-oxo species are the most active species in these systems. Due to its greater stability in comparison to **23″** and **25**, the solids from the melt polymerisation initiated by **24′** (entry 4) were recovered from the filtrate after polylactide precipitation and reused in the ROP of *rac*-lactide (Table 15). After two uses, high conversion was retained but the polylactide chain length was shorter with a M_n value reduced by over 50 %. This showed the mixture was reusable and by definition catalytic but suffered reduced performance in comparison to first use of **24′**. Comparing the microstructure of the polylactide samples obtained from entries 10 and 11 with control

experiments with DMAP·H$^+$ (entries 1 and 2) showed a change from a slightly heterotactic to slightly isotactic microstructure. This is an indication that after a single use, DMAP and DMAP·H$^+$ are the dominant active species, implying the deactivation of the titanium-oxo complexes occurs.

Entry	Activator	Time	Conv.[a]	M_n[b]	$M_{n(NMR)}$[c]	PDI[d]	P_r[e]
1	DMAP	24 h	99	12500	13600	1.61	0.46
2	DMAP·HCl	24 h	53	6710	7800	1.44	0.47
4	**24′**	24 h	94	10400	12000	1.57	0.48
10	**24′**	24 h	95	4640	6370	1.46	0.49
11	**24′**	24 h	85	4240	5870	1.39	0.48

Table 15. Reusability study for **24′** in the melt ROP of *rac*-lactide. [a] Conversion (%) from ^{1}H NMR spectra evaluated by integration of the methine regions of polylactide versus lactide. [b] Polymer number average molar mass determined from GPC traces. [c] Calculated polymer molecular weight by ^{1}H NMR end-group analysis. [d] Polydispersity indices (M_w / M_n) obtained from GPC traces. [e] Calculated from analysis of the homonuclear decoupled ^{1}H NMR spectrum of the polymer sample.

Further to this, the ^{1}H NMR spectrum of the recovered catalytic material was compared to that of **24′** and DMAP·H$^+$. This revealed a significant change in comparison to the ^{1}H NMR spectrum of **24′**. Notably, the signals corresponding to the DMAP units are sharper and match those found for 'free' and non-protonated DMAP. This confirms a change from DMAP·H$^+$ to neutral DMAP during the polymerisation. Also, the presence of doublets that are similar to the diastereotopic proton signals observed for **24′** and **25** are visible. It was noted that the two signals were present for the *R′* methyl groups. This spectrum does not correspond to **24′**, **25** or **19**, suggesting a new titanium species was present in the work-up of the ROP of *rac*-lactide with **24′**. Regardless, this showed that the recovered material is composed of DMAP or DMAP·H$^+$ while the $[Ti_4O_3\mathbf{2}_4]^{4-}$ fragment has degraded. After first-use, it is likely free DMAP or DMAP·H$^+$ is acting as an organocatalyst while the remaining, unidentified titanium species have little influence over the polymerisation.

5.4 Conclusions

The presence of DMAP·H^+ counter-ions in $[Ti_4O_3L_4(H_2O)_2][DMAP{\cdot}H]_2$ and $[Ti_4O_4L_4][DMAP{\cdot}H]_4$ compounds led to our studies of DMAP and DMAP·HCl in the ROP of *rac*-lactide as control experiments. It was found that DMAP and DMAP·HCl are capable of activating *rac*-lactide by ring-opening to a linear monoester of lactide as well as a subsequent degradation to lactic acid. This monomer activation was observed in aliquots of the polymerisations, confirming DMAP effects this reaction under polymerisation conditions. To control the loading of DMAP in the systems, crystalline samples of the $[Ti_4O_3L_4(H_2O)_2][DMAP{\cdot}H]_2$ and $[Ti_4O_4L_4][DMAP{\cdot}H]_4$ compounds were applied to the ROP of *rac*-lactide. Under solution and melt polymerisation conditions, adding methyl substituents in the *para*-positions of the phenolate groups (L = **2**) of $[Ti_4O_4L_4][DMAP{\cdot}H]_4$ decreased activity, a contrasting observation to our previous systems where this was beneficial to performance. Comparing the performance of the titanium-oxo compounds to their control experiments confirmed that the active species during the polymerisation process involved titanium metal centres. In this way, it could be said that the DMAP·H^+ counter-ions and titanium-oxo fragments participate cooperatively as activators in the ROP of *rac*-lactide. Further analysis into the reusability of the linear compound **24′** revealed the recovered catalytic material from the melt polymerisation is primarily composed of DMAP/DMAP·H^+, which is proposed to be the active species after first-use.

5.5 References

1. D. Chakraborty, D. Mandal, V. Ramkumar, V. Subramanian and J. V. Sundar, *Polymer*, 2015, **56**, 157-170.
2. R. R. Gowda, D. Chakraborty and V. Ramkumar, *Inorg. Chem. Commun.*, 2011, **14**, 1777-1782.
3. B. Rajashekhar, S. K. Roymuhury, D. Chakraborty and V. Ramkumar, *Dalton Trans.*, 2015, **44**, 16280-16293.
4. F. Nederberg, E. F. Connor, M. Möller, T. Glauser and J. L. Hedrick, *Angew. Chem. Int. Ed. Eng.*, 2001, **40**, 2712-2715.
5. F. Nederberg, E. F. Connor, T. Glausser and J. L. Hedrick, *Chem. Commun.*, 2001, 2066-2067.
6. O. Coulembier and P. Dubois, *J. Polym. Sci. Pol. Chem.*, 2012, **50**, 1672-1680.
7. A. Sauer, A. Kapelski, C. Fliedel, S. Dagorne, M. Kol and J. Okuda, *Dalton Trans.*, 2013, **42**, 9007-9023.
8. C. J. Casewit, D. E. Coons, L. L. Wright, W. K. Miller and M. R. Dubois, *Organometallics*, 1986, **5**, 951-955.
9. J. M. E. P. Cols, C. E. Taylor, K. J. Gagnon, S. J. Teat and R. D. McIntosh, *Dalton Trans.*, 2016, **45**, 17729-17738.

Chapter 6 – Towards solution-stable titanium-oxo compounds

Abstract

The dynamic nature of the cyclic $[Ti_4O_4L_4][DMAP{\cdot}H]_4$ compounds investigated in chapter 4 was attributed to the ambidentate nature of the carboxylate donor on the ligand. Replacing this donor with a pyridyl group and building an analogous $Ti_4O_4L_4$ system confirmed this to be the case. Using pyridylamine bis(phenolate) ligands allowed the formation of a variety of titanium-oxo compounds, with solvothermal conditions leading to $Ti_2OL_2(O\textit{n}Pr)_2$, $Ti_2O_2L_2$, $Ti_3O_3L_3$ and $Ti_4O_4L_4$ structures. Characterising these species revealed a relationship between decreasing titanium-oxo nuclearity and increasing steric bulk on the ligand periphery, giving insight into the processes involved in the assembly of cyclic titanium-oxo compounds.

6.1 Introduction

Controlled hydrolysis of titanium(IV) compounds supported by amine bis(phenolate) ligands was investigated by Martins et al.[1] where the use of a titanium(III) chloride precursor was found to react with a variety of reagents via radical reactions to yield titanium(IV) products. Of particular interest to our research was the reaction with molecular oxygen to form a compound, with the general formula $Ti_2OL_2(Cl)_2$, containing a linear dimetallic Ti–O–Ti motif. Waters and Nielson synthesised a $Ti_2OL_2(OEt)_2$ diethoxide analogue with the same amine bis(phenolate) ligand, effecting hydrolysis of the $TiL(OEt)_2$ precursor by reflux in wet ethanol, which was understood to cause an *in situ* alcoholysis of the titanium isopropoxide species while the heated mixture of alcohol and water incited the formation of a Ti–O–Ti bridge.[2]

These examples show how linear Ti–O–Ti bridges can be formed but there are many reports of further hydrolysis of these species to cyclic titanium-oxo compounds, although most of these feature ligands that exhibit lower denticity than the amine bis(phenolate) ligands employed herein.[3-6] Tetradentate ligands amine bis(phenolate) and salan ligands have been found to form cyclic Ti_xO_x compounds with a nuclearity x of two,[7-9] three[8,10-13] and four.[14-16] These have been applied in the fields of anti-cancer research[8,9,13,14,17] and nanoparticle synthesis.[6,10] It was noted that the assembly of Ti–O–Ti motifs could be promoted by the use of solvothermal conditions as observed with polyoxotitanates.[6,18-21] A study of titanium-oxo compounds supported by a diamine bis(carboxylate) ligands found reaction conditions and ligand modification were key to controlling the assembly of different titanium species.[15] In many cases, separating of the titanium-oxo species could only be achieved by fractional crystallisation. Using the knowledge from these literature reports, the reaction conditions and ligand modification were used as tools to incite Ti–O–Ti expansion and tailor product formation while fractional crystallisation was relied upon to purify and characterise the compounds.

6.2 Pyridylamine bis(phenolate) supported titanium-oxo compounds

Amine bis(phenolate) ligands have been shown so far to be a successful scaffold for polynuclear titanium compounds. Although the use of a carboxylate pendant arm was found to stabilise a multitude of compounds, it was also proposed to induce dynamic processes in solution in linear and cyclic titanium-oxo compounds **23**-**27**. This prompted us to use the tunability of amine bis(phenolate) compounds to investigate the involvement of the pendant donor in the *R* position of the ligand. The ambidentate nature of the carboxylate donor allowed ligands **1**-**3** to switch between LX_3 and L_2X_2-type donation, which stabilised the metal centre when undergoing changes in oxidation state. For this reason, we chose to investigate the use of amine bis(phenolate) ligands with a pyridyl in the *R* position; this L_2X_2-type donor ligand has found success in binding titanium compounds.[2,22] The ensuing research was completed with a time-constraint as a final, short project to investigate the continuity of the work presented in this thesis and identify future research leads, with an emphasis on crystallographic characterisation to draw the most insightful structural conclusions from this project.

6.2.1 Synthesis and characterisation of building blocks

The amine bis(phenolate) ligands with a pyridyl in the *R* position were synthesised using similar synthetic routes used to access the carboxylate analogues and using modified procedures from the literature (Figure 65).[23,24] Compound **30**$(H)_2$ was synthesised using two successive reductive aminations starting from a 2-picolylamine core and salicylaldehyde and purified by recrystallization with dichloromethane and methanol.[23] Compounds **31**-**33**$(H)_2$ were synthesised via a one-pot Mannich condensation using 2-picolylamine, paraformaldehyde and the appropriately-substituted phenolic starting materials to yield the desired groups at the *R*′/*R*″ positions, leading to a white or off-white precipitates that were purified by trituration in methanol at room temperature.[24]

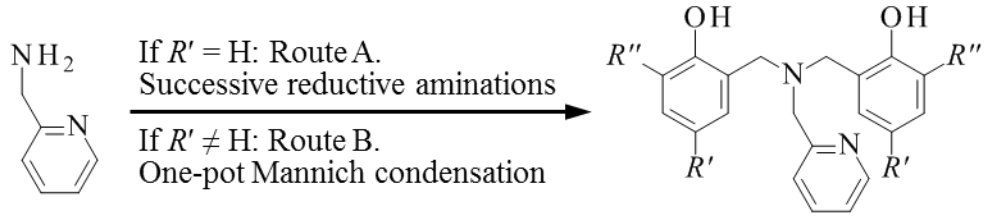

Route A: Salicylaldehyde (2 h) then $NaBH_4$. Repeat.
Route B: Phenol and paraformaldehyde. MeOH, reflux, N_2

30$(H)_2$: R' = H; R'' = H
31$(H)_2$: R' = Me; R'' = H
32$(H)_2$: R' = Me; R'' = Me
33$(H)_2$: R' = *t*Bu; R'' = *t*Bu

Figure 65. Synthetic routes to amine bis(phenolate) ligand precursors **30**-**33**$(H)_2$. Route A: salicylaldehyde in methanol and stir for 2 h then add sodium borohydride under N_2, repeat. Route B: *R′*/*R″*-substituted phenol and paraformaldehyde reflux in methanol under N_2 for 24 h or 48 h.

Synthesis and characterisation of suitable titanium building blocks was sought to allow for understanding and control over the assembly of polynuclear titanium compounds. Compound **30**$(H)_2$ and **33**$(H)_2$ were sought to form the least sterically and most sterically bulky titanium fragments accessible within the range of ligands synthesised and compare their ability to form titanium-oxo clusters. When reacted with titanium isopropoxide in dry THF under a dry nitrogen atmosphere, compounds **30**$(H)_2$ and **33**$(H)_2$ were deprotonated *in situ* to give the titanium diisopropoxide complexes **34** and **35** (Figure 66). Analogous to the reported complex **35**,[22] complex **34** was identified by ^{1}H and ^{13}C NMR spectra and showed similar signals with identical integration values and multiplicities as well as similar chemical shifts excluding the *tert*-butyl groups to the spectrum obtained for complex **37**.

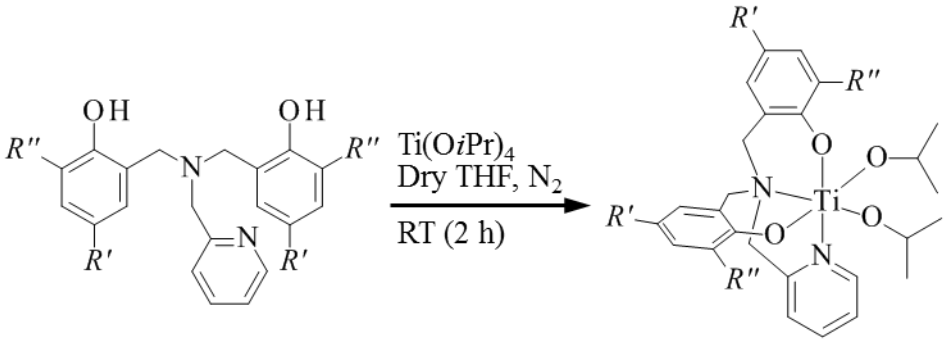

30$(H)_2$: R' = H; R'' = H
33$(H)_2$: R' = *t*Bu; R'' = *t*Bu

34: R' = H; R'' = H
35: R' = *t*Bu; R'' = *t*Bu

Figure 66. Structures of complexes **34** and **35**, formed by the reaction of ligand precursor **30**$(H)_2$ or **33**$(H)_2$ with titanium isopropoxide.

Compound **30**$(H)_2$ and **33**$(H)_2$ were also reacted with titanium tetrachloride in dry toluene under a dry nitrogen atmosphere to synthesise analogues of complexes **36** and **37** with the more labile chloride ligand,[1] which could be more reactive or lead to different titanium-oxo compounds when used as building blocks in comparison to the diisopropoxide analogues **34** and **35**. Where compound **31**$(H)_2$ was used, the linear dimetallic complex **36** (Figure 67) was isolated as a result of the hydrolysis of the intermediate complex **36′** under the reaction conditions (Figure 67). Conversely, using compound **35** yielded the expected complex **37,** as reported in the literature,[7] appearing as large red crystals when standing in toluene at –20 °C. These were analysed by SCXRD (Figure 68) to reveal the structure. We proposed the bulky di-*tert*-butylphenols would protect the titanium centre from hydrolysis, granting greater stability to complex **37** in the presence of trace amounts of water. This lack of steric protection is observed to cause intermediate **36′** to readily react *in situ* with water to form the hydrolysis product **36**.

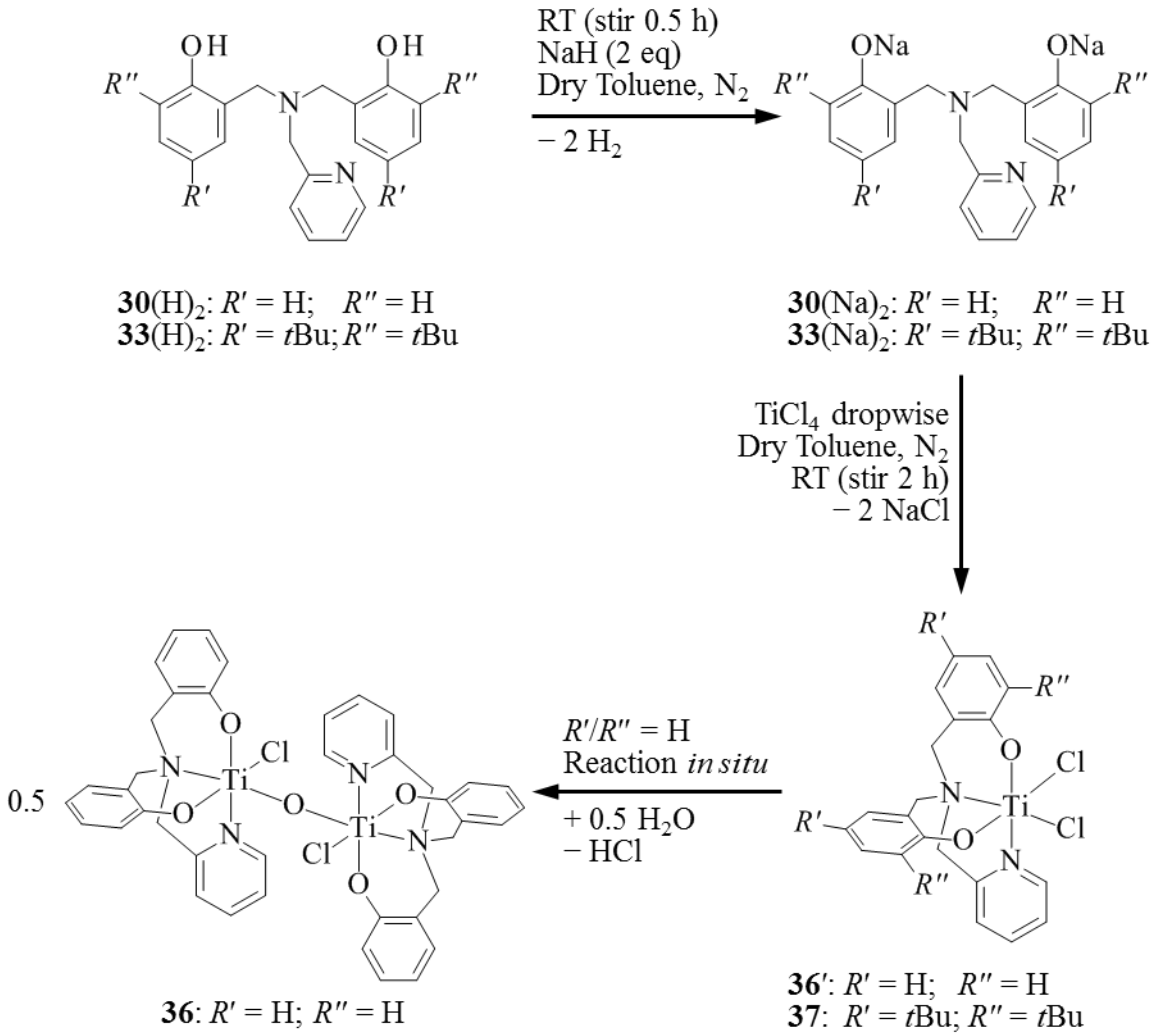

Figure 67. Synthetic routes to complexes **36** and **37** via the deprotonated, sodium salt of compounds **30**$(H)_2$ and **33**$(H)_2$. Note **36′** was not isolated and is a proposed intermediate.

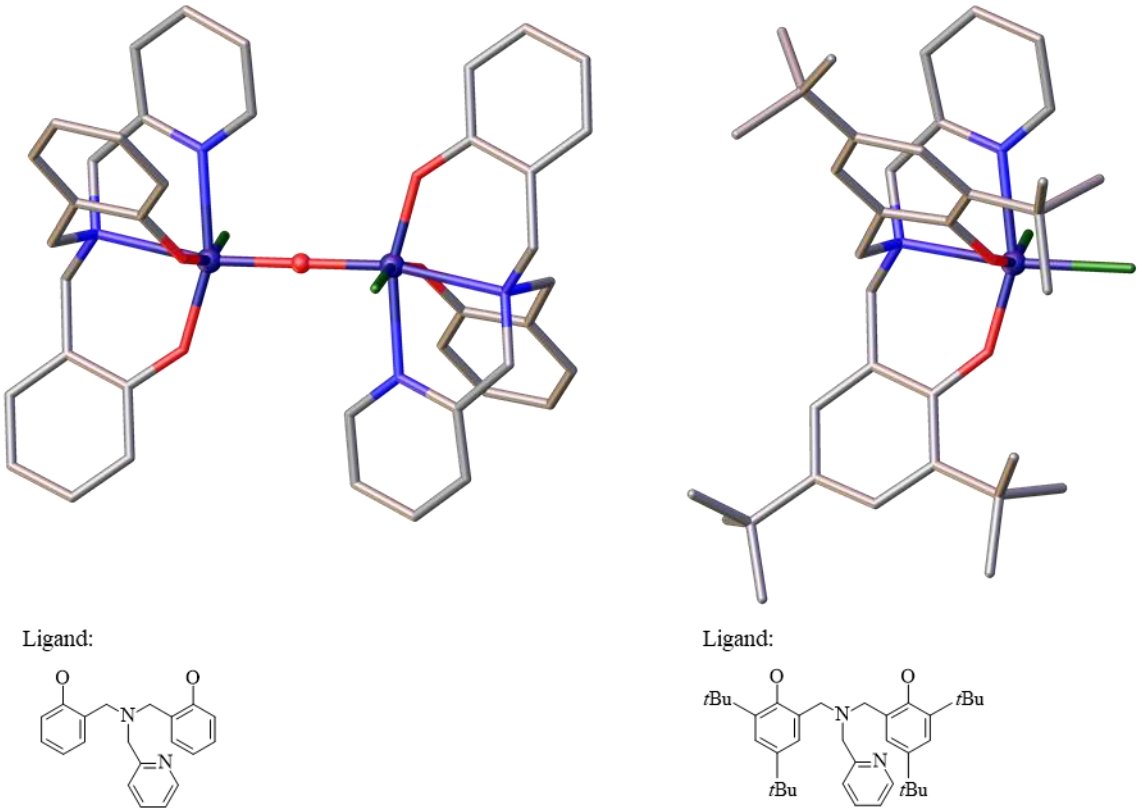

Figure 68. Asymmetric units of **36** (left) and **37** (right). Titanium-oxo core and aqua ligands are shown as spheres and ligand framework. Solvent of crystallisation and hydrogen atoms omitted for clarity. Ti = purple; C = grey; N = blue; O = red; Cl = green.

6.3 Synthesis and characterisation of titanium-oxo compounds

Complexes **34-37** are bound by two, labile isopropoxide or chloride ligands that we anticipated could be displaced to form titanium-oxo bridges as seen in the cases of the previously synthesised linear and cyclic tetrametallic titanium-oxo clusters **23-27**. To form analogous compounds of **23-27** with a pyridyl donor replacing the carboxylate, the hydrolysis of the diisopropoxide and dichloride fragments **34-37** was investigated using similar synthetic routes: a stepwise synthetic route or a one-pot solvothermal reaction.

6.3.1 Stepwise synthesis

Hydrolysis of these fragments occurred under a variety of conditions, with two synthetic routes presented in

Figure **69**. In the instances where titanium diisopropoxide complexes **34** and **35** were used, a pale white insoluble powder was obtained. In a similar fashion, hydrolysis reactions of the titanium dichloride fragment **37** led to insoluble brownish/orange solids. However, when the dimetallic dichloride fragment **36** was used, a change in colour

(orange to yellow) under both hydrolysis conditions A and B indicated a reaction had occurred (

Figure **69**).

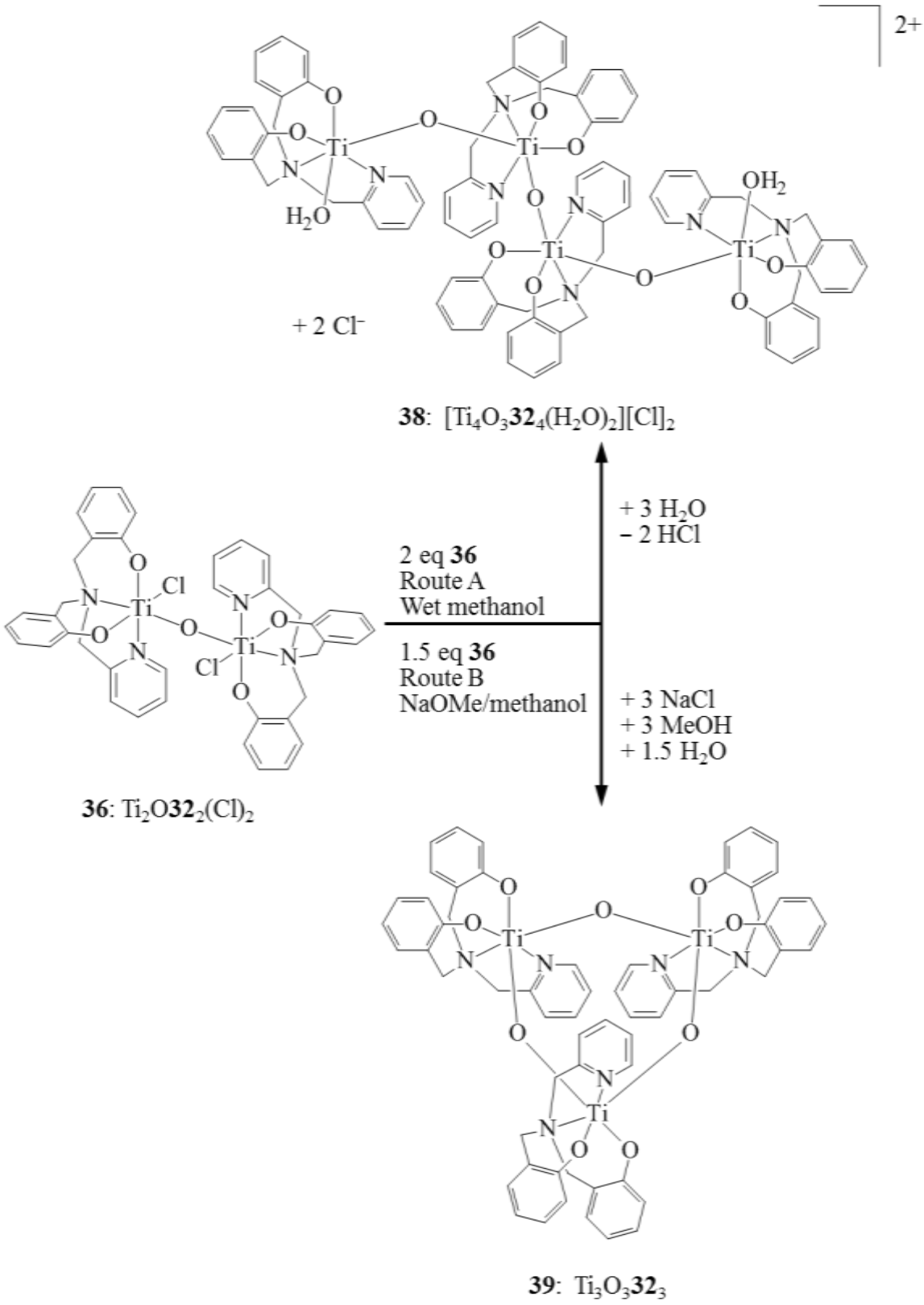

Figure 69. Hydrolysis of **36** via Route A and Route B leading to products **38** and **39**.

The linear tetrametallic compound **38** (Figure 70) was formed when **36** was stirred in a water/methanol mixture, with hydrolysis occurring in a similar reaction to that reported for monometallic diisopropoxide fragments bearing salan ligands under equivalent conditions.[11,12] Structural similarities between **38** and **24′**, a linear tetrametallic compound previously synthesised (see chapter 4), are apparent, with both compounds showing equivalent 4 × C_1 symmetric Ti_4O_3 cores terminated by aqua ligands and adopting the same unfolded conformation. This conformation exhibits planarity, with low RMSD of 0.041 Å and 0.095 Å for **38** and **24′** respectively from a calculated plane, drawn through the four titanium(IV) and four oxo centres. While both compounds crystallised in space group $P\bar{1}$ with the terminal oxo ligand occupying the special position in the unit cell. A contrasting observation is that **38** crystallises with chloride anions to balance the positive charge left on the Ti_4O_3**30**$_4(H_2O)_2$ fragment whereas **24′** required cations to stabilise residual negative charge left by the ambidentate carboxylate donors on the Ti_4O_3**2**$_4(H_2O)_2$ fragment. Further analysis of the geometrical parameters in **38** shows that **24′** share similar values for selected parameters (Table 16), although these show slight deviations which we explain by the different pyridyl and carboxylate donors on the ligands supporting the Ti_4O_3 cores.

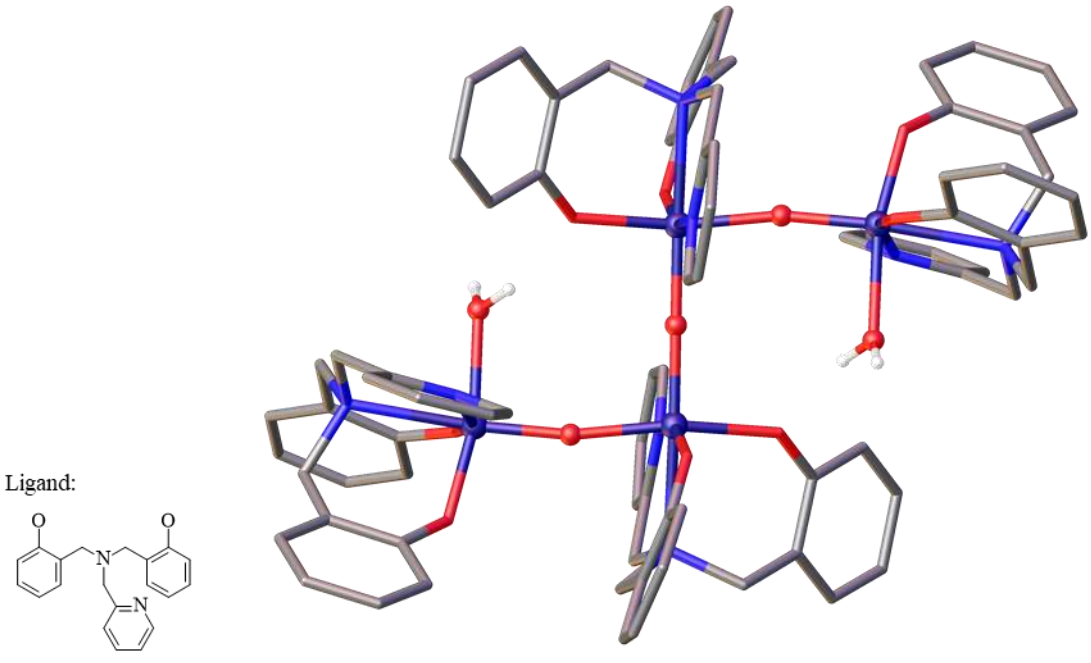

Figure 70. Crystal structure of **38** grown from the asymmetric unit. Titanium-oxo core and aqua ligands are shown as spheres and ligand framework. Solvent of crystallisation, anions and hydrogen atoms omitted for clarity except in the case of aqua ligands. Ti = purple; C = grey; N = blue; O = red.

Parameter	Mean1	Mean2	Deviation	Deviation %
Ti–O	1.815(2)	1.823(5)	0.004	0.20
Ti–O–Ti	168.4(3)	163.9(2)	2.3	1.35
Ti–OPh	1.884(1)	1.909(3)	0.012	0.66
Ti–OH_2	2.099(1)	2.138(3)	0.019	0.92

Table 16. Deviations for selected geometrical parameters, bond lengths (Å) and angles (°) for compounds **38** (Mean1) and **24′** (Mean2).

Stirring **36** in a sodium methoxide/methanol mixture resulted in formation of the cyclic trimeric compound **39** (Figure 71) that was isolated as large, colourless block crystals after slow evaporation of the reaction mixture. A SCXRD study of these crystals showed the ligand binding mode of C_1 is conserved from the source fragment **36** to the structure of **39**. It was noted that the ligands were arranged with one facing "up" while two faced "down" with respect to the direction of the Ti–N pyridyl bond. The cyclic Ti_3O_3 core was found to be in a twist-boat conformation with a RMSD of 0.162 Å from a compromise between steric relief and favouring the formation of thermodynamically-favourable π-interactions about the Ti–O bonds. Lengthening of the Ti–OPh bonds *trans*- to the Ti–O–Ti bridge (Mean1, Table 17) in comparison to those *trans*- to the pyridyl ligand (Mean2, Table 17) was attributed to the stronger *trans*-influence of the oxo ligand. The weaker *trans*-influence of the tertiary nitrogen leads to a shortening of the corresponding Ti–O bonds by 4.8 % (Mean1, Table 17) while the stronger *trans*-influence of the phenolate results in a longer Ti–O bond.

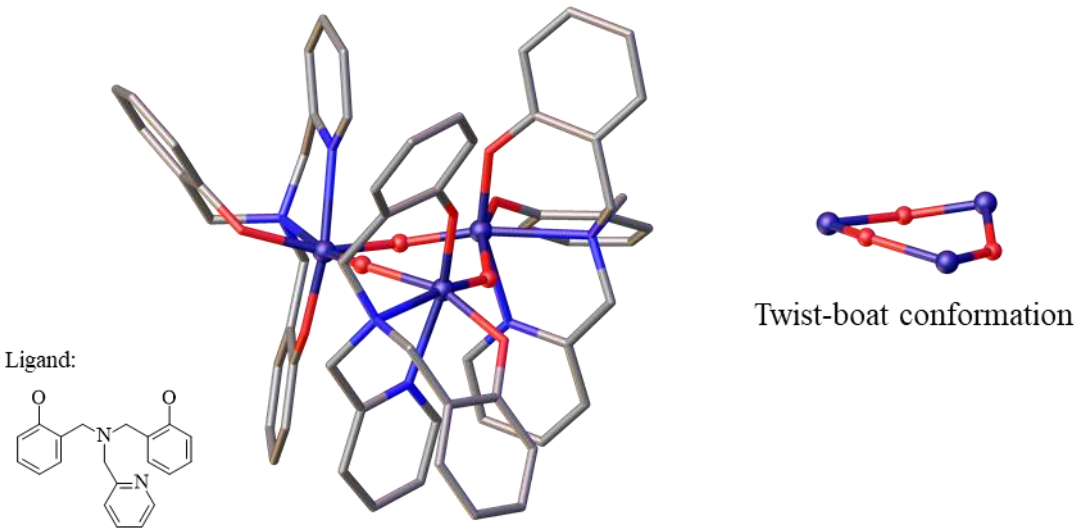

Figure 71. Asymmetric unit of **39** (left) and Ti_3O_3 core (right). Titanium-oxo core and aqua ligands are shown as spheres and ligand framework. Solvent of crystallisation, anions and hydrogen atoms omitted for clarity except in the case of aqua ligands. Ti = purple; C = grey; N = blue; O = red.

Parameter	Mean1	Mean2	Deviation	Deviation %
Ti–O	1.754(4)	1.929(4)	0.088	4.8
Ti–O–Ti	139.3(4)	-	-	-
O–Ti–O	96.70(2)	-	-	-
Ti–OPh	1.948(4)	1.880(4)	0.034	1.8
Ti_3O_3 plane RMSD	0.162	-	-	-

Table 17. Deviations for selected geometrical parameters, bond lengths (Å) and angles (°) for compound **39**, highlighting differences between the bond distances when a phenolate is *cis*- (Mean1) or *trans*- (Mean2) to the Ti–O–Ti bridge.

We envisaged that the terminal aqua ligands of compound **38** could be removed and the final product cyclised yet further stirring of this species, as well as heating, did not yield the expected cyclic tetrameric product. This lack of success in isolating a cyclised analogue of compound **38** through a stepwise synthesis was akin to the observations made with compound **24′**. In this previous work, solvothermal synthetic conditions were found to yield cyclic products and this method was applied herein.

6.3.2 Solvothermal synthesis

Initially, a solvothermal reaction, adapted from the literature[21] (with ligand precursor **30**$(H)_2$ and titanium(IV) propoxide in a 3 : 1 ratio of acetonitrile : THF), yielded a small quantity of pale yellow crystals that indicated the method could successfully lead to the

cyclic tetrameric compound **40**. The low yield (< 5 %) and weakly-diffracting crystals it produced, indicated that improvement of the method, by changing the reaction conditions, was required. The solvothermal conditions established in the synthesis of compounds **23-27** were employed and are summarised in Figure 72. Under these conditions, DMAP was used as a strong base to incite the weakening or breaking of Ti–O bonds and deprotonation of water to form oxo-bridges. Similarly, triethylamine was added as a base instead of DMAP, with an example in the literature of its use in the dissociation of Ti–O–Ti bridges.[25]

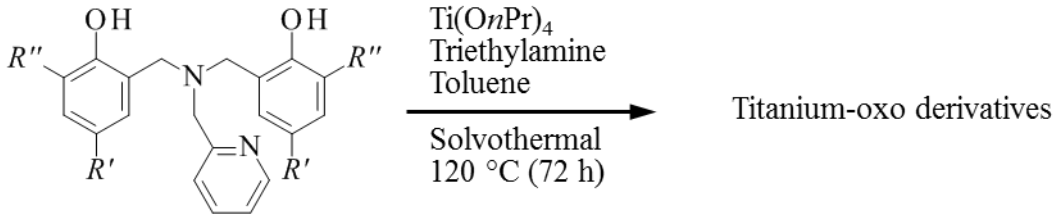

30$(H)_2$: R' = H; R'' = H
31$(H)_2$: R' = Me; R'' = H
32$(H)_2$: R' = Me; R'' = Me
33$(H)_2$: R' = *t*Bu; R'' = *t*Bu

Figure 72. Solvothermal conditions used to access titanium-oxo compounds supported by ligands **30-33**.

Treating titanium dichloride compounds **36** or **37** with triethylamine and titanium(IV) propoxide in toluene under solvothermal conditions resulted in the formation of an insoluble brown solid in the Teflon vessel, which we associated with degradation to polymeric products. The Ti–Cl bond is more reactive towards water and this may not be a stable building block to be used under solvothermal conditions. Reaction of compound **34**, formed *in situ*, at 120 °C for 72 h yielded pale yellow crystals after cooling that were identified as compound **40**. The improved diffraction quality provided by these crystals revealed the structure presented in Figure 73 featuring a cyclic tetrameric Ti_4O_4 core adopting a chair-chair conformation with RMSD of 0.156 Å from a plane drawn between the four titanium(IV) and four oxo centres, with selected geometrical parameters shown in Table 18. It was noted that the Ti–O bonds across the Ti–O–Ti bridges are asymmetrical, with a significant deviation of 3.6 % between the two values of 1.759(1) and 1.892(1). We proposed this to be the a *trans*-effect from the stronger trans influence of the oxo ligands in comparison to the tertiary nitrogen donor, with the shorter Ti–O bond *trans*- to the weaker tertiary nitrogen while the longer Ti–O bond is found to be *trans*- to a phenolate donor, with corresponding lengthening of this Ti–OPh bond.

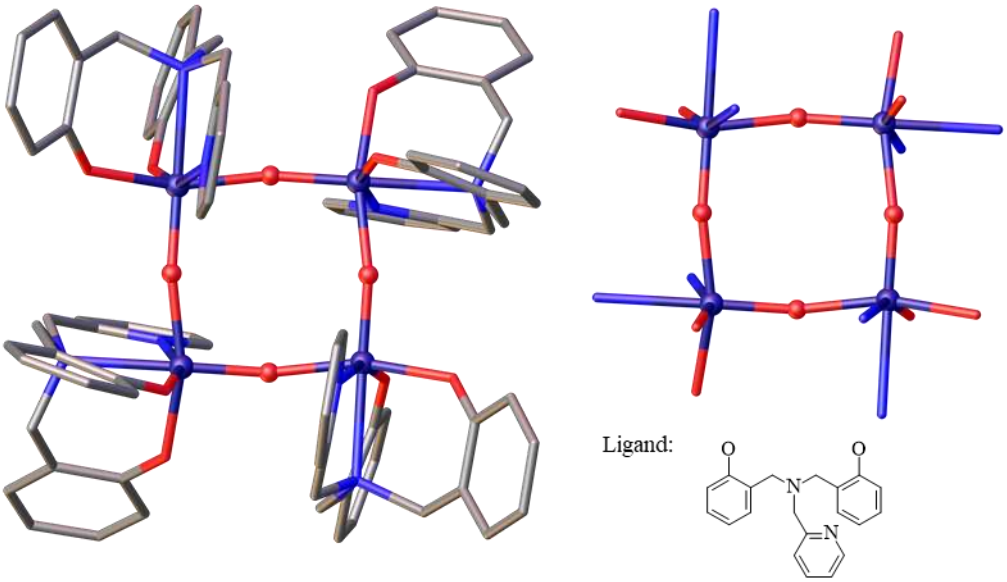

Figure 73. Left: Crystal structure of **40** grown from the asymmetric unit; Right: view of the coordination spheres of the titanium centres in **40**. Titanium-oxo core is shown as spheres and ligand framework displayed as tubes. Solvent of crystallisation and hydrogen atoms omitted for clarity. Ti = purple; C = grey; N = blue; O = red.

Parameter	Value1	Value2	Deviation	Deviation %
Ti–O	1.759(1)	1.892(1)	0.067	3.6
Ti–O–Ti	163.8(6)	-	-	-
O–Ti–O	100.3(6)	-	-	-
Ti–OPh	1.957(1)	1.888(1)	0.035	1.8

Table 18. Deviations for selected geometrical parameters, bond lengths (Å) and angles (°) for compound **40**, highlighting differences between the bond distances when a phenolate is *cis*- (Value1) or *trans*- (Value2) to the Ti–O–Ti bridge.

This synthetic route successfully increased the yield to 34.9 % compared to the conditions previously used.[21] This increase in yield could be driven by the poor solubility of compound **40** in toluene as well as other organic solvents, preventing us from studying this compound in solution. We proposed adding four equivalents of DMAP and heating in toluene could lead to increased solubility by reaction of the cyclic Ti_4O_4 core, as was observed for the cyclic analogue **23″**, but this lead to no change, with ^{1}H NMR spectra revealing the reaction mixture to yield unreacted **40** and DMAP.

We sought to improve the solubility of the cyclic titanium-oxo product by adding methyl groups to the *R′* positions through use of ligand **31**. Additionally, the solubility of the compound would allow purification of the crude mixture by column chromatography.

Solvothermal reaction of **31**$(H)_2$ with titanium propoxide and triethylamine in toluene gave an orange solution, from which the volatiles were removed and the mixture purified by column chromatography. Three bands were separated with the first yielding the desired cyclic tetrameric compound, the second cyclic trimeric and dimeric compounds and the third a mixture from the baseline. Each cyclic titanium-oxo compound was isolated by crystallisation in low yield and characterised by SCXRD. It was noted that after separation by column chromatography, the vials containing the yellow bands developed a white film after resting under ambient conditions for 20 mins, a possible indication the compounds are degrading via hydrolysis reactions to TiO_2 particles as reported in the literature.[10,26] Refinement of the column chromatography step (silica loading, eluent system, percentage triethylamine in eluent system, dry conditions) could lead to better purification of the reaction mixture.

The first band yielded small, yellow crystals that were studied by SCXRD to reveal the cyclic tetrameric structure **41** with formula Ti_4O_4**31**$_4$ (Figure 74), with all ligands exhibiting a C_1 binding mode to support a Ti_4O_4 core adopting a chair-chair conformation with RMSD of 0.081 Å for the plane drawn between the four titanium(IV) and four oxo centres. As observed with the other titanium-oxo compounds presented in this chapter, asymmetry was found across the Ti–O–Ti bridges of **41** with a significant deviation of 4.3 % between the Ti–O bonds, driven by the difference in *trans*-influence of phenolate and tertiary nitrogen donors in the structure (Table 19). A corresponding lengthening of the Ti–OPh bonds *trans*- to the oxo ligand was also observed, confirming the *trans*-influence of the different moieties is responsible for the asymmetric bonding through the Ti_4O_4 core. The structure of **41** was found to be isostructural with **40**, with low deviation between selected geometrical parameters (Table 20). The geometrical parameters for the Ti_4O_4 core show good agreement with reported parameters from the CSD, although the mean value for the Ti–O–Ti angle in **40** and **41** deviates towards a straight angle by 6.7 % (see Appendix).

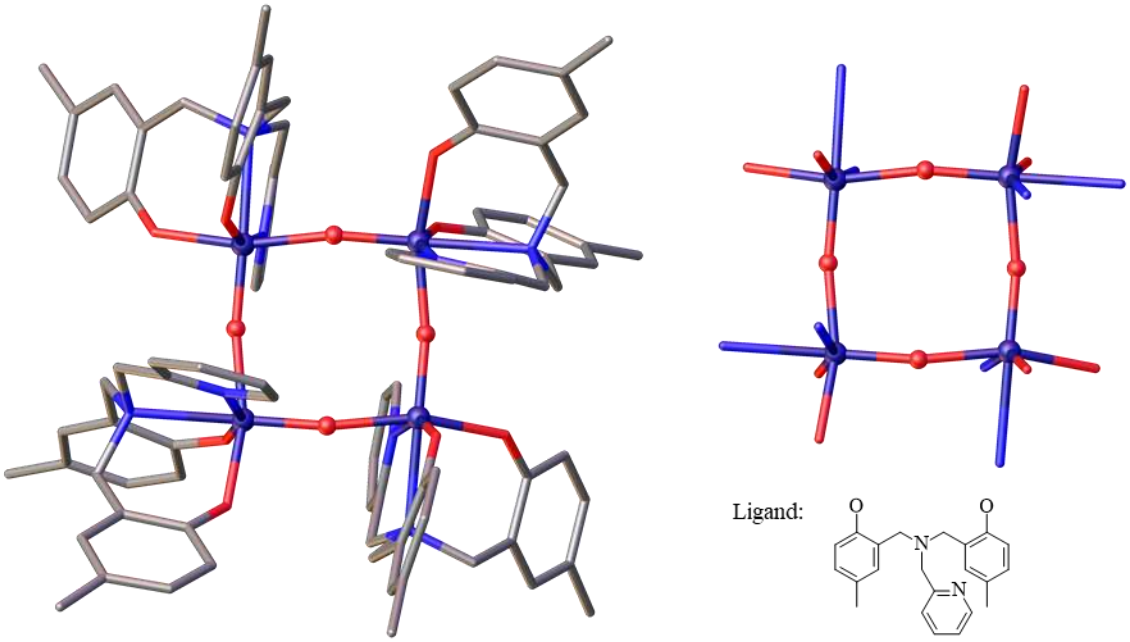

Figure 74. Left: Crystal structure of **41** grown from the asymmetric unit; Right: view of the coordination spheres of the titanium centres in **41**. Titanium-oxo core is shown as spheres and ligand framework displayed as tubes. Solvent of crystallisation and hydrogen atoms omitted for clarity. Ti = purple; C = grey; N = blue; O = red.

Parameter	Mean1	Mean2	Deviation	Deviation %
Ti–O	1.750(2)	1.908(2)	0.079	4.3
Ti–OPh	1.951(2)	1.891(2)	0.030	1.6

Table 19. Deviations for selected geometrical parameters, bond lengths (Å) and angles (°) from mean values of compounds **40** and **41**, highlighting differences between the bond distances when a phenolate is *cis*- (Mean1) or *trans*- (Mean2) to the Ti–O–Ti bridge.

Parameter	Mean1	Mean2	Deviation	Deviation %
Ti–O	1.823(1)	1.829(2)	0.003	0.2
Ti–O–Ti	163.8(6)*	167.8(2)	2.0	1.2
O–Ti–O	100.3(6)*	99.77(5)	0.3	0.3
Ti–OPh	1.923(1)	1.921(2)	0.001	0.1

Table 20. Deviations for selected geometrical parameters, bond lengths (Å) and angles (°) for compound **40** (Mean1) and compound **41** (Mean2).*indicates where a single value is available due to the symmetry in **40**.

The first compound characterised by SCXRD from the second band was the cyclic trimeric titanium-oxo compound **42** (Figure 75), which shares the same general formula $Ti_3O_3L_3$ as the cyclic trimeric compound **39**. Although these two compounds show similar share geometrical parameters with low deviation (Table 21), they cannot be said to be

isostructural since **39** displays 3 × C_1 symmetry while **42** displays a mixed 2 × C_1 plus 1 × C_S symmetry, leading to a core in a twist-boat conformation with RMSD of 0.081 Å. Furthermore, asymmetry about the Ti–O–Ti bridges was found and compared to the analogous cyclic trimeric compound **39**, with elongations of Ti–O bonds correlating with differences in *trans*-influence between the ligands (Table 22). There are several examples of Ti_3O_3 cores deposited on the CSD which show agreement with the geometrical parameters of the cores found in **39** and **42** (see Appendix).

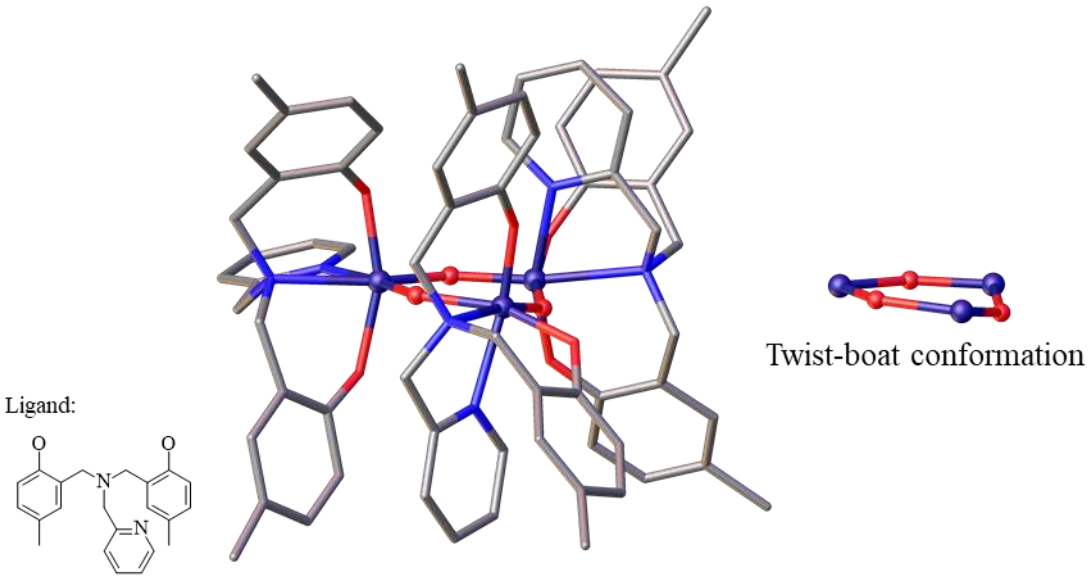

Figure 75. Left: Asymmetric unit of **42**; Right: view of the coordination spheres of the titanium centres in **42**. Titanium-oxo core is shown as spheres and ligand framework displayed as tubes. Solvent of crystallisation and hydrogen atoms omitted for clarity. Ti = purple; C = grey; N = blue; O = red.

Parameter	Mean1	Mean2	Deviation	Deviation %
Ti–O	1.842(4)	1.840(1)	0.001	0.1
Ti–O–Ti	139.3(4)	140.6(1)	0.6	0.5
O–Ti–O	96.70(3)	98.25(1)	0.8	0.8
Ti–OPh	1.914(4)	1.901(1)	0.006	0.3

Table 21. Deviations for selected geometrical parameters, bond lengths (Å) and angles (°) for compound **39** (Mean1) and compound **42** (Mean2).

Parameter	Mean1	Mean2	Deviation	Deviation %
Ti–O	1.763(4)	1.919(4)	0.078	4.2
Ti–OPh	1.944(4)	1.870(4)	0.037	1.9

Table 22. Deviations for selected geometrical parameters, bond lengths (Å) and angles (°) from mean values of compounds **39** and **42**, highlighting differences between the bond distances when a phenolate is *cis*- (Mean1) or *trans*- (Mean2) to the Ti–O–Ti bridge.

The final compound isolated by column chromatography was a cyclic dimeric structure, **43**, with formula $Ti_2O_2L_2$ (Figure 76). The Ti_2O_2 core was grown by symmetry from the space group $P\bar{1}$, with an inversion centre occupying the centroidal position of the Ti_2O_2 plane. Examples of similar Ti_2O_2 cores can be found in the literature,[7-9] with key geometrical parameters matching those found by SCXRD for **43** (see Appendix).

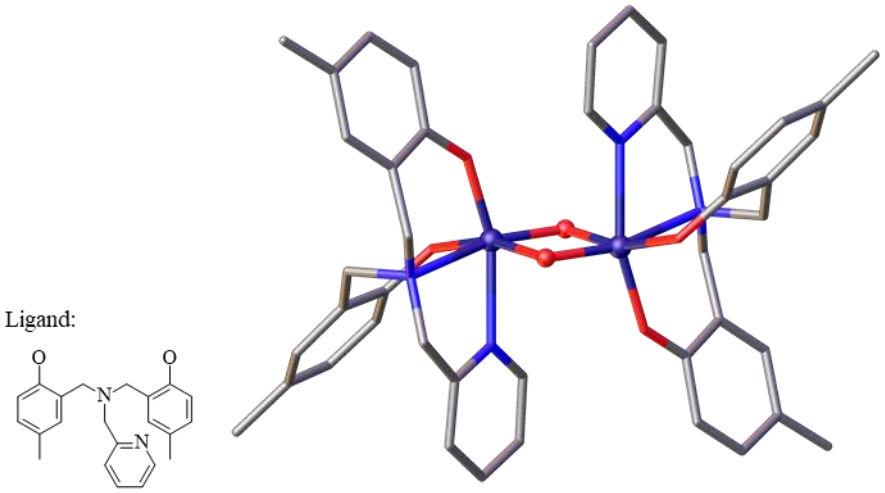

Figure 76. Crystal structure of **43** grown from the asymmetric unit. Titanium-oxo core is shown as spheres and ligand framework displayed as tubes. Solvent of crystallisation and hydrogen atoms omitted for clarity. Ti = purple; C = grey; N = blue; O = red.

Once again, asymmetry about the Ti–O–Ti bridges was observed with a lengthening of the Ti–O bonds associated with the differing *trans*-influence of the donors about the bridge. This lengthening was compared for the Ti–O–Ti bridges of **39**-**43**, whereby the lengthening of Ti–O and Ti–OPh bonds by 9.0 % and 3.1 % respectively was found to be characteristic of these amine bis(phenolate) supported cyclic titanium-oxo compounds, expressing low deviation in the lengthening of the bonds (Table 23).

Parameter	|Mean1 – Mean2|	Lengthening (%)	Deviation	Deviation %
Ti–O	0.158	9.0	0.010	0.5
Ti–OPh	0.061	3.1	0.011	0.6

Table 23. Deviations for lengthening of bond lengths (Å) associated with *trans*-effects across the Ti–O–Ti bridges of compounds **39**-**43**, when a phenolate is *cis*- (Mean1) or *trans*- (Mean2) to the Ti–O–Ti bridge.

The bulkier analogues, ligands **32** and **33**, were also used to synthesise titanium diisopropoxide precursors. These were subjected to the same solvothermal conditions but were found to yield different products after separation by fractional crystallisation. Using ligand **32**, the cyclic dimeric structure **44** with formula Ti_2O_2**32**$_2$ was isolated (Figure 77) and was found to be isostructural with **43** (Table 24), displaying the same asymmetry about the Ti–O–Ti bridges, and geometrical parameters in agreement with structures with a Ti_2O_2 core deposited on the CSD (see Appendix).

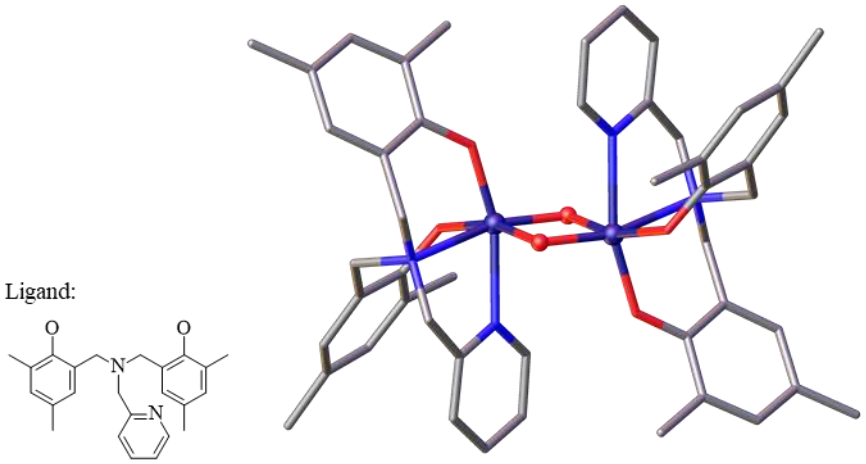

Figure 77. Crystal structure of **44** grown from the asymmetric unit. Titanium-oxo core is shown as spheres and ligand framework displayed as tubes. Solvent of crystallisation and hydrogen atoms omitted for clarity. Ti = purple; C = grey; N = blue; O = red.

Parameter	Value1	Value2	Deviation	Deviation %
Ti–O	1.864(1)	1.873(1)	0.004	0.2
Ti–O–Ti	96.54(3)	96.41(2)	0.1	0.1
O–Ti–O	83.46(3)	83.59(2)	0.1	0.1
Ti–OPh	1.906(1)	1.912(1)	0.003	0.1

Table 24. Deviations for selected geometrical parameters, bond lengths (Å) and angles (°) for compound **43** (Value1) and compound **44** (Value2).

6.4 The effect of steric bulk

The crude mixture from the reaction of **33** with titanium(IV) propoxide and triethylamine under solvothermal conditions yielded a mixture of a major and minor product as seen from the ^{1}H NMR spectrum of the crude reaction mixture. Fractional crystallisation yielded the titanium dipropoxide compound **45** and the linear dimetallic titanium-oxo dipropoxide compound **46** (Figure 78), with no higher nuclearity fragments observed. Overlaying the ^{1}H NMR spectra of **45** and **46** with the ^{1}H NMR spectrum of the crude reaction mixture, it was found that **45** is the major product (61.0 % conversion) while **46** is the minor product (27.4 % conversion), followed by signals showing traces of unidentified products accounting for the remaining 11.6 % of the reaction mixture (Figure 79). This confirmed the inability of titanium fragments bearing the bulkier ligand **33** to act as building blocks in the assembly of larger titanium-oxo structures.

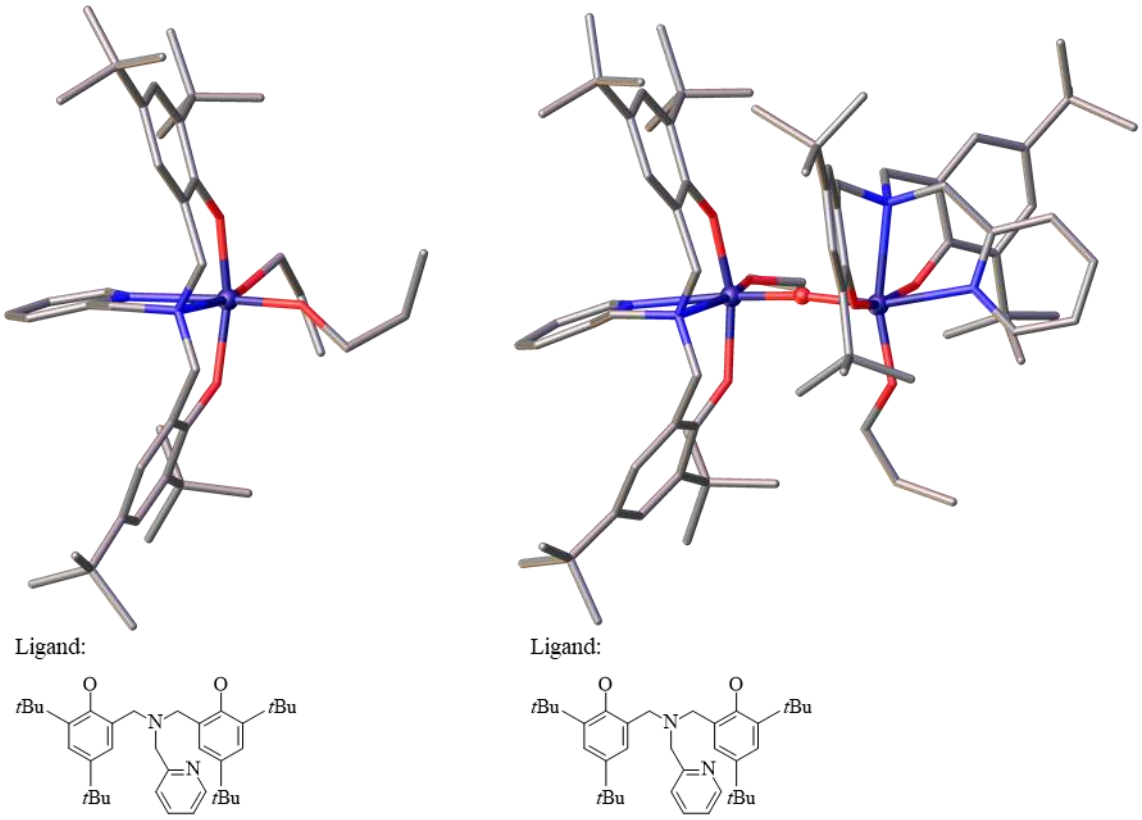

Figure 78. Left: Asymmetric unit of **45**; Right: Crystal structure of **46** grown from the asymmetric unit. Titanium-oxo core is shown as spheres and ligand framework displayed as tubes. Solvent of crystallisation and hydrogen atoms omitted for clarity. Ti = purple; C = grey; N = blue; O = red.

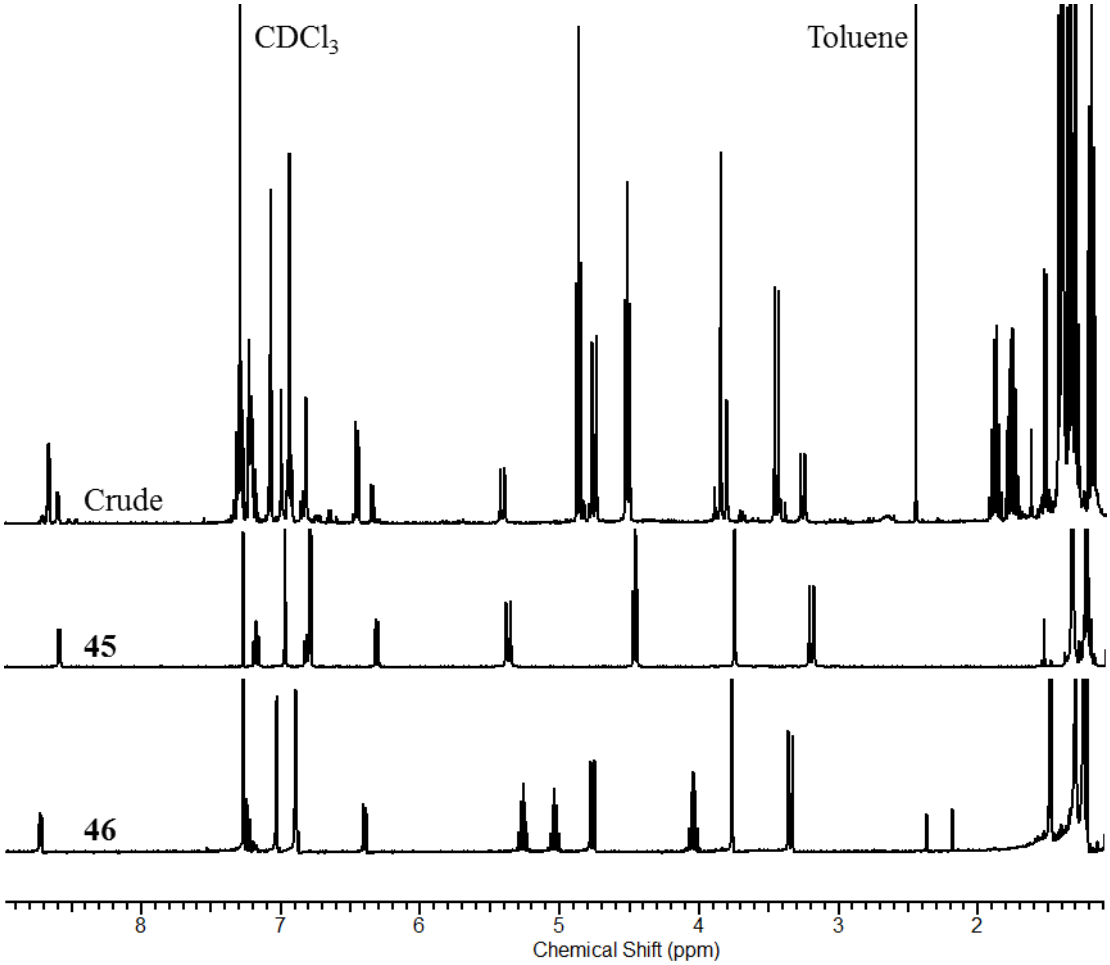

Figure 79. Overlay of ^{1}H NMR spectra for the crude reaction mixture and isolated products **45** and **46**.

To investigate the role of **33** in the assembly of larger titanium-oxo fragments, space-filling models were built using the crystal structures of **41** and **42** by addition of computed, idealised *tert*-butyl fragments to the *R′*/*R″* positions using the Olex2 software package (Figure 80).[27] These showed the extent of distortion required to accommodate *tert*-butyl groups in the *R″* positions for a cyclic trimeric or tetrameric core to form, with steric clashes between *tert*-butyl groups and phenolate rings from ligands bound to adjacent titanium centres. We related this to previous evidence of *tert*-butyl groups in the *R′*/*R″* positions exhibiting steric clashes preventing the formation of a cyclic $Ti_4O_4L_4$ core (L = **3** or **4**). The steric clashes from these models are strongly suggestive that steric bulk greatly influences the assembly of polynuclear titanium-oxo compounds, with increasing bulk correlating with decreasing nuclearity.

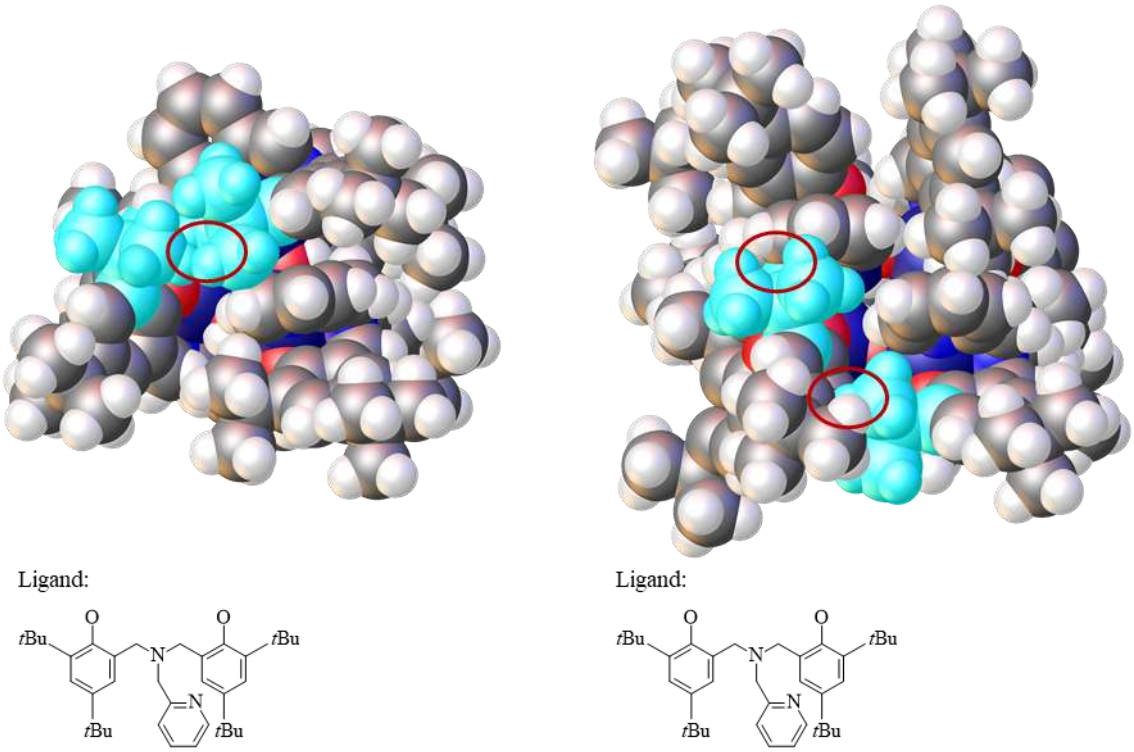

Figure 80. Left: model of Ti_3O_3**33**$_3$ built from the crystal structure of compound **42**. Right: model of Ti_4O_4**33**$_4$ built from the crystal structure of compound **41**. The *tert*-butyl groups in the *R″* positions of ligands exhibiting a steric clash are highlighted in light blue. Solvent of crystallisation omitted for clarity. Ti = purple; C = grey; N = blue; O = red; H = white.

6.5 Assembly of titanium-oxo species

Additionally, the increased steric bulk of **33** has enabled us to gain insight into the assembly of cyclic titanium-oxo compounds under solvothermal conditions (Figure 81). The dimetallic titanium-oxo fragment **45** was found to dimerise to the cyclic dimeric structure **47** when for two weeks in a solution of chloroform under ambient conditions (Figure 82), indicating this could occur by an alcohol self-condensation. Additionally, it could be imagined that the alcohol condensation between the dimetallic titanium-oxo fragment **45** and the monometallic fragment **46** could lead to the cyclic trimeric Ti_3O_3 core, which was found with compounds **39** and **42**, although the *tert*-butyl group in the *R″* positions of ligand **33** would prevent its formation in this system. Lastly, the assembly of a cyclic tetrameric Ti_4O_4 core could occur by alcohol condensation of two dimetallic fragments of **45** or the sequential addition of two monometallic fragments of **46** to the dimetallic fragment of **47**. Under this regime, we propose the ring closure to a cyclic trimeric core is in competition with the addition of the fourth monometallic fragment,

whereby adding steric bulk can slow this addition and favouring the formation of the cyclic trimeric core.

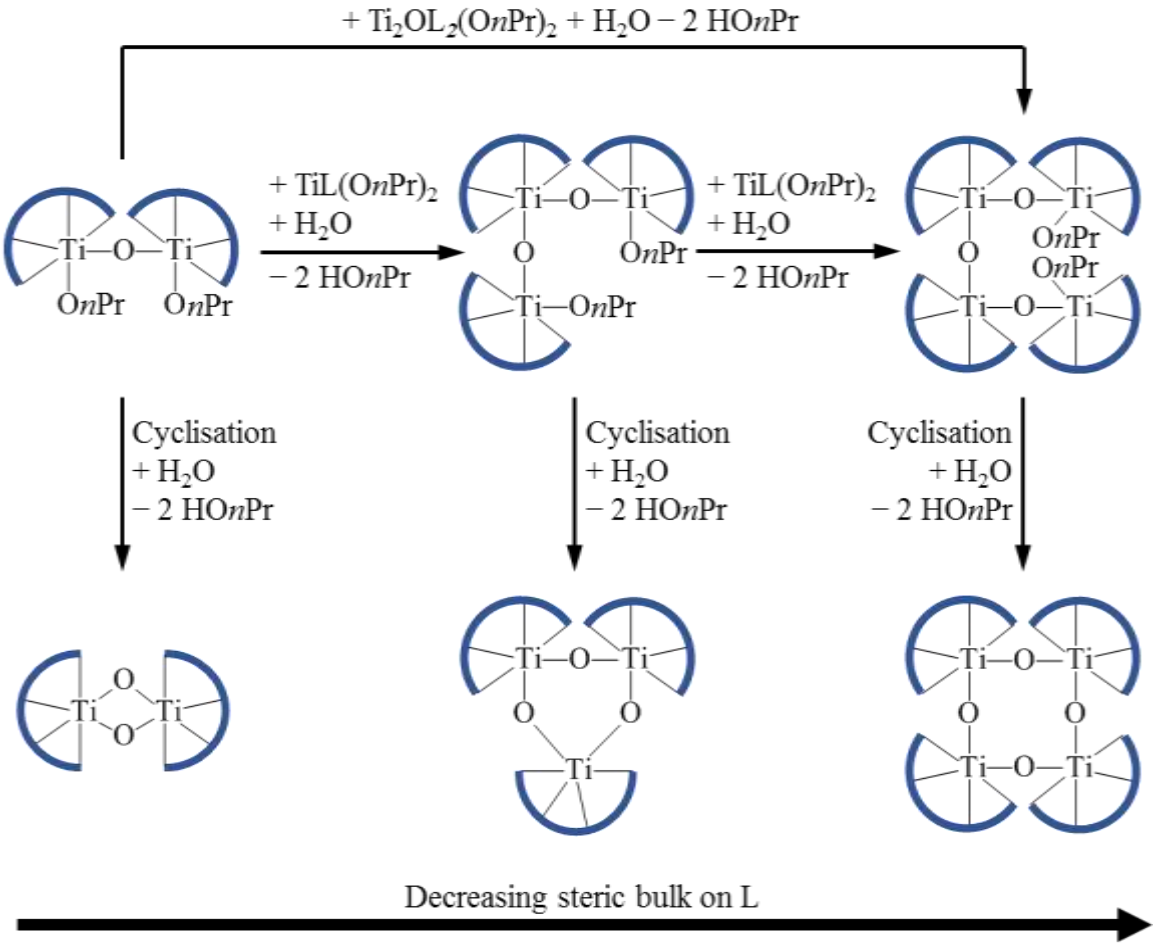

Figure 81. Schematic of proposed reaction steps in the assembly and cyclisation of di-, tri- and tetrametallic titanium-oxo compounds. The multidentate ligand, L, is denoted by a dark blue arc.

It was noted that the Ti_2O_2**33**$_2$ dimer (**47**), is isostructural to **43** and **44**, also proposed to be a minor product from the reaction. Interestingly, a change in ligand binding mode was observed between **45** ($2 \times C_S$) and **47** ($2 \times C_1$), another indication this ligand rearrangement process can occur at room temperature. Furthermore, the rearrangement must occur during the conversion of **45** to **47**, limiting the potential factors influencing the isomerisation. In this case, no DMAP was present and the presence of a strong, external base cannot be the drive for the ligand rearrangement to occur.

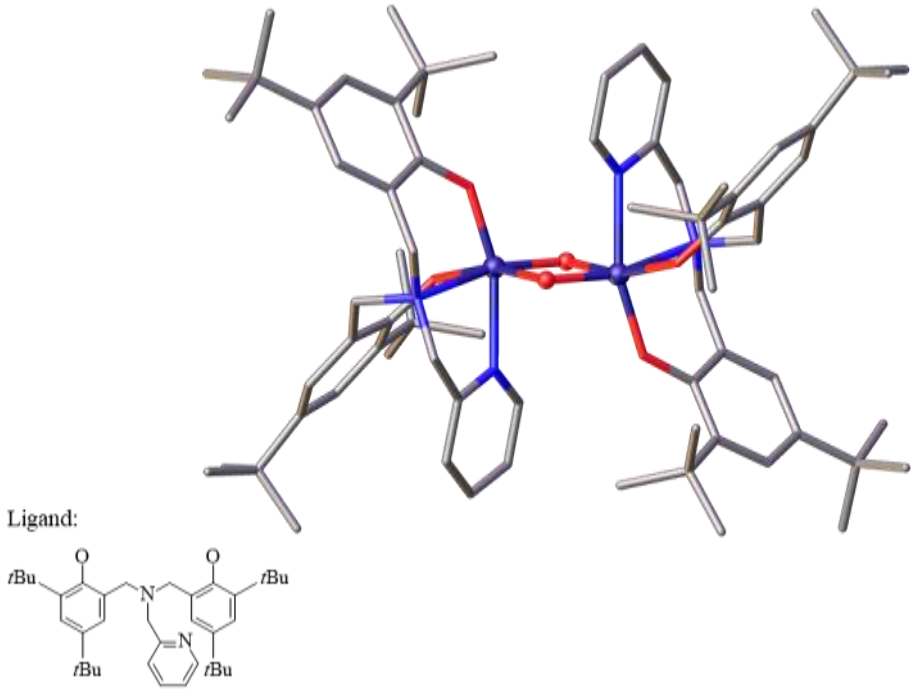

Figure 82. Crystal structure of **47** grown from the asymmetric unit. Titanium-oxo core is shown as spheres and ligand framework displayed as tubes. Solvent of crystallisation and hydrogen atoms omitted for clarity. Ti = purple; C = grey; N = blue; O = red.

Overall, increasing the bulk on the ligand has led to the formation of products with decreasing nuclearity (Figure 81). Much like with compound **26**, adding bulk in the form of *tert*-butyl group in the *R′* position prevented the formation of a cyclic tetrameric titanium-oxo compound. In this case, ligand **31** can support a less-sterically demanding cyclic trimeric titanium-oxo core as shown in compound **42**. Adding bulk in the *R″* position would in turn prevent the formation of the cyclic trimeric titanium-oxo species, resulting in a dimeric $Ti_2O_2L_2$ structure, which was observed with ligand **32** in compound **44**. In the case where *R′* = *R″* = *tert*-butyl (ligand **33**), we proposed the additional steric bulk is able to shield the titanium centre and slow the hydrolysis of the propoxide groups, leading to the stabilisation of the dipropoxide and linear titanium-oxo dipropoxide species **45** and **46**.

6.6 Conclusions

Replacing the carboxylate with a pyridine, an L-type donor, yielded analogous tetrametallic titanium-oxo compounds. Investigation of synthetic routes, using a stepwise via $Ti_4O_2L_4$ species or one-pot solvothermal conditions, yielded a variety of titanium-oxo compounds, with steric bulk leading to lower reactivity towards hydrolysis. Further to this, computed models revealed that bulk on the ligand periphery could lead to steric clashes in the formation of larger titanium-oxo compounds. These studies revealed a correlation between decreasing [TiOL] nuclearity when supported by ligands with increasing steric bulk. Finally, the characterisation of di-, tri- and tetrametallic titanium-oxo compounds that gave insight into the assembly between these species.

6.7 References

1. S. Barroso, F. Madeira, M. J. Calhorda, M. J. Ferreira, M. T. Duarte and A. M. Martins, *Inorg. Chem.*, 2013, **52**, 9427-9439.
2. A. J. Nielson and J. M. Waters, *Polyhedron*, 2010, **29**, 1715-1726.
3. J. L. Lamboy, A. Pasquale, A. L. Rheingold and E. Melendez, *Inorg. Chim. Acta*, 2007, **360**, 2115-2120.
4. P. Sobota, K. Przybylak, J. Utko, L. B. Jerzykiewicz, A. J. L. Pombeiro, M. F. C. G. da Silva and K. Szczegot, *Chem. Eur. J.*, 2001, **7**, 951-958.
5. L. A. Lesikar, A. F. Gushwa and A. F. Richards, *J. Organomet. Chem.*, 2008, **693**, 3245-3255.
6. Y. L. Fu, Y. L. Liu, Z. Shi, B. Z. Li and W. Q. Pang, *J. Solid State Chem.*, 2002, **163**, 427-435.
7. C. L. Boyd, T. Toupance, B. R. Tyrrell, B. D. Ward, C. R. Wilson, A. R. Cowley and P. Mountford, *Organometallics*, 2005, **24**, 309-330.
8. S. Meker, C. M. Manna, D. Peri and E. Y. Tshuva, *Dalton Trans.*, 2011, **40**, 9802-9809.
9. M. Miller and E. Y. Tshuva, *Eur. J. Inorg. Chem.*, 2014, **2014**, 1485-1491.
10. N. Sharma, V. Sharma, R. Bohra, V. S. Raju, I. P. Lorenz, C. Krinninger and P. Mayer, *Inorg. Chim. Acta*, 2007, **360**, 3002-3012.
11. T. Okamatsu, R. Irie and T. Katsuki, *J. Organomet. Chem.*, 2007, **692**, 645-653.
12. D. Peri, S. Meker, M. Shavit and E. Y. Tshuva, *Chem. Eur. J.*, 2009, **15**, 2403-2415.
13. D. Peri, S. Meker, C. M. Manna and E. Y. Tshuva, *Inorg. Chem.*, 2011, **50**, 1030-1038.
14. C. M. Manna, G. Armony and E. Y. Tshuva, *Inorg. Chem.*, 2011, **50**, 10284-10291.
15. M. Shavit and E. Y. Tshuva, *Eur. J. Inorg. Chem.*, 2008, 1467-1474.
16. L. Liu, J. Li, Z. G. Sun, D. P. Dong, N. Zhang, X. Lu, W. N. Wang and F. Tong, *Z. anorg. allg. Chem.*, 2010, **636**, 247-252.
17. E. Y. Tshuva, M. Versano, I. Goldberg, M. Kol, H. Weitman and Z. Goldschmidt, *Inorg. Chem. Commun.*, 1999, **2**, 371-373.
18. S. Ali, C. A. Muryn, F. Tuna and R. E. P. Winpenny, *Dalton Trans.*, 2010, **39**, 124-131.
19. S. Ali, C. A. Muryn, F. Tuna and R. E. P. Winpenny, *Dalton Trans.*, 2010, **39**, 9588-9597.
20. I. S. Tidmarsh, L. J. Batchelor, E. Scales, R. H. Laye, L. Sorace, A. Caneschi, J. Schnack and E. J. L. McInnes, *Dalton Trans.*, 2009, 9402-9409.
21. K. Hong, W. Bak and H. Chun, *Inorg. Chem.*, 2014, **53**, 7288-7293.
22. A. J. Chmura, M. G. Davidson, M. D. Jones, M. D. Lunn, M. F. Mahon, A. F. Johnson, P. Khunkamchoo, S. L. Roberts and S. S. F. Wong, *Macromolecules*, 2006, **39**, 7250-7257.
23. Y.-L. Wong, Y. Yan, E. S. H. Chan, Q. Yang, T. C. W. Mak and D. K. P. Ng, *J. Chem. Soc., Dalton Trans.*, 1998, 3057-3064.
24. H. Sopo, A. Lehtonen and R. Sillanpaa, *Polyhedron*, 2008, **27**, 95-104.
25. S. Barroso, A. M. Coelho, S. Gomez-Ruiz, M. J. Calhorda, Z. Zizak, G. N. Kaluderovic and A. M. Martins, *Dalton Trans.*, 2014, **43**, 17422-17433.
26. G. Y. Zhang, J. Hou, C. H. Tung and Y. F. Wang, *Inorg. Chem.*, 2016, **55**, 3212-3214.
27. O. V. Dolomanov, L. J. Bourhis, R. J. Gildea, J. A. K. Howard and H. Puschmann, *J. Appl. Crystallogr.*, 2009, **42**, 339-341.

Chapter 7 – Conclusions

Titanium metal is relatively cheap, abundant and biocompatible, polynuclear complexes were synthesised with an emphasis on the use of amine bis(phenolate) ligands with a bridging carboxylate pendant donor. Our initial attempt to synthesise a metal cluster through ligand-directed assembly led to a series of polynuclear titanium aggregate supported by amine bis(phenolate) ligands. The presence of a labile donor on the titanium centre resulted in dynamic behaviour in solution, which could be prevented by addition of strong donors. These polynuclear aggregates were successfully applied as initiators in the ROP of *rac*-lactide, where the activity in solution correlated with decreasing nuclearity of the aggregates, in turn directed by the steric bulk on the ligand. Overall, adding steric bulk in the *ortho* position of the phenolate groups led to different performance under solution or melt conditions, with increased activity under solution conditions (less aggregation) and less activity under melt conditions (steric bulk hinders monomer approach to active site). Adding a chiral backbone to the ligand framework further decreased aggregation while inducing stereoselectivity in the ROP of *rac*-lactide, yielding polylactide with increased isotacticity. The presence of two active sites, one achiral and the other chiral, revealed the need for steric bulk in the *ortho* position to favour catalysis at the chiral site.

Further work explored the incorporation of titanium-oxo motifs to improve stability of the polynuclear complexes. Hydrolysis of the dynamic, polynuclear titanium aggregates leading to formation of a single product. This titanium-oxo compound adopted a tetragonal disphenoid motif, characterised as a tetranuclear Ti_4 'dimeric form' in the solid state. In the presence of a strong donor solvent, the Ti_4 'dimeric form' was found to dissociate to two Ti_2 'monomeric' units. This feature was proposed to contribute to the air/water and thermal stability of the compounds, establishing the Ti_4 form as pre-catalysts while the Ti_2 form is the active species in the ROP of *rac*-lactide under melt conditions. Altering the peripheral groups on the ligands was shown to affect the primary solvation sphere, with increased solubility correlating with increased activity. A fluorinated analogue was found to be the most active under melt polymerisation conditions, where the polar fluoro groups improve solubility in polar molten *rac*-lactide.

The reaction of $Ti_4O_2L_4$ complexes with DMAP led to the synthesis and characterisation of linear and cyclic tetrametallic titanium-oxo compounds, with structural formulae $[Ti_4O_3L_4(H_2O)_2][DMAP{\cdot}H]_2$ and $[Ti_4O_4L_4][DMAP{\cdot}H]_4$ respectively. Solvothermal conditions were observed to favour the formation of cyclic titanium-oxo compounds, although the use of *tert*-butyl groups on the ligand periphery prevented the formation of cyclised compounds. The cyclic tetrameric compounds were dynamic when solubilised and, surprisingly, the dissociation of a Ti–O–Ti bridge was favoured to yield the linear tetrametallic species. Furthermore, ligand rearrangement reactions, resulting in a chiral or achiral environment at the titanium centre, were found to occur under ambient conditions and polymerisation conditions. This has implications for complexes in chiral catalysis supported by amine bis(phenolate) ligands.

The linear and cyclic tetrametallic compounds were evaluated in the ROP of *rac*-lactide and found to be active under solution and melt polymerisation conditions. The microstructure of the polylactide produced using these titanium-oxo compounds differed to that produced by DMAP, while agreement was found with the microstructure produced by other titanium-oxo catalysts. This demonstrated that the titanium centres were likely to be the active sites during the polymerisation process. However, a study of the catalytic mixture recovered after melt polymerisation of *rac*-lactide found the titanium-oxo species had degraded to unidentifiable products, where residual DMAP/$DMAP{\cdot}H^+$ was the active species when reused.

The dynamic nature of the linear and cyclic titanium-oxo compounds was attributed to the ambidentate carboxylate donor, which provides stability to the titanium centre undergoing changing oxidation states. In light of this, a pyridyl donor was installed on the ligand and we synthesised a series of pyridyl-amine bis(phenolate) ligands with altered steric bulk on the phenolate groups. Using these ligands, monometallic and dimetallic titanium fragments were synthesised and hydrolysed in a stepwise fashion. Sterically-bulky fragments, as well as those featuring isopropoxide versus chloride groups, were found to be less reactive towards hydrolysis. Solvothermal conditions were observed to favour the formation of cyclic titanium-oxo compounds. The nuclearity of the compounds correlated with the degree of steric bulk on the ligand, with di-*tert*-butyl derivatives limiting product formation to monometallic titanium $TiL(OnPr)_2$ and dimetallic titanium-oxo $Ti_2OL_2(OnPr)_2$ species. Decreasing the steric bulk allowed for the formation of cyclic Ti_xO_x compounds with a nuclearity x of two, three and four.

Overall, our investigations gave insight into the stepwise construction of titanium-oxo compounds using multidentate ligands. Ultimately, this will allow for controlled construction of stable titanium-oxo metal clusters and nanoparticles. Applying these systems in the ROP of *rac*-lactide revealed interesting trends between catalyst/initiator design and performance. Further to this, the in-depth solution/solid state studies of these polynuclear complexes revealed interesting features, such as *in situ* activation of $Ti_4O_2L_4$ compounds under melt conditions or steric effects inducing chirality in TiL(O*i*Pr) aggregates. The homogeneity of the systems allowed for the depth of characterisation necessary to obtain this knowledge and transfer it to future designs of polynuclear complexes to improve performance.

Chapter 8: Appendix

8.1 Experimental details

Starting materials were purchased and used as received from Sigma-Aldrich, Acros and Fluorochem. Where stated, *rac*- and *L*-lactide were sublimed and stored under a dry N_2 atmosphere prior to use. Dry solvents were purified in an MBRAUN SPS-800 and stored over activated 4 Å molecular sieves under a dry N_2 atmosphere. NMR spectroscopy data was acquired with a Bruker AVIII 300 MHz instrument or Bruker AVIII 400 MHz instrument at 298 K unless otherwise stated. ^{1}H DOSY NMR experiments were recorded on a Bruker AVIII 400 MHz instrument with samples at 50 nM concentration and tetramethylsilane standard. Electrospray ionisation (ESI) and electron impact ionisation (EI) were recorded using a Bruker micrOTOF II. Nanoelectrospray ionisation (NSI) and matrix-assisted laser desorption (MALDI) mass spectra were obtained by the EPSRC National Mass Spectrometry Facility (NMSF), Swansea, UK. Elemental microanalysis was carried out on an Exeter CE-440 Elemental Analyse. Single crystal X-ray diffraction data was acquired using a Bruker Apex-II diffractometer operating at 173 K with Mo-K_α radiation or Rigaku SuperNova diffractometer operating at 120 K with Cu-K_α radiation. CCDC numbers containing supplementary crystallographic information are given where applicable. These data can be obtained free of charge from The Cambridge Crystallographic Data Centre. Molecular weights (M_n) and molecular mass distributions (M_w / M_n) of polymers were determined by GPC at 35 °C using THF as eluent with a flow rate of 1.0 mL min^{-1}. The experimental values were obtained relative to a calibration curve using polystyrene standards, which were corrected with Mark-Houwink parameters and by a factor of 0.58.[1]

8.2 Synthesis of carboxylamine bis(phenolate) ligand precursors

Compound 1(H)$_3$[2,3]

Under N_2, glycine (1.50 g, 20 mmol) was dissolved in a solution of sodium hydroxide (0.80 g, 20 mmol) in methanol (50 mL). Salicylaldehyde (2.12 mL, 20 mmol) was added to yield a yellow solid in suspension which then dissolved to give a clear yellow solution. Sodium borohydride (0.83 g, 22 mmol) was added slowly to yield a white precipitate in a clear colourless solution. After 15 mins stirring, the reaction mixture was evaporated to dryness and the resulting white solids dissolved in water (20 mL) and acidified to pH 4 with 1 M aqueous hydrochloric acid. The white precipitate was filtered, dried and weighed (3.128 g, 86%). This was identified as the monophenolate adduct by ^{1}H and ^{13}C NMR. The above procedure was repeated to obtain the bis(phenolate) adduct, **1**(H)$_3$, as a white precipitate. Yield (1.816 g, 32%); ^{1}H NMR (400 MHz, [D$_6$]DMSO): δ 10.73 (br, ArOH), 7.12 (m, 4H, ArH), 6.77 (m, 4H, ArH), 3.77 (s, 4H, CH_2), 3.20 (s, 2H, CH_2); ^{13}C NMR (75.5 MHz, [D$_6$]DMSO): δ 172.55, 156.93, 130.60, 129.08, 122.99, 119.32, 115.85, 53.86, 53.40; HRMS (NSI$^+$): *m*/*z* calcd for $C_{16}H_{17}NO_4$: 288.1230 [*M*+H]$^+$; found 288.1235; elemental analysis calcd (%) for $C_{16}H_{17}NO_4$: C 66.89, H 5.96, N 4.87; found: C 66.77, H 5.83, N 4.65. Crystal data available in Section 8.11.1 and the CD-R found inside the back cover of this thesis.

Compound 2(H)$_3$[4]

Sodium hydroxide (0.80 g, 20 mmol) was dissolved in methanol (60 mL) with *p*-cresol (4.326 g, 40 mmol) and glycine (1.50 g, 20 mmol). Paraformaldehyde (1.20 g, 40 mmol) was added and the reaction mixture was heated to reflux for 24 h under N_2. The suspension turned clear and the reaction was quenched with water (120 mL) and washed with diethyl ether (5 × 50 mL). The aqueous phase was concentrated, acidified with 1 M aqueous hydrochloric acid to pH 4 to yield a white solid that was filtered and recrystallised from methanol. Yield (0.836 g, 13%); ^{1}H NMR (300 MHz, [D$_6$]DMSO): δ 10.49 (br, ArOH), 6.97 (m, 4H, ArH), 6.72 (m, 2H, ArH), 3.89 (s, 2H, CH_2), 3.34 (s, 4H, CH_2); 2.19 (s, 3H, CH_3). ^{13}C NMR (75.5 MHz, [D$_6$]DMSO): δ 171.86, 154.15, 130.68, 129.04, 127.17, 121.96, 115.21, 53.31, 52.83, 20.13; HRMS (NSI$^+$): *m*/*z* calcd for $C_{18}H_{22}NO_4$: 316.1543 [*M*+H]$^+$; found 316.1544; elemental analysis calcd (%) for $C_{18}H_{21}NO_4$: C 68.55; H 6.71; N 4.44; found:

C 68.46; H 6.57; N 4.24. Crystal data available in Section 8.11.1 and the CD-R found inside the back cover of this thesis.

Compound 3(H)$_3$

Paraformaldehyde (1.20 g, 40 mmol) was added to a colourless solution in methanol (30 mL) of sodium hydroxide (0.80 g, 20 mmol), 4-*tert*-butylphenol (4.326 g, 40 mmol) and glycine (1.50 g, 20 mmol). The reaction mixture was heated to reflux for 48 h under N_2. The suspension turned clear and the reaction was quenched with water (120 mL) and washed with diethyl ether (3 × 30 mL). The aqueous phase was concentrated on the rotary evaporator. The resulting viscous liquid was acidified with 1 M aqueous hydrochloric acid from pH 10 to pH 4 to yield a white solid that was filtered, triturated with chloroform and recrystallised from methanol. Yield (3.279g, 41%); ^{1}H NMR (300 MHz, [D$_6$]DMSO): δ 10.54 (br, ArOH), 7.12 (m, 4H, ArH), 6.72 (d, 4H, ArH), 3.75 (s, 4H, CH_2), 3.19 (s, 2H, CH_2); 1.22 (s, 18H, CH_3). ^{13}C NMR (75.5 MHz, [D$_6$]DMSO): δ 172.59, 154.57, 141.28, 127.25, 125.56, 121.99, 115.35, 53.81, 34.08, 31.88; HSQC spectroscopy experiment showed both methylene environments resonate at 53.81 ppm; HRMS (NSI$^-$): *m*/*z* calcd for $C_{24}H_{32}NO_4$: 398.2337 [M–H]$^-$; found 398.2326; elemental analysis calcd (%) for $C_{24}H_{33}NO_4$: C 72.15, H 8.33, N 3.51; found: C 72.05, H 8.16, N 3.25. Crystal data available in Section 8.11.1 and the CD-R found inside the back cover of this thesis.

Compound 4(H)$_3$[5,6]

To a solution of sodium hydroxide (0.80 g, 20 mmol) in methanol (30 mL) was added 2,4-di-*tert*-butylphenol (8.253 g, 40 mmol) and glycine (1.50 g, 20 mmol). Paraformaldehyde (1.20 g, 40 mmol) was added and the reaction mixture was heated to reflux for 48 h under N_2. A white precipitate formed and was filtered, washed with 3 × 30 mL ice-cold methanol and dried. A white precipitate formed and was filtered, washed with 3 × 30 mL ice-cold methanol and dried. Yield: 6.834 g (66.8 %). ^{1}H NMR (300 MHz, $CDCl_3$): δ 7.22 (d, 2H, ArH), 6.89 (d, 2H, ArH), 3.69 (s, 4H, CH_2), 3.29 (s, 2H, CH_2), 1.40 (s, 18H, CH_3), 1.29 (s, 18H, CH_3); ^{13}C NMR (75.5 MHz, $CDCl_3$): δ 171.4, 152.7, 141.2, 136.3, 125.2, 124.2, 120.0, 60.5, 57.3, 34.9, 34.1, 31.6, 29.6; HRMS (ESI$^+$): m/z calcd for $C_{32}H_{50}NO_4$: 512.3734 [M+H]$^+$; found 512.3709; elemental analysis calcd (%) for $C_{32}H_{49}NO_4$: C, 75.11; H, 9.65; N, 2.74; found: C 74.98; H 9.52; N 2.69.

Compound *rac*-9(H)$_3$

S-alanine (1.782 g, 20 mmol) and 2,4-di-*tert*-butylphenol (4.326 g, 40 mmol) were dissolved in a solution of sodium hydroxide (0.80 g, 20 mmol) in methanol (30 mL). Paraformaldehyde (1.20 g, 40 mmol) was added and the reaction mixture was heated to reflux for 72 h under N_2. The solvents were removed to give off-white solids that were dissolved in methanol (30 mL). The yellow solution was acidified with aqueous 1 M hydrochloric acid and the white precipitate collected and thoroughly dried. The product was isolated by column chromatography (gradient 90:10 to 50:50, dichloromethane:ethyl acetate with 0.1 % acetic acid) as a white powder. Yield: 4.036 g (48.8 %). ^{1}H NMR (400 MHz, $CDCl_3$): δ 7.17 (d, 2H, ArH), 7.03 (s, 2H, ArH), 6.87 (d, 2H, ArH), 4.53 (br, 2H, CH_2), 4.18 (br, 2H, CH_2). 3.86 (br, 1H, CH), 1.58 (br, 3H, CH_3), 1.18 (s, 18H, CH_3); ^{13}C NMR (100.6 MHz, $CDCl_3$): δ 176.2, 154.3, 142.2, 128.0, 127.7, 116.7, 116.1, 60.6, 59.9, 53.8, 31.5, 14.2; HRMS (ESI$^+$): m/z calcd for $C_{25}H_{36}NO_4$: 414.2642 $[M+H]^+$; found 414.2657; elemental analysis calcd (%) for $C_{25}H_{35}NO_4$: C, 72.61; H, 8.53; N, 3.39; found: C 72.32; H 8.22; N 3.31.

Compound *rac*-10(H)$_3$

Sodium hydroxide (0.80 g, 20 mmol) was dissolved in methanol (30 mL) followed by additions of 2,4-di-*tert*-butylphenol (8.253 g, 40 mmol) and *S*-alanine (1.782 g, 20 mmol). Paraformaldehyde (1.20 g, 40 mmol) was added and the reaction mixture was heated to reflux for 96 h under N_2. After removing the solvents, the resulting off-white solids that were dissolved in methanol (30 mL). Acidification of the yellow solution with aqueous 1 M hydrochloric acid yielded a white precipitate that was collected and thoroughly dried. The product was isolated by column chromatography (gradient 95:5 to 70:30, dichloromethane:ethyl acetate with 0.1 % acetic acid) as a white powder. Yield: 6.224 g (59.2 %). ^{1}H NMR (300 MHz, $CDCl_3$): δ 7.16 (d, 2H, ArH), 6.81 (d, 2H, ArH), 4.11 (d, 2H, CH_2), 3.73 (q, 1H, CH), 3.36 (d, 2H, CH_2), 1.38 (d, 3H, CH_3), 1.30 (s, 18H, CH_3), 1.19 (s, 18H, CH_3); ^{13}C NMR (75.5 MHz, $CDCl_3$): δ 174.5, 152.8, 141.2, 136.3, 125.2, 124.1, 119.9, 60.3, 55.9, 53.0, 34.9, 34.1, 31.6, 29.6, 14.3; HRMS (ESI$^+$): m/z calcd for $C_{33}H_{52}NO_4$: 526.3890 $[M+H]^+$; found 526.3883; elemental analysis calcd (%) for $C_{33}H_{51}NO_4$: C, 75.39; H, 9.78; N, 2.66; found: C 75.30; H 9.54; N 2.67. Crystal data available in Section 8.11.1 and the CD-R found inside the back cover of this thesis.

Compound 17(H)$_3$

Method A: Following the same procedure as for compound **2**(H)$_3$, brown solids were obtained. The product was isolated by column chromatography with 90:10 dichloromethane:methanol as eluent as a light brown solid. Yield (0.466 g, 7%).

Method B:[7] To a mixture of ethanol (15 mL) and water (2 mL) was added glycine (0.8258 g, 11 mmol), 4-fluorophenol (2.803 g, 25 mmol), triethylamine (0.500 mL, 4 mmol) and 37 wt% formaldehyde solution (3.30 mL, 40 mmol). The solution was heated to 50 °C for 10 days followed by stirring at RT for 24 h. The light brown precipitate was filtered and recrystallised from methanol. Yield (0.483 g, 14%);^{1}H NMR (300 MHz, [D$_6$]DMSO): δ 10.62 (br, ArOH), 6.98 (dd, 2H, ArH), 6.90 (td, 2H, ArH), 6.73 (dd, 2H, ArH) 3.69 (s, 4H, CH_2), 3.15 (s, 2H, CH_2); ^{13}C NMR (75.5 MHz, [D$_6$]DMSO): δ 172.70, 156.35, 154.03, 152.58, 124.84, 124.77, 116.17, 116.09, 116.02, 115.79, 114.56, 114.33, 54.09, 52.96; ^{19}F NMR (376.5 MHz, [D$_6$]DMSO): δ –125.97 (sxt, ArF); HRMS (NSI$^-$): *m*/*z* calcd for $C_{16}H_{14}F_2NO_4$: 322.0896 $[M–H]^-$; found 322.0887; elemental analysis calcd (%) for $C_{16}H_{15}F_2NO_4$: C 59.44, H 4.68, N 4.33; found: C 59.29, H 4.56, N 4.21. Crystal data available in Section 8.11.1 and the CD-R found inside the back cover of this thesis.

8.3 Synthesis of polynuclear titanium isopropoxide complexes

The dynamic nature of these polynuclear titanium aggregates leads to complex NMR spectra. For **10**-**14**, NMR data will be presented for the complex in $CDCl_3$ followed by $CDCl_3$ with DMAP inserted as a strong donor to reduce aggregation. Additional data for **12** in D$_6$-DMSO was also obtained and displayed two sets of signals with a 1 : 0.4 ratio. The dynamic mixture of these aggregates can lead to non-integer integration values.

8.3.1 General method

Under N_2, titanium(IV) isopropoxide (0.154 mL, 0.5 mmol) was added to a suspension of the ligand precursor (0.5 mmol) in dry THF (5 mL). The yellow/orange reaction mixture was stirred for 2 h after which solvents were removed under vacuum.

Complex 5

The yellow solid was suspended in dry toluene, filtered, dried and weighed. Yield: 0.3764 g (96.2 %). ^{1}H NMR (400 MHz, 293 K, inferred by HMQC): δ 9.67-5.49 (ArH),

6.70-5.92 (CH), 5.25-4.01 (CH_2), 3.66-2.21 (CH_3); ^{13}C CP-MAS NMR (100.6 MHz, 293 K): δ 182.2, 181.7, 181.5, 165.6, 161.9, 160.3, 133.5, 131.3, 130.4, 129.6, 129.0, 127.8, 127.2, 125.6, 125.3, 124.6, 124.0, 122.9, 121.5, 120.0, 118.3, 115.9, 115.0, 114.5, 82.6, 81.0, 64.7, 63.7, 63.2, 62.9, 60.9, 59.9, 27.0, 26.1, 24.8; HRMS (EI): m/z calcd for $C_{19}H21NO_5$: 391.1 $[M]^{\cdot+}$; found 391.0.

Complex 6

The yellow solid was suspended in dry acetonitrile, filtered, dried and weighed. Yield: 0.3668 (87.5 %). ^1H NMR (400 MHz, $CDCl_3$): δ 7.14-5.99 (m, 6H, ArH), 5.27-2.50 (m, 7H, CH / CH_2), 2.41-0.74 (m, 15H, CH_3); ^1H NMR (400 MHz, $CDCl_3$ / DMAP): δ 8.23 (br, 2H, ArH DMAP), 7.03-6.24 (br, 8H, ArH / ArH DMAP), 4.66 (br, 1 H, CH), 3.96 (m, 0.5H, CH), 3.68 (br, 2H, CH_2), 3.24 (br, 2H, CH_2), 2.96 (s, 6H, CH_3 DMAP), 2,18 (br, 6H, CH_3), 1.17 (br, 10H, CH_3); ^{13}C NMR (100.6 MHz, $CDCl_3$ / DMAP): δ 181.8, 174.6 (br), 164.0, 158.7, 155.1, 149.2 (br), 130.3 (br), 130.1, 130.0, 129.8, 129.7, 129.0 (br), 128.8, 125.7, 125.0, 123.9, 116.7, 115.9, 115.8, 106.6, 81.1 (br), 64.6, 64.4, 62.5, 60.0, 39.1, 25.4, 24.5, 20.6, 20.5; MS (MALDI): m/z calcd for $C_{24}H_{34}NO_6Ti$: 480.2 $[M+H+HOiPr]^+$; found 480.1. HRMS (ESI^-): m/z calcd for $C_{21}H_{28}NO_5Ti$: 422.1447 $[M+(H)_3]^-$; found 422.1146.

Complex 7

The orange solid was suspended in dry acetonitrile, filtered, dried and weighed. Yield: 0.4286 (85.1 %). ^1H NMR (400 MHz, $CDCl_3$): δ 7.26-6.21 (m, 6H, ArH), 5.42-2.61 (m, 7H, CH / CH_2), 2.11-0.79 (m, 24H, CH_3); ^1H NMR (400 MHz, $CDCl_3$ / DMAP): δ 8.22 (br, 2H, ArH DMAP), 7.17 (d, 2H, ArH), 6.96 (s, 2H, ArH), 6.71 (br, 2H, ArH), 6.41 (d, 2H, ArH DMAP), 4.67 (br, 1H, CH), 3.96 (m, 0.5H, CH), 3.77 (br, 2H, CH_2), 3.24 (br, 2H, CH_2), 2.96 (s, 6H, CH_3 DMAP), 1.17 (br, 28H, CH_3); ^{13}C NMR (100.6 MHz, $CDCl_3$ / DMAP): δ 181.7, 174.7 (br), 163.5, 158.5, 154.8 (br), 149.3 (br), 142.5 (br), 126.5 (br), 126.0, 124.7, 123.5 (br), 116.4 (br), 106.6, 80.8 (br), 64.4, 63.4 (br), 39.2, 34.1, 31.6, 25.4, 24.6; HRMS (ESI^-): m/z calcd for $C_{27}H_{40}NO_5Ti$: 506.2386 $[M+(H)_3]^-$; found 506.2104.

Complex 8

The orange solid was dissolved in dry THF. Clear, orange crystals were obtained at –20 °C which were filtered, dried and weighed. Yield: 0.5236 g (85.0 %). ^1H NMR (400 MHz, $CDCl_3$): δ 10.41 (d, 0.1H, C=O···HO*i*Pr), 7.38-6.55 (m, 4H, ArH),

5.45-2.34 (m, 7H, CH / CH_2), 1.83-0.67 (m, 42H, CH_3); ^{1}H NMR (400 MHz, $CDCl_3$ / DMAP): δ 8.46 (d, 0.75H, ArH DMAP), 8.20 (br, 3.25H, ArH DMAP), 7.19 (d, 2H, ArH), 6.83 (d, 2H, ArH), 6.41 (m, 4H, DMAP), 4.46 (sept, 0.75H, CH), 3.95 (sept, 1H, CH), 3.78 (d, 1H, CH_2), 3.35 (s, 1H, CH_2), 3.22 (br, 1H, CH_2), 3.15 (d, 1H, CH_2), 2.96 (m, 12H, DMAP), 1.45 (m, 18H, CH_3), 1.21 (m, 18H, CH_3), 1.13 (d, 6H, CH_3), 1.08 (d, 2.5H, CH_3), 1.00 (d, 2.5H, CH_3); ^{1}H NMR (400 MHz, CD_6SO): δ 7.12 (br, 2H, ArH), 7.06 (m, 0.4H, ArH), 7.00 (m, 2H, ArH), 6.87 (m. 0.4H, ArH), 5.01 (br, 0.8H, CH), 4.28 (m, 0.4H, CH_2), 4.04 (s, 1.5H, CH_2), 3.78 (sept, 2H, CH), 3.48 (m, 3H, CH_2), 3.25 (m, 0.4H, CH_2), 2.88 (d, 0.4H, CH_2), 2.78 (br, 1,5H, CH_2), 1.41 (m, 25.2H, CH_3), 1.23 (m, 25.2H, CH_3), 1.05 (m, 16.2H, CH_3); ^{13}C NMR (100.6 MHz, $CDCl_3$ / DMAP): δ 175.0, 174.0, 160.1, 155.3, 154.7, 150.4, 149.4, 141.5, 141.3, 136.1, 135.3 (br), 125.0, 124.3, 124.2, 124.0, 123.6, 106.6, 106.3, 80.9, 79.7, 64.3, 64.2, 63.8, 62.5 (br), 57.6, 39.2, 39.1, 35.2, 35.1, 34.3, 31.7, 29.9, 29.8, 25.4, 25.3; MS (MALDI): m/z calcd for $C_{35}H_{53}NO_5Ti$: 615.3 $[M+H]^+$; found 615.3. Crystal data available in Section 8.11.1 and the CD-R found inside the back cover of this thesis.

Complex *rac*-13

The orange solid was dissolved in dry toluene. An orange precipitate was obtained at –20 °C which was filtered, washed, dried and weighed. Yield: 0.4857 g (93.9 %). ^{1}H NMR (400 MHz, $CDCl_3$): δ 7.19 (d, 1H, ArH), 7.15 (dd, 1H, ArH), 7.02 (d, 1H, ArH), 6.97 (d, 1H, ArH), 6.54 (t, 2H, ArH), 4.67 (sept, 1H, CH), 4.28 (d, 1H, CH_2), 4.07 (sept, 1H, CH), 3.53 (d, 1H, CH_2), 3.43 (d, 1H, CH_2), 3.23 (q, 1H, CH), 3.07 (d, 1H, CH_2), 1.45 (d, 3H, CH_3), 1.32 (m, 30H, CH_3); ^{1}H NMR (400 MHz, $CDCl_3$ / DMAP): δ 8.19 (br, 2H, ArH DMAP), 7.17 (dd, 1H, ArH), 7.12 (br, 1H, ArH), 7.00 (d, 1H, ArH), 6.97 (br, 1H, ArH), 6.77 (d, 1H, ArH), 6.59 (d, 1H, ArH), 6.40 (d, 2H, ArH DMAP), 4.73 (br, 1H, CH), 3.95 (sept, 1H, CH), 3.63 (d, 1H, CH_2), 3.48 (m, 3H, CH_2 / CH), 3.10 (m, 1H, CH_2), 2.94 (s, 6H, CH_3 DMAP), 1.22 (s, 9H, CH_3), 1.18 (m, 12H, CH_3), 1.13 (d, 12H, CH_3); ^{13}C NMR (100.6 MHz, $CDCl_3$ / DMAP): δ 176.4, 164.2 (br), 159.6 (br), 154.7 (br), 149.6 (br), 142.7, 141.7, 126.4, 124.1, 123.1, 116.6, 115.5, 106.6, 80.7 (br), 77.3, 77.0, 76.7, 64.3 (br), 61.1, 39.0, 34.1, 34.0, 31.6, 31.6, 25.4, 24.6, 24.5, 9.1; MS (EI): m/z calcd for $C_{31}H_{47}NO_6Ti$: 577.3 $[M+HO\textit{i}Pr]^+$; found 577.5; m/z calcd for $C_{28}H_{40}NO_5Ti$: 518.2 $[M+H]^+$; found 518.2.

Complex *rac*-14

The orange solid was dissolved in dry THF. An orange precipitate was obtained at –20 °C which was filtered, washed, dried and weighed. Yield: 0.5692 g (90.4 %). ^{1}H NMR (400 MHz, $CDCl_3$): δ 7.21 (dd, 2H, ArH), 6.96 (d, 1H, ArH), 6.84 (d, 1H, ArH), 4.49 (sept, 1H, CH), 4.03 (m, 3.5H, CH_2), 3.82 (q, 1H, CH), 3.40 (d, 0.75H, CH_2), 3.32 (d, 0.75H, CH_2), 1.56 (d, 3H, CH_3), 1.49 (d, 9H, CH_3), 1.44 (d, 9H, CH_3), 1.29 (d, 9H, CH_3), 1.26 (d, 15H, CH_3); ^{1}H NMR (400 MHz, $CDCl_3$ / DMAP): δ 8.26 (br, 2H, ArH DMAP), 7.21 (d, 1H, ArH), 7.10 (br, 1H, ArH), 6.87 (m, 2H, ArH), 6.38 (d, 2H, ArH DMAP), 4.46 (br, 1H, CH), 3.94 (sept, 0.5H, CH), 3.56 (m, 2H, CH_2 / CH), 3.36 (d, 1H, CH_2), 3.00 (d, 2H, CH_2), 2.95 (s, 6H, CH_3 DMAP), 1.48 (s, 9H, CH_3), 1.37 (m, 12H, CH_3), 1.22 (s, 9H, CH_3), 1.16 (s, 9H, CH_3), 1.12 (d, 3H, CH_3), 1.03 (d, 3H, CH_3), 0.95 (d, 3H, CH_3); ^{13}C NMR (100.6 MHz, $CDCl_3$ / DMAP): δ 176.7, 163.1 (br), 158.8, 155.0, 149.5 (br), 141.4, 140.8, 136.3, 135.1, 124.7, 124.5 (br), 124.3 (br), 124.1, 123.6, 123.3, 106.6, 79.6 (br), 65.1 (br), 64.3, 61.4, 53.0 (br), 39.1, 35.2, 34.8, 34.3, 34.2, 31.7, 31.7, 29.9, 29.9, 25.4, 25.3, 9.4; MS (ESI$^+$): m/z calcd for $C_{36}H_{56}NO_5Ti$: 630.3633 $[M+H]^+$; found 630.3596.

8.4 Synthesis of titanium-oxo tetragonal disphenoids

8.4.1 General method

Under N_2, titanium(IV) isopropoxide (0.308 mL, 1 mmol) was added to a suspension of the ligand precursor (1 mmol) in dry THF (6 mL). The yellow/orange reaction mixture was stirred for 2 h after which excess water (four equivalents) was added dropwise. Stirring was continued overnight (in the case of **21**, the solution was warmed to 35 °C). The suspension was concentrated under vacuum and the yellow/orange precipitate was filtered and triturated.

Compound 18

After trituration from THF, the yellow solids were dried and weighed. Yield 0.167 g (49%); ^{1}H NMR (400 MHz, $CDCl_3$): δ 7.26 (m, 2H, ArH), 7.01 (m, 2H, ArH), 6.86 (m, 3H, ArH), 6.72 (td, 1H, ArH), 3.77 (d, 1H, CH_2), 3.30 (d, 1H, CH_2), 3.17 (d, 1H, CH_2), 3.06 (d, 1H, CH_2), 2.94 (d, 1H, CH_2), 2.67 (d, 1H, CH_2); ^{13}C NMR (100.6 MHz, $CDCl_3$): δ 181.85, 165.74, 160.49, 130.05, 129.75, 129.61, 129.41, 125.67, 125.16, 120.86, 119.75, 116.26, 116.03, 64.55, 62.53, 60.00; HRMS (NSI$^+$): *m*/*z* calcd

for: 681.0834 $C_{32}H_{29}N_2O_9Ti_2$ $[0.5(M)+H]^+$; found 681.0827; elemental analysis calcd (%) for $C_{64}H_{56}N_4O_{18}Ti_4$: C 56.49, H 4.15, N 4.12; found: C 56.35, H 4.06, N 4.25. Crystal data available in Section 8.11.1 and the CD-R found inside the back cover of this thesis.

Compound 19

After trituration from THF, the yellow solids were dried and weighed. Yield 0.169 g (53%); ^{1}H NMR (400 MHz, $CDCl_3$): δ 7.03 (td, 2H, ArH), 6.79 (d, 2H, ArH), 6.72 (dd, 2H, ArH), 3.74 (d, 1H, CH_2), 3.29 (d, 1H, CH_2), 3.10 (d, 1H, CH_2), 3.07 (d, 1H, CH_2), 2.88 (d, 1H, CH_2), 2.58 (d, 1H, CH_2), 2.27 (s, 3H, CH_3), 2.19 (s, 3H, CH_3); ^{13}C NMR (100.6 MHz, $CDCl_3$): δ 181.81, 163.94, 158.64, 130.23, 130.11, 129.98, 129.83, 129.70, 128.77, 125.61, 124.92, 115.91, 115.74, 64.62, 62.44, 60.03, 20.61, 20.52; HRMS (NSI^+): *m*/*z* calcd for $C_{36}H_{37}N_2O_9Ti_2$: 737.1461 $[0.5(M)+H]^+$; found 737.1454; elemental analysis calcd (%) for $C_{72}H_{72}N_4O_{18}Ti_4$: C 58.72, H 4.93, N 3.80; found: C 58.36, H 4.96, N 3.81. Crystal data available in Section 8.11.1 and the CD-R found inside the back cover of this thesis.

Compound 20

After trituration from toluene, the orange solids were dried and weighed. Yield 0.223 g (50%); ^{1}H NMR (400 MHz, $CDCl_3$): δ 7.25 (dd, 1H, ArH), 7.19 (dd, 1H, ArH), 7.01 (d, 1H, ArH), 6.92 (d, 1H, ArH), 6.76 (d, 1H, ArH), 6.72 (d, 1H, ArH), 3.78 (d, 1H, CH_2), 3.41 (d, 1H, CH_2), 3.21 (d, 1H, CH_2), 3.10 (d, 1H, CH_2), 2.89 (d, 1H, CH_2), 2.72 (d, 1H, CH_2), 1.25 (s, 9H, $C(CH_3)_3$), 1.20 (s, 9H, $C(CH_3)_3$); ^{13}C NMR (100.6 MHz, $CDCl_3$): δ 181.62, 163.41, 158.48, 143.22, 142.51, 126.43, 126.39, 126.23, 125.27, 124.70, 124.66, 115.39, 115.26, 64.56, 62.74, 60.72, 34.12, 34.06, 31.80, 31.47; HRMS (NSI^+): *m*/*z* calcd for $C_{48}H_{61}N_2O_9Ti_2$: 905.3342 $[0.5(M)+H]^+$; found 905.3487; elemental analysis calcd (%) for $C_{96}H_{120}N_4O_{18}Ti_4$: C 63.72, H 6.68, N 3.10; found: C 63.85, H 6.84, N 2.92. Crystal data available in Section 8.11.1 and the CD-R found inside the back cover of this thesis.

Compound 21

After trituration from toluene, the orange solids were dried and weighed. Yield 0.282 g (50 %);^{1}H NMR (400 MHz, $CDCl_3$): δ 7.30 (d, 1H, ArH), 7.22 (d, 1H, ArH), 6.87 (d, 1H, ArH), 6.76 (d, 1H, ArH), 3.58 (d, 1H, CH_2), 3.37 (d, 1H, CH_2), 3.23 (d, 1H, CH_2), 3.07 (d, 1H, CH_2), 2.76 (d, 1H, CH_2), 2.62 (d, 1H, CH_2), 1.59 (s, 1H, CCH_3), 1.49 (s, 1H, CCH_3), 1.25 (s, 1H, CCH_3), 1.24 (s, 1H, CCH_3); ^{13}C NMR

(100.6 MHz, $CDCl_3$): δ 181.2, 162.4, 158.5, 141.8, 141.3, 136.0, 135.4, 126.1, 125.1, 124.7, 123.6, 123.5, 66.1, 62.5, 60.9, 35.3, 35.0, 34.3, 34.2, 32.0, 31.6, 31.1, 30.8; HRMS (NSI^+): *m*/*z* calcd for $C_{64}H_{93}N_2O_9Ti_2$: 1129.5850 $[0.5(M)+H]^+$; found 1129.5823; elemental analysis calcd (%) for $C_{128}H_{184}N_4O_{18}Ti_4$: C 68.08, H 8.21, N 2.48; found: C 67.82, H 8.11, N 2.04. Crystal data available in Section 8.11.1 and the CD-R found inside the back cover of this thesis.

Compound 22

After trituration from THF, the orange solids were dried and weighed. Yield 0.168 g (49%); ^1H NMR (400 MHz, $CDCl_3$): δ 6.97 (m, 2H, ArH), 6.80 (m, 4H, ArH), 3.76 (d, 1H, CH_2), 3.23 (s, 2H, CH_2), 3.16 (d, 1H, CH_2), 3.01 (d, 1H, CH_2), 2.70 (d, 1H, CH_2); ^{13}C NMR (100.6 MHz, $CDCl_3$): δ 181.77, 162.00, 158.09, 157.19, 156.56, 155.69, 154.81, 126.05, 125.98, 125.83, 125.76, 117.21, 117.13, 116.66, 116.59, 116.45, 116.22, 116.14, 115.98, 115.92, 115.74, 64.48, 61.94, 59.63; ^{19}F NMR (376.5 MHz, $CDCl_3$): δ –121.61 (sxt, ArF), –123.62 (sxt, ArF); HRMS (NSI^+): *m*/*z* calcd for $C_{32}H_{25}F_4N_2O_9Ti_2$: 753.0457 $[0.5(M)+H]^+$; found 753.0452; elemental analysis calcd (%) for $C_{64}H_{48}F_8N_4O_{18}Ti_4$: C 51.09, H 3.22, N 3.72; found: C 51.21, H 3.44, N 3.59. Crystal data available in Section 8.11.1 and the CD-R found inside the back cover of this thesis.

8.5 Synthesis of titanium-oxo tetrametallic species

8.5.1 Stepwise synthesis

In a sealed flask, $Ti_4O_2L_4$ (0.1 mmol) and DMAP (0.122 g, 0.1 mmol) were stired in toluene (2 mL) for 2 h at 130 °C. The reaction mixture was cooled to room temperature to give crystals after standing overnight.

Compound 23′

Yield 0.009 g (5%). Crystal data available in Section 8.11.1 and the CD-R found inside the back cover of this thesis.

Compound 24′

Note that this is a major product. Yield 0.122 g (68.9%); ^1H NMR (400 MHz, $CDCl_3$): δ 9.40 (br s, 2H, DMAP·H), 8.44 (d, 4H, DMAP·ArH), 6.99 (d, 2H, ArH), 6.90 (d, 2H, ArH), 6.73 (m, 10H, ArH+DMAP ArH), 6.63 (m, 4H, ArH),

6.51 (d, 2H, ArH), 6.23 (m, 6H, ArH+CH_2), 6.10 (br, 2H, ArH), 5.77 (br, 2H, ArH), 5.28 (br d, 2H, CH_2), 3.57 (m, 6H, CH_2), 3.37 (m, 6H, CH_2), 3.02 (d, 2H, CH_2), 2.89 (m, 14H, CH_2+DMAP CH_3), 2.58 (m, 4H, CH_2), 2.27 (s, 6H, CH_2), 2.18 (s, 6H, CH_2), 2.14 (s, 6H, CH_2), 2.09 (s, 6H, CH_2); ^{13}C NMR (100.6 MHz, $CDCl_3$): δ 176.5, 174.7, 163.6, 161.1, 160.1, 157.8, 156.8, 141.9 ,137.9, 130.9, 130.4, 130.1, 129.9, 129.2, 129.1, 128.8, 128.3, 128.2, 127.9, 126.1, 125.3, 124.8, 124.6, 124.4, 117.5, 117.3, 116.5, 114.9, 107.4, 64.2, 63.5, 62.1, 61.2, 60.0, 57.5, 39.5, 21.4, 20.6, 20.6, 20.5, 20.4; HRMS (NSI^+): *m*/*z* calcd for $C_{86}H_{96}N_8O_{19}Ti_4$: 1736.4710 $[M-2H_2O+2H]^+$; found 1736.4607; elemental analysis calcd (%) for $C_{86}H_{98}N_8O_{21}Ti_4$: C 58.32, H 5.58, N 6.33; found: C 57.88, H 6.03, N 5.92. Crystal data available in Section 8.11.1 and the CD-R found inside the back cover of this thesis.

Compound 24″

Note that this is a minor product. Crystal data available in Section 8.11.1 and the CD-R found inside the back cover of this thesis.

8.5.2 Solvothermal synthesis

Compound 23″

Titanium(IV) propoxide (0.55 mL, 2 mmol), compound **1**$(H)_3$ (0.5742 g, 2 mmol) and triethylamine (0.279 mL, 2 mmol) were stirred for 5 mins in toluene (4 mL) in a Teflon vessel. A clear, yellow solution was obtained from which the stirrer bar was removed and the Teflon vessel sealed in an autoclave and heated to 120 °C for 72 h. After cooling for 24 h, the vessel was opened, the yellow crystals filtered, washed with toluene and dried. Yield 0.652 g (69.1%); ^{1}H NMR (400 MHz, $CDCl_3$): δ 14.00 (br s, 4H, DMAP·H), 8.52 (br s, 8H, DMAP ArH), 7.13 (dd, 4H, ArH), 6.73 (td, 4H, ArH), 6.59 (td, 4H, ArH), 6.47 (td, 4H, DMAP ArH), 6.39 (dd, 4H, ArH), 6.13 (m, 12H, ArH+CH_2), 5.96 (dd, 4H, ArH), 5.30 (br s, 8H, DMAP ArH), 4.56 (d, 4H, CH_2), 3.20 (d, 4H, CH_2), 3.09 (d, 4H, CH_2), 2.87 (m, 8H, CH_2), 2.65 (s, 24H, DMAP CH_3); elemental analysis calcd (%) for $C_{92}H_{100}N_{12}O_{20}Ti_4$: C 58.61, H 5.35, N 8.92; found: C 58.31, H 5.32, N 8.63. Crystal data available in Section 8.11.1 and the CD-R found inside the back cover of this thesis.

Compound 25

In a Teflon vessel, titanium(IV) propoxide (0.55 mL, 2 mmol), compound **2**$(H)_3$ (0.6307 g, 2 mmol) and triethylamine (0.279 mL, 2 mmol) were stirred for

5 mins in toluene (4 mL). A clear, yellow solution was obtained from which the stirrer bar was removed and the Teflon vessel sealed in an autoclave and heated to 120 °C for 72 h. After cooling for 24 h, the yellow solution was filtered and yellow crystals isolated by vapour diffusion with acetonitrile. Yield 0.552 g (55.3%); ^{1}H NMR (400 MHz, $CDCl_3$): δ 13.94 (br s, 4H, DMAP·H), 8.53 (br s, 8H, DMAP ArH), 6.91 (d, 4H, ArH), 6.51 (d, 4H, ArH), 6.38 (d, 4H, ArH), 6.17 (d, 4H, DMAP ArH), 6.07 (d, 4H, CH_2), 5.97 (d, 4H, ArH), 5.80 (d, 4H, ArH), 5.32 (br s, 8H, DMAP ArH), 4.51 (d, 4H, CH_2), 3.07 (m, 8H, CH_2), 2.84 (m, 8H, CH_2), 2.66 (s, 24H, DMAP CH_3), 2.06 (s, 12H, CH_3), 1.92 (s, 12H, CH_3); elemental analysis calcd (%) for $C_{100}H_{116}N_{12}O_{20}Ti_4$: C 60.13, H 5.85, N 8.41; found: C 59.30, H 5.98, N 7.83. Crystal data available in Section 8.11.1 and the CD-R found inside the back cover of this thesis.

Compound 26

Titanium(IV) propoxide (0.55 mL, 2 mmol), compound **1**$(H)_3$ (0.5742 g, 2 mmol) and triethylamine (0.279 mL, 2 mmol) were stirred for 5 mins in toluene (4 mL) in a Teflon vessel. A clear, yellow solution was obtained from which the stirrer bar was removed and the Teflon vessel sealed in an autoclave and heated to 120 °C for 72 h. After cooling for 24 h, the orange solution was left to slowly evaporate to yield a small quantity of orange crystals. Yield (0.028 g, 2.7%). Crystal data available in Section 8.11.1 and the CD-R found inside the back cover of this thesis.

8.5.3 Conversion in solution

Compound 27

Compound **26** (0.020 g, 0.011 mmol) was dissolved in $CDCl_3$ and left to stand in a sealed NMR tube. Large, plate-like, yellow crystals appeared after 2 days, which were filtered, dried and weighed. Yield (0.012 g, 68.2%). Crystal data available in Section 8.11.1 and the CD-R found inside the back cover of this thesis.

8.6 DMAP control experiments

Compound 28[8]

In toluene (12 mL), lactide (0.1441 g, 1 mmol) and DMAP (0.1222 g, 1 mmol) were stirred in a sealed flask and heated to 130 °C for 30 mins. After cooling, the flask was left open to air and the toluene slowly evaporated to yield large,

colourless crystals. Yield 0.225 g (79.2%); ^{1}H NMR (300 MHz, $CDCl_3$): δ 9.05 (br, 1H, DMAP·H), 8.19 (d, 2H, DMAP ArH), 6.54 (d, 2H, DMAP ArH), 5.10 (q, 1H, CH), 4.30 (q, 1H, CH), 3.06 (s, 6H, DMAP CH_3), 1.49 (d, 3H, CH_3), 1.44 (d, 3H, CH_3); ^{13}C NMR (100.6 MHz, $CDCl_3$): δ 175.2, 156.2, 143.1, 106.4, 72.0, 67.1, 39.6, 20.4, 17.8; MS (ESI^-) *m*/*z* calcd for $C_{20}H_{20}N_2O_2$ $[M-H]^-$: 161.0450, found 161.0442. Crystal data available in Section 8.11.1 and the CD-R found inside the back cover of this thesis.

Compound 29

In a sealed flask, lactide (0.1441 g, 1 mmol) and DMAP (0.1222 g, 1 mmol) were stirred in toluene (12 mL) and heated to 130 °C for 30 mins. After cooling, the flask was left open to air and the toluene slowly evaporated to yield large, colourless crystals. After filtration, toluene (6 mL) was added to the filtrate (*ca*. 2 mL) and was left to stand for two weeks prior to slow evaporation. Yield (0.087 g, 15.6%). Crystal data available in Section 8.11.1 and the CD-R found inside the back cover of this thesis.

8.7 Synthesis of pyridylamine bis(phenolate) ligand precursors

Compound 30(H)$_2$[2]

Under N_2, salicylaldehyde (2.12 mL, 2.44 g, 20 mmol) was added to a solution of 2-picolylamine (2.06 mL, 20 mmol) in methanol (50 mL) to give a yellow solution that was stirred for 2 hours. Sodium borohydride (0.83 g, 22 mmol) was added slowly after which the solution became colourless. After 1 hour of stirring the volatiles were removed and the resulting oil was incorporated into water (50 mL), acidified to pH 6 using 1 M hydrochloric acid solution, extracted with 3 × 30 mL dichloromethane, dried over sodium sulfate and evaporated to dryness to yield the intermediate as an orange oil. The oil was stirred in methanol (50 mL) and salicylaldehyde (2.12 mL, 2.44 g, 20 mmol) was added to give a yellow solution that was stirred for 2 hours. Sodium borohydride (0.83 g, 22 mmol) was added slowly after which the solution became colourless and a white precipitate formed. The solvents were removed and the solids dissolved in water (50 mL), acidified to pH 6 using 1 M hydrochloric acid solution, extracted with 3 × 30 mL dichloromethane, dried over sodium sulfate and evaporated to dryness to yield crude product as an off-white solid. The pure product was obtained by recrystallisation from hot chloroform and methanol to give **30**(H)$_2$. Yield: 3.264 g (51.0 %). ^{1}H NMR (400MHz) $CDCl_3$: δ 10.81 (s, 2H, ArOH), 8.71 (dd, 1H, PyH), 7.75

(td, 1H, PyH), 7.33 (td, 1H, PyH), 7.21 (m, 3H, overlapping PyH/ArH), 7.10 (dd, 2H, ArH),6.93 (dd, 2H, ArH), 6.83 (td, 2H, ArH), 3.94 (s, 2H, CH_2), 3.86 (s, 4H, CH_2); ^{13}C NMR (75.5 MHz) $CDCl_3$: δ 157.34, 156.01, 148.18, 137.17, 130.37, 129.49, 123.54, 122.72, 121.57, 119.19, 117.10, 56.45, 55.71; HRMS (NSI^+): *m*/*z* calcd for $C_{20}H_{20}N_2O_2$ $[M+H]^+$: 321.1598, found 321.1604; elemental analysis (%) calculated for $C_{20}H_{20}N_2O_2$: C, 74.98; H, 6.29; N, 8.74. Found: C, 74.14; H, 6.24; N, 8.30. Crystal data available in Section 8.11.1 and the CD-R found inside the back cover of this thesis.

Compound 31(H)$_2$[9,10]

Stirring in methanol (20 mL) under N_2, a mixture of *p*-cresol (4.326 g, 40 mmol), 2-picolylamine (2.06 mL, 20 mmol) and paraformaldehyde (1.20 g, 40 mmol) was heated to reflux for 48 h. After cooling at −20 °C, the mother liquor was decanted to yield a yellow oil that was dried in air and triturated with methanol to yield a white solid, which was filtered, washed with methanol (3 × 15 mL) and dried under vacuum. Yield: 2.465 g (35.4%). ^{1}H NMR (300MHz) $CDCl_3$: δ 10.45 (s, 2H, PhOH), 8.73 (dq, 1H, PyH), 7.73 (td, 1H, PyH), 7.32 (dd, 1H, PyH), 7.12 (d, 1H, PyH), 6.91 (d, 2H, ArH), 6.73 (d, 2H, ArH), 3.86 (s, 2H, CH_2), 3.76 (s, 4H, CH_2), 2.21 (s, 6H, CH_3); ^{13}C NMR (CDCl3, 75.5 MHz): δ 156.10, 154.92, 148.18, 137.61, 130.82, 129.90, 128.19, 123.54, 122.66, 121.29, 116.82, 56.40, 55.73, 50.87, 20.41. Crystal data available in Section 8.11.1 and the CD-R found inside the back cover of this thesis.

Compound 32(H)$_2$[7]

Compound **32**$(H)_2$ was formed and isolated according a modified literature procedure: a mixture of 2,4-di-*tert*-methylphenol (8.251 g, 40 mmol), 2-picolylamine (2.06 mL, 20 mmol) and paraformaldehyde (1.20 g, 40 mmol) in methanol (20 mL) was heated to reflux for 48 h under N_2. After cooling to room temperature, a white precipitate formed, which was filtered, washed with ice-cold methanol (3 × 20 mL) and dried. Yield: 6.578 g (94.3%). ^{1}H NMR (300MHz) $CDCl_3$: δ 10.51 (br, 2H, PhOH), 8.68 (d, 1H, PyH), 7.73 (t, 1H, PyH), 7.32 (d, 1H, CH, PyH), 7.15 (d, 1H, PyH), 7.00 (d, 1H, PyH), 6.95 (d, 2H, ArH), 6.89 (d, 2H, ArH), 6.82 (d, 2H, ArH), 3.91 (s, 2H, CH_2), 3.80 (s, 4H, CH_2), 2.27 (s, 6H, CH_3), 1.44 (s, 6H, CH_3); ^{13}C NMR (CDCl3, 75.5 MHz): δ 153.1, 148.3, 142.8, 137.5, 131.2, 128.5, 127.6, 125.5, 123.8, 122.5, 120.8, 56.4, 55.4, 20.4, 16.2.

Compound 33(H)$_2$[7,11]

Compound **33**(H)$_2$ was formed and isolated according a modified literature procedure: a suspension of 2,4-di-*tert*-butylphenol (8.251 g, 40 mmol), 2-picolylamine (2.06 mL, 20 mmol) and paraformaldehyde (1.20 g, 40 mmol) in methanol (20 mL) was heated to reflux for 48 h under N_2. A white precipitate formed, which was filtered, washed with ice-cold methanol (3 × 20 mL) and dried. Yield: 4.551 g (41.8%). ^{1}H NMR (300MHz) $CDCl_3$: δ 10.47 (s, 2H, PhOH), 8.62 (dq, CH, PyH), 7.62 (td, 1H, PyH), 7.20 (dd, 1H, PyH), 7.14 (dd, 2H, ArH), 7.04 (dd, 1H, PyH), 6.86 (dd, 2H, ArH), 3.77 (s, 2H, CH_2), 3.72 (s, 4H, CH_2), 1.33 (s, 9H, CH_3), 1.22 (s, 9H, CH_3); ^{13}C NMR ($CDCl_3$, 75.5 MHz): δ 156.3, 153.8, 148.2, 140.4, 137.3, 136.3, 125.1, 123.7, 123.4, 122.4, 121.3, 56.9, 55.4, 35.1, 34.1, 31.7, 29.6.

8.8 Synthesis of pyridylamine bis(phenolate) titanium building blocks

Complex 34

Under a dry N_2 atmosphere, compound **30**(H)$_2$ (0.160 g, 0.5 mmol) and titanium(IV) isopropoxide (0.154 mL, 0.5 mmol) were stirred in dry THF (4 mL) for 2 h, after which the volatiles were removed. The resulting yellow solids were dissolved in dry DCM and precipitated at −20 °C, filtered and dried with gentle heat (35 °C) under vacuum. Yield: 0.231 g (95.4%); ^{1}H NMR (400MHz) $CDCl_3$: δ 8.66 (d, 1H, PyH), 7.23 (td, 1H, PyH), 6.89 (m, 5H, PyH+ArH), 6.49 (td, 2H, ArH), 6.40 (d, 1H, PyH), 6.35 (dd, 2H, ArH), 5.19 (sept, 1H, CH), 4.75 (sept, 1H, CH), 4.57 (d, 2H, CH_2), 3.69 (s, 2H, CH_2), 3.35 (d, 2H, CH_2), 1.43 (d, 6H, CH_3), 1.09 (d, 6H, CH_3); ^{13}C NMR ($CDCl_3$, 100.6 MHz): δ 137.4, 128.7, 122.1, 120.5, 116.4, 116.2, 78.0, 76.9, 63.3, 62.8, 58.7, 26.1, 25.8.

Complex 35[12]

Compound **33**(H)$_2$ (0.160 g, 0.5 mmol) and titanium(IV) isopropoxide (0.154 mL, 0.5 mmol) were stirred in dry THF (4 mL) for 2 h under a dry N_2 atmosphere. The volatiles were removed give orange solids, which were dissolved in dry DCM and precipitated at −20 °C, filtered and dried with gentle heat (35 °C) under vacuum. Yield: 0.347 g (97.9%); ^{1}H NMR (400MHz) $CDCl_3$: δ 8.64 (dq, 1H, PyH), 7.16 (td, 1H, PyH), 6.95 (dd, 2H, ArH), 6.81 (m, 3H, ArH+PyH), 6.32 (d, 1H, PyH), 5.19 (sept, 1H, CH), 4.95 (sept, 1H, CH), 4.69 (d, 2H, CH_2), 3.69 (s, 2H, CH_2), 3.26 (d, 2H, CH_2), 1.40 (d, 6H, CH_3), 1.22 (s, 18H, CH_3), 1.16 (s, 18H, CH_3), 1.14

(d, 6H, CH_3); ^{13}C NMR ($CDCl_3$, 100.6 MHz): δ 160.9, 156.7, 150.2, 138.5, 137.3, 135.4, 124.3, 123.7, 123.1, 121.2, 119.6, 64.4, 57.8, 34.9, 34.0, 31.8, 29.8, 26.8, 26.3, 25.4.

Complex 36

Under a dry N_2 atmosphere, sodium hydride as 60 wt% dispersion in oil (0.040 g, 1 mmol) was added to a stirred solution of compound **30**$(H)_2$ (0.160 g, 0.5 mmol) in dry toluene (10 mL). After 30 mins, the evolution of gas had ceased and titanium(IV) chloride (0.056 mL, 0.5 mmol) was added dropwise to give an immediate red suspension. After 2 h stirring, the mixture was filtered and triturated with dry acetone to give an orange solid, which was filtered and dried. Yield: 0.198 g (48.3%); ^1H NMR (400MHz) $CDCl_3$: δ 9.03 (dq, 1H, PyH), 7.47 (td, 1H, PyH), 7.15 (m, 3H, ArH), 6.88 (m, 4H, ArH), 6.77 (td, 1H, ArH), 6.48 (td, 1H, ArH), 6.26 (d, 1H, ArH), 5.24 (d, 1H, CH_2), 4.89 (d, 1H, CH_2), 3.89 (d, 1H, CH_2), 3.61 (d, 1H, CH_2), 3.11 (d, 1H, CH_2); ^{13}C NMR ($CDCl_3$, 100.6 MHz): δ 163.8, 160.3, 155.6, 149.0, 139.3, 129.7, 129.7, 129.3, 128.5, 125.9, 124.6, 123.6, 122.8, 121.6, 120.8, 115.4, 115.2, 65.9, 64.8, 60.7; MS (EI^+): *m*/*z* calcd for $C_{40}H_{35}ClN_4O_5Ti_2$ $[M-HCl]^+$: 782.1265, found 782.1279. Crystal data available in Section 8.11.1 and the CD-R found inside the back cover of this thesis.

Complex 37[13]

Under stirring in a dry N_2 atmosphere, sodium hydride as 60 wt% dispersion in oil (0.040 g, 1 mmol) was added to compound **33**$(H)_2$ (0.160 g, 0.5 mmol) in dry toluene (10 mL), resulting in the evolution of gas. After 30 mins, titanium(IV) chloride (0.056 mL, 0.5 mmol) was added dropwise to give an immediate red suspension. After 2 h stirring, the mixture was filtered and recrystallized from dry toluene at −20 °C. Yield: 0.232 g (70.3%) ^1H NMR (400MHz) $CDCl_3$: δ 8.97 (dd, 1H, PyH), 7.44 (td, 1H, PyH), 7.23 (d, 1H, ArH), 7.01 (m, 2H, PyH+ArH), 6.93 (d, 1H, PyH), 6.83 (d, 1H, ArH), 6.73 (d, 1H, ArH), 5.31 (d, 1H, CH_2), 4.93 (d, 1H, CH_2), 3.86 (m, 2H, CH_2), 3.50 (d, 1H, CH_2), 3.03 (d, 1H, CH_2), 1.50 (s, 9H, CH_3), 1.26 (s, 9H, CH_3), 1.23 (s, 9H, CH_3), 1.04 (s, 9H, CH_3); ^{13}C NMR ($CDCl_3$, 100.6 MHz): δ 162.1, 160.4, 155.8, 149.2, 144.0, 142.1, 138.7, 136.9, 135.4, 126.7, 125.2, 123.9, 124.1, 123.5, 123.1, 122.7, 122.5, 66.1, 65.7, 61.5, 35.9, 35.1, 32.2, 30.8, 30.2, 29.7, 28.1, 27.1. Crystal data available in Section 8.11.1 and the CD-R found inside the back cover of this thesis.

8.9 Synthesis of pyridylamine bis(phenolate) titanium compounds

8.9.1 Stepwise synthesis

Complex 38

Complex **36** (0.082 g, 0.1 mmol) was stirred in methanol (5 mL) with 3 drops of deionised water to give a yellow solution after 5 mins. Stirring was discontinued after 30 mins. Slow evaporation and subsequent storage at −20 °C led to the isolation of yellow crystals. Yield: 0.039 g (24.3%). Crystal data available in Section 8.11.1 and the CD-R found inside the back cover of this thesis.

Complex 39

Complex **36** (0.082 g, 0.1 mmol) was stirred in a fresh 0.2 M solution of sodium methoxide (0.005 g, 1 mmol) in methanol (5 mL). The yellow solution was stirred for 30 mins under N_2 and left to stand. Large, colourless crystals formed with an insoluble brown solid. The crystals were washed with methanol and dried. Yield: 0.015 g (19.9 %). Crystal data available in Section 8.11.1 and the CD-R found inside the back cover of this thesis.

8.9.2 Solvothermal synthesis

Complex 40

Titanium(IV) propoxide (0.55 mL, 2 mmol), compound **30**$(H)_2$ (0.6408 g, 2 mmol) and triethylamine (0.279 mL, 2 mmol) were stirred for 5 mins in toluene (4 mL) in a Teflon vessel. A clear, yellow solution was obtained from which the stirrer bar was removed and the Teflon vessel sealed in an autoclave and heated to 120 °C for 72 h. After cooling for 24 h, the vessel was opened, the yellow crystals filtered, washed with toluene and dried. Yield: 0.534 g (68.1%). Crystal data available in Section 8.11.1 and the CD-R found inside the back cover of this thesis.

Complex 41

In a Teflon vessel, titanium(IV) propoxide (0.55 mL, 2 mmol), compound **30**$(H)_2$ (0.6408 g, 2 mmol) and triethylamine (0.279 mL, 2 mmol) were stirred for 5 mins in toluene (4 mL). A clear, yellow solution was obtained from which the stirrer bar was removed and the Teflon vessel sealed in an autoclave and heated to 120 °C for 72 h. After cooling for 24 h, the vessel was opened and the volatiles removed to give

orange solids, which were purified by column chromatography. The first elution band was extracted using 90:10 DCM:ethyl acetate with 0.1 % triethylamine. The solvents were removed and the yellow solids left to stand in $CDCl_3$ to give yellow crystals. Yield: 0.137 g (16.7 %); ^{1}H NMR (400MHz) $CDCl_3$: δ 8.50 (dd, 1H, PyH), 7.28 (td, 1H, PyH), 6.94 (dd, 1H, PyH), 6.72 (m, 6H, PyH+ArH), 6.50 (m, 2H, ArH+CH_2), 6.23 (m, 2H, ArH), 5.36 (m, 2H, CH_2), 3.84 (d, 1H, CH_2), 3.52 (d, 1H, CH_2), 3.29 (d, 1H, CH_2), 2.68 (d, 1H, CH_2), 2.14 (s, 3H, CH_3), 1.91 (s, 3H, CH_3). Crystal data available in Section 8.11.1 and the CD-R found inside the back cover of this thesis.

Complex 42

As for compound **41** except the second elution band was collected using ethyl acetate with 0.1 % triethylamine. The solvents were removed and the yellow solids left to stand in $CDCl_3$ to give yellow crystals. Yield: 0.093 g (11.4%). Crystal data available in Section 8.11.1 and the CD-R found inside the back cover of this thesis.

Complex 43

The sample of **42** in was redissolved in $CDCl_3$ and left open to air for two weeks, yielding pale, yellow crystals. Yield: 0.067 g (8.2%). Crystal data available in Section 8.11.1 and the CD-R found inside the back cover of this thesis.

Complex 44

In a Teflon vessel, titanium(IV) propoxide (0.55 mL, 2 mmol), compound **32**$(H)_2$ (0.750 g, 2 mmol) and triethylamine (0.279 mL, 2 mmol) were stirred for 5 mins in toluene (4 mL). A clear, yellow solution was obtained from which the stirrer bar was removed and the Teflon vessel sealed in an autoclave and heated to 120 °C for 72 h. After cooling for 24 h, the vessel was opened and the orange solution filtered. Pale, yellow crystals were obtained from a vapour diffusion with diethyl ether. Yield: 0.396 g (45.2%). Note NMR signals are weak due to poor solubility. ^{1}H NMR (400MHz) $CDCl_3$: δ 8.60 (dd, 1H, PyH), 7.30 (td, 1H, PyH), 6.70 (m, 3H, PyH+ArH), 6.64 (td, 1H, PyH), 6.32 (d, 1H, ArH), 6.29 (d, 1H, ArH), 4.66 (d, 1H, CH_2), 4.56 (d, 1H, CH_2), 3.71 (d, 1H, CH_2), 3.49 (d, 1H, CH_2), 3.19 (d, 1H, CH_2), 2.59 (d, 1H, CH_2), 2.16 (s, 3H, CH_3), 1.90 (s, 3H, CH_3), 1.83 (s, 3H, CH_3), 1.45 (s, 3H, CH_3). Crystal data available in Section 8.11.1 and the CD-R found inside the back cover of this thesis.

Complex 45

Titanium(IV) propoxide (0.55 mL, 2 mmol), compound **32**$(H)_2$ (1.090 g, 2 mmol) and triethylamine (0.279 mL, 2 mmol) were stirred for 5 mins in toluene (4 mL) in a Teflon vessel. A clear, yellow solution was obtained from which the stirrer bar was removed and the Teflon vessel sealed in an autoclave and heated to 120 °C for 72 h. After cooling for 24 h, the vessel was opened and the orange solution filtered. Vapour diffusion with diethyl ether gave yellow crystals. Yield: 0.384 g (38.4%); ^{1}H NMR (400MHz) $CDCl_3$: δ 8.60 (dq, 1H, PyH), 7.19 (td, 1H, PyH), 6.97 (d, 2H, ArH), 6.81 (m, 3H, ArH+PyH), 6.31 (d, 1H, CH_2), 5.37 (d, 2H, CH_2), 4.46 (t, 2H, CH_2), 3.75 (s, 2H, CH_2), 3.20 (d, 2H, CH_2), 1.33 (s, 18H, CH_3), 1.22 (s, 20H, CH_3+CH_2), 0.59 (t, 3H, CH_3); ^{13}C NMR ($CDCl_3$, 100.6 MHz): δ 161.1, 157.0, 150.0, 138.0, 137.0, 135.0, 124.7, 124.3, 122.5, 120.9, 119.4, 78.1, 64.4, 58.2, 34.9, 33.9, 31.8, 30.1, 30.0, 26.6, 10.3. Crystal data available in Section 8.11.1 and the CD-R found inside the back cover of this thesis.

Complex 46

As for complex **45** except for the use of acetonitrile as counter-solvent to obtain crystals from a vapour diffusion. Yield: 0.260 g (19.8%); ^{1}H NMR (400MHz) $CDCl_3$: δ 8.55 (dq, 1H, PyH), 7.13 (td, 1H, PyH), 6.95 (d, 2H, ArH), 6.80 (m, 3H, ArH+PyH), 6.29 (dd, 1H, PyH), 4.72 (t, 2H, CH_2), 4.60 (d, 2H, CH_2), 3.69 (s, 2H, CH_2), 3.28 (d, 2H, CH_2), 1.70 (sext, 2H, CH_2), 1.22 (s, 18H, CH_3), 1.16 (s, 18H, CH_3), 1.01 (t, 3H, CH_3); ^{13}C NMR ($CDCl_3$, 100.6 MHz): δ 161.0, 156.9, 150.4, 138.3, 137.2, 135.1, 124.3, 123.9, 123.5, 121.1, 119.2, 77.9, 57.9, 35.0, 34.1, 31.6, 29.9, 30.4, 30.2, 26.5, 10.2. Crystal data available in Section 8.11.1 and the CD-R found inside the back cover of this thesis.

Complex 47

A solution of complex **45** in toluene was left open to air for two weeks, leading to the formation of yellow crystals. Yield: 0.136 g (11.2%). Crystal data available in Section 8.11.1 and the CD-R found inside the back cover of this thesis.

8.10 ROP of lactide

8.10.1 Solution polymerisation procedure

Under N_2, a Schlenk flask was charged with *rac*-lactide* (1.000 g, 6.938 mmol) and an appropriate amount of initiator/catalyst. Dry toluene (6.94 mL) was added and the solution was stirred and heated in an oil bath at 130 °C. Once the polymerisation time was reached, the vessel was removed from the oil bath and the reaction terminated by the addition of methanol (5 mL). The solvents were removed and the resulting solids were dissolved in dichloromethane. The polymers were precipitated with excess methanol, washed with methanol and dried at 40 °C under vacuum. * Sublimed and stored under N_2 when complexes **6**-**8** and *rac*-**13**/**14** were used.

8.10.2 Melt polymerisation procedure

Under N_2, a vessel was charged with sublimed *rac*-lactide* (1.000 g, 6.938 mmol) and appropriate amounts of initiator/catalyst. The vessel was sealed and immersed in an oil bath at 130 °C. Once polymerisation time was reached, the vessel was removed from the oil bath and the reaction terminated by the addition of the methanol (5 mL). The solids were dissolved in dichloromethane and the polymers were dissolved with excess methanol. The collected polymers were washed with methanol and dried at 40 °C under vacuum.* Sublimed and stored under N_2 when complexes **6**-**8** and *rac*-**13**/**14** were used.

8.10.3 Kinetic studies

A solution of sublimed *rac*- or *L*-lactide (0.5 g, 3.469 mmol) in dry toluene (3.47 mL) was added to a sealed flask containing *rac*-**14** (0.071 g, 0.116 mmol) under stirring and immediately lowered into a pre-heated oil bath (130 °C). Aliquots (0.07 mL), which were quenched with methanol (3 drops) and dried under vacuum, were taken every 2 mins starting at 4 mins for 20 mins and every 5 mins thereafter.

8.11 Single crystal X-ray diffraction studies

Structure solution was performed using direct methods with the solving program SHELXT.[14] Structure refinement was completed with the SHELXL program[15] using the Olex2 software package.[16] Diffuse electron density attributed to disordered solvent was refined using the SQUEEZE routine.[17]

8.11.1 Crystal data tables

This section contains the SCXRD data tables, generated using the Olex2 software package,[16] for all crystal structures presented in this thesis. Supplementary data can be obtained from the crystallographic information files (CIFs) and CheckCIF reports included on a data disc in the back cover. CCDC entries are included where applicable and these data can be obtained free of charge from The Cambridge Crystallographic Data Centre.

Compound 1(H)$_3$

Identification code	Compound **1**(H)$_3$
Crystal growth method	Co-crystallisation with triethylamine in water
Empirical formula	$C_{22}H_{34}N_2O_5$
Formula weight	406.51
Temperature/K	100.0
Crystal system	orthorhombic
Space group	*Pbca*
a/Å	11.7699(19)
b/Å	11.636(2)
c/Å	33.317(5)
α/°	90
β/°	90
γ/°	90
Volume/Å^3	4563.1(13)
Z	8
ρ_{calc} g/cm^3	1.183
μ/mm^{-1}	0.083
F(000)	1760.0
Crystal size/mm^3	0.2 × 0.2 × 0.05
Radiation	MoK_α (λ = 0.71073 Å)
2Θ range for data collection/°	4.89 to 52.274
Index ranges	$-14 \leq h \leq 14$, $-14 \leq k \leq 14$, $-41 \leq l \leq 38$
Reflections collected	44524
Independent reflections	4544 [R_{int} = 0.1132, R_{sigma} = 0.0626]
Data/restraints/parameters	4544/0/285
Goodness-of-fit on F^2	1.011
Final *R* indexes [$I > 2\sigma(I)$]	R_1 = 0.0482, wR_2 = 0.0971
Final *R* indexes [all data]	R_1 = 0.0972, wR_2 = 0.1170
Largest diff. peak/hole e$^-$/Å^{-3}	0.20/-0.21

Compound 2(H)$_3$

Identification code	Compound **2**(H)$_3$
Crystal growth method	Slow evaporation in methanol
Empirical formula	$C_{19}H_{25}NO_5$
Formula weight	347.40
Temperature/K	100
Crystal system	monoclinic
Space group	$P2_1/n$
a/Å	10.1071(4)
b/Å	15.4013(7)
c/Å	12.4184(6)
α/°	90
β/°	104.439(2)
γ/°	90
Volume/Å^3	1872.02(15)
Z	4
ρ_{calc} g/cm^3	1.233
μ/mm^{-1}	0.089
F(000)	744.0
Crystal size/mm^3	0.3 × 0.3 × 0.2
Radiation	MoK_α (λ = 0.71073 Å)
2Θ range for data collection/°	4.932 to 54.394
Index ranges	$-10 \leq h \leq 12$, $-19 \leq k \leq 18$, $-15 \leq l \leq 15$
Reflections collected	29636
Independent reflections	4122 [R_{int} = 0.0191, R_{sigma} = 0.0131]
Data/restraints/parameters	4122/0/245
Goodness-of-fit on F^2	1.036
Final R indexes [$I > 2\sigma(I)$]	R_1 = 0.0388, wR_2 = 0.1061
Final R indexes [all data]	R_1 = 0.0442, wR_2 = 0.1109
Largest diff. peak/hole e$^-$/Å^{-3}	0.35/-0.32

Compound 3(H)$_3$

Identification code	Compound **3**(H)$_3$
Crystal growth method	Slow evaporation in methanol
Empirical formula	$C_{27}H_{45}NO_7$
Formula weight	495.64
Temperature/K	100
Crystal system	triclinic
Space group	*P*-1
a/Å	9.6753(4)
b/Å	9.7151(4)
c/Å	16.2135(7)
α/°	99.589(2)
β/°	105.513(2)
γ/°	99.080(2)
Volume/Å^3	1414.75(10)
Z	2
ρ_{calc} g/cm^3	1.163
μ/mm^{-1}	0.083
F(000)	540.0
Crystal size/mm^3	0.1 × 0.1 × 0.1
Radiation	MoK_α (λ = 0.71073 Å)
2Θ range for data collection/°	4.464 to 54.3
Index ranges	$-12 \leq h \leq 12$, $-12 \leq k \leq 11$, $-20 \leq l \leq 20$
Reflections collected	32592
Independent reflections	6193 [R_{int} = 0.0353, R_{sigma} = 0.0397]
Data/restraints/parameters	6193/0/349
Goodness-of-fit on F^2	1.082
Final *R* indexes [$I > 2\sigma(I)$]	R_1 = 0.0473, wR_2 = 0.1217
Final *R* indexes [all data]	R_1 = 0.0693, wR_2 = 0.1321
Largest diff. peak/hole e$^-$/Å^{-3}	0.61/-0.28

Compound 8_3(HO*i*Pr)

CCDC number	1562058
Crystal growth method	Saturated solution in THF at −20 °C
Identification code	Compound **8**$_3$(HO*i*Pr)
Empirical formula	$C_{108}H_{167}N_3O_{16}Ti_3$
Formula weight	1907.14
Temperature/K	173.0
Crystal system	monoclinic
Space group	$P2_1/n$
a/Å	14.2420(6)
b/Å	30.8848(14)
c/Å	32.6649(13)
α/°	90
β/°	92.799(2)
γ/°	90
Volume/Å^3	14350.9(11)
Z	4
ρ_{calc} g/cm^3	0.883
μ/mm^{-1}	0.209
F(000)	4120.0
Crystal size/mm^3	0.45 × 0.4 × 0.4
Radiation	MoK_α (λ = 0.71073 Å)
2Θ range for data collection/°	1.816 to 54.452
Index ranges	$-17 \le h \le 18$, $-39 \le k \le 39$, $-41 \le l \le 41$
Reflections collected	223865
Independent reflections	31655 [R_{int} = 0.0502, R_{sigma} = 0.0458]
Data/restraints/parameters	31655/50/1232
Goodness-of-fit on F^2	1.040
Final *R* indexes [$I > 2\sigma(I)$]	R_1 = 0.0695, wR_2 = 0.1704
Final *R* indexes [all data]	R_1 = 0.1003, wR_2 = 0.1872
Largest diff. peak/hole e$^-$/Å^{-3}	1.22/-0.80

Compound 10(H)$_3$

CCDC number	1562059
Crystal growth method	Slow evaporation in methanol
Identification code	Compound **10**(H)$_3$
Empirical formula	$C_{35}H_{59}NO_6$
Formula weight	589.83
Temperature/K	120.01(10)
Crystal system	orthorhombic
Space group	$P2_12_12_1$
a/Å	9.02228(2)
b/Å	11.92120(2)
c/Å	33.55582(6)
α/°	90
β/°	90
γ/°	90
Volume/Å^3	3609.143(12)
Z	4
ρ_{calc} g/cm^3	1.086
μ/mm^{-1}	0.574
F(000)	1296.0
Crystal size/mm^3	0.303 × 0.228 × 0.139
Radiation	CuK_α (λ = 1.54178 Å)
2Θ range for data collection/°	7.87 to 152.734
Index ranges	$-11 \leq h \leq 10$, $-15 \leq k \leq 15$, $-42 \leq l \leq 42$
Reflections collected	307438
Independent reflections	7534 [R_{int} = 0.0683, R_{sigma} = 0.0161]
Data/restraints/parameters	7534/0/414
Goodness-of-fit on F^2	1.057
Final R indexes [$I > 2\sigma(I)$]	R_1 = 0.0352, wR_2 = 0.0948
Final R indexes [all data]	R_1 = 0.0353, wR_2 = 0.0950
Largest diff. peak/hole e$^-$/Å^{-3}	0.25/-0.37

Compound 17(H)$_3$

Identification code	Compound **17**(H)$_3$
Crystal growth method	Slow evaporation in methanol
Empirical formula	$C_{17}H_{19}F_2NO_5$
Formula weight	355.33
Temperature/K	100.15
Crystal system	monoclinic
Space group	$P2_1/n$
a/Å	5.8292(3)
b/Å	13.0939(6)
c/Å	22.8342(10)
α/°	90
β/°	96.515(2)
γ/°	90
Volume/Å^3	1731.61(14)
Z	4
ρ_{calc} g/cm^3	1.363
μ/mm^{-1}	0.140
F(000)	744.0
Crystal size/mm^3	0.1 × 0.1 × 0.06
Radiation	synchrotron (λ = 0.7749 Å)
2Θ range for data collection/°	5.18 to 57.98
Index ranges	$-7 \leq h \leq 7$, $-16 \leq k \leq 16$, $-28 \leq l \leq 28$
Reflections collected	16169
Independent reflections	3543 [R_{int} = 0.0358, R_{sigma} = 0.0277]
Data/restraints/parameters	3543/0/243
Goodness-of-fit on F^2	1.029
Final R indexes [$I > 2\sigma(I)$]	R_1 = 0.0435, wR_2 = 0.1130
Final R indexes [all data]	R_1 = 0.0493, wR_2 = 0.1179
Largest diff. peak/hole e$^-$/Å^{-3}	0.36/-0.34

Compound 18

CCDC number	1483652
Crystal growth method	Vapour diffusion in THF with acetonitrile
Identification code	Compound **18**
Empirical formula	$C_{68}H_{62}N_6O_{18}Ti_4$
Formula weight	1442.83
Temperature/K	100
Crystal system	triclinic
Space group	*P*-1
a/Å	12.0501(4)
b/Å	12.0820(4)
c/Å	23.2457(8)
α/°	85.061(2)
β/°	89.175(2)
γ/°	86.151(2)
Volume/Å^3	3364.0(2)
Z	2
ρ_{calc} g/cm^3	1.424
μ/mm^{-1}	0.670
F(000)	1488.0
Crystal size/mm^3	0.1 × 0.09 × 0.01
Radiation	synchrotron (λ = 0.7749 Å)
2Θ range for data collection/°	4.308 to 67.336
Index ranges	$-17 \leq h \leq 17$, $-17 \leq k \leq 17$, $-33 \leq l \leq 33$
Reflections collected	57801
Independent reflections	20585 [R_{int} = 0.0497, R_{sigma} = 0.0673]
Data/restraints/parameters	20585/0/867
Goodness-of-fit on F^2	1.027
Final *R* indexes [$I > 2\sigma(I)$]	R_1 = 0.0518, wR_2 = 0.1081
Final *R* indexes [all data]	R_1 = 0.0832, wR_2 = 0.1185
Largest diff. peak/hole e$^-$/Å^{-3}	0.52/-0.77

Compound 19

CCDC number	1483653
Crystal growth method	Vapour diffusion in THF with acetonitrile
Identification code	Compound **19**
Empirical formula	$C_{76}H_{80}N_4O_{19}Ti_4$
Formula weight	1545.04
Temperature/K	100.0
Crystal system	tetragonal
Space group	*I*-4
a/Å	13.8620(5)
b/Å	13.8620(5)
c/Å	23.4683(8)
α/°	90
β/°	90
γ/°	90
Volume/Å^3	4509.6(4)
Z	2
ρ_{calc} g/cm^3	1.138
μ/mm^{-1}	0.402
F(000)	1608.0
Crystal size/mm^3	0.4 × 0.4 × 0.4
Radiation	MoK_α (λ = 0.71073 Å)
2Θ range for data collection/°	5.416 to 54.234
Index ranges	$-17 \leq h \leq 17$, $-17 \leq k \leq 17$, $-30 \leq l \leq 30$
Reflections collected	36957
Independent reflections	4978 [R_{int} = 0.0342, R_{sigma} = 0.0242]
Data/restraints/parameters	4978/0/247
Goodness-of-fit on F^2	1.068
Final *R* indexes [$I > 2\sigma(I)$]	R_1 = 0.0381, wR_2 = 0.1107
Final *R* indexes [all data]	R_1 = 0.0417, wR_2 = 0.1145
Largest diff. peak/hole e$^-$/Å^{-3}	0.35/-0.29

Compound 20

CCDC number	1483654
Crystal growth method	Slow evaporation in toluene
Identification code	Compound **20**
Empirical formula	$C_{180}H_{216}N_4O_{18}Ti_4$
Formula weight	2915.16
Temperature/K	100.0
Crystal system	tetragonal
Space group	*I*-4
a/Å	19.5294(8)
b/Å	19.5294(8)
c/Å	20.7148(9)
α/°	90
β/°	90
γ/°	90
Volume/Å^3	7900.6(7)
Z	2
ρ_{calc} g/cm^3	1.225
μ/mm^{-1}	0.261
F(000)	3112.0
Crystal size/mm^3	0.6 × 0.4 × 0.4
Radiation	MoK_α (λ = 0.71073 Å)
2Θ range for data collection/°	4.916 to 54.284
Index ranges	$-25 \leq h \leq 23$, $-22 \leq k \leq 25$, $-26 \leq l \leq 26$
Reflections collected	57486
Independent reflections	8746 [R_{int} = 0.0377, R_{sigma} = 0.0352]
Data/restraints/parameters	8746/0/490
Goodness-of-fit on F^2	1.078
Final *R* indexes [$I > 2\sigma(I)$]	R_1 = 0.0383, wR_2 = 0.0925
Final *R* indexes [all data]	R_1 = 0.0543, wR_2 = 0.1036
Largest diff. peak/hole e$^-$/Å^{-3}	0.27/-0.32
Flack parameter	0.005(6)

Compound 21

Identification code	Compound **21**
Crystal growth method	Vapour diffusion in toluene with hexane
Empirical formula	$C_{146}H_{226}N_4O_{18}Ti_4$
Formula weight	2516.89
Temperature/K	100.15
Crystal system	monoclinic
Space group	*P*2/n
a/Å	20.3392(8)
b/Å	16.8746(6)
c/Å	21.8456(9)
α/°	90
β/°	92.287(2)
γ/°	90
Volume/Å^3	7491.8(5)
Z	2
ρ_{calc} g/cm^3	1.116
μ/mm^{-1}	0.725
F(000)	2724.0
Crystal size/mm^3	0.08 × 0.025 × 0.02
Radiation	synchrotron (λ = 1.0332 Å)
2Θ range for data collection/°	3.9 to 81.798
Index ranges	$-25 \leq h \leq 25$, $-21 \leq k \leq 21$, $-27 \leq l \leq 27$
Reflections collected	61584
Independent reflections	15931 [R_{int} = 0.0482, R_{sigma} = 0.0499]
Data/restraints/parameters	15931/30/753
Goodness-of-fit on F^2	1.025
Final *R* indexes [$I > 2\sigma(I)$]	R_1 = 0.0576, wR_2 = 0.1400
Final *R* indexes [all data]	R_1 = 0.0816, wR_2 = 0.1536
Largest diff. peak/hole e$^-$/Å^{-3}	0.86/-0.71

Compound 22

CCDC number	1483655
Crystal growth method	Vapour diffusion in DCM with pet. ether (40-60 °C)
Identification code	Compound **22**
Empirical formula	$C_{64}H_{48}F_8N_4O_{18}Ti_4$
Formula weight	1504.66
Temperature/K	100.0
Crystal system	monoclinic
Space group	$P2_1/n$
a/Å	12.3528(5)
b/Å	28.6409(12)
c/Å	19.2930(8)
α/°	90
β/°	95.215(2)
γ/°	90
Volume/Å^3	6797.5(5)
Z	4
ρ_{calc} g/cm^3	1.470
μ/mm^{-1}	0.681
F(000)	3056.0
Crystal size/mm^3	0.05 × 0.02 × 0.005
Radiation	synchrotron (λ = 0.7749 Å)
2Θ range for data collection/°	4.388 to 45.77
Index ranges	$-12 \leq h \leq 12$, $-28 \leq k \leq 28$, $-19 \leq l \leq 19$
Reflections collected	107298
Independent reflections	7186 [R_{int} = 0.1533, R_{sigma} = 0.0665]
Data/restraints/parameters	7186/0/883
Goodness-of-fit on F^2	1.017
Final R indexes [$I > 2\sigma(I)$]	R_1 = 0.0457, wR_2 = 0.0985
Final R indexes [all data]	R_1 = 0.0720, wR_2 = 0.1101
Largest diff. peak/hole e$^-$/Å^{-3}	0.50/-0.28

Compound 23′

Identification code	Compound **23′**
Crystal growth method	Cooling reaction mixture in toluene
Empirical formula	$C_{92}H_{104}N_{12}O_{22}Ti_4$
Formula weight	1921.47
Temperature/K	100.15
Crystal system	monoclinic
Space group	$P2_1/n$
a/Å	14.3593(5)
b/Å	19.5823(7)
c/Å	20.0897(7)
α/°	90
β/°	102.521(2)
γ/°	90
Volume/Å^3	5514.6(3)
Z	2
ρ_{calc} g/cm^3	1.157
μ/mm^{-1}	0.434
F(000)	2008.0
Crystal size/mm^3	0.05 × 0.03 × 0.01
Radiation	synchrotron (λ = 0.7749 Å)
2Θ range for data collection/°	4.146 to 51.178
Index ranges	$-15 \leq h \leq 15$, $-21 \leq k \leq 21$, $-22 \leq l \leq 22$
Reflections collected	25860
Independent reflections	7934 [R_{int} = 0.0597, R_{sigma} = 0.0791]
Data/restraints/parameters	7934/0/606
Goodness-of-fit on F^2	1.047
Final R indexes [$I > 2\sigma(I)$]	R_1 = 0.0593, wR_2 = 0.1435
Final R indexes [all data]	R_1 = 0.0820, wR_2 = 0.1544
Largest diff. peak/hole e$^-$/Å^{-3}	0.37/-0.53

Compound 23″

Identification code	Compound **23″**
Crystal growth method	Vapour diffusion in toluene with acetonitrile
Empirical formula	$C_{92}H_{100}N_{12}O_{20}Ti_4$
Formula weight	1885.43
Temperature/K	120.00(10)
Crystal system	tetragonal
Space group	*P*-4
a/Å	21.7036(5)
b/Å	21.7036(5)
c/Å	13.5173(4)
α/°	90
β/°	90
γ/°	90
Volume/Å^3	6367.3(3)
Z	2
ρ_{calc} g/cm^3	0.983
μ/mm^{-1}	0.297
F(000)	1968.0
Crystal size/mm^3	0.332 × 0.259 × 0.19
Radiation	MoK_α (λ = 0.71073 Å)
2Θ range for data collection/°	5.936 to 52.742
Index ranges	$-27 \leq h \leq 27$, $-27 \leq k \leq 27$, $-16 \leq l \leq 16$
Reflections collected	74104
Independent reflections	12849 [R_{int} = 0.0831, R_{sigma} = 0.0634]
Data/restraints/parameters	12849/0/589
Goodness-of-fit on F^2	1.027
Final *R* indexes [$I > 2\sigma(I)$]	R_1 = 0.0489, wR_2 = 0.1042
Final *R* indexes [all data]	R_1 = 0.0594, wR_2 = 0.1091
Largest diff. peak/hole e$^-$/Å^{-3}	0.35/-0.35
Flack parameter	0.233(12)

Compound 24′

Identification code	Compound **24′**
Crystal growth method	Cooling reaction mixture in toluene
Empirical formula	$C_{114}H_{134}N_8O_{23}Ti_4$
Formula weight	2175.88
Temperature/K	100
Crystal system	triclinic
Space group	*P*-1
a/Å	13.5535(8)
b/Å	14.2076(9)
c/Å	16.0538(10)
α/°	66.289(3)
β/°	84.147(3)
γ/°	71.372(3)
Volume/Å^3	2680.9(3)
Z	1
ρ_{calc} g/cm^3	1.348
μ/mm^{-1}	0.363
F(000)	1146.0
Crystal size/mm^3	0.2 × 0.2 × 0.1
Radiation	MoK_α (λ = 0.71073 Å)
2Θ range for data collection/°	3.37 to 50.21
Index ranges	$-16 \le h \le 16$, $-15 \le k \le 16$, $-19 \le l \le 19$
Reflections collected	63273
Independent reflections	9319 [R_{int} = 0.0749, R_{sigma} = 0.0779]
Data/restraints/parameters	9319/0/694
Goodness-of-fit on F^2	1.026
Final *R* indexes [$I > 2\sigma(I)$]	R_1 = 0.0625, wR_2 = 0.1460
Final *R* indexes [all data]	R_1 = 0.1109, wR_2 = 0.1673
Largest diff. peak/hole e$^-$/Å^{-3}	0.73/-0.49

Compound 24″

Identification code	Compound **24″**
Crystal growth method	Cooling reaction mixture in toluene
Empirical formula	$C_{93}H_{110}N_{10}O_{22}Ti_4$
Formula weight	1911.50
Temperature/K	100.15
Crystal system	triclinic
Space group	*P*-1
a/Å	17.8310(6)
b/Å	18.1330(7)
c/Å	23.2482(9)
α/°	81.948(3)
β/°	81.651(3)
γ/°	60.859(2)
Volume/Å^3	6474.8(4)
Z	2
ρ_{calc} g/cm^3	0.980
μ/mm^{-1}	0.367
F(000)	2004.0
Crystal size/mm^3	0.45 × 0.04 × 0.01
Radiation	synchrotron (λ = 0.7749 Å)
2Θ range for data collection/°	4.44 to 44.648
Index ranges	$-17 \leq h \leq 17$, $-17 \leq k \leq 17$, $-22 \leq l \leq 21$
Reflections collected	31402
Independent reflections	12758 [R_{int} = 0.0608, R_{sigma} = 0.0817]
Data/restraints/parameters	12758/8/1145
Goodness-of-fit on F^2	1.045
Final *R* indexes [$I > 2\sigma(I)$]	R_1 = 0.0737, wR_2 = 0.1924
Final *R* indexes [all data]	R_1 = 0.1143, wR_2 = 0.2278
Largest diff. peak/hole e$^-$/Å^{-3}	0.55/-0.46

Compound 25

Identification code	Compound **25**
Crystal growth method	Vapour diffusion in toluene with acetonitrile
Empirical formula	$C_{100}H_{118}N_{12}O_{21}Ti_4$
Formula weight	2015.66
Temperature/K	100.0
Crystal system	triclinic
Space group	*P*-1
a/Å	12.8840(4)
b/Å	19.0406(7)
c/Å	26.5274(9)
α/°	98.537(2)
β/°	98.541(2)
γ/°	109.598(2)
Volume/Å^3	5923.8(4)
Z	2
ρ_{calc} g/cm^3	1.130
μ/mm^{-1}	0.407
F(000)	2116.0
Crystal size/mm^3	0.12 × 0.1 × 0.03
Radiation	synchrotron (λ = 0.7749 Å)
2Θ range for data collection/°	3.744 to 65.422
Index ranges	$-17 \leq h \leq 17$, $-26 \leq k \leq 26$, $-36 \leq l \leq 36$
Reflections collected	75961
Independent reflections	33523 [R_{int} = 0.0467, R_{sigma} = 0.0743]
Data/restraints/parameters	33523/0/1273
Goodness-of-fit on F^2	1.025
Final *R* indexes [$I > 2\sigma(I)$]	R_1 = 0.0607, wR_2 = 0.1394
Final *R* indexes [all data]	R_1 = 0.0970, wR_2 = 0.1573
Largest diff. peak/hole e$^-$/Å^{-3}	0.62/-0.68

Compound 26

Identification code	Compound **26**
Crystal growth method	Vapour diffusion in toluene with hexane
Empirical formula	$C_{117}H_{160}N_{10}O_{23}Ti_4$
Formula weight	2266.14
Temperature/K	100.15
Crystal system	monoclinic
Space group	*C*2/*c*
a/Å	22.8088(10)
b/Å	35.2642(15)
c/Å	19.2452(8)
α/°	90
β/°	114.941(2)
γ/°	90
Volume/Å^3	14036.0(11)
Z	4
ρ_{calc} g/cm^3	1.072
μ/mm^{-1}	0.512
F(000)	4816.0
Crystal size/mm^3	0.05 × 0.05 × 0.03
Radiation	synchrotron (λ = 0.8857 Å)
2Θ range for data collection/°	4.092 to 56.436
Index ranges	$-24 \leq h \leq 24$, $-37 \leq k \leq 37$, $-20 \leq l \leq 20$
Reflections collected	43831
Independent reflections	8903 [R_{int} = 0.0621, R_{sigma} = 0.0467]
Data/restraints/parameters	8903/66/704
Goodness-of-fit on F^2	1.052
Final *R* indexes [$I > 2\sigma(I)$]	R_1 = 0.0631, wR_2 = 0.1718
Final *R* indexes [all data]	R_1 = 0.0868, wR_2 = 0.1881
Largest diff. peak/hole e$^-$/Å^{-3}	1.48/-1.06

Compound 27

Identification code	Compound **27**
Crystal growth method	Standing solution of **23″** in $CDCl_3$ for 2 days
Empirical formula	$C_{78}H_{70}N_8O_{21}Ti_4$
Formula weight	1647.02
Temperature/K	100.0
Crystal system	monoclinic
Space group	$P2_1/n$
a/Å	15.6739(11)
b/Å	26.2825(19)
c/Å	28.8326(19)
α/°	90
β/°	96.894(2)
γ/°	90
Volume/Å^3	11791.7(14)
Z	4
ρ_{calc} g/cm^3	0.928
μ/mm^{-1}	0.313
F(000)	3400.0
Crystal size/mm^3	0.02 × 0.02 × 0.005
Radiation	MoK_α (λ = 0.71073 Å)
2Θ range for data collection/°	2.104 to 43.452
Index ranges	$-16 \leq h \leq 16$, $-26 \leq k \leq 27$, $-30 \leq l \leq 29$
Reflections collected	78267
Independent reflections	13907 [R_{int} = 0.1071, R_{sigma} = 0.0948]
Data/restraints/parameters	13907/20/572
Goodness-of-fit on F^2	1.864
Final R indexes [$I > 2\sigma(I)$]	R_1 = 0.1572, wR_2 = 0.4556
Final R indexes [all data]	R_1 = 0.2201, wR_2 = 0.5036
Largest diff. peak/hole e$^-$/Å^{-3}	1.18/-0.97

Compound 28

Identification code	Compound **28**
Crystal growth method	Slow evaporation in toluene
Empirical formula	$C_{13}H_{20}N_2O_5$
Formula weight	284.31
Temperature/K	100
Crystal system	triclinic
Space group	*P*-1
a/Å	7.7494(10)
b/Å	8.8869(12)
c/Å	10.8088(15)
α/°	101.323(8)
β/°	105.805(8)
γ/°	93.097(8)
Volume/Å^3	697.72(17)
Z	2
ρ_{calc} g/cm^3	1.353
μ/mm^{-1}	0.104
F(000)	304.0
Crystal size/mm^3	0.12 × 0.1 × 0.08
Radiation	MoK_α (λ = 0.71073 Å)
2Θ range for data collection/°	5.474 to 54.432
Index ranges	$-9 \leq h \leq 9$, $-11 \leq k \leq 11$, $-13 \leq l \leq 13$
Reflections collected	14004
Independent reflections	3003 [R_{int} = 0.0304, R_{sigma} = 0.0332]
Data/restraints/parameters	3003/0/261
Goodness-of-fit on F^2	1.037
Final *R* indexes [$I > 2\sigma(I)$]	R_1 = 0.0355, wR_2 = 0.0804
Final *R* indexes [all data]	R_1 = 0.0545, wR_2 = 0.0890
Largest diff. peak/hole e$^-$/Å^{-3}	0.21/-0.23

Compound 29

Identification code	Compound **29**
Crystal growth method	Slow evaporation in toluene
Empirical formula	$C_{10}H_{16}N_2O_3$
Formula weight	212.25
Temperature/K	100
Crystal system	triclinic
Space group	*P*-1
a/Å	7.0412(7)
b/Å	8.4631(8)
c/Å	9.6791(9)
α/°	71.504(6)
β/°	89.471(7)
γ/°	84.657(7)
Volume/Å^3	544.49(9)
Z	2
ρ_{calc} g/cm^3	1.295
μ/mm^{-1}	0.096
F(000)	228.0
Crystal size/mm^3	0.1 × 0.05 × 0.02
Radiation	MoK_α (λ = 0.71073 Å)
2Θ range for data collection/°	5.098 to 50.044
Index ranges	$-7 \leq h \leq 8$, $-10 \leq k \leq 10$, $-11 \leq l \leq 11$
Reflections collected	6936
Independent reflections	1839 [R_{int} = 0.0364, R_{sigma} = 0.0488]
Data/restraints/parameters	1839/0/147
Goodness-of-fit on F^2	1.041
Final *R* indexes [$I > 2\sigma(I)$]	R_1 = 0.0443, wR_2 = 0.0968
Final *R* indexes [all data]	R_1 = 0.0642, wR_2 = 0.1045
Largest diff. peak/hole e$^-$/Å^{-3}	0.17/-0.18

Compound 30

Identification code	Compound **30**
Crystal growth method	Slow evaporation in THF
Empirical formula	$C_{20}H_{20}N_2O_2$
Formula weight	320.38
Temperature/K	100.0
Crystal system	monoclinic
Space group	$P2_1$
a/Å	11.3693(7)
b/Å	6.1526(4)
c/Å	12.2746(8)
α/°	90
β/°	111.231(3)
γ/°	90
Volume/Å^3	800.34(9)
Z	2
ρ_{calc} g/cm^3	1.329
μ/mm^{-1}	0.087
F(000)	340.0
Crystal size/mm^3	0.44 × 0.16 × 0.08
Radiation	MoK_α (λ = 0.71073 Å)
2Θ range for data collection/°	4.188 to 65.51
Index ranges	$-17 \leq h \leq 17$, $-9 \leq k \leq 9$, $-18 \leq l \leq 18$
Reflections collected	22203
Independent reflections	5878 [R_{int} = 0.0266, R_{sigma} = 0.0298]
Data/restraints/parameters	5878/1/225
Goodness-of-fit on F^2	1.045
Final R indexes [$I > 2\sigma(I)$]	R_1 = 0.0356, wR_2 = 0.0886
Final R indexes [all data]	R_1 = 0.0413, wR_2 = 0.0926
Largest diff. peak/hole e$^-$/Å^{-3}	0.30/-0.20
Flack parameter	-0.2(3)

Compound 31

Identification code	Compound **31**
Crystal growth method	Slow evaporation in methanol
Empirical formula	$C_{22}H_{24}N_2O_2$
Formula weight	348.43
Temperature/K	100.15
Crystal system	orthorhombic
Space group	$P2_12_12_1$
a/Å	5.9898(3)
b/Å	14.6514(8)
c/Å	20.1010(11)
α/°	90
β/°	90
γ/°	90
Volume/Å^3	1764.04(16)
Z	4
ρ_{calc} g/cm^3	1.312
μ/mm^{-1}	0.142
F(000)	744.0
Crystal size/mm^3	0.11 × 0.05 × 0.002
Radiation	synchrotron (λ = 0.8857 Å)
2Θ range for data collection/°	4.288 to 63.848
Index ranges	$-7 \leq h \leq 7$, $-17 \leq k \leq 17$, $-23 \leq l \leq 23$
Reflections collected	14151
Independent reflections	3136 [R_{int} = 0.0533, R_{sigma} = 0.0444]
Data/restraints/parameters	3136/0/245
Goodness-of-fit on F^2	1.076
Final *R* indexes [$I > 2\sigma(I)$]	R_1 = 0.0364, wR_2 = 0.0771
Final *R* indexes [all data]	R_1 = 0.0477, wR_2 = 0.0812
Largest diff. peak/hole e$^-$/Å^{-3}	0.15/-0.19
Flack parameter	0.1(5)

Compound 36

Identification code	Compound **36**
Crystal growth method	Slow evaporation of reaction mixture in methanol
Empirical formula	$C_{44.5}H_{45}Cl_2N_4O_{6.5}Ti_2$
Formula weight	906.54
Temperature/K	100.15
Crystal system	monoclinic
Space group	$P2_1/n$
a/Å	12.2685(4)
b/Å	14.5952(5)
c/Å	23.4509(8)
α/°	90
β/°	92.151(2)
γ/°	90
Volume/Å^3	4196.2(2)
Z	4
ρ_{calc} g/cm^3	1.435
μ/mm^{-1}	0.712
F(000)	1880.0
Crystal size/mm^3	0.14 × 0.1 × 0.02
Radiation	synchrotron (λ = 0.7749 Å)
2Θ range for data collection/°	4.73 to 62.314
Index ranges	$-16 \leq h \leq 16$, $-19 \leq k \leq 19$, $-31 \leq l \leq 31$
Reflections collected	45623
Independent reflections	10433 [R_{int} = 0.0442, R_{sigma} = 0.0364]
Data/restraints/parameters	10433/0/542
Goodness-of-fit on F^2	1.027
Final R indexes [$I > 2\sigma(I)$]	R_1 = 0.0458, wR_2 = 0.1142
Final R indexes [all data]	R_1 = 0.0645, wR_2 = 0.1250
Largest diff. peak/hole e$^-$/Å^{-3}	0.95/-0.59

Compound 37

Identification code	Compound **37**
Crystal growth method	Solution in dry toluene at −20 °C
Empirical formula	$C_{36}H_{50}Cl_2N_2O_2Ti$
Formula weight	661.58
Temperature/K	100.15
Crystal system	orthorhombic
Space group	$Pna2_1$
a/Å	12.1700(5)
b/Å	22.2111(9)
c/Å	13.9583(6)
α/°	90
β/°	90
γ/°	90
Volume/Å^3	3773.1(3)
Z	4
ρ_{calc} g/cm^3	1.165
μ/mm^{-1}	0.501
F(000)	1408.0
Crystal size/mm^3	0.17 × 0.07 × 0.07
Radiation	synchrotron (λ = 0.7749 Å)
2Θ range for data collection/°	3.998 to 79.042
Index ranges	$-19 \leq h \leq 19$, $-36 \leq k \leq 36$, $-22 \leq l \leq 22$
Reflections collected	67908
Independent reflections	17242 [R_{int} = 0.0445, R_{sigma} = 0.0455]
Data/restraints/parameters	17242/1/401
Goodness-of-fit on F^2	1.032
Final R indexes [$I > 2\sigma(I)$]	R_1 = 0.0671, wR_2 = 0.1887
Final R indexes [all data]	R_1 = 0.0771, wR_2 = 0.1963
Largest diff. peak/hole e$^-$/Å^{-3}	1.49/-0.72
Flack parameter	0.05(3)

Compound 38

Identification code	Compound **38**
Crystal growth method	Slow evaporation of reaction mixture in methanol
Empirical formula	$C_{43}H_{52}ClN_4O_{10.5}Ti_2$
Formula weight	923.96
Temperature/K	100.15
Crystal system	triclinic
Space group	*P*-1
a/Å	13.1984(5)
b/Å	13.3144(5)
c/Å	14.3764(6)
α/°	65.929(2)
β/°	70.886(2)
γ/°	76.392(2)
Volume/Å^3	2164.29(15)
Z	2
ρ_{calc} g/cm^3	1.418
μ/mm^{-1}	0.623
F(000)	966.0
Crystal size/mm^3	0.2 × 0.04 × 0.04
Radiation	synchrotron (λ = 0.7749 Å)
2Θ range for data collection/°	4.312 to 88.186
Index ranges	$-23 \leq h \leq 23$, $-23 \leq k \leq 23$, $-25 \leq l \leq 25$
Reflections collected	93679
Independent reflections	25979 [R_{int} = 0.0369, R_{sigma} = 0.0383]
Data/restraints/parameters	25979/0/582
Goodness-of-fit on F^2	1.030
Final *R* indexes [$I > 2\sigma(I)$]	R_1 = 0.0560, wR_2 = 0.1414
Final *R* indexes [all data]	R_1 = 0.0795, wR_2 = 0.1573
Largest diff. peak/hole e$^-$/Å^{-3}	2.27/-1.86

Compound 39

Identification code	Compound **39**
Crystal growth method	Standing reaction mixture in methanol
Empirical formula	$C_{61}H_{58}N_6O_{10}Ti_3$
Formula weight	1178.83
Temperature/K	100
Crystal system	monoclinic
Space group	$P2_1/n$
a/Å	13.206(3)
b/Å	31.668(7)
c/Å	13.726(3)
α/°	90
β/°	103.374(11)
γ/°	90
Volume/Å^3	5585(2)
Z	4
ρ_{calc} g/cm^3	1.402
μ/mm^{-1}	0.484
F(000)	2448.0
Crystal size/mm^3	0.4 × 0.32 × 0.32
Radiation	MoK_α (λ = 0.71073 Å)
2Θ range for data collection/°	4.882 to 52.744
Index ranges	$-16 \leq h \leq 15$, $-38 \leq k \leq 39$, $-17 \leq l \leq 17$
Reflections collected	101465
Independent reflections	11304 [R_{int} = 0.0497, R_{sigma} = 0.0442]
Data/restraints/parameters	11304/0/723
Goodness-of-fit on F^2	1.013
Final R indexes [$I > 2\sigma(I)$]	R_1 = 0.0410, wR_2 = 0.0950
Final R indexes [all data]	R_1 = 0.0763, wR_2 = 0.1083
Largest diff. peak/hole e$^-$/Å^{-3}	0.95/-0.42

Compound 40

Identification code	Compound **40**
Crystal growth method	Slow cooling of reaction mixture in toluene
Empirical formula	$C_{87}H_{80}N_8O_{12}Ti_4$
Formula weight	1621.19
Temperature/K	100
Crystal system	tetragonal
Space group	$I4_1/a$
a/Å	21.7423(10)
b/Å	21.7423(10)
c/Å	16.3483(8)
α/°	90
β/°	90
γ/°	90
Volume/Å^3	7728.3(8)
Z	4
ρ_{calc} g/cm^3	1.393
μ/mm^{-1}	0.468
F(000)	3368.0
Crystal size/mm^3	0.6 × 0.6 × 0.4
Radiation	MoK_α (λ = 0.71073 Å)
2Θ range for data collection/°	4.874 to 54.316
Index ranges	$-26 \leq h \leq 27$, $-19 \leq k \leq 27$, $-20 \leq l \leq 19$
Reflections collected	50235
Independent reflections	4277 [R_{int} = 0.0318, R_{sigma} = 0.0177]
Data/restraints/parameters	4277/0/248
Goodness-of-fit on F^2	1.017
Final R indexes [$I > 2\sigma(I)$]	R_1 = 0.0304, wR_2 = 0.0745
Final R indexes [all data]	R_1 = 0.0380, wR_2 = 0.0794
Largest diff. peak/hole e$^-$/Å^{-3}	0.50/-0.37

Compound 41

Identification code	Compound **41**
Crystal growth method	Slow evaporation in chloroform
Empirical formula	$C_{100}H_{118}N_8O_{15}Ti_4$
Formula weight	1863.62
Temperature/K	100.15
Crystal system	monoclinic
Space group	$P2_1/c$
a/Å	21.135(3)
b/Å	16.305(2)
c/Å	27.476(4)
α/°	90
β/°	92.926(4)
γ/°	90
Volume/Å^3	9456(2)
Z	4
ρ_{calc} g/cm^3	1.309
μ/mm^{-1}	0.494
F(000)	3928.0
Crystal size/mm^3	0.21 × 0.03 × 0.03
Radiation	synchrotron (λ = 0.7749 Å)
2Θ range for data collection/°	3.758 to 45.672
Index ranges	$-20 \leq h \leq 21$, $-16 \leq k \leq 16$, $-27 \leq l \leq 27$
Reflections collected	98633
Independent reflections	9902 [R_{int} = 0.0834, R_{sigma} = 0.0396]
Data/restraints/parameters	9902/0/1086
Goodness-of-fit on F^2	1.101
Final R indexes [$I > 2\sigma(I)$]	R_1 = 0.0747, wR_2 = 0.1931
Final R indexes [all data]	R_1 = 0.0925, wR_2 = 0.2082
Largest diff. peak/hole e$^-$/Å^{-3}	0.90/-0.80

Compound 42

Identification code	Compound **42**
Crystal growth method	Slow evaporation in chloroform
Empirical formula	$C_{66}H_{66}N_6O_9Ti_3$
Formula weight	1230.94
Temperature/K	120.00(10)
Crystal system	monoclinic
Space group	*I*2/*a*
a/Å	31.297(3)
b/Å	13.9598(11)
c/Å	37.568(3)
α/°	90
β/°	101.298(7)
γ/°	90
Volume/Å^3	16095(2)
Z	8
ρ_{calc} g/cm^3	1.016
μ/mm^{-1}	2.856
F(000)	5136.0
Crystal size/mm^3	0.098 × 0.063 × 0.033
Radiation	Cu*Kα* (λ = 1.54184 Å)
2Θ range for data collection/°	6.736 to 136.498
Index ranges	$-37 \leq h \leq 37$, $-15 \leq k \leq 16$, $-44 \leq l \leq 45$
Reflections collected	143088
Independent reflections	14737 [R_{int} = 0.5403, R_{sigma} = 0.2173]
Data/restraints/parameters	14737/0/481
Goodness-of-fit on F^2	1.226
Final *R* indexes [$I > 2\sigma(I)$]	R_1 = 0.1949, wR_2 = 0.4866
Final *R* indexes [all data]	R_1 = 0.3060, wR_2 = 0.5473
Largest diff. peak/hole e$^-$/Å^{-3}	1.31/-0.67

Compound 43

Identification code	Compound **43**
Crystal growth method	Slow evaporation in chloroform (two weeks)
Empirical formula	$C_{46}H_{46}Cl_6N_4O_6Ti_2$
Formula weight	1059.37
Temperature/K	100.15
Crystal system	triclinic
Space group	*P*-1
a/Å	6.7912(3)
b/Å	11.3274(5)
c/Å	15.3400(7)
α/°	83.166(2)
β/°	79.993(2)
γ/°	86.359(2)
Volume/Å^3	1152.74(9)
Z	1
ρ_{calc} g/cm^3	1.526
μ/mm^{-1}	0.748
F(000)	544.0
Crystal size/mm^3	0.13 × 0.05 × 0.01
Radiation	MoK_α (λ = 0.71073 Å)
2Θ range for data collection/°	4.282 to 76.288
Index ranges	$-11 \leq h \leq 11$, $-19 \leq k \leq 19$, $-26 \leq l \leq 25$
Reflections collected	23703
Independent reflections	12257 [R_{int} = 0.0350, R_{sigma} = 0.0573]
Data/restraints/parameters	12257/0/291
Goodness-of-fit on F^2	1.057
Final *R* indexes [$I > 2\sigma(I)$]	R_1 = 0.0567, wR_2 = 0.1350
Final *R* indexes [all data]	R_1 = 0.0790, wR_2 = 0.1449
Largest diff. peak/hole e$^-$/Å^{-3}	0.92/-1.00

Compound 44

Identification code	Compound **44**
Crystal growth method	Slow evaporation in toluene
Empirical formula	$C_{48}H_{52}N_4O_6Ti_2$
Formula weight	876.73
Temperature/K	100
Crystal system	trigonal
Space group	*R*-3
a/Å	32.5918(18)
b/Å	32.5918(18)
c/Å	13.0510(7)
α/°	90
β/°	90
γ/°	120
Volume/Å^3	12005.8(15)
Z	9
ρ_{calc} g/cm^3	1.091
μ/mm^{-1}	0.343
F(000)	4140.0
Crystal size/mm^3	0.2 × 0.2 × 0.1
Radiation	MoK_α (λ = 0.71073 Å)
2Θ range for data collection/°	4.932 to 54.142
Index ranges	$-41 \leq h \leq 41$, $-34 \leq k \leq 41$, $-15 \leq l \leq 16$
Reflections collected	60628
Independent reflections	5842 [R_{int} = 0.0573, R_{sigma} = 0.0324]
Data/restraints/parameters	5842/0/275
Goodness-of-fit on F^2	1.082
Final *R* indexes [$I > 2\sigma(I)$]	R_1 = 0.0346, wR_2 = 0.0955
Final *R* indexes [all data]	R_1 = 0.0447, wR_2 = 0.0997
Largest diff. peak/hole e$^-$/Å^{-3}	0.31/-0.40

Compound 45

Identification code	Compound **45**
Crystal growth method	Vapour diffusion in toluene with diethyl ether
Empirical formula	$C_{86}H_{134}N_4O_9Ti_2$
Formula weight	1463.76
Temperature/K	100
Crystal system	monoclinic
Space group	*I*2/*a*
a/Å	24.5123(15)
b/Å	15.6194(6)
c/Å	25.2257(10)
α/°	90
β/°	118.263(2)
γ/°	90
Volume/Å^3	8506.7(7)
Z	4
ρ_{calc} g/cm^3	1.143
μ/mm^{-1}	0.243
F(000)	3176.0
Crystal size/mm^3	0.3 × 0.3 × 0.2
Radiation	MoK_α (λ = 0.71073 Å)
2Θ range for data collection/°	5.216 to 54.358
Index ranges	$-31 \leq h \leq 25$, $-20 \leq k \leq 19$, $-32 \leq l \leq 32$
Reflections collected	69028
Independent reflections	9266 [R_{int} = 0.0315, R_{sigma} = 0.0249]
Data/restraints/parameters	9266/33/520
Goodness-of-fit on F^2	1.036
Final *R* indexes [$I > 2\sigma(I)$]	R_1 = 0.0424, wR_2 = 0.1031
Final *R* indexes [all data]	R_1 = 0.0566, wR_2 = 0.1120
Largest diff. peak/hole e$^-$/Å^{-3}	0.46/-0.63

Compound 46

Identification code	Compound **46**
Crystal growth method	Vapour diffusion in toluene with acetonitrile
Empirical formula	$C_{42}H_{64}N_2O_4Ti$
Formula weight	708.85
Temperature/K	100.15
Crystal system	monoclinic
Space group	$P2_1/c$
a/Å	11.4250(4)
b/Å	19.9902(7)
c/Å	18.3806(7)
α/°	90
β/°	98.082(2)
γ/°	90
Volume/Å^3	4156.2(3)
Z	4
ρ_{calc} g/cm^3	1.133
μ/mm^{-1}	0.307
F(000)	1536.0
Crystal size/mm^3	0.12 × 0.11 × 0.09
Radiation	synchrotron (λ = 0.7749 Å)
2Θ range for data collection/°	4.512 to 62.314
Index ranges	$-15 \leq h \leq 15$, $-26 \leq k \leq 26$, $-24 \leq l \leq 24$
Reflections collected	48284
Independent reflections	10329 [R_{int} = 0.0564, R_{sigma} = 0.0440]
Data/restraints/parameters	10329/0/532
Goodness-of-fit on F^2	1.035
Final R indexes [$I > 2\sigma(I)$]	R_1 = 0.0627, wR_2 = 0.1584
Final R indexes [all data]	R_1 = 0.0862, wR_2 = 0.1736
Largest diff. peak/hole e$^-$/Å^{-3}	1.22/-0.75

Compound 47

Identification code	Compound **47**
Crystal growth method	Standing solution of **46** in chloroform
Empirical formula	$C_{72}H_{100}N_4O_6Ti_2$
Formula weight	1213.35
Temperature/K	100
Crystal system	monoclinic
Space group	$P2_1/c$
a/Å	9.3595(7)
b/Å	15.2046(12)
c/Å	24.0191(18)
α/°	90
β/°	90.331(3)
γ/°	90
Volume/Å^3	3418.0(5)
Z	2
ρ_{calc} g/cm^3	1.179
μ/mm^{-1}	0.286
F(000)	1304.0
Crystal size/mm^3	0.25 × 0.25 × 0.2
Radiation	MoK_α (λ = 0.71073 Å)
2Θ range for data collection/°	5.358 to 43.92
Index ranges	$-9 \leq h \leq 7$, $-11 \leq k \leq 16$, $-25 \leq l \leq 17$
Reflections collected	11387
Independent reflections	4100 [R_{int} = 0.0615, R_{sigma} = 0.0917]
Data/restraints/parameters	4100/0/391
Goodness-of-fit on F^2	1.028
Final R indexes [$I > 2\sigma(I)$]	R_1 = 0.0483, wR_2 = 0.0925
Final R indexes [all data]	R_1 = 0.0893, wR_2 = 0.1071
Largest diff. peak/hole e$^-$/Å^{-3}	0.27/-0.36

8.12 Geometrical Parameters from CSD Database

The following section contains range data plots of geometrical parameters from search queries of the CSD database. Each plot illustrates the ranges of values for a given parameter, with the mean and standard deviation for the distribution inset.

8.12.1 Ti–OH_2 and Ti–OH bond distances

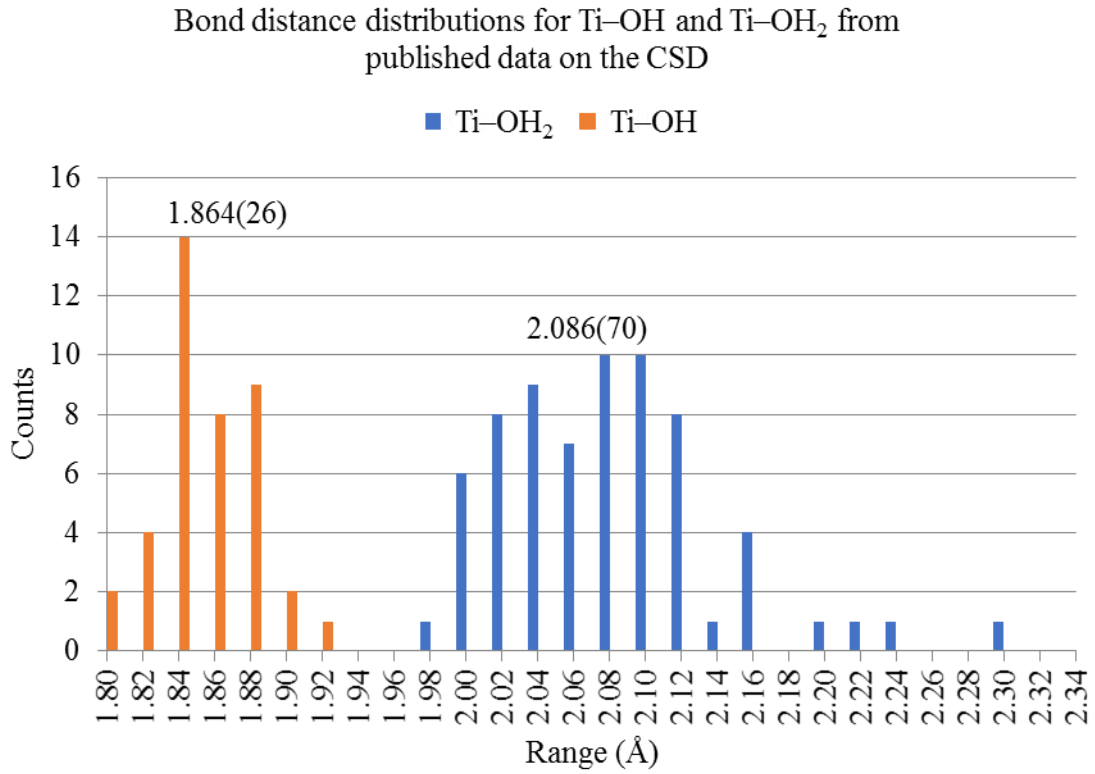

8.12.2 L-type and X-type O→Ti donor bond distances

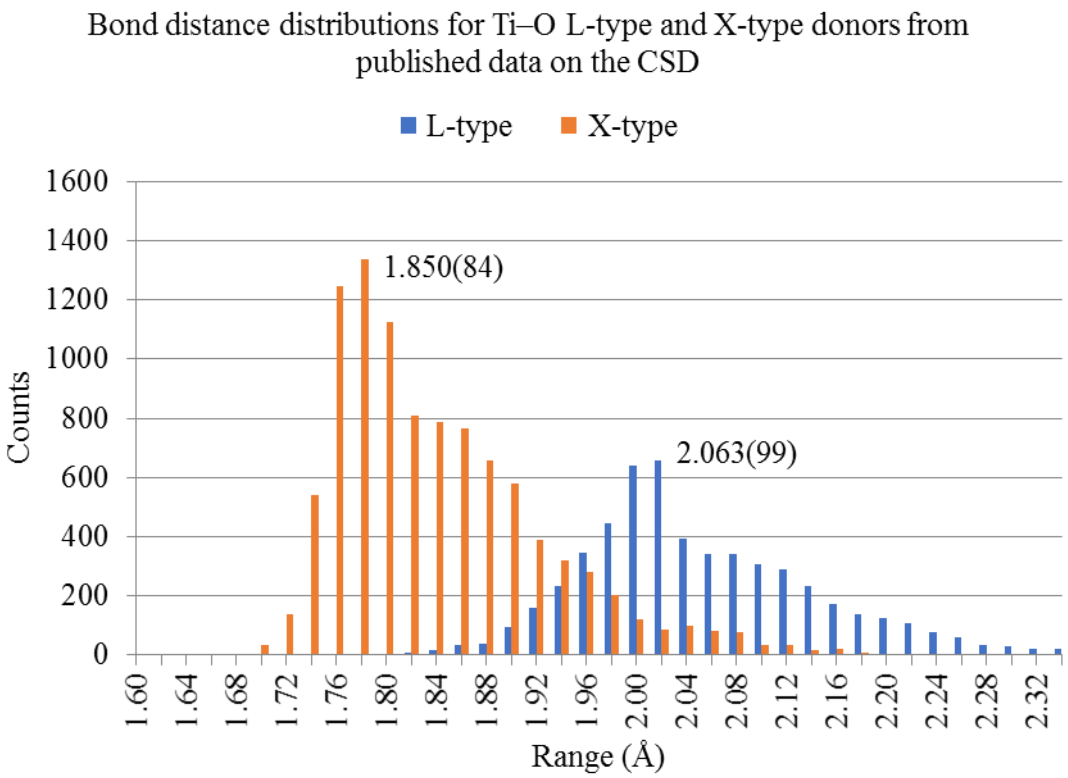

8.12.3 Ti–O distance in cyclic Ti_4O_4, Ti_3O_3 or Ti_2O_2 cores

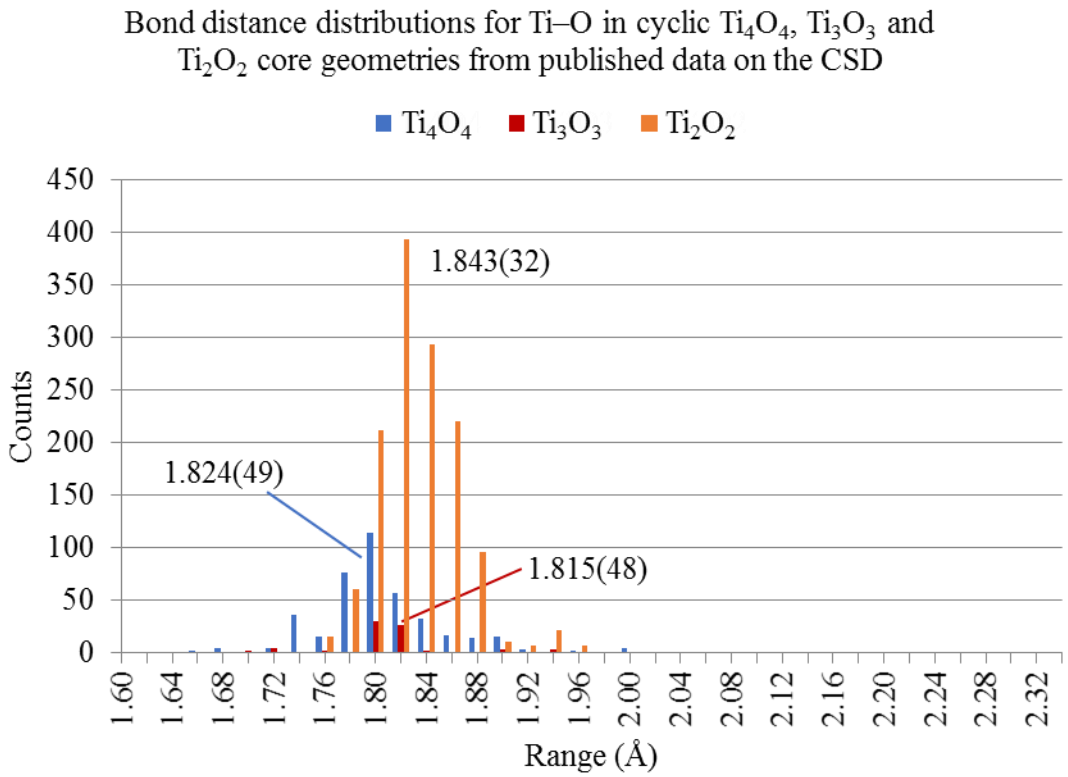

8.12.4 Ti–O–Ti and O–Ti–O angle in cyclic Ti_4O_4, Ti_3O_3 or Ti_2O_2 cores

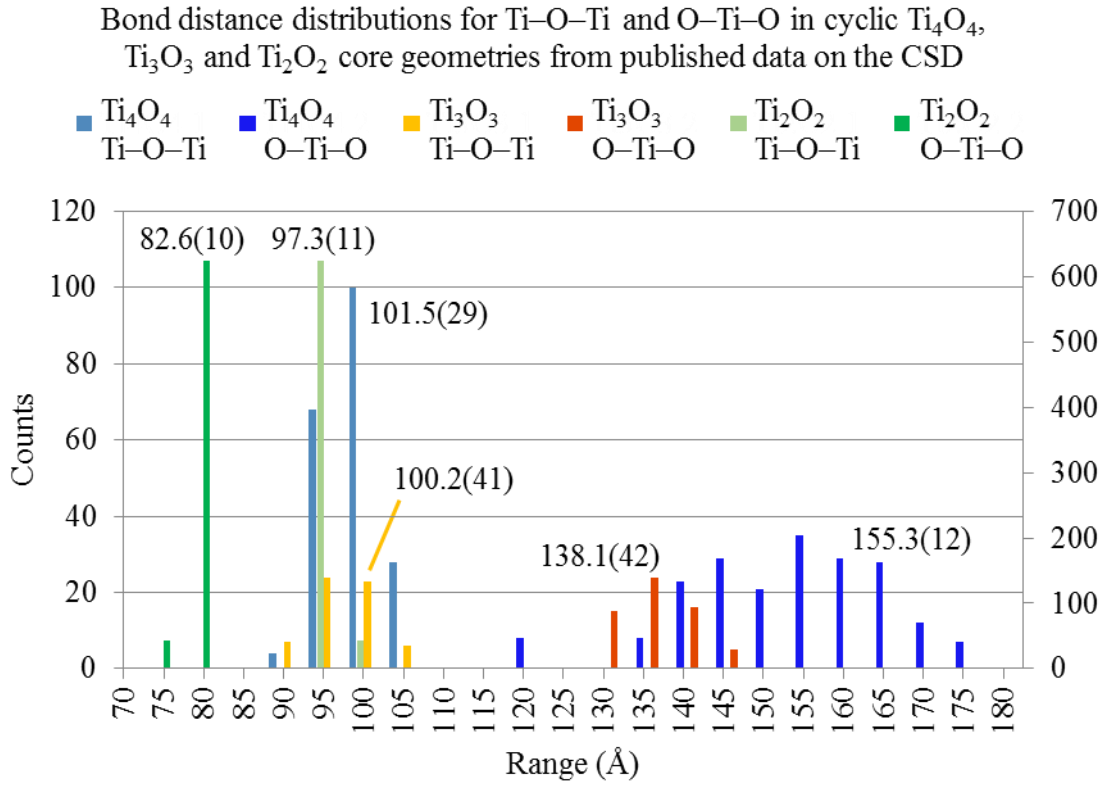

8.13 References

1. T. Biela, A. Duda and S. Penczek, *Macromol. Symp.*, 2002, **183**, 1-10.
2. Y.-L. Wong, Y. Yan, E. S. H. Chan, Q. Yang, T. C. W. Mak and D. K. P. Ng, *J. Chem. Soc., Dalton Trans.*, 1998, 3057-3064.
3. A. S. Ceccato, A. Neves, M. A. De Brito, S. M. Drechsel, A. S. Mangrich, R. Werner, W. Haase and A. J. Bortoluzzi, *J. Chem. Soc., Dalton Trans.*, 2000, 1573-1577.
4. Z. Taheri, B. Ghanbari and H. Hajibabaei, *Chem. Pap.*, 2014, **68**, 989-994.
5. E. Safaei, H. Sheykhi, A. Wojtczak, Z. Jaglicic and A. Kozakiewicz, *Polyhedron*, 2011, **30**, 1219-1224.
6. T. Weyhermuller, R. Wagner and P. Chaudhuri, *Eur. J. Inorg. Chem.*, 2011, 2547-2557.
7. H. Sopo, A. Lehtonen and R. Sillanpaa, *Polyhedron*, 2008, **27**, 95-104.
8. O. Coulembier and P. Dubois, *J Polym Sci Pol Chem*, 2012, **50**, 1672-1680.
9. R. Davila, N. Farias, E. C. Sanudo, A. Vega, A. Escuer, M. Soler and J. Manzur, *New J. Chem.*, 2016, **40**, 6164-6170.
10. J. Manzur, A. Vega and A. Escuer, *Polyhedron*, 2014, **76**, 117-121.
11. V. Kumar, S. Ghosh, A. K. Saini, S. M. Mobin and B. Mondal, *Dalton Trans.*, 2015, **44**, 19909-19917.
12. A. J. Chmura, M. G. Davidson, M. D. Jones, M. D. Lunn, M. F. Mahon, A. F. Johnson, P. Khunkamchoo, S. L. Roberts and S. S. F. Wong, *Macromolecules*, 2006, **39**, 7250-7257.
13. C. L. Boyd, T. Toupance, B. R. Tyrrell, B. D. Ward, C. R. Wilson, A. R. Cowley and P. Mountford, *Organometallics*, 2005, **24**, 309-330.
14. G. M. Sheldrick, *Acta Crystallogr., Sect A: Found. Crystallogr.*, 2015, **71**, 3-8.
15. G. M. Sheldrick, *Acta Crystallogr., Sect C: Cryst. Struct. Commun.*, 2015, **71**, 3-8.
16. O. V. Dolomanov, L. J. Bourhis, R. J. Gildea, J. A. K. Howard and H. Puschmann, *J. Appl. Crystallogr.*, 2009, **42**, 339-341.
17. A. L. Spek, *Acta Crystallogr., Sect C: Cryst. Struct. Commun.*, 2015, **71**, 9-18.